



UNIVERSITAT POLITÈCNICA
DE CATALUNYA
BARCELONATECH



Ingeniería Ambiental

Tesis Doctoral

Programa de Doctorado Interdepartamental en
Ingeniería Ambiental

Universidad Politécnica de Cataluña

Understanding the mobility of caesium, nickel and selenium released from waste disposal: Chemical retention mechanisms of degraded cement

Author: Christoph Borkel

Director: Prof. Jorge Bruno Salgot

Codirector: Dr. Mireia Grivé Solé

Ponente: Prof. Joan de Pablo Ribas

Karlsruhe, 11th November 2015

This work was funded by the EU Initial Training Network Delta-Min (Mechanisms of Mineral Replacement Reactions), Grant PITN-GA-2008-215360. In this frame Christoph Borkel was employed at Amphos 21 Consulting S.L. (Barcelona).



Passeig de Garcia i Fària, 49-51, 1^o-1^a - 08019 Barcelona

This work benefited from a grant by the *Ministerio de Educación, Cultura y Deporte*, BOE-A-2012-680 with reference MHE2011-00179, supporting the first 2-week-stage at the *Dpto. Mineralogía y Petrología, Universidad de Granada*, to characterise cement samples.

The experimental work was performed at Fundació CTM Centre Tecnològic (Manresa, Barcelona).



Plaça de la Ciència, 2 - 08243 Manresa (Barcelona)

Content

Content	3
List of figures	7
List of tables	14
Acknowledgements	17
Abbreviations	19
Solid phases	20
Abstract	21
Resumen	23
1 Introduction	25
1.1 Nuclear Waste Management Context.....	25
1.2 Cementitious Materials in the Multibarrier Concept.....	26
1.3 Radionuclide Retention Processes in Cementitious Materials.....	28
1.4 Experimental Approaches to Investigate Cement Degradation and Radionuclide Retention.....	30
1.5 Choice of Cement Type and Investigated Radionuclides.....	32
2 Objectives	36
3 State of Knowledge & Theoretical Background	39
3.1 Basic Cement Chemistry.....	39
3.2 Chemical Degradation of Hardened Cement Paste.....	42
3.2.1 Major Cement Phases Controlling Degradation Stages.....	42
3.2.2 Other Cement Phases.....	46
3.3 Contaminant Retention in a Cementitious Environment.....	48
3.3.1 General Considerations.....	48
3.3.2 Nickel.....	54
3.3.3 Selenium.....	63
3.3.4 Caesium.....	69
4 Methodology	75
4.1 Starting Material.....	75
4.1.1 Cement Clinker.....	75
4.1.2 Hardened Cement Paste.....	75
4.1.3 Solutions.....	76
4.2 Degradation Experiments.....	76
4.2.1 Batch Experiments.....	76
4.2.2 Flow-Through Experiments.....	77
4.2.3 Thermodynamic Data.....	79
4.2.4 Thermodynamic Equilibrium Approach.....	81
4.2.5 Kinetic Degradation Approach.....	82
4.3 Contaminant Retention experiments.....	83
4.4 Analytical Methods.....	84
4.4.1 Analysis of Solid Phases.....	84
4.4.2 Analysis of Aqueous Solutions.....	85
5 Results on Starting Material Properties	87
5.1 Composition of Cement Clinker.....	87
5.2 Composition of Hardened Cement Paste.....	87
6 Results on HCP Degradation	90
6.1 Batch Experiments.....	90
6.1.1 Solid Phases.....	90

6.1.2	Solutions	94
6.2	Flow-Through Experiments.....	98
6.2.1	Role of Cement Type and Mass	98
6.2.2	Degradation of Major HCP Phases in CO ₂ -‘free’, deionised water.....	98
6.2.2.1	Dissolution of Portlandite and C-S-H.....	98
6.2.2.2	Evolution of Outflow Solution pH	99
6.2.2.3	Evolution of Outflow Solution Ca Concentration	100
6.2.2.4	Evolution of Outflow Solution Si Concentration	101
6.2.2.5	Evolution of Outflow Solution Ca/Si Ratio.....	102
6.2.2.6	Mass Balances of Calcium and Silicate.....	105
6.2.3	Degradation of Major HCP Phases in Different Solutions	106
6.2.3.1	Dissolution of Portlandite and C-S-H and precipitation of calcite	106
6.2.3.2	Evolution of Outflow Solution pH	108
6.2.3.3	Evolution of Outflow Solution Ca and Si Concentrations.....	109
6.2.3.4	Mass balances of Calcium and Silicate	111
6.2.4	Colloid Generation During Experiments.....	111
6.2.5	Degradation of Minor Hardened Cement Paste Phases.....	112
6.2.5.1	Behaviour of Minor Cement Phases.....	112
6.2.5.2	Evolution of Outflow Ion Concentrations in Deionised Water	113
6.2.5.3	Evolution of Outflow Ion Concentrations in Granitic Groundwater	115
6.2.5.4	Mass Balances of Aluminium and Sulphate.....	117
6.3	Modelling of Chemical HCP Degradation	118
6.3.1	Starting Point.....	118
6.3.2	Batch Degradation Model.....	120
6.3.2.1	Solid Phases.....	120
6.3.2.2	Solutions.....	123
6.3.3	Flow-Through Degradation Model.....	126
6.3.3.1	Thermodynamic Equilibrium Model	126
6.3.3.2	Kinetic Degradation Model	128
6.3.3.2.1	Specific Assumptions and Parameters.....	128
6.3.3.2.2	Degradation of Major HCP Phases in CO ₂ -‘free’ DI Water	129
6.3.3.2.3	Degradation of Major HCP Phases in Air-Equilibrated DI Water	133
6.3.3.2.4	Degradation of Major HCP Phases in GG Water	138
6.3.3.2.5	Degradation of Minor HCP Phases in DI Water.....	142
6.3.3.2.6	Degradation of Minor HCP Phases in GG Water	145
6.4	Discussion and Conclusions from the Degradation Experiments.....	148
6.4.1	Practicability and Limitations of the Methodology	148
6.4.2	Major Cement Phases	149
6.4.2.1	Successive Stages of Degradation	149
6.4.2.2	Dissolution of C-S-H.....	152
6.4.2.3	Buffering Effects	154
6.4.2.4	Carbonation	155
6.4.3	Minor Phases	156
6.4.3.1	Incomplete Clinker Hydration.....	156
6.4.3.2	Evolution of AFm and AFt Phases	157

6.4.3.3	Buffering Effect of Brucite Precipitation	159
7	Results on Contaminant Retention by HCP	160
7.1	Nickel	160
7.1.1	Retention in Batch Conditions.....	160
7.1.1.1	Ni Solid Phases.....	160
7.1.1.2	Ni Solutions.....	170
7.1.2	Retention in Flow-Through Conditions.....	172
7.1.2.1	Ni Solid Phases.....	172
7.1.2.2	Ni Solutions.....	172
7.1.3	Discussion and Conclusions.....	172
7.2	Selenium.....	175
7.2.1	Retention in Batch Conditions.....	175
7.2.1.1	Se Solid Phases.....	175
7.2.1.2	Solutions.....	175
7.2.2	Retention in Flow-Through Conditions.....	177
7.2.2.1	Se Solid Phases.....	177
7.2.2.2	Se Solutions.....	179
7.2.3	Discussion and Conclusions.....	181
7.3	Caesium.....	183
7.3.1	Retention in Batch Conditions.....	183
7.3.1.1	Cs Solid Phases	183
7.3.1.2	Cs Solutions.....	184
7.3.2	Retention in Flow-Through Conditions.....	187
7.3.2.1	Cs Solid Phases	187
7.3.2.2	Cs Solutions.....	187
7.3.3	Discussion and Conclusions.....	188
8	Conclusions	192
9	Bibliography	199
10	Annex.....	211
10.1	Experimental Parameters.....	211
10.2	Input Files in Phreeqc Format	217
10.3	Chemical Analyses from flow-through experiments using Holcim-1 HCP.....	224
10.4	SEM-Analyses.....	230
10.5	XRD-Analyses.....	235

List of figures

- Figure 1 Conceptual illustration of the waste classification scheme of the IAEA, as published in (IAEA 2009). Wastes are distinguished by the radionuclides half-life in the waste inventory and the activity content. Additionally, general disposal options for the different waste types are given..... 26
- Figure 2 Belgian, so-called supercontainer concept for final disposal of vitrified waste resulting from reprocessing commercial irradiated fuel and non-reprocessed irradiated fuel declared as waste, reproduced in modified form from ONDRAF/NIRAS (2011). 27
- Figure 3 Schematic atomic structure of 1.4-nm tobermorite projected along [010]. Building blocks and a Dreierkette are indicated in the figure. P and B denote paired and bridging silicate tetrahedra (dark blue) with oxygen atoms at each corner (red circles). Ca atoms (light blue circles) are in 7-fold coordination with oxygen atoms. Figure modified from Richardson (2004). 40
- Figure 4 Estimation of the main degradation stages of a waste repository consisting mainly of SRPC, redrawn and modified from (Atkinson, Everitt et al. 1989). Degradation was computed by Atkinson and co-authors as a function of the water/cement ratio which then was related to time, basing on an estimated mean water flow. Both entities are given on the abscissa and link to the same graph. Thin, stippled lines are a guide for the eye. The major phases controlling the different stages are indicated in the figure. 43
- Figure 5 Abundance of crystalline cement hydrates in a degradation rim. The profile reaches from the unaltered cement to the surface where solid is in contact with bulk solution. Phase assemblages developed during 6 months contact between cement and demineralised water. Numbers on vertical axis give relative abundance with reference to the intact zone. Figure extracted from Faucon, Adenot et al. (1998). 45
- Figure 6 Structure of Ettringite, illustrated by coordination spheres of metal cations and sulphur. Blue polyhedra: Ca(II), red octahedra: Al(III), yellow tetrahedra: S(VI), blue circles: H₂O. The hexagonal frame indicates the typical macroscopic shape (extracted from Bollmann (2000)). 47
- Figure 7 Graphic illustration of the general conditions where contaminant concentration reducing processes actuate, extracted from Glasser (1997). 51
- Figure 8 Modifications in the surface structure of C-S-H due to incorporation of foreign ions from solution, observed by Mössbauer spectroscopy and NMR. Figure from Faucon, Adenot et al. (1998). 52
- Figure 9 Collection of Zeta potential (ζ) measurements, published by Pointeau, Reiller et al. (2006b). 53
- Figure 10 Comparison of experimentally determined and modelled Ni(OH)_{2(cr)} solubility (mol/l), calculated for 25°C at infinite dilution. Figure from Palmer, Bénézeth et al. (2005) with modified citations in the legend. 55
- Figure 11 Left: High Ni concentrations measured in natural waters and from experimental studies in the cement system (triangles and diamonds). Right: experimental data from solubility measurements of crystalline Ni(OH)₂. Lines in both figures give the modelled, pH-dependent solubility of Ni(OH)_{2(cr)} at 0.1 M ionic strength and the associated uncertainty. Figures extracted from Hummel and Curti (2003). 56
- Figure 12 Visualisation of the Ni-Al LDH structure, a hydrocalcite type phase (Mg-Al LDH phases). The interlayer anion can be substituted, e.g., by OH⁻, SO₄²⁻, Cl⁻ or NO₃⁻. Green balls represent oxygen atoms. Graphic extracted from Vespa, Dähn et al. (2006a). 58
- Figure 13 Backscattered electron image and elemental mapping (SEM-EDS) revealing a rim of mainly Ni-Al LDH, formed around inner C-S-H (i-C-S-H) and bordered by outer C-S-H (o-C-S-H) as well as portlandite (P). Images extracted from Vespa, Dähn et al. (2006a). 59
- Figure 14 Selenate sorption on ettringite, published by Ochs, Lothenbach et al. (2002). In batch experiments performed at 2.5 · 10⁻³ kg/l (solid/liquid ratio) the added amount of Se was varied while the sum of sulphate and selenate was kept constant. D, λ is the heterogeneous distribution coefficient the authors used to model Se uptake by ettringite (XSe). 66
- Figure 15 Evolution of the distribution coefficient for Cs sorption on Portland cement under cementitious conditions (extracted and modified from Pointeau, Coreau et al. (2008)). 72
- Figure 16 Scheme of the employed thin-layer flow-through reactor (not to scale). 77

Figure 17 X-ray diffractogram of Holcim-1 HCP after 3 years of dry storage in air. $\text{Ca}(\text{OH})_2$, CaCO_3 , aluminoferrite, Ca_3SiO_5 and Ca_2SiO_4 (orthorhombic and hexagonal modifications) were identified.	88
Figure 18 Differential thermogravimetric analyses results from Sulfadur (stippled line) and Holcim-1 HCP (solid line). Only major phases responsible for peaks are indicated in the figure.	89
Figure 19 Representative XRD patterns of the different states of degraded HCP, from freshly hydrated and sane (top pattern) to severely degraded HCP. The legend indicates the type of solution used and the L/S ratio. Reflections were assigned to phases: a aluminoferrite, c calcite, p portlandite, s bi-tricalcium silicate, e ettringite, h hydrotalcite, x artefact (aluminium sample-holder).	91
Figure 20 SEM images of HCP after batch experiments with GG water at low L/S ratio. In metal sputtered powder (left, SE image) ettringite needles are present, together with scalenohedral darker grains which are calcite and irregular shaped C-S-H. In the polished and carbon coated section of epoxy embedded grains (right, BSE image) inner and outer C-S-H (black and white arrow, respectively) and aluminoferrite (stippled arrows) are identified.	91
Figure 21 XRD diffractograms recorded after batch experiments with GG water at high L/S ratio (two almost identical patterns in green tones) and DI water (three almost identical patterns in grey tones). Notice the higher amorphous hump of the grey patterns from DI water, caused by amorphous C-S-H.	92
Figure 22 SEM images of cement after batch experiments at high L/S ratio with GG water. In metal sputtered powder (left, SE image) idiomorphic calcite rhombohedra are surrounded by irregular shaped C-S-H. In the polished and carbon coated section of epoxy embedded grains (right, BSE image) the rhombohedral shape of calcite crystals, which are randomly dispersed in the epoxy resin (black), can still be recognised. The white arrow points to inner C-S-H which is surrounded by fibrillar outer C-S-H. Brightest spots are aluminoferrite.	92
Figure 23 Polished section of a Sulfadur HCP sample after a batch experiment at $L/S = 0.1 \text{ m}^3/\text{kg}$ in GG water. Indicated are the two distinct morphologies of sluggishly reacting aluminoferrite.	94
Figure 24 Solution composition after batch experiments as given in Table 18. Dashes with arrows indicate maximum concentrations with concentrations below detection limit.	96
Figure 25 Diagram visualising repartition of HCP inherent elements after degradation at both L/S ratios (negative values indicate diminution). For experiments with GG water (black symbols) the yielded contribution of elements from GG water was subtracted from the measured concentrations before calculating repartitions. Each data point was derived from 2 to 4 individual experiments.	97
Figure 26 XRD diffractograms of sane Holcim-1 HCP and of degraded HCPs after short FL4, as well as after long flow-through experiment FL7. Since measurement conditions were different in each case, diffractograms are offset in y-direction and rescaled for comparability. Note that portlandite (red bars) is absent from diffractograms of both degraded HCPs. Reflections of dicalcium silicate are most important in sane HCP (highlighted by arrows) and decrease significantly in HCP from experiment FL4 until they disappear in experiment FL7 (discussed in chapter 6.2.5.1).	99
Figure 27 Evolution of pH, measured in outflow solutions of flow-through experiments with Sulfadur (FLS1) and Holcim-I HCP. Size of symbols corresponds to the error of pH measurement. Dashed lines highlight changing trend in pH decrease at around $1.5 \text{ m}^3/\text{kg}$ degree of leaching.	100
Figure 28 Evolution of Ca concentration, measured in outflow solutions of flow-through experiments with Sulfadur (FLS1) and Holcim-I HCP. Four last samples above $20 \text{ m}^3/\text{kg}$ have a mean Ca concentration of $3.6(\pm 0.7) \cdot 10^{-5} \text{ mol/l}$	101
Figure 29 Evolution of Si concentration, measured in outflow solutions of flow-through experiments with Sulfadur (FLS1) and Holcim-I HCP.	102
Figure 30 Ratio between measured Ca and Si concentrations in outflow solutions of flow-through experiments with Sulfadur (FLS 1) and Holcim-I HCP.	103
Figure 31 Aqueous speciation of Ca and Si as function of pH, calculated with the Cemdata07 database. Total Ca and Si concentrations are constant at 10^{-4} mol/l and 10^{-6} mol/l , respectively, and ionic strength is 0.1 mol/l . Species with fractions < 0.001 are omitted in the figures.	104
Figure 32 Calculated pH based on Ca and Si concentrations versus experimentally measured pH (FL9). ...	105

- Figure 33 XRD pattern stack from degraded Sulfadur HCP samples after flow-through experiments. All patterns were recorded at the same conditions. The ordinate scale is measured intensity, but patterns were offset from zero. Experiments with DI water are shown in green. Blue tones are used for GG water and sane Sulfadur HCP is shown in black. FLS 1 has lower relative intensity as the sample holder could not be entirely filled. Peaks are assigned as follows: c calcite, p portlandite, a aluminoferrite and s di-/tricalcium silicate. Sane HCP was analysed with a different sample holder and the reflection marked 'x' is an artefact from this sample holder. 106
- Figure 34 Flow-through experiments FLS 8 (blue), FLS 11 (orange) and FLS 15 (green) with GG water. Experiment FLS 8 which has higher background intensities was stopped after short time (see text). Notice the higher amorphous hump in the diffractogram from FLS8, alongside with lower intensity of calcite reflections (highlighted by arrows), compared to the two longer experiments..... 107
- Figure 35 Evolution of pH versus degree of leaching in course of flow-through experiments. On the left hand side only results from the initial stages of reaction up to 3 m³/kg are shown to highlight differences between the individual series. On the right hand side all data is shown. Symbols: grey - experiments with Holcim-1 HCP and CO₂-'free' DI water, green - experiments with Sulfadur HCP and varying CO₂(aq) concentration in DI water, coloured - experiments with Sulfadur HCP and GG water. Errors correspond to or are smaller than symbols. The blue, stippled line gives pH of pure GG water as a reference. 108
- Figure 36 Evolution of pH, Si and Ca concentrations in outflow solutions with time. Measured concentrations are all given in mol/l. Black symbols: Experiments with Holcim-1 HCP in DI water. Green symbols: experiments with Sulfadur HCP in DI water, coloured symbols: experiments with Sulfadur HCP in GG water. Concentrations in GG water input solution are indicated by blue, stippled lines. Where helpful, results are split into two graphs, from 0 to 25 · 10³ s in the left column and the full experimental length in the right column..... 110
- Figure 37 Ratio between measured Ca and Si concentrations in outflow solutions of flow-through experiments with DI water of varying CO₂(aq) content and GG water. The black line indicates Ca/Si ratio of unity. 111
- Figure 38 SEM backscattered electron image of epoxy embedded and polished HCP grain after a flow-through experiment using DI water equilibrated in ambient air. Aluminoferrite's honeycomb structure (bright in image) is maintained while C-S-H, formerly filling the voids, is partly dissolved..... 113
- Figure 39 Evolution of S(VI) and Al concentrations in outflow solutions with time. Measured concentrations are all given in mol/l. Black symbols: Experiments with Holcim-1 HCP in CO₂-'free' DI water. Green symbols: experiments with Sulfadur HCP in DI water with varying CO₂ content. 115
- Figure 40 Evolution with time of Al, S(VI) and Mg concentrations in outflow solutions. Measured concentrations are given in mol/l. Green symbols: experiments with Sulfadur HCP and DI water. Coloured symbols: experiments with Sulfadur HCP and GG water. Base load concentrations in GG water input solution are indicated by blue, stippled lines..... 116
- Figure 41 Computed evolution of solid phases as a function of added DI (top figure) and GG water (bottom figure) volumes, expressed as L/S ratio. 121
- Figure 42 Computed evolution of C-S-H amount and composition as function of added solution in batch experiments, expressed as L/S ratio. Figures show the influence of the solution that is used by comparing DI water (left) with GG water (right). 122
- Figure 43 Comparison between computed (lines) and measured (points) ion concentrations and pH from batch experiments with DI water (left column) and GG water (right column), plotted as a function of L/S ratio. Due to large differences in concentrations and keep decimal scale the top figures give elements at higher concentrations while the bottom figures give elements at lower concentrations. 124
- Figure 44 Diagram visualising calculated repartition of HCP inherent elements after degradation at both experimental L/S ratios (negative values indicate diminution). For experiments with GG water (black symbols) the yielded contribution of elements from GG water was subtracted from the measured concentrations before calculating repartitions. The diagram is analogous to Figure 25 giving mass balances from experiments..... 125

Figure 45 Comparison between computed (lines) and measured (points) ion concentrations and pH from flow-through experiments with air-equilibrated DI water, plotted versus time. Computed values base on the thermodynamic equilibrium approach.	127
Figure 46 Kinetic degradation model: Computed evolution of solid phases during degradation of cement in the flow-through reactor using CO ₂ -free DI water. Phases are shown in two plots for major (top) and minor (bottom) phases to avoid logarithmic scale.	130
Figure 47 Kinetic degradation model: Comparison between computed (lines) and measured (points) ion concentrations (in mol/l) as well as pH from flow-through experiments with CO ₂ -‘free’ DI water, plotted versus time. To represent data in decimal scale two diagrams are shown per element, representing only the initial phase (left column) and the entire length of experiments (right column).	131
Figure 48 Kinetic degradation model with reduced amount of water-accessible C-S-H: Comparison between computed (lines) and measured (points) ion concentrations (in mol/l) with CO ₂ -‘free’ DI water, plotted versus time. The dotted line represents calculation results obtained with 25 % C-S-H reactive, the dashed line 50 % and the long-dashed line 75 %.	132
Figure 49 Kinetic degradation model with reduced amount of water-accessible C-S-H: Comparison between computed (lines) and measured (points) ion concentrations (in mol/l) as well as pH from flow-through experiments with CO ₂ -‘free’ DI water, plotted versus time. To represent data in decimal scale two diagrams are shown per element, representing only the initial phase (left column) and the entire length of experiments (right column).	133
Figure 50 Kinetic degradation model: Computed evolution of solid phase dissolution and precipitation during degradation of cement in the flow-through device, reacting with ambient air (CO ₂) equilibrated DI water. Phases are shown in two plots for major (top) and minor (bottom) phases to avoid logarithmic scale.	134
Figure 51 Kinetic degradation model with reduced amount of water-accessible C-S-H: Computed evolution of solid phase dissolution and precipitation during degradation of cement in the flow-through device, reacting with ambient air (CO ₂) equilibrated DI water. Phases are shown in two plots for major (top) and minor (bottom) phases to avoid logarithmic scale.	135
Figure 52 Kinetic degradation model: Comparison between computed evolution of pH in flow-through experiments with CO ₂ -‘free’ DI water (orange line), with ambient air (CO ₂) equilibrated DI water (black line) and measured pH (points). Notice that both model results do not reproduce the sudden pH drop after 75·10 ³ s which is observed experimentally with ambient air equilibrated DI water.	136
Figure 53 Kinetic degradation model with reduced amount of water-accessible C-S-H: Comparison between computed (lines) and measured (points) pH with air (CO ₂) equilibrated DI water, plotted versus time. The dotted line represents calculation results obtained with 25 % reactive C-S-H, the dashed line 50 % and the long-dashed line 75 %.	137
Figure 54 Kinetic degradation model with reduced amount of water-accessible C-S-H: Comparison between computed (lines) and measured (points) ion concentrations (in mol/l) as well as measured pH from flow-through experiments with ambient air (CO ₂) equilibrated DI water, plotted versus time. To represent data in decimal scale two diagrams are shown per element, representing only the initial phase (left column) and the entire length of experiments (right column).	138
Figure 55 Kinetic degradation model: Computed evolution of solid phase formation and dissolution during degradation of Sulfadur HCP in the flow-through experiments due to reaction with GG water. Results for major and minor phases are split into two diagrams for visibility and plotted versus time.	139
Figure 56 Kinetic degradation model: Comparison between computed (thick lines) and measured (points) ion concentrations (in mol/l) as well as measured pH from flow-through experiments with GG water, plotted versus time. To represent data in decimal scale two diagrams are shown per element, representing only the initial phase (left column) and the entire length of experiments (right column).	141
Figure 57 Kinetic degradation model with reduced amount of water-accessible C-S-H: Comparison between computed (thick lines) and measured (points) ion concentrations (in mol/l) as well as measured pH from flow-through experiments with GG water, plotted versus time. To represent data in decimal	

- scale two diagrams are shown per element, representing only the initial phase (left column) and the entire length of experiments (right column). 142
- Figure 58 Kinetic degradation model with reduced amount of water-accessible C-S-H: Comparison between computed (thick lines) and measured (points) ion concentrations (in mol/l) from flow-through experiments with DI water, plotted versus time. To represent data in decimal scale two diagrams are shown per element, representing only the initial phase (left column) and the entire length of experiments (right column). 144
- Figure 59 Kinetic degradation model with reduced amount of water-accessible C-S-H: Comparison between computed (thick lines) and measured (points) ion concentrations (in mol/l) from flow-through experiments with GG water, plotted versus time. To represent data in decimal scale two diagrams are shown per element, representing only the initial phase (left column) and the entire length of experiments (right column). 147
- Figure 60 Characteristic evolution of HCP degradation under the investigated conditions. Different stages are indicated in the figure and refer to a system of air-equilibrated DI water (red). In all solutions stages (I_{FL} – III_{FL}) establish, but stage (b) only applies for CO₂(aq) containing water, indicating the moment when carbonate buffering leads to drop of pH. 150
- Figure 61 Plot of mean measured aqueous concentrations of Si versus Ca after batch experiments. Experimental results from degradation of Sulfadur HCP (coloured points) are compared with data from solubility measurements of pure C-S-H phases by Chen, Thomas et al. (2004). They assigned C/S ratios to corresponding C-S-H phases and indicated dissolution behaviour of different types of C-S-H by lines. The vertical line 'CH' gives the thermodynamic solubility limit of portlandite. Lines A and B border the range of possible Ca and Si concentrations in equilibrium with C-S-H. Lines C and C'' indicate different trends of solubility for C-S-H phases synthesised in different ways. 152
- Figure 62 Plot showing the dependence of pH on different concentrations of dissolved CO₂(aq), derived with Phreeqc and the Cemdata07 database. The abscissa gives the pH of alkaline solution free of CO₂ and the ordinate gives pH of the same solution after addition of CO₂(aq) concentrations corresponding to GG water and atmosphere (p(CO₂) = -3.26) equilibrated DI water. Black, dashed line has slope 1 and is inserted only for comparison. 155
- Figure 63 SEM-BSE image and analysed spots of Sulfadur HCP sample B6 after equilibration. The bright rim surrounding the left grain is the Ni bearing phase, here called 'nickel-rim'. The enclosed C-S-H like phase and the other grain on the right hand side are identical in composition. Experimental conditions and mean compositions of the phases, obtained from SEM-EDX, are given in the tables. Individual analyses can be found in Table 35 of annex 10.4. 161
- Figure 64 Photographs (not colour edited) of HCP after batch experiments with 2 m³/kg L/S ratio. Added Ni concentrations are indicated in the figure. Images from experiments with DI water show HCP in contact with solution and images of HCP from experiments with GG water shows the dried filtrate. Note the solids change in appearance with high Ni concentration. Images were made from duplicate experiments and better quality images selected (therefore round and rectangular containers for DI water experiments). 162
- Figure 65 Comparison of XRD diffractograms from blank experiment B9 (bottom, step size 0.02 ° and count time 2 s) and experiment B10 (bottom, step size 0.008 ° and count time 5 s) with high Ni load, both equilibrated with DI water at 2 m³/kg L/S ratio. Note that the diffractogram of HCP from experiment B10 was recorded with an X-ray beam not properly focused. 163
- Figure 66 Comparison of XRD diffractograms (step size 0.02 ° and count time 2 s) from blank experiment B13 (bottom) and experiment B14 with high Ni load, both equilibrated with GG water at 2 m³/kg L/S ratio. Note that diffractogram of HCP from experiment B14 was recorded with not properly focused X-ray beam. 163
- Figure 67 Comparison of XRD diffractograms from the same degraded HCP sample measured directly after experiments (black) and after two years storage (red), as well as from a duplicate experiment after two years storage (orange). Aragonite reflections are indicated by blue sticks. Samples are from experiments with DI water and high Ni load at high L/S ratio. Note that diffractogram of HCP from experiment B10 (bottom) was recorded with not properly focused X-ray beam. 164
- Figure 68 Comparison of XRD diffractograms from the same degraded HCP sample measured directly after the experiment (black) and after two years storage (red). Additionally, a diffractogram from a duplicate experiment after two years storage is shown (blue). Aragonite reflections are indicated by

- blue sticks. Samples are from experiments with GG water and high Ni load at high L/S ratio. Both upper diffractograms were recorded with step size 0.015° and count time of 5 s/step while the measurement shortly after the experiment was made with 0.02° step size and count time of 2 s/step. 165
- Figure 69 XRD diffractograms recorded after two years storage in air of degraded HCP at high L/S ratio. Samples B9, B12 and B13 were not doped with Ni while sample B24 was equilibrated with 10^{-7} mol/l Ni in GG water. Note the reflection occurring at $18.58^\circ 2-\Theta$ in sample B9..... 165
- Figure 70 SEM-BSE image from polished powder after experiment B14. Very bright phases are aluminoferrite, dispersed medium-bright minerals are calcite and the grey matrix is Ni-S-H. Experimental conditions and the mean composition of Ni-S-H, obtained from SEM-EDX analyses of 11 individual spots, are given in the tables. Individual analyses can be found in annex 10.4... 166
- Figure 71 Upper left: SEM-BSE image of sample B14, equilibrated at $2 \text{ m}^3/\text{kg}$ L/S ratio with GG water. The grey matrix (analysis spots 1, 2 and 3) is Ni-S-H phase. The red circle indicates the Ni-ring which is shown enlarged in the upper right image. C-S-H with C/S ratio 0.8 is indicated by analysis spot 7. Bottom: SEM-BSE image of sample B6, equilibrated at $0.1 \text{ m}^3/\text{kg}$ L/S ratio with GG water. Analysis spots 1,3,4,5 correspond to C-S-H phase. Notice similarity of cracks in C-S-H from sample B6 compared to cracks in Ni-S-H phase from sample B14..... 168
- Figure 72 Plot of mean measured aqueous concentrations of Si versus Ca after batch experiments without and with $5 \cdot 10^{-4}$ mol/l Ni. Results from both degradation stages of Sulfadur HCP (coloured points) are compared in the solubility diagram of pure C-S-H phases by Chen, Thomas et al. (2004) which is already shown in Figure 61. The right figure is a zoom on results from high L/S ratio which is also included in left figure. Arrows indicate lower concentrations in high Ni concentration experiments compared to blank experiments. 171
- Figure 73 Sorption isotherms of Se(VI) on Sulfadur HCP after equilibration at $0.1 \text{ m}^3/\text{kg}$ L/S ratio and pH 12.5. With each solution three sorption experiments were performed at initial concentrations of $9.95 \cdot 10^{-7}$ and $9.95 \cdot 10^{-5}$ mol/l. Stippled lines indicate slope of 1. 176
- Figure 74 SEM-EDX element maps of loose Sulfadur HCP powder from a flow-through experiment with air-equilibrated DI water and $7.6 \cdot 10^{-6}$ mol/l Se(VI) concentration (FLS10). At the bottom is an SE image of the area corresponding to elemental maps. Note that distributions of Al, Ca, S and Si show similar patterns. 178
- Figure 75 Breakthrough plot of Se(VI), giving the ratio of measured outflow solution concentration (C) and spiked input solution concentration (C_0) for flow-through experiments with DI and GG water and varying Se(VI) concentration..... 179
- Figure 76 Concentrations of Se(VI) and S(VI) in outflow solution from two experiments with equal initial Se(VI) concentration of $7.75 \cdot 10^{-5}$ mol/l. Note that S(VI) concentration in GG water is always higher than Se(VI) concentration..... 180
- Figure 77 Fitting of retardation factors to experimentally measured Se(VI) concentration in outflow solution at the beginning of experiments. To obtain the stippled lines retardation factor was varied between 24 and 36. Only initial, stronger Se(VI) retention is considered, why computed lines approach $C/C_0 = 1$ very fast. 181
- Figure 78 Measured Cs concentrations from batch experiments equilibrated at $0.1 \text{ m}^3/\text{kg}$ L/S ratio with DI water (left) and GG water (right). Blank experiments without Cs addition and experiments with $1 \cdot 10^{-7}$ mol/l added Cs are compared. 184
- Figure 79 Measured Cs concentrations from batch experiments equilibrated at $2 \text{ m}^3/\text{kg}$ L/S ratio with DI water (left) and GG water (right). Blank experiments without Cs addition and experiments with $1 \cdot 10^{-7}$ mol/l added Cs are compared. 185
- Figure 80 Measured Cs concentrations in outflow solutions from flow-through experiments without added Cs (filled squares) and with varying Cs addition (other symbols). 188
- Figure 81 Comparison of measured $R_{d,bc}$ and calculated K_d values according to Ochs, Pointeau et al. (2006) at equilibrium conditions. The dashed line indicates equality between measured and calculated values. Solution type, L/S ratio and the experiment number are given in the legend. Dash signs represent experiments with final pH 11.55-11.65 and geometric symbols represent experiments at pH 12.5. 189

Figure 82 Cement samples, analysed by FESEM after flow-through experiments with Holcim-1 HCP. Points and areas marked in figures were analysed for elements and results are shown in Table 34.....	230
Figure 83 SEM-EDX spectrum of Ni-rim from experiment B6.....	232
Figure 84 SEM-EDX spectrum of Ni-ring from experiment B14.....	233
Figure 85 SEM-EDX spectrum of Ni-S-H (spot 1) from experiment B14.....	234
Figure 86 XRD diffractograms of A) Holcim-1 clinker - only C3S and brownmillerite were identified and B) 28 days long hydrated Holcim-1 HCP, shortly after hardening. C3S, brownmillerite, portlandite and CaCO ₃ were identified (all work for these 2 figures was performed previously by CTM).....	235
Figure 87 X-ray diffractogram of sample B5 and identified phases.	236

List of tables

Table 1 Cement types specified in the European norm EN(V) 197-1.	39
Table 2 Summary of cement chemist notation. It uses capital letters (left) to account for oxides (right column) in abbreviated form. Lowercase letters (left column) are used to give stoichiometric information when appropriate (right).	40
Table 3 Mean solid composition of hydrated Portland cement as given by Berner (1992).	41
Table 4 Summary of sorption study results investigating Ni retention on different cement formulations and C-S-H phases.	61
Table 5 Summary of suggested Ni retention mechanisms and solubility limiting phases.	62
Table 6 Summary of sorption study results investigating Se(VI) retention on different cement formulations and single solid phases.	68
Table 7 Summary of sorption study results investigating Cs retention on different cementitious materials formulations and C-S-H.	74
Table 8 Chemical composition of artificial granitic groundwater as added from the reactants, prepared according to a recipe by Vuorinen and Snellman (1998). In laboratory atmosphere pH was stable at 8.17.	76
Table 9 Conditions of flow-through experiments with Holcim-1 HCP. Two CO ₂ -‘free’ input solutions were used: pure deionised water and 0.1 mol/l NaClO ₄ solution.	79
Table 10 Experimental parameters in flow-through experiments with Sulfadur HCP.	79
Table 11 CSH3T model with 4 bridging tetrahedral interlayer sites as suggested by Kulik (2011). Dissolution reactions according to Table 12.	81
Table 12 CSH3T model, recalculated and adapted for consistency with Cemdata07 in Phreeqc format.	81
Table 13 Overview on flow-through experiments with Sulfadur HCP in which Cs(I), Ni(II) or Se(VI) were added to input solution.	84
Table 14 Cement composition from duplicate XRF analysis. Results are given in wt.% of the oxides, referring to the ignited mass which was determined from TGA. Results for Na (<i>narrowed</i>) are below calibration limit of 0.5 wt.%. The given mineralogical compositions were determined according to the (modified) Bogue-method.	87
Table 15 Mineralogical composition of HCPs. Where determined by TG analysis, mineral content is given in wt.-% referring to the mass of HCP at laboratory conditions. For details on the indicated calcium carbonate content in Sulfadur HCP see explanations given in text.	89
Table 16 Phase assemblies formed during batch experiments with Sulfadur HCP in GG and DI water.	90
Table 17 Compositions of C-S-H phases from HCP degraded in GG water at both L/S ratios. Mean concentrations and standard deviations from semi-quantitative SEM-EDX analysis of 14 individual points and corresponding C/S ratios are given.	93
Table 18 Solution composition after batch experiments with Sulfadur HCP. Values are means from 2 to 6 individual experiments and errors give corresponding standard deviation. Only S(VI) concentrations at low L/S ratio are from single analyses and give analytical errors. Concentrations are given in μmol/l (10 ⁻⁶ mol/l) for all elements.	95
Table 19 Cumulated loss of Ca and Si mobilised from Holcim-1 and Sulfadur HCP during degradation experiments with CO ₂ -‘free’ DI water, referred to the sane HCPs.	105
Table 20 Cumulated loss of Ca and Si mobilised from Sulfadur HCP during degradation experiments with GG water and varying CO ₂ (aq) content in DI water, referred to the sane HCP. ‘Air equilibrated’ is abbreviated ‘air eq.’	111
Table 21 Cumulated loss of Al and S(VI) mobilised from Holcim-1 HCP during degradation experiments, referred to the sane HCP. For mass balances of S(VI) in GG water systems see explanation in the main text.	117
Table 22 Composition of sane Sulfadur HCP used for modelling.	118
Table 23 Compliance of modelled with measured elemental inventories of sane Sulfadur HCP.	119

Table 24	Surface area and kinetic dissolution rate constants used for modelling flow-through experiments.....	128
Table 25	Possible mineral compositions of the different Ni phases, based on SEM-EDX analyses and charge-balance. Since we do not have information on contents of water in the lattice, H ₂ O is omitted in molar weights.....	169
Table 26	Maximum amounts of Ni phases that may form if all added Ni (0.5 mmol/l) precipitates as one of these phases. Molar weight used for calculations is specified in Table 25.....	169
Table 27	Comparison of experiments without Ni and with high initial Ni concentration of 0.5 mmol/l, equilibrated at high and low L/S ratio with DI and GG water.....	170
Table 28	Measured Cs concentrations in equilibrated solutions and mobilised Cs from Sulfadur HCP inventory, all from experiments where Cs was not added. Results are given for different L/S ratios, solution types, and Ni concentrations.....	186
Table 29	Distribution coefficients R _{d,bc} for Cs adsorption on severely degraded HCP at 2 m ³ /kg L/S ratio. All solutions were spiked with 10 ⁻⁷ mol/l CsCl and NiNO ₃ , as well as variable amounts of Na ₂ SeO ₄ . Ca, Na and K concentrations are approximated quantities, derived from experiments without Cs addition.....	187
Table 30	Experimental conditions and results from batch experiments with Sulfadur HCP. Red number indicate quantification below the lower linear calibration limit.....	211
Table 31	Conditions of flow-through experiments. Experiment FL 1 was carried out open to the atmosphere; all other experiments were performed in N ₂ atmosphere. Sample names are composed of the columns “experiment series” and “sample”, e.g., the outflow solution (20 ml) of experiment “FL 1-4” was collected between 2630 and 3550 s after start of experiment. The cement mass is given as weighed in the laboratory before starting degradation of cement.....	213
Table 32	Experimental conditions of flow-through experiments with Sulfadur HCP.....	215
Table 33	A and B: Flow-through experiment performed in ambient air and N ₂ atmosphere, respectively. All concentrations given in mol/l. Red colour indicates values below, blue indicates values above linear calibration range and yellow background flags results lying less than 10 % out of linear calibration range. Where concentrations show “<<<”, there was no quantifiable signal detected. Each experimental series is represented in one block, divided in two parts: The upper part giving all information making strict exclusions basing on analytical detection limits; the lower part of each block (marked as <i>italics</i>) giving only the quantifications of samples that were identified out of calibration range in the upper part.....	224
Table 34	Results from point analyses and line scan areas indicated in Figure 82. First column indicates elements including which electron transfer was used for quantification. Results are given in atomic percent. In the lower part ion correlations are shown.....	231
Table 35	Single-spot analyses from sample B6, reported in At.-%. Instrument and correction parameters: kV : 15.01 Tilt: 0.00 Take-off:35.03 AmpT: 102.4., Detector Type: SUTW, Sapphire Resolution:129.39 Lsec:30, EDAX ZAF Quantification (Standardless), Oxygen by difference, calculated without carbon to 100 % element sum. Sample spots are indicated in Figure 63.....	232
Table 36	Ni-S-H single-spot analyses from sample B14, reported in At.-%. Instrument and correction parameters: kV : 15.01 Tilt: 0.00 Take-off:35.03 AmpT: 102.4., Detector Type: SUTW, Sapphire Resolution:129.39 Lsec:30, EDAX ZAF Quantification (Standardless), Element Normalised, calculated without carbon to 100 % element sum.....	232

Acknowledgements

A number of people have generously given time, advice, encouragement and valuable input during this research study. I am particularly grateful to my supervisors Jordi Bruno and Mireia Grivé for accepting this topic, for providing me an inspiring working environment at Amphos 21 and for their patience and knowledge. Their review of earlier versions of this document helped me finishing this thesis. Jordi's idea of using the thin-layer flow-through reactor with cementitious material was the starting point of my study, which then took me to exciting research issues.

My sincere thanks also go to Joan de Pablo who first was my tutor and then took over as "ponente" for my work.

From Amphos 21 I also thank my former colleagues of the WBCC group, Alba, Carolina, Cristina, David, Eli, Laurent, Maria, Mireia, Olga, Teresa and Vanessa. I miss the group and the nice time we had a lot.

The team of CTM gave me access to laboratory and research facilities. Without their support it would not have been possible to conduct this research. I am particularly grateful to Miquel Rovira who reviewed my research plan, to Neus Bahí for organizing work in the lab and to Isabel Rojo, Sandra Meca, Iban Gonzalez and Xavier Martínez for help with analytics as well as for practical experimental advice. Thanks to my PhD-colleagues at CTM Albert, Gemma, Laia, for making hard days in the office or lab shorter.

Carlos Rodríguez-Navarro invited me twice to the University of Granada. I am very grateful for having had this opportunity, for the discussions and for Carlos' valuable support and guidance during my stays. From the UGR I also thank Daniel Martín for his advice on and help with XRD analysis and introduction to Xpoder. Thanks to my PhD colleagues Eduardo, Iñaki, Krzysztof, Mara and Vanesa for discussions, help with the instruments and the nice time in Granada!

I thank the Deltamin-members for the pleasant as well as productive meetings and especially Andrew Putnis for all his efforts to set up this network and his great interest in motivating and encouraging the younger generation.

Furthermore, I thank Ignasi Casas as well as Oriol Font for facilitating access to the planetary ball mill at CSIC.

Thanks to Elisenda Seguí from the Universitat de Barcelona for assistance with XRF measurements. I also thank David Parkhurst who helped me out with advice when I got stuck in the Phreeqc modelling.

I am sincerely grateful to Horst Geckeis, Bernhard Kienzler and Volker Metz from INE for encouraging me to finish this work, which I started some years ago. Thanks also to my long-term roommate Vanessa for discussions on several topics and to Ernesto for the great help in translating the abstract.

Besonders dankbar bin ich Franziska dafür, dass sie mich immer darin unterstützt hat, diese Arbeit fertigzustellen. Sie hat den gesamten Text gelesen und mir dabei geholfen, meine Gedanken verständlicher zu machen. Henri und Theo danke ich dafür, dass sie die unkompliziertesten Babys der

Welt sind und auch während der langen Abende und Wochenenden nie aufgehört haben, mich anzulächeln.

Abbreviations

BET surface area	Method developed by Brunauer, Emmett and Teller to determine specific surface area of porous, solid material by gas adsorption
BFS	Blast Furnace Slag
BSE	BackScattered Electron (in Scanning Electron Microscopy)
C/S ratio	Molar Ca/Si ratio of C-S-H phase
Ca/Si ratio	Molar Ca/Si ratio of aqueous solutions
DIW / DI water	Delonised Water
EDX	Energy-Dispersive X-ray spectroscopy (in Scanning Electron Microscopy)
ENRESA	Empresa Nacional de Residuos Radioactivos S.A. (National Company for Radioactive Wastes)
GGW / GG water	Granitic GroundWater
HCP	Hardened Cement Paste
HLW	High Level Waste
ICP-MS	Inductively Coupled Plasma Mass Spectrometry
ILW	Intermediate Level Waste
L/S ratio	Liquid to Solid ratio (m ³ /kg) used in experiments
LLW	Low Level Waste
NEA	Nuclear Energy Agency
NRVB	Nirex Reference Vault Backfill
OECD	Organisation for Economic Co-operation and Development
OPC	Ordinary Portland Cement
PFA	Pulverised Fly Ash
SE	Secondary Electron (in Scanning Electron Microscopy)
SF	Silica Fume
SEM	Scanning Electron Microscopy
SHE	Standard Hydrogen Electrode
SKB	Svensk Kärnbränslehantering AB (Swedish Nuclear Fuel and Waste Management Company)
SRPC	Sulphate Resisting Portland Cement
w/c ratio	Water to binder ratio (l/kg, kg/kg) for hydration of cement clinker to form HCP
XRD	X-Ray Diffraction

Solid phases

AFm phases	$\text{Al}_2\text{O}_3 - \text{Fe}_2\text{O}_3$ – monosulphate phases
Aft phases	$\text{Al}_2\text{O}_3 - \text{Fe}_2\text{O}_3$ – trisulphate phases
Brucite	$\text{Mg}(\text{OH})_2$
C-S-H phases	Calcium silicate hydrate phases. Hyphens indicate variable composition
C2S	Ca_2SiO_4 – dicalcium silicate
C3A	$\text{Ca}_3\text{Al}_2\text{O}_6$ – tricalcium aluminate
C3S	Ca_3SiO_5 – tricalcium silicate
C4AF	$\text{Ca}_4\text{Al}_2^{3+}\text{Fe}_2^{3+}\text{O}_{10}$ - calcium aluminoferrite
Calcite	CaCO_3
CSH3T	Thermodynamic solid-solution model for C-S-H phases by Kulik (2011)
Dolomite	$\text{CaMg}(\text{CO}_3)_2$
Ettringite	$\text{Ca}_6\text{Al}_2(\text{SO}_4)_3(\text{OH})_{12} \cdot 26\text{H}_2\text{O}$
Gypsum	$\text{CaSO}_4 \cdot 2\text{H}_2\text{O}$
Hemicarboaluminate	$\text{Ca}_4\text{Al}_2(\text{CO}_3)_{0.5}(\text{OH})_{13} \cdot 5.5\text{H}_2\text{O}$
Hydrogarnet	$\text{Ca}_3\text{Al}_2(\text{OH})_{12}$
Hydrotalcite	$\text{Mg}_4\text{Al}_2(\text{OH})_{14} \cdot 3\text{H}_2\text{O}$
Monosulphoaluminate	$\text{Ca}_4\text{Fe}_2(\text{SO}_4)(\text{OH})_{12} \cdot 6\text{H}_2\text{O}$
Monocarboaluminate	$\text{Ca}_4\text{Al}_2(\text{CO}_3)(\text{OH})_{12} \cdot 5\text{H}_2\text{O}$
Portlandite	$\text{Ca}(\text{OH})_2$
T2C	C-S-H1.5 in the CSH3T model
T5C	C-S-H1.0 in the CSH3T model
Thaumasite	$(\text{CaSiO}_3)_2(\text{CaSO}_4)_2(\text{CaCO}_3)_2(\text{H}_2\text{O})_{30}$
TobH	C-S-H0.67 in the CSH3T model

Abstract

Cementitious materials are used to condition or stabilise waste and to build infrastructure in the disposal sites. Moreover, they are envisaged to form part of engineered barrier systems as container, backfill or liner materials in radioactive waste disposal concepts. In the event of contact with water, contaminants dissolve and their mobility is influenced by the employed cementitious materials. Therefore, sound understanding of the interactions between contaminants and degrading cementitious materials in flowing water is essential for safety assessment.

In literature, retention of contaminants has widely been studied with fresh hardened cement paste (HCP), but less attention has been paid to contaminant behaviour in contact with degrading HCP. Those studies involving degradation of cementitious materials have shortcomings regarding their experimental setups because they either look at equilibrated systems, or involve large sample heterogeneity. These experimental approaches hamper direct observation of retention mechanisms on degrading HCP during ‘transient conditions’ as well as of the fate of retained contaminants during the degradation process. There is also a lack of experimental observations regarding kinetically controlled dissolution and degradation of HCP at transient conditions.

The aim of this study was to identify the processes affecting retention of caesium, nickel and selenium on HCP during its degradation, from sane to severely degraded states. The focus was put on the underlying mechanisms and possible remobilisation of previously retained contaminants due to the changing composition of the HCP. Caesium, as Cs(I), nickel, as Ni(II) and selenium, as Se(VI), were chosen because they are considered as safety relevant radionuclides for nuclear waste disposal, represent different chemical characteristics and their stable isotopes can be used in experiments. To address shortcomings of previous studies in this field a combined approach was developed. First, a previously used thin-layer flow-through reactor was adapted and improved for the needs of studying contaminant retention and release during degradation of the multiphase material HCP. Second, retention and degradation were studied in equilibrated batch systems as well.

Regarding degradation of HCP the following results were obtained:

1. The thin-layer flow-through setup was established for degradation of HCP at far-from-equilibrium conditions and a number of relevant experimental data were obtained.
2. A kinetic degradation model satisfactorily reproduced experimental results on HCP degradation. For this, a set of dissolution rate constants of cement phases was optimised which can also be used for other modelling studies.
3. The same model also satisfactorily reproduces results from experiments with different aqueous CO₂ concentrations and with different solution types, i.e. synthesised granitic groundwater (GG water) and deionised (DI) water.
4. When quantitatively comparing different solution types, degradation of HCP equilibrated with GG water is stronger than after equilibration with DI water, due to higher aqueous

CO₂ concentration. Further, the effects of carbonate buffering and carbonation on HCP at far-from-equilibrium conditions were identified and quantified.

5. Four characteristic stages of HCP degradation in flow-through conditions were classified, taking into account carbonate buffering effects. The different stages can be discerned on-line by measurement of pH, Ca and Si concentrations in outflow solutions.

Regarding retention of Cs, Ni and Se(VI) in HCP conditioned systems the following results were obtained:

1. Cs and selenate distribution coefficients were determined in equilibrated systems at different degradation states of HCP.
2. Cs and Se(VI) retention was quantified at flow conditions during continuous degradation of HCP in DI and GG water and likely retention mechanisms were narrowed down.
3. In the case of Ni, the solubility limiting phases formed in presence of HCP were identified at different degradation states.
4. The formation of a so far non-described nickel-silicate-hydrate was observed in the more degraded system at pH around 11.6.
5. The influence of different aqueous CO₂ concentrations on Cs, Ni and Se(VI) retention was demonstrated to be minor.

This study showed that the persistency of contaminant retention by adsorption in degrading cementitious systems is not only a question of distribution coefficients at different degradation states, but also a question of how fast these degradation states are reached.

Resumen

Los materiales cementosos son usados para acondicionar y estabilizar los residuos, así como para construir las infraestructuras de los almacenes en los cuales son depositados. Además, dentro del concepto de la eliminación de los residuos radiactivos, dichos materiales están concebidos para formar parte de las barreras de ingeniería, como los contenedores, el relleno o los materiales de revestimiento. En el caso de contacto con el agua, los contaminantes presentes en los residuos se disolverán y su movilidad se verá afectada por los materiales cementosos utilizados. Por lo tanto, un profundo y completo conocimiento de las interacciones entre los contaminantes y los materiales cementosos degradados por el agua corriente es esencial para evaluar la seguridad de los almacenes de residuos.

En la bibliografía, se encuentran disponibles numerosos y detallados estudios referentes a la retención de contaminantes en cemento endurecido (en inglés 'Hardened Cement Paste' o HCP) sin degradar; sin embargo, los estudios referentes a la evolución de los contaminantes en contacto con HCP degradado son escasos. Estos últimos, además, tienen deficiencias que atañen al montaje experimental, ya sea porque están enfocados a sistemas en equilibrio o porque implican una gran heterogeneidad en las muestras utilizadas. Estos enfoques experimentales dificultan la observación directa de los mecanismos de retención acaecidos sobre el HCP degradado durante las condiciones transitorias, así como del destino de los contaminantes retenidos durante el proceso de degradación. Además, existe una falta de observaciones experimentales que conciernen al control cinético de la disolución y a la degradación de HCP en condiciones transitorias.

El objetivo del estudio fue la identificación de los procesos de retención que afectan al cesio, níquel y selenio durante la degradación del HCP, desde la no degradación hasta estados de degradación elevados. El foco fue puesto en los mecanismos subyacentes y en la posible removilización de los contaminantes, previamente retenidos, debido a la cambiante composición del HCP. El cesio, como Cs(I), el níquel, como Ni(II), y el selenio, como Se(VI), fueron seleccionados debido a que son considerados radionúclidos relevantes para la seguridad en el almacenamiento de los residuos nucleares, poseen propiedades químicas diferentes entre sí y sus isótopos estables se pueden usar para llevar a cabo experimentos. Para hacer frente a las deficiencias de los estudios previos realizados en este campo, se desarrolló un enfoque combinado. Por un lado, se adaptó y mejoró un reactor de flujo de capa fina, utilizado anteriormente, para poder abordar las necesidades requeridas en el estudio de la retención y la liberación de los contaminantes durante la degradación del material de HCP multifase. Por otro lado, los procesos de retención y degradación fueron también estudiados mediante el uso de sistemas de tipo 'batch'.

Con respecto a la degradación de HCP se obtuvieron los siguientes resultados:

1. Se estableció la configuración de flujo continuo en capa fina para la degradación del HCP en condiciones alejadas del equilibrio y se obtuvieron una serie de datos experimentales relevantes.

2. Los resultados experimentales obtenidos para la degradación del HCP fueron reproducidos satisfactoriamente mediante un modelo de degradación cinética. Para ello, se optimizaron un conjunto de constantes de velocidad de disolución de las fases de cemento, las cuales también pueden ser utilizadas para otros estudios de modelización.
3. El mismo modelo también reprodujo, satisfactoriamente, los resultados de experimentos realizados con diferentes concentraciones acuosas de CO₂ y con los dos tipos de agua, la subterránea granítica sintetizada (en inglés, ‘granitic groundwater’ o GG) y la desionizada (en inglés, “deionised” o DI).
4. Se compararon cualitativamente diferentes tipos de solución, obteniéndose una mayor degradación del HCP cuando está equilibrado con agua GG que cuando está equilibrado con agua DI. Este efecto es debido a una mayor concentración acuosa de CO₂ en el agua GG. Además, se identificó y cuantificó el efecto tampón del carbonato y de la carbonatación del HCP en condiciones alejadas del equilibrio.
5. Se clasificaron cuatro etapas características de la degradación del HCP en condiciones de flujo continuo, teniendo en cuenta los efectos del tampón carbonato. Las diferentes etapas se pueden distinguir durante el experimento mediante la medición del pH y de las concentraciones de Ca y Si en la solución a la salida del reactor.

Con respecto a la retención de Cs, Ni y Se(VI) en sistemas acondicionados con HCP se obtuvieron los siguientes resultados:

1. Se determinaron los coeficientes de distribución de Cs y Se(VI) en sistemas equilibrados a diferentes estados de degradación del HCP.
2. Se cuantificó la retención de Cs y Se(VI) en condiciones de flujo durante la degradación continua de HCP en agua del tipo DI y GG, y los posibles mecanismos de retención se acotaron.
3. En el caso del Ni, se identificaron las diferentes fases limitantes de la solubilidad formadas en presencia del HCP a diferentes estados de degradación.
4. Se observó la formación de un silicato de níquel hidratado, no descrito hasta la fecha, en el sistema más degradado con un valor de pH alrededor de 11.6.
5. Se demostró que la influencia de diferentes concentraciones acuosas de CO₂ en la retención de Cs, Ni y Se(VI) es mínima.

Este estudio ha demostrado que la persistencia de la retención de contaminantes, atribuida a la adsorción, no es sólo debida a los coeficientes de distribución a diferentes estados de degradación, sino que depende también de la velocidad a la cual los diferentes estados de degradación son alcanzados.

1 Introduction

1.1 Nuclear Waste Management Context

In the beginning of nuclear waste management it was a common practice to dispose radioactive waste by dumping it into the ocean. This practice was stopped only after 1975 through the international Convention on the Prevention of Marine Pollution by Dumping of Wastes and Other Matter (also called London convention), organised by the UN and ratified initially by 15 countries. More elaborated concepts than ocean dumping were and are being studied, from bringing radioactive waste into the orbit (which was abandoned after the accident of the space shuttle Challenger in 1986), over disposal in tectonic subduction zones below the ocean floor and interim storage at or near the surface to deep geological disposal in stable rock formations. Proper handling of radioactive waste was learned in a step-by-step process and until today is being improved and adjusted according to technical inventions, needs and new scientific findings.

For the purpose of sound management of radioactive wastes these have to be distinguished by physical and/or chemical characteristics. An internationally widespread classification scheme from the International Atomic Energy Agency (IAEA) is shown in Figure 1. It bases on the activity content of the waste (comprising activity concentration, specific activity as well as total activity) and the half-life of the radionuclides contained in the waste. Each waste type has to be treated differently due to its unique properties and different radionuclide inventory, which is important to consider in safety assessment.

Concepts for disposal or interim storage of radioactive wastes vary depending on the geological, hydrological and geographical characteristics of the sites, the specific waste type, managerial, societal and legal aspects of each country (IAEA 2012). For the disposal of high level waste (HLW) which mainly stems from nuclear power plants, but also from nuclear weapon programs, deep geological formations are widely regarded as the safest long-term option. Finland is currently building such a final repository for spent nuclear fuel at a depth greater than 420 m below ground in granitic bedrock. Deep geological disposal in stable rock formations is likely to be realised in several radioactive waste possessing countries within the next decades. There are many disposal facilities in operation around the world that are situated at or near the surface (IAEA 2012). An example in Spain is the at/near surface disposal site of El Cabril which holds low to intermediate level waste, stemming from nuclear installations, hospitals, industry and research institutes (Enresa 2010). An interim storage site called ATC (Almacén Temporal Centralizado), which is meant to serve for 60 years is designated to accept HLW of the whole country, was agreed to be built in 2011.

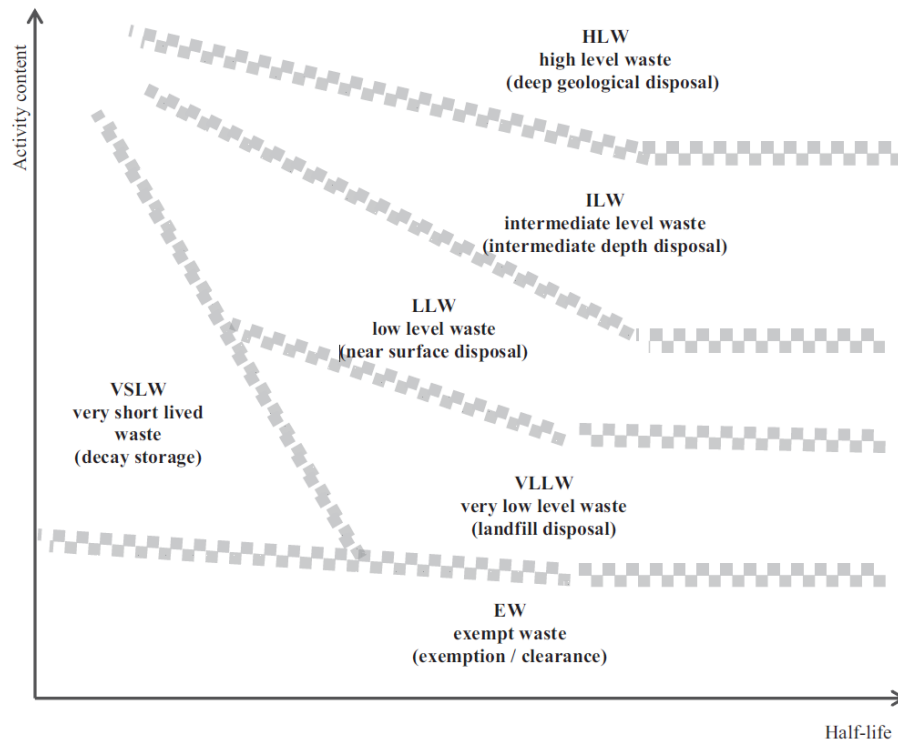


Figure 1 Conceptual illustration of the waste classification scheme of the IAEA, as published in (IAEA 2009). Wastes are distinguished by the radionuclides half-life in the waste inventory and the activity content. Additionally, general disposal options for the different waste types are given.

1.2 Cementitious Materials in the Multibarrier Concept

For the safest possible containment of radioactive waste in deep geological formations or at/near surface disposal different multibarrier concepts have been developed. They consist of a natural barrier (usually the host rock), an Engineered Barrier System (EBS) and the stabilised waste form itself. An EBS is composed of several independent layers to prevent contamination of the environment (OECD 1984, IAEA 2012). Cementitious materials can be used in any barrier part: to condition and stabilise the waste materials, to construct parts of the EBS (container, backfill and liner materials) or to build infrastructure. Cementitious materials have high mechanical strength which qualifies them to prevent collapse of cavities. They can be designed to have low permeability and therewith influence groundwater flow into and out of the repository when used as container and/or backfill. In backfilled storage tunnels or boreholes groundwater contact with waste is minimised (without relying on functioning as a hydraulic barrier) and thereby radionuclide mobilisation restrained. Further, cementitious materials may be used to seal rock fractures, tunnels and shafts or as hydraulic barrier between geologically separated aquifers, artificially connected by, e.g., boreholes. For example, France and Switzerland are conducting studies for HLW repositories in clay formations which will after all require concrete for stabilisation of tunnels and shafts (ANDRA 2005).

Also in Belgium a disposal concept is being developed that is supposed to be in a clay rock formation. Here cementitious materials are envisaged for infrastructure stabilisation, as well as for key

elements of the EBS (OECD-NEA 2012). Hence, many multibarrier concepts for radioactive waste disposal involve cementitious materials as an important part of the EBS (e.g. Glasser (2002)), due to advantageous physical and chemical properties of cementitious materials (Vejmelka, Rudolph et al. (1990), ANDRA (2005), SKB (2006)) – discussed in more detail below. As an example, the Belgian multibarrier concept involving cementitious materials in various layers of the engineered barriers and infrastructural parts is given in Figure 2.

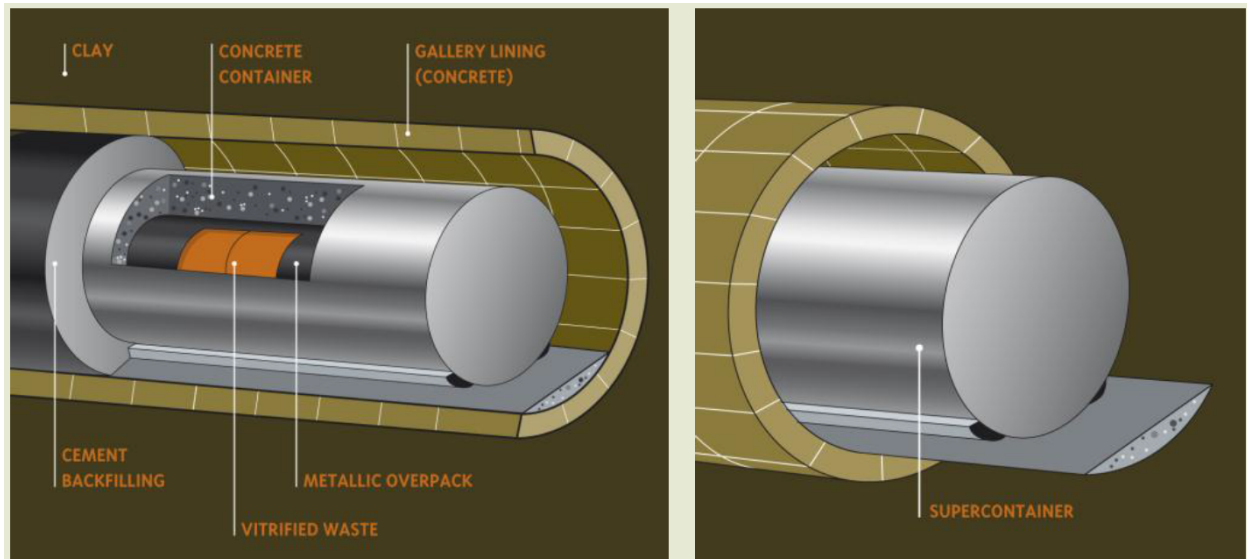


Figure 2 Belgian, so-called supercontainer concept for final disposal of vitrified waste resulting from reprocessing commercial irradiated fuel and non-reprocessed irradiated fuel declared as waste, reproduced in modified form from ONDRAF/NIRAS (2011).

In Scandinavia, repositories in granitic rock are developed. They may widely be constructed exclusive of cementitious materials since clay backfill as well as copper canisters are foreseen as the main engineered barriers for Spent Nuclear Fuel and stabilisation of underground installations is widely not necessary. However, fractures are the preferential water pathways in this type of rock and still have to be sealed with cementitious material (SKB 2006). Even though not crucial part of the concept, cementitious material may affect groundwater composition in the near-field of radioactive waste and come in contact with mobilised radionuclides, too.

In Germany and the United States of America radioactive waste disposal in salt formations is considered for future sites and already implemented (*Waste Isolation Pilot Plant* in New Mexico, e.g.). In such repositories for HLW or Transuranic waste crushed salt is envisaged as a suitable backfill, but also cementitious material may be used for sealing structures (DBE 2009, Müller-Hoeppe, Buhrmann et al. 2012). In Germany, a former mining site which was converted into a disposal site in 1970 (*Endlager für radioaktive Abfälle in Morsleben*), additionally had to be stabilised using salt-concrete (DBE 2011), a hydraulic mixture of Portland cement, salt, aggregate and powdered limestone.

In the case of LLW and ILW, which are being disposed at or near surface, cementitious materials are almost ubiquitous. For these waste types cement is often used to stabilise or solidify liquid waste forms. Also, containers made of concrete are frequently used and voids between containers stored in

galleries are sometimes filled with cement (Niedersächsisches Ministerium für Umwelt 2002, ANDRA 2005, Enresa 2010).

This brief overview on disposal options considered by different countries regarding various waste types demonstrates that for any currently designed or implemented HLW as well as for most LLW and ILW disposal concepts, cementitious materials are or will be used in future. All in all, cementitious materials play an important role for radionuclide mobility during the ‘lifetime’ of a disposal.

According to IAEA guidelines (IAEA 2012) for the design and implementation of a HLW disposal a *safety assessment* study of radiation hazards that is discussing all technical and scientific questions should be elaborated. Further, a *safety case* should be conducted which may integrate the safety assessment without being limited to it, but additionally bases on a broader argumentation line including its financing and public acceptance among other issues. A key part of safety assessment studies focuses on the fate of radionuclides in the near-field of a repository, including local geochemical conditions and interplay of engineered barriers with radionuclides over long time-scales. Deciphering the involved chemical processes, the driving forces and the influencing parameters is the fundamental basis for long-term predictions on the fate of waste disposal. In many countries these predictions are legally required for safety assessment studies of repositories. Against this background the present study focuses on degradation of cementitious material as barrier or structural unit in the near-field of a disposal site and retention of selected radionuclides on such material.

1.3 Radionuclide Retention Processes in Cementitious Materials

Cement based materials stand out due to their high alkalinity and their capability to buffer chemical conditions efficiently over extended periods of time. Atkinson, Everitt et al. (1989) expect for a cementitious repository to buffer cement pore water above circa pH 12.5 for several ten thousands of years and above pH 10.5 for several hundred thousands of years. Thus, it is assumed that any radionuclide, regardless of its half-life, may come in contact with cement materials if these are employed at the disposal site.

Some radionuclides, especially actinides, are less mobile in the alkaline regime (Abdelouas and Grambow 2012) than in neutral to acidic conditions. This is generally the case for elements that tend to precipitate as hydroxides (Glasser 2001) and also for ^{14}C in cementitious systems (Abdelouas and Grambow 2012) which may be immobilised upon carbonation of the cement. Especially where redox conditions are reducing this creates an environment in which most radionuclides have a low solubility equilibrium in solution (e.g., ANDRA (2005)). The solubility of a substance limits maximum aqueous radionuclide concentrations, irrespective of the absolute inventory by the precipitation of a stable solid phase. Therefore, generally low solubility of radionuclides at cementitious conditions is sometimes put forward when arguing for the use of cementitious material in context of radioactive waste disposal (Glasser (2001)).

The fact that at solubility equilibrium the maximum concentrations of radionuclides in solution are thermodynamically limited effectively reduces dissemination in the geosphere. The concept of solubility equilibrium control is based on thermodynamic equilibrium state of a given system. Any solid phase in solution ideally dissolves until the solid is in equilibrium with the solution. This equilibrium solution composition depends on the given temperature, pressure and activities of the species involved in the dissolution reaction. If the activity of a radionuclide-hosting mineral is at equilibrium with the solution in a closed system, the activity of the dissolved radionuclide species corresponds to a unique aqueous concentration of the radionuclide. Vice versa, when porewater infiltrates radioactive waste radionuclides will dissolve. If the solubility of the thermodynamically stable phase is low, the radionuclide will again precipitate from solution and thus be immobilised in a secondary phase. If the radionuclide is a component of the solubility limiting phase itself, net dissolution will stop once the equilibrium concentrations in solution are achieved. Ideally, in very dilute solutions concentrations may be used to calculate the ion activity product, which allows knowing the saturation state of any solid by comparison with the solubility product of the solid. However, in real solutions the activity of ions has to be evaluated instead as reactivity of ions is influenced by several other factors. The most relevant of them are temperature, pressure, solution composition and ionic strength. Thermodynamic models thus have to be complete and include any relevant soluble complexes, including the ones with organic ligands, that are present in the system. Apart from this, the thermodynamic solubility limit may be altered if conditions favour colloid formation (this is generally most likely in dilute solutions), which may stabilise radionuclides in solution beyond thermodynamic equilibrium. This process cannot be determined by thermodynamic equilibrium solubility calculations and must be evaluated separately.

A 'special case' of solubility control occurs if solid-solution forming solids are involved (which in nature frequently is the case). Generally, a solid-solution is a crystalline structure which consists of one or more components that may partly substitute atoms or molecules of the host crystal. This may lead to distortion and changes of the crystal lattice, as long as the crystal structure remains unchanged. Solid-solutions of two or more end-members may be ideal, i.e. the enthalpy of mixing is zero. If this is not the case we talk about non-ideal solid-solutions (Bruno, Bosbach et al. 2007). Solid-solution formation generally has the effect that equilibrium concentration of an involved radionuclide drops below that of the respective pure phase. Their formation is thermodynamically difficult to predict for real systems because most solid-solutions are not ideal and any compositional change implies another aqueous equilibrium concentration of incorporated radionuclides. However, some radionuclides, like Cs and Se(VI), are highly or moderately soluble in alkaline porewater of cementitious material or in an alkaline plume and thus may be more mobile (chapters 3.3.3 and 3.3.4).

Besides pure phase solubility, the mobility of aqueous radionuclides is influenced by the interplay of the physico-chemical processes like diffusion, sorption and co-precipitation. Due to the relevance of these retention processes they have already been studied under various conditions for different elements (e.g. Pilkington and Stone (1990), Tits, Bradbury et al. (1998), Berner (1999), Aggarwal, Angus et al.

(2000)). The mobility strongly depends on the present surfaces of solid phases and the chemical conditions which are controlled by the actual degradation state of the cement. That there are different degradation states already implies that, over the lifetime of a cementitious disposal site, these states are transient. Existing studies therefore mostly focused on well-defined systems, i.e. conditions of $\text{pH} > 12.5$, but neglecting the transitions that possibly would affect retention upon cement material degradation. Fewer studies have investigated retention mechanisms with degraded material which has a less defined phase composition and is more dependent of the geochemical conditions (Taylor 1997). Cementitious materials themselves have a high capacity for retention of radionuclides, mainly due to adsorption and incorporation to calcium silicate hydrate gel, the major component. To a lower extent adsorption/incorporation also takes place on other cement hydrates like AFm and AFt phases (e.g. ettringite) in the case of (oxy)anions. Still, type and abundance of the latter mineral groups varies with geochemical conditions, clinker and mixing water composition as well as the type of attacking water on the long term. This makes predictions of anion retention more difficult. Especially those radionuclides forming oxyanions (^{79}Se , ^{99}Tc , e.g.), which have a relatively high solubility limit and are significantly less retained by sorption processes due to negative charge, repelling them from mostly equally charged mineral surfaces.

As will be pointed out in the Objectives section of this Thesis, the aim of this study was to identify the processes affecting retention of caesium (as Cs(I)), nickel (as Ni(II)) and selenium (as Se(VI)) on Sulphate Resisting Portland Cement during its degradation, from sane to advanced degradation states. The focus was placed on the underlying mechanisms and possible remobilisation of previously retained radionuclides due to the changing composition of the cement. For applicability, study conditions were chosen as representative as possible for conditions at a disposal site. Better understanding of retention mechanisms will help to improve model-based predictions on radionuclide migration processes in the near-field.

1.4 Experimental Approaches to Investigate Cement Degradation and Radionuclide Retention

Established methods to investigate degradation of cementitious materials and retention of radionuclides on them can be divided into two major groups: First, batch experiments employ monoliths or certain particle fractions of crushed cementitious materials at different solution to solid ratios. They are either static or eventually executed as series of dynamic batch experiments. Second, flow-through experiments of different design mostly use centimetre to decimetre long columns of confined cement particles or cementitious monoliths where transversal flow is induced by pressure. However, for a number of reasons that will be discussed in the following paragraphs these common techniques are not best suited to investigate the transitions occurring during degradation which may affect the retention of species.

Classical (dynamic) batch experiments observe equilibrated, well-defined steps, but miss the evolution between stages where most reactions do occur in reality. For example, solid-solution phases

like C-S-H (the main component of hydrated cement) continuously change composition and surface structure during cement degradation, and thereby sorption abilities of radionuclides. There is therefore a risk of overlooking effects that may release radionuclides during the phase transitions.

In some cases it makes a difference how the solution is exchanged, either continuously, intermittently or not at all. One can imagine that a radionuclide incorporating solid phase becomes unstable with respect to another solid and it transforms. In the simplest case such a transformation occurs without exchange of material or only by uptake of, e.g., additional water molecules. Such a reaction is not affected considerably by the solution exchange method, neither in dynamic batch nor in flow-through experiments. In a more complex case, transformation could be a dissolution and reprecipitation reaction where components get dissolved first and precipitate afterwards. Here, the solution exchange method obviously will influence not only the reactions, but also the retention mechanisms. Considering the groundwater flow at real disposal sites flow-through experiments probably better represent the flow-regime than intermittent dynamic batch experiments.

Still, flow-through columns easily miss information on reactions and radionuclide retention processes associated with the phase transformations, too. Classical columns are usually so long that gradients in phase and solution composition over the longitudinal column length establish. Processes occurring within the column are therefore widely impossible to observe since they are masked, e.g. via reactions taking place in rear parts of the column.

Other shortcomings of encountered methods are that experimental times are extremely long, setups unpractical for late degradation stages (very high liquid to solid ratios necessary), far away from real processes (e.g., degradation with acid) or suffer from gross heterogeneity of the material (long columns) and preferential flow. The combination of these factors leads to larger setups or longer equilibration time which complicate variation of experimental parameters or studied radionuclides.

In this study a combination of classical batch experiments and a thin-layer flow-through reactor, not previously used in this field, is chosen to address the mentioned shortcomings. To be able to investigate also transformations in the multiphase system of cementitious materials with relatively short experimental times and easy variability of experimental parameters a setup was needed that allows for fast degradation of the solid combined with a minimum of heterogeneity such as reaction fronts along flow-through columns or matrix diffusion. For this reason an already existing thin-layer flow-through setup, which had been designed to investigate solubility of monocrystalline materials (Bruno, Casas et al. 1991), was taken as basis, adapted and tested regarding its applicability for the study of cement degradation. The most important characteristic of this setup is its short diffusion length, i.e. only a monolayer of ground cement powder is used. In order to employ sufficient amount of material that allows later analyses of the solid comparatively large lateral dimensions were chosen. Then the setup was used to analyse retention of selected radionuclides under flow-through conditions during degradation of hydrated Sulphate Resisting Portland Cements in deionised (DI) water and granitic groundwater (GG water).

A key aspect of this study is a good understanding of the cement degradation processes occurring in the thin-layer flow-through setup since the chemical and mineralogical composition of cementitious materials influence the retention of radionuclides (Evans 2008). The evolution of the system was followed and interpreted from analyses of the solid phase and the aqueous solution to better understand the chemical processes affecting radionuclide retention and secondary release in cementitious systems upon degradation. Thorough observation is necessary to identify cement hydrate phases which may control the retention of radionuclides. The cement degradation study and the retention study were complemented by batch experiments to allow for comparison between results from a classical setup and the new setup as well as to substantiate the findings.

In addition, computer modelling was used to plan experiments, to derive parameters from the experiments and to test hypotheses on the obtained results that finally support interpretation of the complex and parallel processes occurring in this system. Thermodynamic modelling was used for planning of the experiments by solubility calculations with the radionuclides investigated as well as for solubility calculations with the different cement hydrates over various degradation stages. For flow-through experiments a combined thermodynamic and kinetic approach was developed which proved capable in reproducing experimental results obtained under different experimental conditions.

1.5 Choice of Cement Type and Investigated Radionuclides

To get representative and applicable results Sulphate Resisting Portland Cement was employed in this study. Portland cement is the most widespread cement type in the world and forms part of almost all special cements envisaged for use in disposal sites. In safety assessment studies the potential transfer and mobility of all radionuclides from a given inventory through cementitious materials out to the near and far-field have to be considered for a planned disposal site. This study however was not related to a specific waste inventory, so that a selection of radionuclides was made for feasibility here. Cs, Ni and Se were chosen because they are all considered as safety relevant by responsible agencies of different countries in the context of nuclear waste disposal (e.g., Alder and McGinnes (1994), Berner (1999), Altmaier, Brendler et al. (2004)).

Apart from this similarity Cs, Ni and Se were picked out as representatives for radionuclides showing different behaviour regarding chemical reactivity and mobility in the alkaline conditions imposed by cementitious materials. Cs differs from other relevant radionuclides being the only alkali metal and thus the only radionuclide with 1+ charge. It behaves similarly to other alkali metals, i.e. it is very soluble in cementitious conditions and due to its large ionic radius together with low charge it is only weakly retained by sorption processes.

Ni belongs to the group of transition metals and is present in divalent oxidation state under oxidising and reducing conditions in aqueous solutions. It is a central radionuclide in the safety assessment of low and intermediate waste disposal systems. This is because the relatively short half-life of its ^{63}Ni isotope as well as the half-life of the ^{59}Ni isotope are both in the lifetime ranges of an

intermediate and low level waste repository. Chemically it behaves similarly to other transition metals which are also present in divalent state, e.g. Cd and ^{60}Co . Finally, Se is also a critical radionuclide in some repository systems and it can be seen as a representative for other mobile oxyanion forming (radio)toxic elements like As and Mo. Cs, Ni and Se have the advantage that their non-radioactive isotopes can be investigated in analogy to their radioactive isotopes. In the following each of the three elements is briefly introduced regarding its relevance and important aspects of their behaviour in cementitious systems (further details are provided in chapter 3.3).

Ni belongs to the group of activation products and is formed from irradiation of stable Ni, contained in metallic parts of nuclear fuel and other components present in the reactor (Evans, Lepel et al. 1984, Carbol and Engkvist 1997). The two occurring radioactive isotopes ^{59}Ni and ^{63}Ni have half-lives of $7.5 \cdot 10^4$ and 100 years, respectively. Consequently it is necessary to understand retention of radioactive Ni in a geochemical environment controlled by young (unaged) cementitious material, as well as by degraded (aged) cementitious material. Moreover, cement materials themselves may represent a considerable source of stable Ni, stemming from the raw materials used for cement clinker manufacture or from alloys in case of reinforced concrete. Therefore, stable Ni may play an important role in cement systems and influence mobility of radioactive nuclides (Wieland, Tits et al. 2006).

During the last years there has been active discussion on both Ni speciation as well as the concentration limiting phases in hyperalkaline cement systems and different solubility controlling solids and species in solution were suggested (Gamsjäger, Bugajski et al. 2005, Palmer, Bénézech et al. 2005, Palmer, Bénézech et al. 2011). Measurements of Ni solubility are complicated due to the low concentrations at high ionic strength in the hyperalkaline regime (Mattigod, Rai et al. 1997). Analysis of the present species is even more difficult at these conditions and results of two recent studies indicate that the species $\text{Ni}(\text{OH})_3^-$ (actually selected for the NEA thermodynamic database) does not exist or is not important at $\text{pH} < 13$ (Palmer, Bénézech et al. 2011, González-Siso, Gaona et al. 2015). These uncertainties still interfere proper thermodynamic assessment of Ni solubility in cementitious environments. As solubility limiting phases some studies suggested Ni-Al layered double hydroxides (LDH), while others found Ni hydroxides to fulfil this role in cement conditioned systems (see Hummel and Curti (2003) and citations therein). The present work analysed the formation of the solubility limiting phases of stable Ni in different degradation states of Portland cement and the corresponding aqueous equilibrium concentration (chapters 7.1.1 and 7.1.3). Results confirmed the formation of Ni-Al LDH phases and also proofed their presence in more degraded states compared to earlier studies. Moreover, a previously not described amorphous phase was observed to form, probably a Ni-Si-hydrate that destabilised C-S-H (chapter 7.1.2.1).

Se has a radioactive isotope ^{79}Se which is contained as fission product in high level radioactive waste and has a high radiotoxicity combined with a very long half-life of more than $3 \cdot 10^5$ years (Bienvenu, Cassette et al. 2007, Jörg, Bührenmann et al. 2010). Due to these characteristics Se is relevant for long-term disposal considerations (Bruno and Ewing 2006). Moreover, ^{79}Se may be an element that

gets released almost instantaneously in case of container failure from disposal sites as part of the so-called Instant Release Fraction (IRF) (Kienzler, Altmaier et al. 2012). Consequently, the contact of Se with cement will be likely at any degradation state of cementitious barriers in a disposal site for HLW.

Se is a redox sensitive element and its chemical character is between a metalloid and a non-metalloid. In Portland cement systems where redox conditions are weakly buffered above 100 mV (chapter 3.1), Se is generally present in the form of the two highly mobile divalent oxyanions selenate SeO_4^{2-} and selenite SeO_3^{2-} in which Se is in its hexa- and tetravalent redox-state, respectively. In systems where other materials like reinforcement bars, additives or the surrounding materials create reducing conditions, Se may further reduce to Se(0) and Se(-II). The present study used selenate and worked at geochemical conditions where selenate is considered as dominant species in solution. Due to relatively high solubility of selenate under alkaline conditions investigations of its retention mostly look at sorption mechanisms. A conducted literature review showed large scatter of results regarding the retention of Se on cement. Especially monosulphoaluminate is suspected to retain selenate, but also ettringite and to a lesser extent C-S-H phases were discussed (e.g, Baur and Johnson (2003b)). Contradictory findings make it difficult to conclude which are in fact the responsible cement phases. To date, retention of Se during degradation of a cementitious barrier cannot be predicted realistically. This is why in performance assessment studies distribution coefficients K_d between solid and liquid phase are often assumed to be zero due to high uncertainty about their retention (Bosbach 2010, Kienzler, Altmaier et al. 2012). In this work for the first time we investigate Se(VI) retention by a Portland cement while it degrades in a thin-layer flow-through setup (see chapters 7.2.2.1 and 7.2.2.2) and it is compared with results from distinct degradation states in equilibrated systems (see chapters 7.2.1.1 and 7.2.1.2). Results show weak, but fast retention of Se(VI) probably controlled by C-S-H phases in the transient system (chapter 7.2.3).

Cs is a fission product in nuclear fuel – just as Se – and one of the most critical elements when evaluating the safety of a disposal site since it has a high radiotoxicity, long half-life and is highly mobile under certain geochemical conditions (Bruno and Ewing 2006). There are two radioactive isotopes which are considered in safety studies for nuclear waste disposal: ^{137}Cs and ^{135}Cs . The former has a relatively short half-life of 30 years so that it basically decays within several dozens to a few hundreds of years in a repository. As Cs belongs to the IRF elements, which in case of container failure become easily mobilised, contact with fresh cementitious materials is a possible scenario. ^{135}Cs in contrast has a longer half-life of $2.3 \cdot 10^6$ years and therefore also interacts with degraded cementitious material in a HLW disposal.

The alkali metal ion Cs^+ is not solubility limited under cementitious conditions and hardly retained by cement phases (Berner 1999). In sane cementitious materials Cs is poorly retained due to competition with alkali metals from cement itself for sorption sites. If increasingly degraded cement materials control the chemical conditions, competition with alkali elements diminishes and Cs is stronger retained by cation exchange. In contact with severely degraded hardened cement paste (HCP) (pH ~10) one study observed significant retention (Ochs, Pointeau et al. 2006) without being able to elucidate the responsible

mechanism. In cement systems C-S-H is suspected to be the major phase retaining Cs, but findings on the mechanisms diverge from unspecific sorption over real incorporation to destabilisation of C-S-H by Cs uptake (Iwaida, Nagasaki et al. 2002, Viallis-Terrisse, Nonat et al. 2002). It is generally observed that even if Cs is adsorbed to cementitious materials in a first step it might be desorbed entirely afterwards. Further, Cs is also easily mobilised from cementitious material after being incorporated previously during the hydration step. In this case however, about one third of Cs is permanently retained by the cement (Papadokostaki and Savidou 2009).

In this study adsorption of Cs to hardened cement paste, equilibrated to different degradation states, was observed and distribution coefficients determined (chapter 7.3.1.2). In contrast, no retention of Cs was observed at the experimental conditions in the thin-layer flow-through reactor (chapter 7.3.2.2). Results confirm adsorption of Cs to cement, but show labile binding. Tracer-like passage through degraded HCP in flow-through experiments indicates altered sorption mechanisms of Cs on C-S-H at these conditions (chapter 7.3.3).

2 Objectives

The aim of this study was to identify the processes affecting retention of Cs(I), Ni(II) and Se(VI) on Sulphate Resisting Portland Cement during its degradation, from sane to advanced degradation stages. The focus was put on the underlying mechanisms and possible remobilisation of initially retained radionuclides due to the changing composition of the cement. For applicability, study conditions were chosen as representative as possible for conditions at a disposal site.

Especially the effect of dissolution and (re)precipitation processes occurring during the degradation of cementitious materials on radionuclide retention has not been investigated previously. Moreover, common methods were not optimised to observe such effects. Therefore, this study aims to fill the gap and characterise retention of radionuclides also during transient states. For this aim, in a first step an existing thin-layer flow-through setup was modified and tested to allow better assessment of such transient states.

- 1. Revise and assess the current state of knowledge concerning cement degradation and radionuclide retention on cementitious phases.**
- 2. Modify and test a flow-through reactor that allows identifying radionuclide retention mechanisms during the degradation of cementitious material.**
- 3. Identify to what extent processes of cement degradation differ under flow conditions compared to equilibrated systems:**
 - a. Determine the evolution of solid phase as well as solution composition during cement degradation under flow conditions and compare with experimental data from equilibrated batch experiments.
 - b. Develop a model capable to explain the degradation processes in the flow-through reactor and equilibrated batch experiments.
- 4. Quantify the impact of the attacking solution composition on cement degradation under flow-through conditions:**
 - a. Determine the evolution of solid phase as well as solution composition for different attacking solutions.
 - b. Validate the developed model by applying it to experimental results from degradation in the different applied solutions.
- 5. Evaluate retention mechanisms of Ni, Se and Cs at different degradation stages in different solutions and in both, flow-through and equilibrium systems:**
 - a. Identify solubility limiting Ni(II) phases for different degradation stages in equilibrium conditions.
 - b. Quantify precipitation/adsorption of dissolved Ni(II) on cement in flow-through conditions.
 - c. Identify cement phases controlling aqueous Cs(I) and Se(VI) concentrations below solubility limits in batch and flow-through systems.

- d. Determine distribution coefficients of Cs(I) and Se(VI) for different degradation stages in batch and flow-through systems.
- e. Compare the relevant retention mechanisms in batch and flow-through systems.

3 State of Knowledge & Theoretical Background

3.1 Basic Cement Chemistry

Nowadays cement clinker is produced in large scale cement plants where the principle steps are dehydration and decarbonation of the raw material at about 1450°C in a rotary kiln. During this process raw material, mainly composed of Ca-, Si-, Al- and Fe-phases from quartz, clay and limestone, transform to the main clinker minerals such as tricalcium silicate Ca_3SiO_5 , dicalcium silicate Ca_2SiO_4 , tricalcium aluminate $\text{Ca}_3\text{Al}_2\text{O}_6$ and tetracalcium aluminoferrite $\text{Ca}_2(\text{Al,Fe})_2\text{O}_5$. These oxide minerals are ground finely and gypsum is added. Different types of cement compositions with different characteristics exist (Table 1). According to the norm ENV 197-1 (British Standards Institution 1995) Portland cement is a hydraulic material made up by at least two-thirds of calcium silicates plus Al-, Fe- and other oxides. CaO/SiO₂ ratio should be above 2.0 and MgO content below 5% with all amounts given as fractions of weight.

Table 1 Cement types specified in the European norm EN(V) 197-1.

Abbreviation	Cement type
CEM I	Portland cement
CEM II	Portland composite cement
CEM III	Blast furnace cement
CEM IV	Puzzolan cement
CEM V	Composite cement

When cement clinker is mixed with water setting starts immediately and is followed by curing and hardening periods. For common hardened cement paste it typically requires 28 days to achieve guaranteed physical strength of the fabric (Verein Deutscher Zementwerke 2002). The water to cement clinker mass ratio (w/c) varies commonly from 0.3 to 0.6 kg/kg. After mixing a complex series of dissolution, diffusion and precipitation reactions finally results in a ‘fresh’ hardened cement paste and all these reaction stages are commonly summarised under the term hydration.

Processes and conditions during hydration have been investigated in numerous studies (e.g. Lothenbach, Winnefeld et al. (2007), Juilland, Gallucci et al. (2010), Stark (2011) and references therein) and are widely understood. After 28 days more than 70 % of the tricalcium silicate and 30 % of dicalcium silicate have reacted and transformed to hydrate phases, i.e. C-S-H (hyphens indicate variable contents of the components; for symbolism see Table 2) and portlandite (Taylor 2002). A recent review by Bullard, Jennings et al. (2011) gives a comprehensive description of the understanding of clinker hydration from a thermodynamic point of view and identifies the remaining gaps. These gaps are largely attributed to incomplete understanding of the various admixtures chemicals such as polycarboxylates or supplementary cementitious material (so-called SCM’s) such as blast furnace slag. Further, complementary data and knowledge of the rate controlling steps of clinker dissolution as well as of nucleation and growth of the

hydrate phases would be needed. Mechanistically, growth mechanisms of the main constituent of hardened cement paste C-S-H are still unresolved on the nanoscale, according to Bullard, Jennings et al. (2011).

Table 2 Summary of cement chemist notation. It uses capital letters (left) to account for oxides (right column) in abbreviated form. Lowercase letters (left column) are used to give stoichiometric information when appropriate (right).

A	Al ₂ O ₃
C	CaO
F	Fe ₂ O ₃
H	H ₂ O
S	SiO ₂
t	tri
m	mono

The term C-S-H phase comprises a group of more than 30 identified phases that are poorly ordered and can be classified between a gel and crystalline phase (Taylor 2002, Richardson 2008). A successful structural model is based on ‘Dreierketten’ (‘chains of three’ (literally translated); in German starting with a capital letter and written with a terminating *n* (Dreierketten) in plural form) that are chains of silicate tetrahedra. The building blocks of these chains consist of three silicate tetrahedra which have been defined basing on the structure of 1.4-nm tobermorite, Ca₅Si₆O₁₆(OH)₂·8H₂O (Figure 3). In this case two tetrahedra share two oxygen atoms with a Ca-O layer and are called ‘bridging tetrahedra’. The third tetrahedron shares only one oxygen atom with the Ca-O layer (Chen, Thomas et al. 2004). Bridging tetrahedra may be missing and the periodicity of the building units is variable, but always >2. These variations affect the composition of the solid, resulting in different C/S ratios. Ca to Si ratios are found to vary from 3 to 0.6, but the mostly encountered values in literature are between 1.5 for C-S-H in equilibrium with portlandite and 0.8 at pH 11 (Harris, Manning et al. 2002). Higher ratios than 1.6 are often considered as an indication for portlandite layers intergrown into C-S-H phase instead of distinct C-S-H compositions.

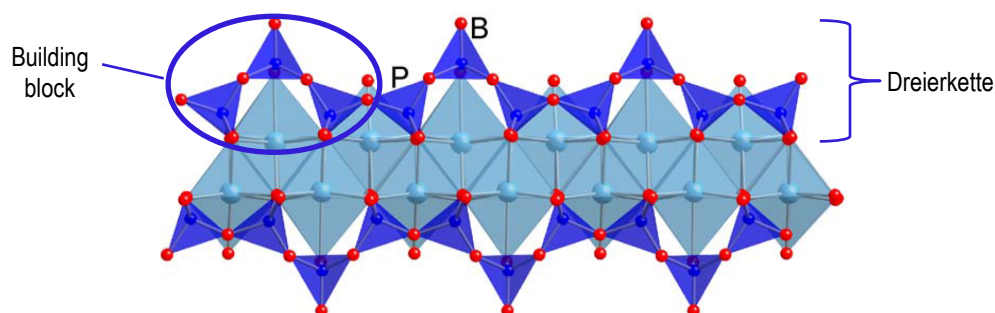


Figure 3 Schematic atomic structure of 1.4-nm tobermorite projected along [010]. Building blocks and a Dreierkette are indicated in the figure. P and B denote paired and bridging silicate tetrahedra (dark blue) with oxygen atoms at each corner (red circles). Ca atoms (light blue circles) are in 7-fold coordination with oxygen atoms. Figure modified from Richardson (2004).

Portland Cements mainly produce the hydrated solid phases calcium silicate hydrate C-S-H, portlandite $\text{Ca}(\text{OH})_2$, AFm ($\text{Al}_2\text{O}_3 - \text{Fe}_2\text{O}_3 - \text{monosulphate}$) and AFt phases ($\text{Al}_2\text{O}_3 - \text{Fe}_2\text{O}_3 - \text{trisulphate}$). Typical ranges of contents of the different phases are summarised in Table 3

Table 3 Mean solid composition of hydrated Portland cement as given by Berner (1992).

Hydrated cement phases	Amount in weight %
C-S-H gel	50-63
Portlandite	25-31
AFm, AFt and aluminous-ferrous phases	13-25
Minor components NaOH, KOH, $\text{Mg}(\text{OH})_2$, etc.	0-6

Portlandite appears as idiomorphic crystals of hexagonal plates with relatively small specific surface area in fresh cement pastes, but it also is found finely intermixed with C-S-H (Taylor 1997). The latter phase instead shows a high variety of physical properties in cement which is also due to the chemical versatility. C-S-H is morphologically distinguished in the two types inner and outer product. Inner product refers to C-S-H that has formed by hydration of massive clinker tricalcium and dicalcium silicate grains that were replaced in-situ. This type has a dense structure with fine, but few pores and it is characterised by relatively low specific surface area. The outer product in contrast has high specific surface area and is C-S-H that precipitated from solution in the open pore space. This type has a more open pore geometry, is less dense and can be distinguished already by grey-levels when using a backscattered electron detector in SEM analysis. It appears in columns or radiating fibres around calcium silicate clinker minerals (Taylor 1997).

Cement clinker mixed with water and fine aggregate (particles that are less than 4 mm in diameter) gives the final hardened product called mortar and when gravel is used instead of sand it is called concrete. These two modifications differ in their characteristics and application fields. In both cases adequate rock types are selected as filler material which can be regarded as widely inert. Reactivity, contribution to strength and microstructure development with different types of fillers (carbonates, granites, etc.) have been intensively investigated (Taylor 2002). Typically, orientated crystals are found at the interface between filler and paste, but even though there is a large influence on the structure and physics (strength, fracture formation, porosity) of the hardened product this barely modifies the chemical behaviour of the system (Taylor 2002). More precisely, the chemical system of hardened cement paste, mortar or concrete in contact with water can be sufficiently described only considering cement hydrate phases. Consequently, these phases also control contaminant retention in cementitious systems (Hewlett 2004) which will be explained in chapter 3.3.

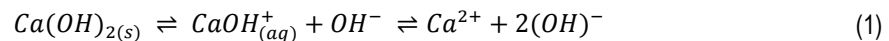
Portland Cement is the most widespread cement that is used in the world and also the most simple one that actually is in use. However, in other classes of cement reactive admixtures like silica fume or blast furnace slag are used to control, e.g., porosity, mechanical strength, initial shrinkage, heat evolution during curing or the phase assemblage. Such admixtures can modify the chemical conditions which influence retention of radionuclides. The redox potential in a Portland Cement dominated system is weakly buffered due to lack of strong redox pairs and easily affected by external parameters. Generally, it

is expected to be positive, above +100 mV, conditioned by Fe(III) (Glasser 1997). However, some materials used for blending cement such as blast furnace slag may create Eh conditions lower than -100 mV (Glasser 1997) and also steel reinforcement in contact with solution can cause more reducing conditions in case of corrosion.

3.2 Chemical Degradation of Hardened Cement Paste

3.2.1 Major Cement Phases Controlling Degradation Stages

Portland Cement is very efficient in establishing alkaline conditions. This is due to the hydrated cement phases that constitute a sequence of pH buffering solids. The well characterised degradation scheme of cement is therefore usually expressed in terms of the master variable pH (Taylor 1997) and citations therein). Fresh hardened Portland Cement establishes a pH up to 13.5 in the porewater due to readily dissolving Na and K hydroxide phases. However, this effect is diluted rapidly in systems with water exchange. Portlandite dissolution constitutes the next pH buffer and keeps pH efficiently around 12.5 by liberating hydroxyl ions (Atkinson, Everitt et al. 1989, Seewald and Seyfried Jr 1991, Atkins and Glasser 1992) according to equation (1), while controlling the Ca concentration in cement pore water.



As long as portlandite is present in the system, C-S-H is regarded to be stable. Once portlandite is exhausted, C-S-H starts dissolving incongruently and buffers pH continuously down to pH ~ 10.5 (Atkinson, Everitt et al. 1989, Atkins and Glasser 1992). When C-S-H dissolves completely, it depends on the system which phases further control pH. Typically, these will be brucite, calcite or both in common groundwater. A global overview on the different stages of pH control and estimated timescales of degradation is given in Figure 4 at the example of a hypothetical waste repository using mainly cementitious materials.

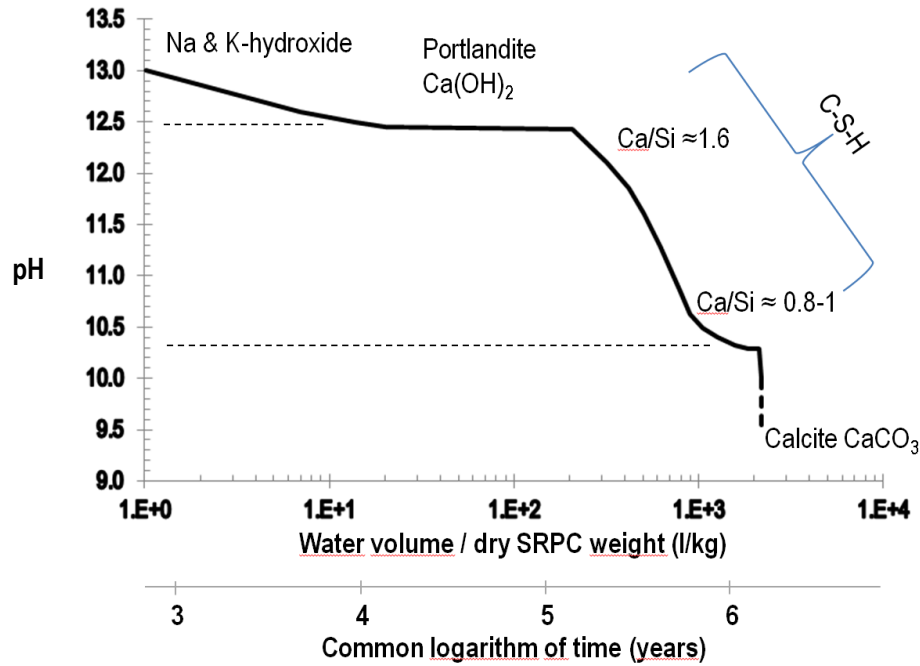
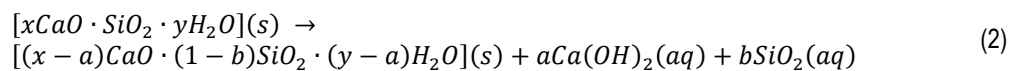


Figure 4 Estimation of the main degradation stages of a waste repository consisting mainly of SRPC, redrawn and modified from (Atkinson, Everitt et al. 1989). Degradation was computed by Atkinson and co-authors as a function of the water/cement ratio which then was related to time, basing on an estimated mean water flow. Both entities are given on the abscissa and link to the same graph. Thin, stippled lines are a guide for the eye. The major phases controlling the different stages are indicated in the figure.

The dissolution behaviour of C-S-H is complex, therefore several thermodynamic models have been suggested to reproduce experimental results by geochemical modelling (e.g. Berner (1988), Kersten (1996), Harris, Manning et al. (2002), Sugiyama and Fujita (2006), Kulik (2011)). These models differ in number and composition of end-members and therefore must be considered as empirical since obtained solubility constants are derived from fitting to the respected experimental data (Harris, Manning et al. 2002).

The incongruent dissolution of C-S-H was generally described by Berner (1988) as given in equation (2) where a, b, x and y are stoichiometric coefficients.



According to Chen, Thomas et al. (2004) dissolution behaviour of C-S-H depends on C/S ratio, silicate structure and $Ca(OH)_2$ content. Dissolution is incongruent at higher C/S ratio where preferentially Ca is dissolved and becomes more congruent when the ratio is lower (Taylor 1997). With increasing Si content the atomic structure adapts to the compositional changes by polymerisation. Formation of C-S-H phase with foil-like morphology, accompanied by increasing specific surface area is reported to go along with decalcification (Thomas, Chen et al. 2004). Congruent dissolution is assumed to occur at C/S ratio about 0.7 to 1.0, according to experimental data and fitting from modelling studies (e.g. Harris, Manning

et al. (2002), Kersten (1996)). Ideally it is assumed that a C-S-H phase of crystalline tobermorite composition (which has a C/S ratio of 0.83) dissolves congruently (Taylor 1997) which Trapote-Barreira, Cama et al. (2014) have recently reconfirmed, extended by measuring and fitting dissolution rates of C-S-H from high to low C/S ratio in a flow-through reactor until achievement of steady-state conditions.

C-S-H phases are often described as *stable*, but thermodynamically they are unstable at ambient conditions with respect to crystalline afwillite, jennite, or tobermorite (with C/S ratios 3, 1.5, 0.83, respectively) among other crystalline phases, which are generally not observed in cement. However, even though thermodynamically not stable, C-S-H phases persist in cement over extremely long time scales. On the long term they mainly determine the chemistry of cement pore water, due to their extensive metastability. Recently the formation of C-(A,F)-S-H phase gained more and more scientific attention. However, compared to C-S-H, mechanisms of formation, structure and stability are less well understood. Several authors found an increasing content of Al in C-S-H phase with progress of degradation. Hidalgo, Petit et al. (2007) found that below pH 10.2 and therefore late stages of cement degradation, a C-A-S-H matrix formed that replaced C-S-H.

The actually observed features of cement degradation depend on characteristics of the experimental method employed in the investigation. An example is the difference between use of particulate material with an increased reactive surface area and a solid monolith that mainly is in contact at the outer surface or if water penetrates it at areas accessible by the connected pore system (Atkinson, Nelson et al. 1986). Further, the presence or absence of a carbonate source modifies cement degradation effectively. A source may be the atmosphere or the carbonate content of infiltrating water which in a natural environment could be regulated either by plants and microorganisms, degradation of organic matter or again by exchange with the atmosphere. If there is carbonate in the system so that precipitation of carbonate minerals takes place most studies find that it is combined with a volume increase of the solid phase which may form crusts, block the pores and decrease importantly the porosity of the cement (Pfingsten 2001). Porosity decrease is reasonable as dissolution of portlandite with a molar volume of $32.8 \text{ cm}^3/\text{mol}$ followed by calcite precipitation brings an increase of molar volume by 11.1 % (Ruiz-Agudo, Kudłacz et al. 2013).

If such clogging occurs and the carbonate minerals are stable, further progress of degradation is bound to diffusion processes which are very slow (Taylor 1997, Glasser, Marchand et al. 2008). Typically, this is observed in form of rims on the surface of cement. These rims do reflect on very short distance almost the complete series of cement degradation in terms of solid phase assemblages. Fresh cement can in such a case still be found in the core while completely degraded HCP is in contact with the solution (Figure 5). The processes leading to the different mineral assemblages at different distances between surface and core are often referred to be due to *local equilibrium* conditions within the pore space where solution exchange is limited.

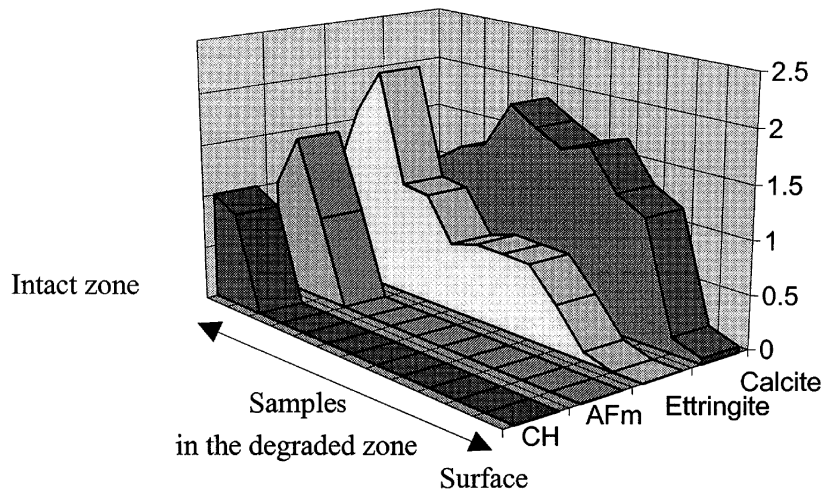


Figure 5 Abundance of crystalline cement hydrates in a degradation rim. The profile reaches from the unaltered cement to the surface where solid is in contact with bulk solution. Phase assemblages developed during 6 months contact between cement and demineralised water. Numbers on vertical axis give relative abundance with reference to the intact zone. Figure extracted from Faucon, Adenot et al. (1998).

A completely different result of cement degradation is obtained when the cement microstructure is in contact with solution allowing for an exchange of the pore water. Taylor (1997) speculated that flowing groundwater probably attacks cement phases simultaneously and that dissolution of aluminosilicates may contribute earlier to the solution composition due to their large specific surface area. The final product of completely degraded HCP would be severely depleted in Ca and mainly consist of hydrous silica, alumina and iron oxide as long as carbonate was absent. Given abundant carbonate, he expected the corresponding metal carbonates to form the final product of degradation.

Côté (1986) evaluated in dynamic batch experiments that Portland cement has the capacity to neutralize 2000 to 3000 times its volume of a leaching solution of pH 3. Butcher, Cheeseman et al. (1993) determined in flow-through experiments that 575 times the solid volume of deionised water (approximate pH 5-6) were necessary to decrease pH in the outflow from initially 12.2 to 10.5. They saw their results in line with the results of Côté even though they applied pressure to force flow through the pores while Côté did not have flow. Côté (1986) found that after almost 2 years of dynamic leaching cumulative fractions of Cd(II), Cr(III) and Pb(II) mobilised from the doped cementitious wastefrom remained below 1 % while the cement was carbonated and degraded. In contrast to the cations mobilisation of As(III) oxyanion was only limited by the renewal rate of the solution in the study. Butcher and co-workers also noticed that metals (Cr, Fe, Zn – redox states not specified) that had been incorporated previously into the cement were not released significantly even though a significant amount of Ca was released from the solid. An initial peak of metal concentrations, also noted by Coté, was interpreted to stem from larger surface area available in the beginning.

Poon, Chen et al. (2001) also investigated metal mobilisation from cement stabilised/solidified waste in a flow-through setup where they varied pressure to maintain constant flow through a solid disk.

Like Côté (1986) and Butcher, Cheeseman et al. (1993) they used Ca and pH as indirect indicators for the condition of the cement and from the leaching behaviour of divalent metals (Pb, Zn, Cu and Ni) compared with that of Ca they concluded that the cementitious matrix basically retains the divalent metals before the structure of the cement is degraded. In one of their experiments, showing almost instantaneous mobilisation of Cr(VI) oxyanion, they observe unexpectedly low Ca mobilisation, but the setup using a solid cement sample did not allow to conclude if this was due to high content of Cr in the solid (1.4 wt.-%) and decelerated portlandite and C-S-H dissolution or just a matter of preferential flow through, e.g., a fracture. This example of uncertainty on chemical mechanisms, possibly caused by flow through fractures, highlights an important aspect for which use of a thin-layer flow-through reactor with crushed HCP material is advantageous. Its use reduces bias due to sample heterogeneity and thereby permits a new view on chemical processes of radionuclide retention and also cement degradation (chapter 1.4).

3.2.2 Other Cement Phases

While portlandite and/or C-S-H are still present, calcium-aluminium sulphates and silicates, which already form during clinker hydration, are also stable and generally define the porewater composition regarding elements apart from Ca and Si. Which phases are actually present in the hydrated cement paste depends on the chemical composition of the starting material and for some phases on external conditions such as temperature or carbonate availability. In any case the fate of Mg, Al and S(VI) is closely connected in cementitious systems due to several phases that may form, containing one, two or all three of these elements.

The most frequently occurring AFt phase in Portland cement is ettringite $\text{Ca}_6\text{Al}_2(\text{SO}_4)_3(\text{OH})_{12}\cdot 26\text{H}_2\text{O}$ which has a variable water content, depending on the conditions. A key parameter for the stability of ettringite is a relatively high activity of S(VI) in the pore water. As a rule of thumb, ettringite may transform to the AFm phase (calcium) monosulphoaluminate ($\text{Ca}_4\text{Al}_2(\text{SO}_4)(\text{OH})_{12}\cdot 6\text{H}_2\text{O}$) when activity falls below a critical level, approximately 10^{-4} mol/l (Verein Deutscher Zementwerke 2002). Therefore, the presence of ettringite depends mainly on the total sulphate content of the cement clinker. If, for example, an external sulphate source is present, ettringite may also form secondarily in HCP (called delayed ettringite formation). This is one of several mechanisms often causing severe structural damage to the cementitious materials since ettringite formation involves an increase in volume that initiates crack formation in hardened pastes (Collepari 2003). Yet, substitution of SO_4^{2-} by, e.g., CO_3^{2-} , OH^- , Cl^- , $\text{H}_2\text{SiO}_4^{2-}$ as well as SeO_4^{2-} (Pöllmann, Kuzel et al. 1990, Baur and Johnson 2003b, Pointeau, Hainos et al. 2006a, Pöllmann 2010) may outweigh a deficit in sulphate concentrations, thereby stabilising AFt phases. Similar substitution processes may occur in AFm phases (Baur and Johnson 2003b).

Due to the atomic structure of ettringite (Figure 6) it forms macroscopically thin fibres or prismatic, hexagonal platelets. The structure is made up by columns of $[\text{Al}(\text{OH})_6]^{3-}$ octahedra which are sharing OH

ions over edges and further connected by Ca, situated in $[\text{Ca}(\text{OH})_4 \cdot 4\text{H}_2\text{O}]$ polyhedra. This arrangement forms columns of $[\text{Ca}_3\text{Al}(\text{OH})_6 \cdot 24\text{H}_2\text{O}]^{3+}$ units, running parallel to c-axis what leaves interstitial open spaces, so-called channels. Water molecules and sulphate occupy these channels maintaining electroneutrality, while staying easily accessible for foreign ions and therefore ion-exchange reactions (Pöllmann (2010) and citations therein). Moreover, the OH^- groups are subject to replacement as well as the octahedral sites of trivalent Al. The latter may be substituted by silica or ferric iron which has been observed by several studies, e.g. Glasser (2002) and references therein. By nuclear magnetic resonance spectroscopy NMR it was found that Si also may occupy sites in the channel structure of synthesised ettringite (Pöllmann 2010).

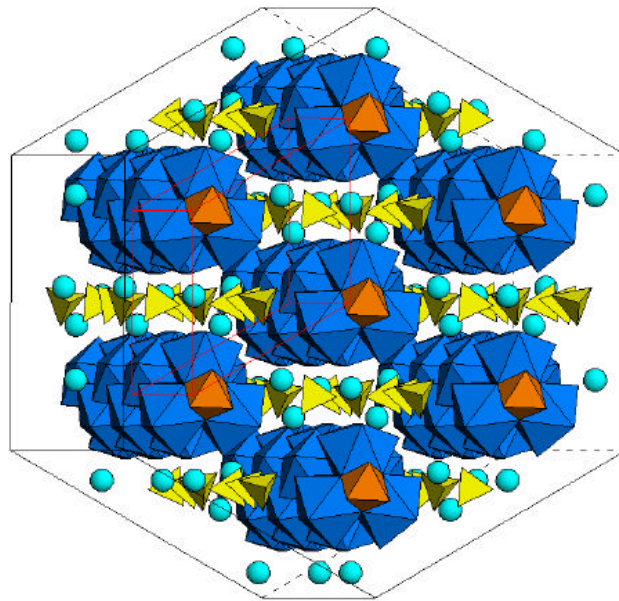
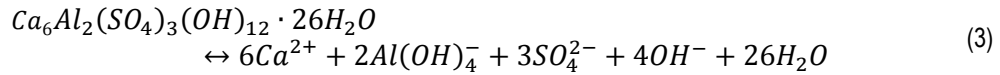


Figure 6 Structure of Ettringite, illustrated by coordination spheres of metal cations and sulphur. Blue polyhedra: Ca(II), red octahedra: Al(III), yellow tetrahedra: S(VI), blue circles: H₂O. The hexagonal frame indicates the typical macroscopic shape (extracted from Bollmann (2000)).

Möschner et al. (2008, 2009) determined the solubility product of Fe-ettringite based on the dissolution reaction given in equation (3) for the Fe analogue. The existence of a solid solution series had been suspected earlier, although questions on the continuity of miscibility still remain open. Möschner and co-workers results proof a solid solution series, but cannot exclude a miscibility gap between 25 and 65 mol% Al on the octahedron site.

When dissolving in water AFm and AFt minerals liberate hydroxyl ions (equations (3) and (4)) and may act as buffer minerals in late stages of C-S-H dissolution by keeping pH in the range of 10.5 to 11 (Atkins and Glasser 1992).

Ettringite dissolution:



Monosulphoaluminate dissolution:



Exact evaluation of the influence of ettringite and monosulphoaluminate on the buffering capacity of cement has not attracted as much interest in studies on chemical cement stability as did portlandite and especially C-S-H due to its importance at early time and to C-S-H because of its major abundance in cement. There is significantly less thermodynamic and kinetic data compiled. However, data on ettringite are available and recently also substituted phases have been getting more and more characterised. Möschner, Lothenbach et al. (2008) described the Fe(III) end-member of ettringite. Ettringite is dissolving congruently and considered to be stable between pH 10.5 and 13, but was even found to be stable down to pH 9.5 (Damidot and Glasser 1992, 1993, Perkins and Palmer 1999). More precisely, experiments show that between pH 10.7 and pH 9.5 ettringite may be present in cement systems (Terai, Mikuni et al. 2007), but starts dissolving incongruently to $CaSO_4 \cdot 2H_2O$ and Al-hydroxide (Myneni, Traina et al. 1998). However, a recent study by Jiménez and Prieto (2015) found that ettringite starts to decompose already below 50 °C, thereby questioning the sense of assuming its persistence over long time scales.

Brucite $Mg(OH)_2$ is sometimes the Mg concentration limiting phase in cement. It is isostructural to portlandite and only stable at very alkaline pH. An occasionally observed, but sometimes important mineral group for the fate of Mg in hydrated cement are hydrotalcite-type minerals (Taylor 1997). The typical chemical composition is $Mg_4Al_2(OH)_{14} \cdot 3H_2O$ and structurally similar are phases such as layered-double hydroxides. The class of minerals is peculiar as it consists of octahedral Mg and Al layers which are positively charged and balanced by easily exchangeable carbonate ions. Unfortunately, there is little thermodynamic data and its consideration in modelling studies not always given. For example, depending on database and applied modelling strategy, hydrotalcite was found to be necessary to explain sulphate evolution of a degrading cement while it had to be discarded to improve model results in another attempt in order to obtain better fit to the same experimental data as was reported in a benchmark modelling study by (Savage, Soler et al. 2011).

3.3 Contaminant Retention in a Cementitious Environment

3.3.1 General Considerations

The low solubility of most metals in alkaline conditions makes them relatively immobile in cementitious systems. Important exceptions from this behaviour are those whose speciation is dominated by oxyanions (e.g., SeO_4^{2-} , SeO_3^{2-} , AsO_4^{3-} , AsO_3^{3-}). The extent of retention of dissolved ions in cement

pore water depends very much on the type of bonds which these ions may form with the solid phases. Ions that form bonds and get adsorbed to mineral surfaces or even incorporated into crystallographic sites have a certain resistance against remobilisation (Achterbosch, Bräutigam et al. 2003).

In the scientific literature there is a considerable body of information, experimental, theoretical and computational, on the different processes that lead to retention of contaminants or aqueous species in general when contaminated solution comes in contact with hydrated cement phases.

A robust method to evaluate maximum concentrations of an inorganic contaminant in cement pore water is to determine the relevant single phase that limits its equilibrium concentration in solution by precipitation. This solubility approach generally provides a threshold of aqueous concentrations to maximum values. Precipitation may occur once the solubility product of the dissolved ions is equal to or exceeding the equilibrium activities in solution. However, regarding this approach care has to be taken that in the concerned systems no parameters or reactions lead to enhanced solubility of the contaminant under investigation. Examples are the occurrence of colloids which may adsorb contaminants and therewith facilitate dissolution and transport or the presence of organics or growth poisons which impede nucleation of nuclei or subsequent growth of mineral layers.

Different processes causing retention of contaminants may go hand in hand. Adsorption on a mineral surface may be followed by surface diffusion to kink-sites and then by attachment of further *growth units* of the host mineral. In such a sequence an initially adsorbed species can finally be incorporated into the structure what could be observed as non-reversible. In sorption-desorption experiments this was often termed *irreversible adsorption*, even though in such a case the process under investigation would have been surface precipitation (Curti 1997) and incorporation is strictly speaking not precipitation, but recrystallisation. A special, but in nature frequently occurring process is uptake of traces by a host phase, leading to formation of a solid solution. However, formation of real solid solutions has to be verified with great care as compositional variations, e.g. zoning, occur frequently (Bruno, Bosbach et al. 2007).

Experiments can be designed to distinguish two mechanisms. Diffusion controlled processes may, e.g., be distinguished from surface reaction controlled precipitation rates. The former may be the kinetic control of mineral precipitation by diffusion of ions through a depleted boundary layer in solution over the growing mineral surface. By sufficient stirring of the solution formation of such a depleted layer may be eliminated. Therewith it can be controlled if the diffusion kinetics is being investigated or the attachment and detachment rates of the ions to/from the growing surfaces are the object of the study.

Formation of such a layer can therewith be anticipated experimentally (Bosbach 2010). Further, reactivity of surfaces for adsorption of radionuclides depends on the presence and availability of competing or complexing ligands in the system, e.g. sulphate or carbonate ions may compete with oxyanions or cations complex and stabilize them in solution.

The different mechanisms influencing or controlling contaminant retention and binding in cement systems can be analysed in detail using isolated solid phases. Theoretically, a complete model could be

based on all determined mechanisms from single systems, thereby explaining retention in a real cement system. In practice, a holistic model is very ambitious, especially if degradation of HCP is also considered. Different HCPs always vary in their compositions and hence (meta)stable mineral paragenesis vary from one cement formulation to another (except for portlandite and C-S-H which are always contained, even though in varying amounts). Moreover, retention as well as cement degradation, depend on site specific conditions (groundwater type, temperature, etc.). These parameters altogether influence the processes involved in contaminant retention. For example, presence or absence of calcite from cement during hydration (sometimes added as a filler) influences the final phase assemblage (Lothenbach and Wieland 2006) and further entrains presence of aqueous carbonate in porewater which may form complexes with radionuclides or other contaminant species.

Glasser (1997) discussed fundamental aspects of concentration limiting processes in cement matrices. Besides investigating only parts of the system, he stressed the importance to derive information for predicting and modelling evolution of contaminant concentrations in cement systems because the interplay between different species and phases in a complex system might easily be overlooked. For example, assuming a metal hydroxide species instead of the corresponding metal aluminate as solubility limiting phase suggests much higher aqueous metal concentrations than actually found in cement systems. In this system Al is generally abundant and the aluminate phase, possessing lower solubility, may determine aqueous concentration of the considered metal. In Figure 7 the general amplitude of sorption and precipitation processes and their 'capacity' in terms of impact on contaminant concentrations in solution are tentatively illustrated. It visualizes that precipitation of contaminants may efficiently reduce extremely high concentrations and that sorption processes become more important when contaminant concentrations are already on a comparatively lower level.

In the solidification/stabilisation approach, (co-)precipitation of contaminants is the chemical process that is aimed for. Whenever a contaminant carrying solution comes in contact with an unpolluted hydrated cement barrier, the contaminant concentrations may not be sufficiently high enough to precipitate pure phases. If so, only co-precipitation, sorption and diffusion processes may reduce aqueous contaminant concentrations.

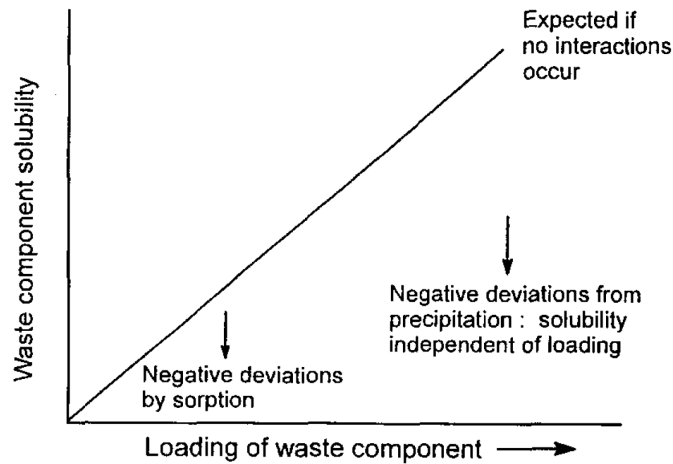


Figure 7 Graphic illustration of the general conditions where contaminant concentration reducing processes actuate, extracted from Glasser (1997).

In general, there is consensus that stoichiometric substitution of contaminant ions into C-S-H phase does not take place to a noteworthy amount (Gougar, Scheetz et al. 1996). However, the high abundance in cement and its high specific surface area due to outer C-S-H and especially in degraded states makes it an important phase for considerations on radionuclide immobilisation. Consequently, the investigated processes that are targeted for in studies usually are limited to sorption or diffusion processes. The most important sites in these reactions, the silanol groups and Ca exchanged silanol groups are presented in equation (5) and (6), with the example of Se complexation ('>' denotes surface species).



In several studies Faucon, Adenot et al. (1998) developed a model of the C-S-H surface layer structure when cement is degrading and less Ca becomes available in the pore solution. They suggested two models for ion-exchange with the trivalent metals Fe and Al based on Mößbauer spectroscopy and NMR analysis. Since pure C-S-H phase lacks trivalent species, each ion exchange has to go along with a charge compensation mechanism. They found replacement reactions according to equation (7) and (8) for Fe(III) and Al(III), for different equilibrium concentrations of Ca.



In the first exchange reaction a Ca ion from the Ca-O layer and an adjacent proton from a dangling OH⁻ group of a bridging tetrahedron are replaced by an Fe(III) atom which takes an unoccupied place in the Ca layer. In comparison, the exchange of Si from a bridging silica tetrahedron by Al is more complex and may be compensated by the coupled substitution of Ca from the neighboured portlandite layer with Fe (Figure 8).

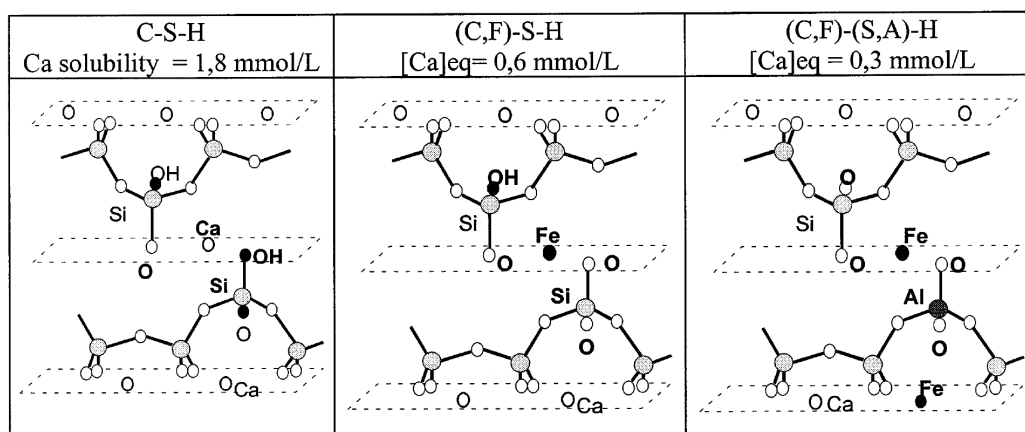


Figure 8 Modifications in the surface structure of C-S-H due to incorporation of foreign ions from solution, observed by Mössbauer spectroscopy and NMR. Figure from Faucon, Adenot et al. (1998).

These structural substitutions of ions in the major cement hydrate influence the stability of the C-S-H phase. Additionally, the substitution also represents an alternative mechanism for incorporation and sorption of contaminant ions from solution. In this sense Hong and Glasser (2002) substituted 6-7 % of Si in C-S-H by Al to investigate the adsorption of alkalis. They considered the incorporation of Al as formation of a ‘solid solution’¹ and measured markedly enhanced partitioning of alkalis between solid and liquid phase compared to pure C-S-H. The authors suggested two explanations, i.e. 1) alkalis adsorb to silanol surface sites and their capability to adsorb alkalis increases with substituted Al on Si sites due to the modified charge and 2) alkalis get incorporated via a charge compensation mechanism where Al replaces Si and the monovalent alkali metal occupies a vacant site. It can be argued that besides alkalis also other positively charged ions such as Ni may get incorporated by the latter mechanisms.

For all solids a point of zero net charge² can be determined, i.e. generalising, the pH at which the surfaces carry no net charge. At lower pH surface charge commonly is positive and at higher pH charge becomes negative. Consequently, alkaline conditions are generally favourable for adsorption of positively charged aqueous species of metals. However, a negative net surface charge does not imply the non-existence of positive sorption sites on the surface and vice versa. Therefore, to a reduced extent, also electrostatic adsorption of cations on positively charged surfaces (as well as anions on negatively charged surfaces) is observed and very common for trace elements (Langmuir, Hall et al. 1997).

The surface charge of different cement pastes as well as the charge of single hydrated minerals has been measured mostly via zeta potential (ζ) (Viallis-Terrisse, Nonat et al. 2001, Pointeau, Reiller et al. 2006b, Elakneswaran, Iwasa et al. 2010) and is used to construct surface complexation models. One method of measurement is electrophoresis where ζ potential is deduced from the velocity of charged particles through a solution. The method bases upon the existence of an electrical double layer between

¹ Quotes were assigned because the term solid solution for a metastable phase is strictly not correct.

² Note that different methods exist to determine the point of zero charge, basing on different concepts and therefore do not always lead to the same results. Also, the point of zero charge can be determined for different crystal surfaces of one single crystal which may lead to different results, depending on the atomic structure.

solid and solution and the existence of an imaginary sheet, adjacent to the mineral surface, in which the liquid is stationary and charged.

For cement generally two isoelectric points result from ζ potential measurements at different stages of degradation: a first one around pH 12.9 (CEM I, Pointeau, Reiller et al. (2006b)) and a second between pH 11.1 (CEM I, Elakneswaran, Iwasa et al. (2010)) and pH 11.7 (CEM I, Pointeau, Reiller et al. (2006b)). At higher and lower pH values, ζ potential is negative while in between the two isoelectric points net charge is positive. Influencing factors are the composition of the cement and the adsorbed ions on surfaces. For example, adsorption of Na^+ on Portland Cement has no influence on ζ potential while Ca^{2+} and Cl^- cause more positive or more negative potential, respectively (Nachbaur 1998, Pointeau, Reiller et al. 2006b, Elakneswaran, Nawa et al. 2009). Pointeau, Reiller et al. (2006b) reassembled results from different studies employing different paste compositions and added data for C-S-H, ettringite and portlandite (Figure 9).

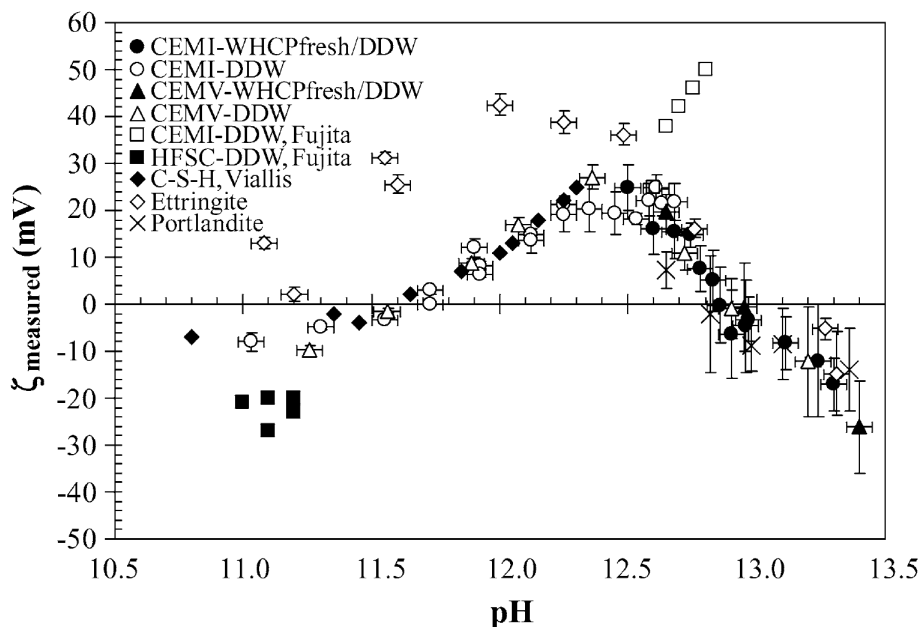


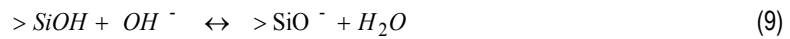
Figure 9 Collection of Zeta potential (ζ) measurements, published by Pointeau, Reiller et al. (2006b).

The authors concluded from ζ potential measurements with hardened cement paste that whenever portlandite has completely dissolved, surface charge of hardened cement paste is determined by C-S-H phase whose silanol groups would be widely deprotonated and negatively charged (equation (9)). When portlandite is still present, Ca^{2+} ions from solution form inner-sphere complexes with silanol sites (equation (10)) and overcompensate the negative charge of C-S-H (Viallis-Terrisse, Nonat et al. 2001). This causes the relatively strong positive potential around pH 12.5 and explains decreasing potential with lower Ca concentrations at advanced degradation stages of cement, as is the case for negative potential of fresh HCP. Due to competition with high concentrations of Ca ($> 10^{-2}$ mol/l) for surface sites, electrostatic adsorption of positively charged cations to hydrated cement should be low as long as the

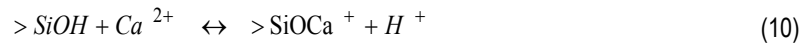
system is in equilibrium with portlandite. Further, cation adsorption should increase with ongoing degradation and net decrease of the zeta potential of C-S-H phase and the cement in general. This is what has been observed in sorption studies of cations, e.g. with Ni^{2+} , on C-S-H phase or hydrated cement paste (Aggarwal, Angus et al. 2000).

It has to be mentioned here that not only less competition with Ca for surface sites and decreasing surface charge enhances Ni adsorption in degraded HCP systems. Further, decreased C/S ratio of polymerised C-S-H promotes Ni adsorption.

Deprotonation of silanol sites:



Inner-sphere complexation of Ca with silanol sites:



3.3.2 Nickel

The retention of Ni in systems containing hardened cement paste is still not well understood and different studies suggest different solids as the ones responsible for the retention of Ni. Moreover, speciation of aqueous Ni at alkaline conditions has recently been put to discussion again. Palmer, Bénézeth et al. (2005) and Palmer, Bénézeth et al. (2011) presented studies questioning the so far widely accepted NEA selection on Ni speciation by Gamsjäger, Bugajski et al. (2005). They could not observe $\text{Ni}(\text{OH})_3^-$ species (up to hydroxyl concentrations of 0.1 mol/kg) and considered only $\text{Ni}(\text{OH})_2^0$, NiOH^+ and Ni^{2+} species to be stable at alkaline pH. Palmer and co-workers (2005, 2010) indicated a solubility limit around $6 \cdot 10^{-9}$ mol/l for $\beta\text{-Ni}(\text{OH})_{2(\text{cr})}$ for $\text{pH} > 11$ at 25 °C and infinite dilution (Figure 10). In contrast, according to the earlier selection of thermodynamic data by Gamsjäger, Bugajski et al. (2005) it would be expected that Ni hydroxide precipitates above concentrations around $5 \cdot 10^{-8}$ mol/l (pH 10-11) and $5 \cdot 10^{-6}$ mol/l (pH 13.3) in the alkaline system (Figure 11). However, already (Gamsjäger, Bugajski et al. 2005) noted biasing influence of the anion (Cl^- , NO_3^- , SO_4^-) used in the preparation of pure Ni hydroxide which may lead to different results among studies. An ongoing study (González-Siso, Gaona et al. 2015) also does not observe indications for the existence of the $\text{Ni}(\text{OH})_3^-$ species in 0.5 molar NaCl-NaOH and NaNO₃ solutions up to pH 13.

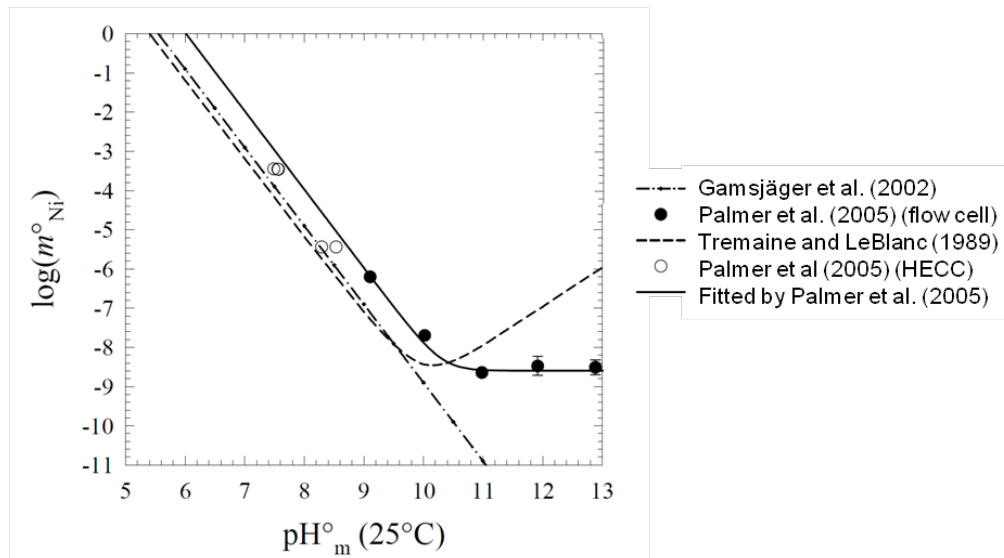


Figure 10 Comparison of experimentally determined and modelled $\text{Ni}(\text{OH})_{2(\text{cr})}$ solubility (mol/l), calculated for 25°C at infinite dilution. Figure from Palmer, Bénézech et al. (2005) with modified citations in the legend.

There is no direct evidence in literature on the phase(s) incorporating the Ni fraction from raw materials of Portland cement based HCP. This is basically due to the relatively low content of Ni in HCP with a mean share of 23 $\mu\text{g/g}$ (Verein Deutscher Zementwerke 2001). However, Glasser (2001) reasoned that during hydration of Portland cement clinker, soluble Ni would most likely precipitate initially as oxide and hydroxide which subsequently react to hydrotalcite (LDH) like phases.

Investigations aimed to determine the retention of Ni in cement materials basically led to two key conclusions. First, a number of studies suggested that Ni-Al layered double hydroxides form at almost any Ni concentration during the cement hydration process (e.g., Scheidegger, Wieland et al. (2000), Scheinost and Sparks (2000), more results will be discussed later in this chapter). However, systematic investigation of this mechanism is still lacking. Second, other studies (see Gougar, Scheetz et al. (1996) and citations therein) do not identify this phase as the one retaining Ni, but suggest α - and β - $\text{Ni}(\text{OH})_2$ as solubility limiting phases. Additionally, another solid Ni hydroxide was encountered which was suspected to play a role in the transition of α into β hydroxide. However, complete description, extraction or synthesis of a pure phase for thermodynamic and crystallographic characterisation has not been successful (Rajamathi, Subbanna et al. 1997, Vespa, Dähn et al. 2006c).

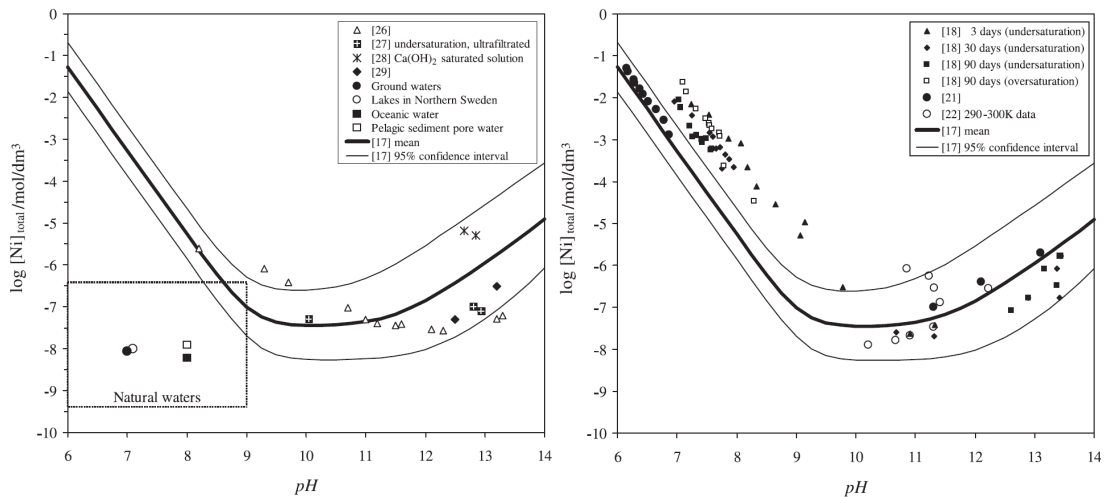


Figure 11 Left: High Ni concentrations measured in natural waters and from experimental studies in the cement system (triangles and diamonds). Right: experimental data from solubility measurements of crystalline Ni(OH)₂. Lines in both figures give the modelled, pH-dependent solubility of Ni(OH)_{2(cr)} at 0.1 M ionic strength and the associated uncertainty. Figures extracted from Hummel and Curti (2003).

Several mechanisms for Ni retention by cement have been suggested over the last decades. Published, measured distribution coefficients and identified retention mechanisms are summarised in Table 4 and Table 5. Gougar, Scheetz et al. (1996) presented some of the possible mechanisms, namely substitution of 8-fold coordinated Ca in ettringite or even Ni²⁺ replacing octahedrally coordinated Al³⁺. In the latter case a mechanism has to be involved, compensating the resulting negative charge. Gougar, Scheetz et al. (1996) further referred to a study by Atkins, Glasser et al. (1993)³ who determined a Ni(OH)₂ gel, intermixed with C-S-H in experiments using blended cement. Other studies by Kumar, Komarneni et al. (1987) and Bonen, Johnson et al. (1994), also cited by Gougar, Scheetz et al. (1996) indicated surface related retention mechanisms, i.e. exchange of adsorbed Ca by Ni on C-S-H phases. A comprehensive investigation by Aggarwal, Angus et al. (2000) found increasing sorption of Ni to C-S-H with decreasing C/S ratio and increasing Al content which they observed on pure phases and correlated with sorption experiments on different cement formulations. From their study they further concluded that the influence of limestone on Ni sorption onto hardened cement paste is negligible. Other studies suggested considerable sorption and incorporation of Ni(II) by calcite (Hoffmann and Stipp 2001, Lakshtanov and Stipp 2007), but the authors performed experiments at calcite equilibrium pH around 8.3, far away from cementitious conditions. Therefore, aqueous speciation of carbonate and Ni as well were distinct and extrapolation of their findings to cement equilibrated systems is uncertain. No study was encountered providing evidence of Ni retaining calcite in cementitious systems. Moreover, a sound study measuring surface charge or streaming potential of calcite at pH in the range 12 - 13 and solution composition typical for cementitious conditions does not exist to the best of our knowledge. However, basing on the surface charge model developed for calcite by Heberling, Trainor et al. (2011) and

³ Atkins, M., Glasser, F. P., Moroni, L. P. and Jack, J. J. (1993) DOE Report No. DOE/HMIP/RR/94.011

Heberling, Bosbach et al. (2014), one can make an educated guess by extrapolating to cementitious conditions. It results that calcite surfaces are expected to carry neutral to positive charge at these conditions, due to high concentration of positively charged Ca in solution. If $\text{Ni}(\text{OH})_2^0$ is the dominant Ni species, no electrostatic attraction or repulsion for adsorption on calcite occurs, but if $\text{Ni}(\text{OH})_3^-$ would be the dominant species, surface charge would be favourable for electrostatic adsorption of Ni at these conditions.

Van Gerven, Cornelis et al. (2006) investigated the release of heavy metals from cement (CEM I) bound waste in dynamic batch experiments as a function of the degree of carbonation. They found that Ni release, contrarily to other metals, is independent of the carbonation of the cement. Unfortunately, no efforts were made to determine the solid Ni containing phase(s). Pöllmann (2010) summarised that on the one hand, replacement of Ca in the structure of C-S-H phases by metal ions like Ni^{2+} occurs to a very low extent, if it does at all. On the other hand he stated that inclusion of complete layers of foreign metals into C-S-H familiar phases would be possible, giving the example of the mineral minehillite, $(\text{K},\text{Na})_2\text{Ca}_{28}\text{Zn}_5\text{Al}_4\text{Si}_{40}\text{O}_{112}(\text{OH})_{16}$ (Dai, Post et al. 1995).

From a literature review on field studies Hummel and Curti (2003) constructed a list of six mineral classes that could potentially limit Ni concentrations in groundwater as pure phases or by formation of solid solutions. They finally concluded with reference to spectroscopic studies that only two groups seem to be relevant in cementitious systems: layered double hydroxides and sheet silicates. Below solubility limits Ni concentrations would be mostly influenced by adsorption to aluminosilicate surfaces.

An X-ray absorption fine structure (XAFS) study by Scheidegger, Wieland et al. (2000) proved precipitation of Ni-Al LDH (Figure 12) in cement paste, a finding which initiated a series of further studies on this topic. For a wide range of Ni concentrations employed in laboratory experiments (from 50 to 5000 $\mu\text{g/g}$ Ni loading in cement) it was found that the main Ni containing solid phase was precipitated layered double hydroxide (Vespa, Dähn et al. 2006a). This occurred under conditions where $\text{Ni}(\text{OH})_2$ phases were oversaturated at the same time (e.g. Scheidegger, Wieland et al. (2000)). The studies by Scheidegger, Wieland et al. (2000) Scheidegger, Wieland et al. (2001) and Vespa, Dähn et al. (2006c) showed that addition of Ni to already hydrated cement and Ni incorporation upon clinker hydration lead to formation of the same solid Ni phases.

Using radioactive ^{63}Ni Wieland, Tits et al. (2006) experimentally determined a solubility limit of Ni in artificial cement pore water of $(2.9 \pm 0.5) \cdot 10^{-7}$ mol/l at pH 13.3. However, when having hardened cement paste present in the system, the maximum Ni concentration in solution decreased to $(7.3 \pm 3.9) \cdot 10^{-8}$ mol/l, quasi-independent of the liquid to solid ratio. They observed rising aqueous Ni concentrations while the added amount of Ni was increased and suggested that a Ni containing solid-solution, Ni-Al LDH, would probably be the solubility limiting phase. They further observed that isotopic exchange of Ni from the cement matrix with radioactive Ni from solution ($5 \cdot 10^{-9}$ mol/l Ni concentration) was fast since equilibrium was reached in less than 7 days. The process was controlling Ni concentration at this low level and a distribution coefficient of $0.15 \text{ m}^3/\text{kg}$ was determined.

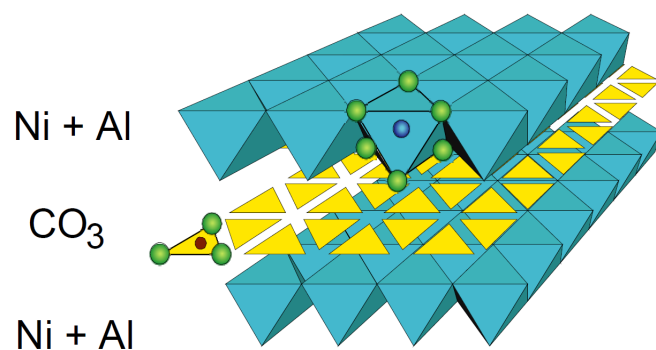


Figure 12 Visualisation of the Ni-Al LDH structure, a hydroxycarbonate type phase (Mg-Al LDH phases). The interlayer anion can be substituted, e.g., by OH^- , SO_4^{2-} , Cl^- or NO_3^- . Green balls represent oxygen atoms. Graphic extracted from Vespa, Dähn et al. (2006a).

The study by Vespa, Dähn et al. (2006a) on Ni-binding by cement during hydration revealed that Ni accumulates at distinct spots and that formation of Ni-Al LDH mainly takes place at rims around the inner C-S-H phase. It was observed that Ni-Al LDH forms rapidly and in parallel to ettringite precipitation which also consumes Al. In their batch experiments cement clinker with Ni loadings from 50 to 5000 $\mu\text{g/g}$ was used. The cement was cured at water to cement ratio of 0.4 and 1.2 l/kg so that resulting Ni concentrations in the pore water initially did exceed the solubility of Ni hydroxides at the hyperalkaline pH by far. Very low concentrations were finally measured in solution, below the Ni hydroxide solubility. Vespa, Dähn et al. (2006c) stated that also precipitated $\alpha\text{-Ni}(\text{OH})_2$ transforms to Ni-Al LDH while $\beta\text{-Ni}(\text{OH})_2$ does not transform to either of these phases. It is therefore possible that $\alpha\text{-Ni}(\text{OH})_2$ may function as a precursor phase of LDH in the cement system. Co-existence of Ni-Al LDH phases with (minor amounts of) Ni hydroxide indicates that either the system could not reach equilibrium conditions, or that there are conditions at which both phases may be stable. However, the setting of LDH around inner C-S-H (Figure 13) indicates that there is a driving force for Ni-Al LDH to form in this location, but so far no explanation was given for this setting. The position suggests that Ni-Al LDH forms before complete filling of the pore space by C-S-H. The occurrence of some encountered hot spots of accumulated Ni by Vespa, Wieland et al. (2007) leaves some degree of uncertainty because of the possibility that these are artefacts inherent from spontaneous precipitation or insufficient homogenisation at the start of experiments which may have influenced the processes.

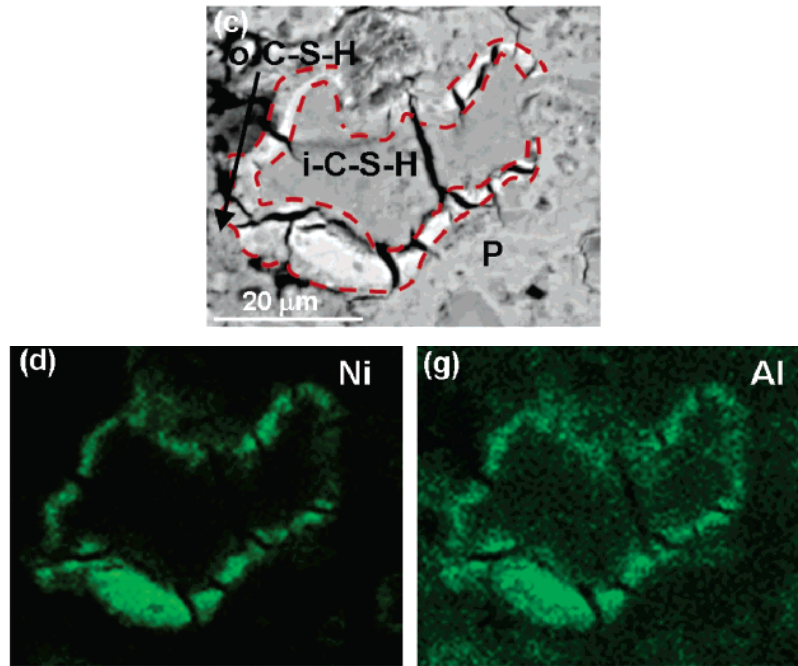


Figure 13 Backscattered electron image and elemental mapping (SEM-EDS) revealing a rim of mainly Ni-Al LDH, formed around inner C-S-H (i-C-S-H) and bordered by outer C-S-H (o-C-S-H) as well as portlandite (P). Images extracted from Vespa, Dähn et al. (2006a).

The investigations on Ni uptake by cement via LDH precipitation strongly contributed to the understanding of Ni behaviour in cement systems. Nevertheless, some mechanistic aspects remain unresolved, which is mainly due to the selected experimental procedures and the complexity of the system. There is a lack of direct proof for the formation of layered double hydroxides during the processes that occur when hardened cement paste is exposed to pore water with Ni concentrations around the $\text{Ni}(\text{OH})_2$ solubility (Wieland, Tits et al. 2006). Scheinost and Sparks (2000) demonstrated the importance of different Al containing phases and Al availability for the formation of metal-Al LDH phases in cementitious conditions. Their results indicated that on Al containing minerals that made Al available LDH phases formed at alkaline pH. However, on minerals not containing Al or on Al containing minerals which did not readily release it, pure Ni hydroxides formed instead. Scheckel, Scheinost et al. (2000) and Peltier, van der Lelie et al. (2010) found a similar influence of available mineral surfaces providing Al in contaminated soils. An example for such a potential host phase is gibbsite. Comparing the spots of metal-Al LDH occurrence in real HCP, around inner C-S-H, and studies that used pure phases it appears that there is an explanation lacking for this specific location in cement.

Livi, Senesi et al. (2009) showed that an amorphous, Ni-Al LDH like phase forms at near neutral pH of 7.5 on pyrophyllite ($\text{Al}_2\text{Si}_4\text{O}_{10}(\text{OH})_2$). A study by Peltier, Allada et al. (2006), conducted for soils at pH between 5 and 9, found that Ni LDH phases are stable, but solubility increases as a function of interlayer anions in the order CO_3^{2-} - SO_4^{2-} - NO_3^- . Further, they stated that Ni LDH as well as precipitated $\text{Ni}(\text{OH})_2$ will on the long term transform to Ni phyllosilicates, the thermodynamically most stable Ni phase at their studied conditions. Ni-hydroxides would reach increasingly higher solubility from pH ~ 10

to neutral pH and therefore remobilisation from more degraded HCP would be expected if Ni would be present in the form of hydroxides. Contrarily, structural uptake of Ni by LDH phases and pyrophyllite would make Ni less soluble. Consequently, the immobilisation of Ni by Ni-Al LDH phases instead of simple hydroxides would be beneficial especially for long-term considerations of a cement barrier involving EBS.

Several studies investigated Ni incorporation during cement clinker hydration by adding Ni salt in solid form before hydration started (Vespa, Dähn et al. 2006a, 2006b, 2006c, 2007). The merit of this method is that high Ni concentrations can be easily added to the system whereby Ni is more easily detectable at the end. Other studies used already hydrated cement before exposing it to Ni. They later added very high Ni concentrations (10^{-2} mol/l) by mixing the Ni stock solution with artificial pore water directly in the vial with the hydrated cement powder already inside (e.g., Scheidegger, Wieland et al. (2000)). Finally, all studies which have reported Ni-Al LDH formation were performed at very high pH: 12.8 or higher. No study was found that reported results from more degraded HCP.

Another potential source of uncertainty from studies performed upon hydration of clinker may arise from the heat of hydration that develops during this exothermal process. Elevated temperatures could be attained which possibly favour formation of double hydroxides, as it is known from synthesis methods (Kühn 2008). However, this aspect is speculative as commonly laboratory samples are so small that severely elevated temperature inside the samples is not expected.

Summing up, it appears that even though sophisticated investigations have been undertaken to unravel the interactions of Ni in the cement system, the concentration limiting phases and prerequisites leading to their formation could not be clearly demonstrated, yet. The conditions under which Ni-Al LDH phases precipitate remain uncertain. From the literature survey it became clear that C-S-H probably plays a role for Ni retention, but there is controversy on the mechanisms it implies - adsorption of Ni to silanol sites, or a mechanistic influence to the formation of Ni-Al LDH phases around inner C-S-H phase. Up to now, the specific conditions under which Ni-Al LDH precipitates and its field of stability have not been deduced, but availability of Al was identified as an important parameter. Nevertheless, the role of surface related mechanisms has not been clarified yet. Formation of LDH was only observed at relatively high initial Ni concentrations, even though results indicate a low solubility at alkaline pH values. Ni retention mechanisms at late stages of cement degradation have not been investigated as far as we are aware.

Table 4 Summary of sorption study results investigating Ni retention on different cement formulations and C-S-H phases.

Cementitious material	pH	Initial Ni concentration mol/l	Solution type	w/c	Particle size mm	L/S ratio	Equilibration Time	Distribution coefficient m ³ /kg	Reference
BFS/OPC									
BFS/OPC/Limestone	11.9-12.7	$4 \cdot 10^{-10}$ - $7 \cdot 10^{-9}$	Pre-equilibrated with corresponding solid	0.33-0.6	0.25-1	0.01-0.033	21-42 days	0.001 - 1.6	[1]
Limestone/OPC									
PFA/OPC/Limestone									
BFS/OPC									
PFA/OPC									
Limestone/OPC	11.2-12.9	$6.7 \cdot 10^{-9}$	Pre-equilibrated with corresponding solids for cements and saturated Ca(OH) ₂ for C-S-H	6 months	<1.4	0.05	28 days	0.1-8	[2]
NRVB ± Limestone C-S-H									
SRPC (CEM I)	13.3	$3 - 6 \cdot 10^{-8}$	Synthesised cement pore water	1.3	Diffusion experiment		500 days	0.02-0.04	[3]
SRPC (CEM I)	13.3	10^{-6} - $5 \cdot 10^{-2}$	Synthesised cement pore water			0.02-1000	> 7 days	0.15	[4]
OPC	13.4		Synthesised cement pore water	0.6		0.03	2 months	0.04	[5]
C-S-H	13.3	$2.5 \cdot 10^{-9}$ (impurities)	Synthesised cement pore water			$3.5 \cdot 10^{-3}$	120 days	0.01	[6]
C-S-H	12.6-12.8	$3 \cdot 10^{-9}$	Equilibrated with CSH	-		0.023	30 days	0.170	[7]

NRVB...Nirex Reference Vault Backfill

[1] Pilkington and Stone (1990) [2] Aggarwal, Angus et al. (2000) [3] Jakob, Sarott et al. (1999) [4] Wieland, Tits et al. (2006) [5] Holgersson, Albinsson et al. (1998)

[6] Tits, Bradbury et al. (1998) [7] Cowper, Green et al. (2005)

Table 5 Summary of suggested Ni retention mechanisms and solubility limiting phases.

Retention mechanism / solubility limiting phases	Reference
Precipitation of α - and β -Ni(OH) ₂ Substitution of Ca in ettringite: $\text{Ca}^{2+} \rightleftharpoons \text{Ni}^{2+}$ Substitution of Al in ettringite: $\text{Al}^{3+} \rightleftharpoons \text{Ni}^{2+}$ (charge compensation mechanism undefined) Sorption to C-S-H by cation exchange with adsorbed Ca^{2+}	[1] (review article)
Ni(OH) ₂ that is neither the α , nor the β modification	[2]
Ni-Al LDH forms during hydration of cement clinker Ni-Al LDH forms when Ni is added to solution in contact with HCP	[3]
Ni-Al LDH forms during hydration of cement clinker	[4]
Ni-Al LDH forms when Ni is added to solution in contact with HCP	[5]
Solubility limiting phases in cementitious systems: layered double hydroxides and sheet silicates Below solubility limits adsorption of Ni to aluminosilicate surfaces	[6] (review article)
Ni-Al LDH is solubility limiting phase	[7]
α -Ni(OH) ₂ is possibly precursor of Ni-Al LDH Ni-Al LDH forms when Ni is added solution in contact with HCP Ni-Al LDH forms preferentially between inner and outer C-S-H	[8]
Ni-Al LDH forms on minerals that serve as source of Al Ni(OH) ₂ forms on minerals that do not liberate Al	[9] [10] [11]
Solubility limits: $(2.9 \pm 0.5) \cdot 10^{-7}$ mol/l Ni in cement pore water at pH 13.3 $(7.3 \pm 3.9) \cdot 10^{-8}$ mol/l in contact with HCP Indications for formation of Ni-Al LDH	[12]
Amorphous Ni-Al LDH like phase forms on pyrophyllite	[13]
Ni LDH are stable over the whole studied range from pH 5 to pH 9 Stability of Ni LDH decreases with interlayer anions in the order $\text{CO}_3^{2-} - \text{SO}_4^{2-} - \text{NO}_3^-$	[14]

[1] Gougar, Scheetz et al. (1996) [2] Rajamathi, Subbanna et al. (1997) [3] Scheidegger, Wieland et al. (2000) [4] Scheinost and Sparks (2000) [5] Scheidegger, Wieland et al. (2001) [6] Hummel and Curti (2003) [7] Vespa, Dähn et al. (2006a) [8] Vespa, Dähn et al. (2006c) [9] Scheinost and Sparks (2000) [10] Scheckel, Scheinost et al. (2000) [11] Peltier, van der Lelie et al. (2010) [12] Wieland, Tits et al. (2006) [13] Livi, Senesi et al. (2009) [14] Peltier, Allada et al. (2006)

3.3.3 Selenium

Selenium is a representative element of those forming oxyanions under oxidising alkaline conditions, so that there is a concern on its potential mobility. Under oxidising conditions and with standard cement compositions selenite and selenate are the dominant species (Olin, Noläng et al. 2005).

Some studies have shown that pure Se phases that may precipitate in the cement system comprise CaSeO_3 , $\text{CaSeO}_3 \cdot \text{H}_2\text{O}$ and $\text{CaSeO}_3 \cdot 2\text{H}_2\text{O}$ as well as $\text{CaSeO}_4 \cdot \text{H}_2\text{O}$ and $\text{CaSeO}_4 \cdot 2\text{H}_2\text{O}$ (Ochs, Lothenbach et al. 2002, Baur and Johnson 2003b, Bonhoure, Baur et al. 2006). Other studies have further suggested that retention of this element can be modelled by its incorporation into secondary AFt solid phases at concentrations below solubility limits of the pure phases (Ochs, Lothenbach et al. 2002, Rojo, Grivé et al. 2010).

For cement pore water at pH 13.3 thermodynamic calculations suggest a SeO_3^{2-} concentration of about $3 \cdot 10^{-3}$ mol/l Se in equilibrium with CaSeO_3 and 10^{-2} mol/l SeO_4^{2-} in equilibrium with CaSeO_4 , respectively (Baur and Johnson 2003a). This is supported by more recent experimental data from Bonhoure, Baur et al. (2006). Besides, also solid-solutions with ettringite and monosulphoaluminate may form in cement systems. Moon, Grubb et al. (2009) found precipitated $\text{CaSeO}_3 \cdot \text{H}_2\text{O}$ and $\text{Ca}_6\text{Al}_2(\text{SeO}_4)_3(\text{OH})_{12} \cdot 26\text{H}_2\text{O}$ (Se-ettringite) in slurries of soil with portlandite cement and cement kiln dust. Baur and Johnson (2003a) synthesised pure selenate-AFt and selenate-AFm crystals to determine the solubility of selenate end-members. They concluded that both minerals are stable under cementitious conditions. In case of low sulphate concentrations and pH values above 12, Se(VI) may be limited by Se-AFm precipitation. In general, AFm and AFt represent potential solubility limiting Se phases in cement by limiting Se(VI) concentrations around 10^{-4} mol/l (AFm) and 10^{-3} (AFt). They found that at lower sulphate concentration the selenate concentration decreases in solution, as Se may occupy sulphate places in AFt and especially AFm more easily in this case.

Solid-solution formation of a selenite- monosulphoaluminate was reported at Se(IV) concentrations above $2.5 \cdot 10^{-4}$ mol/l, accompanied by precipitation of CaSeO_3 and ettringite (Baur and Johnson 2003b). However, the authors speculated that CaSeO_3 in this case was surface precipitated on monosulphoaluminate and did not precipitate spontaneously from solution by heterogeneous nucleation. Further, they interpreted precipitation of ettringite as a sulphate concentration buffering reaction which was dissolved due to exchange by Se(IV). At lower Se(IV) total concentration only adsorption to monosulphoaluminate surfaces was observed.

In order to avoid precipitation of pure solid Se phases, sorption experiments at concentrations below 10^{-2} mol/l and 10^{-3} mol/l with selenate and selenite, respectively, were carried out to investigate sorption and co-precipitation potentials of cement phases. The different studies lead to some contradictory results and conclusions. Briefly, these concern hydrogarnet (does it play a role for Se retention?), C-S-H (does it play a role for Se(IV) retention?), ettringite (is Se(VI) structurally

incorporated or outer-sphere complexed? Does ettringite retain selenite at all?), retention kinetics (periods from 1 to 170 days can be found to reach equilibrium for selenite and selenate uptake on cement phases).

Due to chemical similarity of Se oxyanions with the sulphate ion and ubiquitous abundance of the latter in cement, sulphate containing phases have been investigated frequently by studies on Se retention, but studies also reported results for retention by C-S-H and other cement hydrates. Measured distribution coefficients and identified retention mechanisms are summarised in Table 6.

It was shown experimentally that there is no significant change of redox states when either Se(IV) or Se(VI) is introduced to the cement system in laboratory studies, even if measured conditions suggested that Se should have been reduced or oxidised. It was argued that this is due to slow kinetics of oxidation from Se(IV) to Se(VI) and vice versa to the reduction of selenate (Séby, Potin-Gautier et al. 1998, Johnson, Rudin et al. 2000, Bonhoure, Baur et al. 2006). Comparing dominant redox states the general observation is that retention of selenate is much weaker in the cement system than that of selenite (Solem-Tishmack, McCarthy et al. 1995).

Hydrogarnet was reported to have no or only negligible influence on Se(VI) retention in cement systems (Ochs, Lothenbach et al. 2002, Zhang and Reardon 2003). However, Pointeau, Coreau et al. (2008) cited Macé (2006)⁴ who found that ettringite and hydrogarnet controlled retention of the reduced Se(IV) species in cement. Further, it was stated that adsorption on C-S-H phases would not be significant. The latter conclusion is also supported by Pöllmann (2010) who assumed that no process had been identified that would explain chemical immobilisation of Se(IV) by C-S-H.

The anion-exchange mineral hydrotalcite was rarely investigated with respect to selenate retention. Recently, Paikaray, Hendry et al. (2013) compared uptake of arsenate, molybdate and selenate. They found that selenate was the weakest retained anion and observed further weakening towards higher pH (which in their study was pH 10), caused by increasing hydroxyl concentration. In general at alkaline cement pH it can be expected that there is intensive competition to Se(VI) adsorption by hydrotalcite.

A number of studies were devoted to the potential retention of Se by ettringite. Johnson, Rudin et al. (2000) observed in batch adsorption studies with CEM-V cement and clay as well as silica fume admixtures that selenite adsorption occurred mainly on the cement itself. In adsorption/desorption experiments they determined distribution coefficients from 0.25 to 0.93 m³/kg, determined in the range of initial SeO₃²⁻ concentrations between of $\sim 8 \cdot 10^{-8}$ and $\sim 2 \cdot 10^{-5}$ mol/l, but identified that selenite was irreversibly adsorbed to the cement. Pointeau, Hainos et al. (2006a) measured lower distribution coefficients of 0.12 m³/kg for selenite between fresh cement and pore water at comparable conditions to the study by Johnson, Rudin et al. (2000).

Baur and Johnson (2003b) looked at sorption on pure, synthesised cement phases and found different reactions between Se(VI) and ettringite, C-S-H (C/S ratio = 1) or monosulphoaluminate. The former two phases did hardly adsorb Se(VI), but for ettringite a distribution coefficient of 0.03 m³/kg could be determined. Monosulphoaluminate formed a solid solution via substitution of S(VI), but this

⁴ Macé, N. (2006) Thesis, University Paris XI. Orsay, France. pp 247

could only be proven from X-ray diffractograms at high Se loading. Still, a high distribution coefficient of $2.06 \text{ m}^3/\text{kg}$ derived from a sorption isotherm indicated solid solution formation also at lower concentration. With Se(IV) they reported surface reactions to dominate in all cases and determined distribution coefficients (m^3/kg) of 0.18 (ettringite), 0.38 (C-S-H) and 0.21 (monosulphoaluminate). For ettringite, a maximum adsorption capacity of $0.03 \text{ mol}/\text{kg}$ was estimated. They concluded that in monosulphoaluminate S(VI) may be substituted by Se(IV) if the latter was present at high concentrations. In case of C-S-H and ettringite, Baur and Johnson (2003b) suggested surface complexation or surface precipitation with Ca to retain selenite without being able to discern the processes. Further, they stated fast sorption kinetics for both Se species which reached equilibrium concentrations with all phases within one day. Myneni, Traina et al. (1997) showed that oxyanion arsenate (AsO_4^{3-}) already reached sorption equilibrium within less than 1 minute contact with ettringite.

Bonhoure, Baur et al. (2006) wanted to clarify the Se(IV) and Se(VI) retention mechanisms in cement systematically and undertook sorption experiments with hardened cement paste, portlandite, C-S-H, ettringite and monosulphoaluminate. To gain structural insights, they used spectroscopic methods, i.e. X-ray absorption near edge structure (XANES) and extended X-ray absorption fine structure (EXAFS). They did not find any change in next-neighbour coordination of Se(IV) or Se(VI) with any of the doped solids compared to the aqueous species. No bonds to neighbouring atoms within 0.35 pm were observed. Thus, their conclusion was that non-specific interaction on surfaces or uptake was the most important retention mechanism. However, in the study with cement paste they did not determine to which cement phases Se was actually bound. Distribution coefficients between hydrated cement and solution, determined at pH 13.3 were found to vary with the applied Se concentration (Freundlich-type adsorption) from 0.02 to $0.2 \text{ m}^3/\text{kg}$ for selenite and from 0.002 to $0.02 \text{ m}^3/\text{kg}$ for selenate. Their sorption isotherms covered a range of total Se concentrations from $5 \cdot 10^{-6}$ to $0.02 \text{ mol}/\text{l}$ and decreasing distribution coefficient with higher Se concentrations indicated the presence of more than one sorption site for Se on the cement.

Pointeau, Hainos et al. (2006a) bounded the mechanisms of Se retention to binding to surface complexation or ligand exchange according to equations (5) and (6), respectively. In these models they assumed C-S-H to be the major solid involved in retention of selenite and considered silanol groups as the most important sorption sites. Both processes, surface complexation and ligand exchange, should become increasingly important when degradation advances from sane to portlandite equilibrated cement. This is what Pointeau, Hainos et al. (2006a) observed as the net surface charge of cement became increasingly positive ($K_d = 1 \text{ m}^3/\text{kg}$). Further, they initially noted a fast adsorption followed by a transient change towards slow uptake reaching equilibrium after 170 days. They interpreted their results as a consequence of slow Se diffusion into the solid and therefore reinterpreted the irreversible sorption observed by Johnson and co-workers in this sense. However, the study by Pointeau, Hainos et al. (2006a) does not allow for deducing how the diffusion process has to be understood, i.e. as diffusion into columns of larger ettringite crystals or as a less defined diffusion process into C-S-H and the bulk cement matrix.

Sorption of Se(VI) on fresh, hydrated sulphate resisting cement and degraded, but still portlandite containing cement was investigated Ochs, Lothenbach et al. (2002). They measured no influence of the exerted degradation procedure and determined distribution coefficients in the range of $0.01 \text{ m}^3/\text{kg}$ in both cases for initial Se(VI) total concentration of $8 \cdot 10^{-5} \text{ mol/l}$. In the same study they also studied ettringite and testified high Se(VI) uptake upon fast precipitation of ettringite which may likely be due to physical trapping instead of true structural incorporation, as pointed out by Bosbach (2010). Additional sorption experiments onto already present ettringite initially showed markedly less affinity of Se(VI) for the solid. Still, with longer equilibration times distribution coefficients from both methods converged to a distribution coefficients of $0.2(\pm 0.1) \text{ m}^3/\text{kg}$. Basically, with less competing sulphate in solution and higher Se activity more Se uptake by ettringite was measured (Figure 14). They further found that S(VI) adsorption is preferred over Se(VI). Interestingly, Ochs and co-workers varied the $(\text{SeO}_4^{2-}, \text{SeO}_3^{2-}) / \text{SO}_4^{2-}$ ratio in solution while keeping the sum of sulphate and Se concentrations constant at $6 \cdot 10^{-3} \text{ mol/l}$. They derived a formula to calculate K_d values of cement systems basing only on SO_4^{2-} concentrations of a cement mixture and the corresponding pore water concentration. Pointeau, Hainos et al. (2006a) suggested that Se forms solid-solutions with ettringite and that there would be no difference regarding the Se speciation. However, regarding Se(IV), they suspected other cement phases to be involved in its uptake by cement as well.

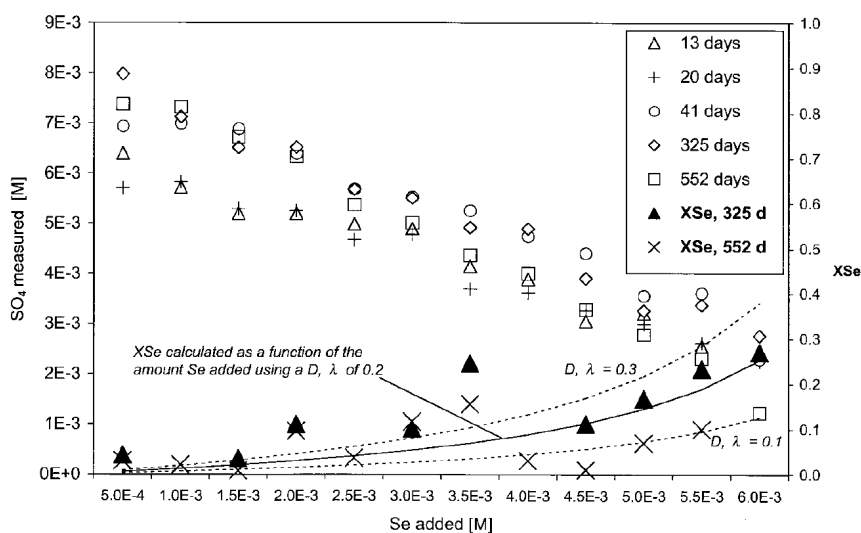


Figure 14 Selenate sorption on ettringite, published by Ochs, Lothenbach et al. (2002). In batch experiments performed at $2.5 \cdot 10^{-3} \text{ kg/l}$ (solid/liquid ratio) the added amount of Se was varied while the sum of sulphate and selenate was kept constant. D, λ is the heterogeneous distribution coefficient the authors used to model Se uptake by ettringite (XSe).

Very short batch sorption experiments of Se(VI) on hydrated, sulphate resisting cement, starting from only 25 minutes were performed by Rojo, Rovira et al. (2007). The obtained distribution coefficient was $0.006 \text{ m}^3/\text{kg}$ for the shortest time and after 1 hour a value of $0.009 \text{ m}^3/\text{kg}$ which was the same distribution coefficient measured in flow-through experiments through a column of packed cement

powder with a residence time of 25 minutes. However, from batch experiments at pH 12.5 they determined 18 days as the time needed for sorption equilibrium at 10^{-6} mol/l total Se(VI) concentration using cement sieved to 0.25-0.5 mm with a surface area of 6.35 m²/g (BET-N₂).

With the same cement, degraded to be in equilibrium pH 12.5, a dynamic batch sorption experiment where the supernatant was replenished in 18 day cycles was performed (Rojo, Grivé et al. 2010). Solution was replenished with a cement pore water of pH 12.6, always doped with $\sim 10^{-6}$ mol/l Se(VI) which remained constant after about 300 days. Uptake could be modelled with a Se(VI)-ettringite end-member of which the thermodynamic properties were derived from the oxides and literature data on S(VI)-ettringite. However, the cement pore water used in the model was not the same as the one used in experiments, differing especially in sulphate concentration – indicating difficulties regarding the thermodynamic description of S(VI) (and connected Al) -containing cement hydrate minerals.

It appears that the fate of Se in terms of retention by cement phases still remains unclear in a broad sense. This is even reflected in performance assessment by disregard of Se retention through adsorption processes. Practically all cement phases with potential to retain Se oxyanions were found to adsorb Se in one study, but were considered as an inefficient adsorbent in another study while the reasons for different results remain unclear. The time allowed for adsorption or solid solution formation with ettringite seems to cause observation of different processes. Fast adsorption ‘equilibria’ (Baur and Johnson 2003a, Bonhoure, Baur et al. 2006) seem to disregard diffusion processes which showed to influence Se uptake up to 170 days (Pointeau, Hainos et al. 2006a). There was no attempt to investigate the fate of Se incorporated or adsorbed to cement while the corresponding phases are subjected to dissolution/degradation in the cementitious system at progressed stages of degradation.

Table 6 Summary of sorption study results investigating Se(VI) retention on different cement formulations and single solid phases.

Cementitious material	pH	Initial Se(VI) concentration mol/l	Solution type	w/c ratio l/kg	L/S ratio m ³ /kg	Particle size mm	Equilibration time	Distribution coefficient m ³ /kg	Observations and mechanistic explanations	Reference
Etringite	~ 11	5·10 ⁻⁴ - 6·10 ⁻³	NaSO ₄ – NaOH solution	-	0.4		552 days	0.2 ± 0.1	S(VI)-Se(VI)-ettringite solid solution model	[1]
SRPC (fresh)	13.2	8·10 ⁻⁵	Synthesised cement pore water	0.40 (28 days)	0.02 ; 0.2	0.25-0.5	~30 days	0.01 ; 0.008; 0.03 ; 0.002		
SRPC (degraded)	12.5				0.02 ; 0.2					
C-S-H1.0	11.8	5·10 ⁻⁶ & 5·10 ⁻⁵	Pre-equilibrated solution	-	0.52		7 days (const. within hours)	Very low		
Etringite	11	3·10 ⁻⁷ -4.5·10 ⁻³	Pre-equilibrated solution	-	0.52, 0.25, 0.05		7 days (const. within hours)	0.03	S(VI)-Se(VI) ettringite solid-solution proven at high Se(V) conc.	[2]
Monosulphoaluminate	11.7	3·10 ⁻⁷ -4.5·10 ⁻³	Pre-equilibrated solution	-	0.52		7 days (const. within hours)	2.06	S(VI)-Se(VI) solid-solution	
HCP	13.3	5·10 ⁻⁶ -0.02	Synthesised cement pore water	1.3	0.04		15 days	0.002 - 0.02	Non-specific sorption	
HCP, Portlandite, C-S-H1.0	13.3	5·10 ⁻³	Synthesised cement pore water	1.3			60 days		No direct bonding (XANES, EXAFS)	[3]
Etringite, monosulphoaluminate	11.0	5·10 ⁻³ & 5·10 ⁻²	Pre-equilibrated solutions	-			30 days		No direct bonding (XANES, EXAFS)	
SRPC (CEM I) (degraded)	12.5	10 ⁻⁶	Synthesised cement pore water	0.40 (28 days)	0.005-0.4	0.25-0.5	25 min 60 min	0.006 0.009		
SRPC (CEM I) (fresh)	12.5	6·10 ⁻⁸ -6·10 ⁻⁵	Synthesised cement pore water	0.40 (28 days)	0.005-0.4	0.25-0.5	18 days	0.05-0.15 (sorption & desorption equal)	1 surface complexation site on ettringite and monosulphoaluminate	[4]
SRPC (CEM I) (degr.)	12.6	1.26·10 ⁻⁶	Synthesised cement pore water	0.40 (28 days)	0.02 replenished 31 times	0.25-0.5	31 cycles of 18-day equilibration	-	S(VI)-Se(VI)-ettringite solid solution model	[5]

[1] Ochs, Lothenbach et al. (2002) [2] Baur and Johnson (2003b) [3] Bonhore, Baur et al. (2006) [4] Rojo, Rovira et al. (2007) [5] Rojo, Grivé et al. (2010)

3.3.4 Caesium

The mechanisms and ability of cement or its constituent phases to retain the monovalent alkali metals such as Cs from solution has been investigated over several decades by different groups. In literature there is clear agreement upon lack of realistic solubility limiting phases for Cs at virtually any possible aqueous Cs concentration. Consequently, the studied mechanisms involved in Cs retention by cement were basically physical entrapment, and sorption processes.

Cs aqueous speciation in cementitious conditions is quite simple: it has only one monovalent redox-state and is mainly present as Cs^+ cation. Only at very high pH a small fraction of Cs becomes hydrolysed to CsOH^0 (Shock, Sassani et al. 1997), but its fraction is negligible compared to the Cs^+ species at $\text{pH} \leq 12.5$. The very weak CsCl^0 complex (Sverjensky, Shock et al. 1997) barely forms at common Cl^- concentrations of cement systems ($< 10^{-6}$ mol/l Cl^-). Since the complex is so weak it is also negligible in granitic groundwater with Cl^- concentration of $\sim 10^{-3}$ mol/l.

Different studies observed that Cs sorption on hydrated cement is very low with sane hydrated cement, but increases subsequently as cement becomes degraded (Pointeau, Marmier et al. 2001, Viallis-Terrisse, Nonat et al. 2002, Ochs, Pointeau et al. 2006). A major factor influencing Cs retention is the concentration of competing elements Na, K and Ca in solution, all of which are most concentrated in cement pore water of sane cement. During these earlier ages of cement lifetime at conditions with pH ranging from above 13 to above 12.5, distribution coefficients are low and were found to vary roughly from $4 \cdot 10^{-4}$ m³/kg (pH = 13.3) (Jakob, Sarott et al. 1999) over $1 \cdot 10^{-3}$ m³/kg (Skagius, Pettersson et al. 1999, Aggarwal, Angus et al. 2000, Savage and Stenhouse 2002), $2 \cdot 10^{-3}$ m³/kg (Bradbury and Sarott 1994) to $3 \cdot 10^{-3}$ m³/kg (pH > 13) (Sarott, Bradbury et al. 1992). Measured distribution coefficients and identified retention mechanisms are summarised in Table 7.

Sorption inhibiting influence of alkali metals was argued to be due to competition for sorption sites (e.g. Wieland and Van Loon (2003), Pointeau, Marmier et al. (2001), Ochs, Pointeau et al. (2006)). In fact, high alkali concentrations prevent higher distribution coefficients on sane cement which otherwise would be expected due to electrostatic retention of Cs on the negatively charged surface at these conditions (cf. chapter 3.3.1).

The role of Ca was found to be more complex than alkali elements in that apart from competing for sorption sites it determines the surface charge of C-S-H, the main Cs adsorbing phase, and cement in general. Detailed studies were performed measuring sorption of Cs onto cement hydrate phases as indirect observations, structural aspects or simply high abundance made it reasonable to suspect different phases, i.e. ettringite, hydrogarnet, hydrotalcite, portlandite and C-S-H to be involved in Cs retention (Ochs, Pointeau et al. 2006, Papadokostaki and Savidou 2009). Of these minerals the most important one in abundance, C-S-H, also was shown to have highest distribution coefficients with more than an order of magnitude difference towards other phases. Further, a strong dependence of distribution coefficients on increasing degradation of C-S-H from jennite-like composition to tobermorite-like composition and thus

on C/S ratio of C-S-H was observed (Pointeau, Marmier et al. 2001, Viallis-Terrisse, Nonat et al. 2002, Ochs, Pointeau et al. 2006). The mechanisms that were found to be responsible for this behaviour are that with increasing chain-length of the Dreierketten more silanol groups, located at the bridging tetrahedra, become available at the surface which are deprotonated or easily become deprotonated at alkaline pH and therewith attract Cs cations. The other reason found is the increasing negative surface charge, allowing for unspecific adsorption on C-S-H.

Cs retention by cement (C-S-H) was generally described with the terms sorption, specific sorption, inner-sphere complexation or 'solid-solution interface' formation and all of them seem to apply (Iwaida, Nagasaki et al. 2002, Viallis-Terrisse, Nonat et al. 2002, Ochs, Pointeau et al. 2006). Viallis-Terrisse and co-workers investigated sorption on C-S-H at ample aqueous Cs concentrations over almost 8 orders of magnitude and analysed the solids by NMR. It was found that with jennite-like composition Cs is only specifically adsorbed, i.e. no Cs is retained by electrostatic interaction which agrees with the positive and Cs repulsing surface charge. With decreasing C/S ratio the fraction of electrostatically bound Cs that can easily be washed off from dried C-S-H with alcohol increases. In the same study the authors concluded that even at high concentrations (up to 3.4 mol/l) complete sorption site saturation was still not achieved. According to their data there is a change in sorption isotherms which are linear for compositions close to jennite, but for C-S-H with lower C/S ratio retention decreases with higher Cs concentration (smaller exponents in corresponding Freundlich isotherms). This effect subsequently becomes stronger with decalcified C-S-H which qualitatively indicates site saturation effects or changing sorption mechanisms with different C-S-H composition and pH.

Iwaida, Nagasaki et al. (2002) showed that Cs adsorption modifies the C-S-H structure. They focused on comparison of different background electrolytes and only used high Cs concentration of 0.1 mol/l. Basing on observations from solid-state NMR, IR and XRD analysis they suggested that Cs does promote shortening of the Dreierketten by breaking bonds between paired tetrahedra and thereby leads to some decrease of pH. To explain this generally controversial observations (shorter chain-length usually is associated with higher C/S ratio and higher equilibrium pH) they presented a mechanistic model in that breaking of polymer chains involves binding of an hydroxyl group from solution on one previously paired silicon tetrahedron and Cs binding to the other tetrahedron. Apparently, no later work has tried to correlate the observations by Iwaida and co-workers with findings from sorption studies.

According to the explained behaviour of the main Cs adsorbing phase C-S-H, most experimental studies found that degraded HCP has a higher affinity for Cs which is reflected in higher distribution coefficients (e.g. Aggarwal, Angus et al. (2000)). Pointeau, Coreau et al. (2008) evaluated an almost constant K_d of $2.5 \cdot 10^{-3} \text{ m}^3/\text{kg}$ for a Sulphate Resisting Portland Cement from fresh state of pH > 13 to portlandite controlled pH 12.5 where highly soluble alkali hydroxides had already been diluted. Values from 10^{-3} to $0.05 \text{ m}^3/\text{kg}$ were measured by Aggarwal, Angus et al. (2000) using various degraded HCP compositions blended with blast furnace slag, fly ash or limestone at pH around 12.5 or maybe slightly lower. In even more degraded states, particularly between pH 12.5 and 11.7 (Ochs, Pointeau et al. 2006,

Pointeau, Coreau et al. 2008) observed further increase of distribution coefficients. Ochs, Pointeau et al. (2006) also investigated severely degraded Portland cement as well as CEM V, reaching distribution coefficients up to $20 \text{ m}^3/\text{kg}$ at pH around 10, i.e. extremely low pH for cementitious systems. These values were measured in relatively short experiments of 7 days and it should be noticed that this was the only encountered study measuring that high values for Cs distribution coefficients. The authors could not explain this observation and with Portland cement Pointeau, Coreau et al. (2008) later published about 100 times lower values, even though not at that low pH (Figure 15). However, the authors ascribe the variability between different studies on Cs retention basically to three different factors. These are the specific cement composition, i.e. especially the absolute content of C-S-H, the degradation stage of the cement with related C-S-H composition, and the exact pore water composition due to sorption competition effects by aqueous alkali elements and Ca with Cs.

Ochs, Pointeau et al. (2006) argued that especially in fresh hydrated cement samples scatter with different cements could be larger due to different alkali contents competing for sorption sites. Consequently, in more degraded states, generally below pH 12.5, they expect less variability of measured sorption on degraded HCP which they attributed to the more uniform conditions where basically C-S-H is controlling Cs retention. Still, few sorption data exist for these conditions and especially for the case of a real repository the presence of severely degraded HCP requires a substantial amount of solution in contact with the cement which may also supply significant alkali concentrations, depending on the groundwater type. Ochs, Pointeau et al. (2006) developed a simple dataset to calculate Cs K_d values basing on a two-site surface complexation model taking into account competition with Na and Ca, surface area of C-S-H, Ca speciation and pH. They successfully reproduced most of their selected literature data from different degradation stages and different types of cement.

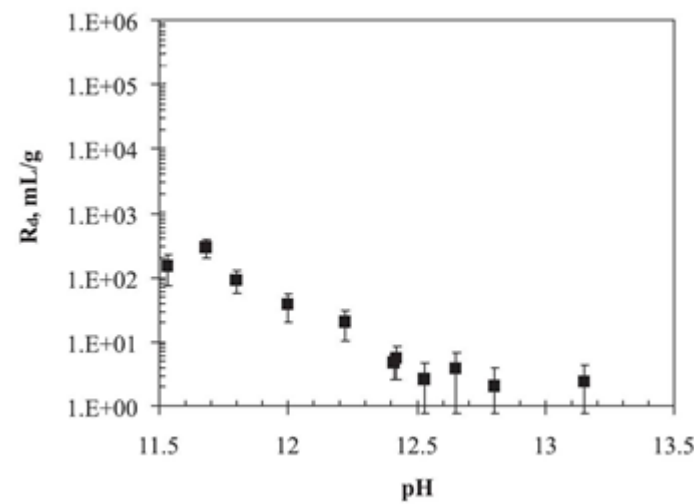


Figure 15 Evolution of the distribution coefficient for Cs sorption on Portland cement under cementitious conditions (extracted and modified from Poiteau, Coreau et al. (2008)).

Only the study of Iwaida, Nagasaki et al. (2002) observed direct influence of Cs on C-S-H structure, but there are indications from other studies that investigated mobilisation of Cs from cement supporting Cs binding. Papadokostaki and Savidou (2009) performed long-term leach experiments on doped Portland cement monoliths at pH probably controlled by portlandite, judging from the liquid to solid ratio they used. They observed diffusive release of about three quarters of the Cs inventory following Fick's law, but also a permanent retention in the cement of about one quarter of the added Cs amount. Still, the authors did only observe permanent retention when Cs was already added during the hydration step of the cement, i.e. the effect was absent in desorption experiments following an anterior adsorption step. Stronger retention of a fraction of upon hydration incorporated Cs was obtained by more authors. For example Hanna, Aldridge et al. (2000) reported permanent retention of 16 wt.-% in white Portland cement, similar to Papadokostaki and co-workers.

Thomas, Chen et al. (2004) showed that inner-product C-S-H mostly has small pores, largely not even accessible for N₂ in surface area measurements, which are opened successively during decalcification. In contrast, outer-product C-S-H has a large and accessible surface area. It could be supposed that sorption of Cs mainly takes place on the outer-product, while inner-product is widely not accessible for it in common adsorption-desorption measurements. In contrast, if Cs was present during clinker hydration, it could be incorporated, co-precipitated or adsorbed Cs could be trapped and not be remobilised until substantial decalcification and opening of the inner-products porosity.

Iwaida, Nagasaki et al. (2002) observed structural changes in C-S-H after only 7 days. In the published literature equilibration times for adsorption experiments go up to years in some cases, but in short-term studies of only 1 day of equilibration time Poiteau, Marmier et al. (2001) measured similar distribution coefficients. From these observations and the described mechanisms involved in Cs retention by cement it can be expected that Cs retention is a fast, surface-related process.

In summary, there is no consensus in literature about which phase(s) retain(s) Cs in Portland cement. Several publications indicate that C-S-H is involved in Cs retention, but the underlying sorption or uptake mechanism is unclear. It could be unspecific by adsorption to negatively charged surfaces of decalcified C-S-H, i.e. electrostatically, or specific by binding to silanol sites.

Table 7 Summary of sorption study results investigating Cs retention on different cementitious materials formulations and C-S-H.

Cementitious material	pH	Initial Cs concentration mol/l	Solution type	w/c ratio l/kg (6 months)	Particle size mm	L/S ratio m ³ /kg	Equilibration time	Distribution coefficient m ³ /kg	Observations and mechanistic explanation	Reference
SRPC	13.3	3.7·10 ⁻⁸	Synthesised cement pore water	1.3	Through-diffusion		170 days	3·10 ⁻³		[1]
OPC & SRPC	~13.3 12.5	<10 ⁻⁵ 5·10 ⁻⁶ -5·10 ⁻²	Review study citing several non-retrievable studies					2·10 ⁻⁴ -3·10 ⁻³ 0.01-0.2		[2]
SRPC	13.3	3.8·10 ⁻⁸	Synthesised cement pore water	1.3	Through-diffusion		90 days	4·10 ⁻⁴ -8·10 ⁻⁴		[3]
BFS/OPC PFA/OPC Limestone/OPC C-S-H	~12.5 or slightly lower	1.3·10 ⁻⁷	Pre-equilibrated with corresponding solid		<1.4	0.05	28 days	10 ⁻³ -5.4·10 ⁻²	Higher K _d with more degraded solid	[4]
C-S-H0.8 C-S-H1.2	11.5-12.2	10 ⁻⁶ -10 ⁻³ M	Pre-equilibrated			1.25-5	1 day	10 ⁻³ -0.6	K _d increases with decreasing C/S ratio	[5]
C-S-H0.7		~5·10 ⁻⁸ -6·10 ⁻⁶						0.3-0.4	Specific sorption on C-S-H1.5;	[6]
C-S-H0.8		~8·10 ⁻⁸ -7·10 ⁻⁶						0.2	Electrostatic adsorption	
C-S-H1.2		~5·10 ⁻⁷ -5·10 ⁻³	Pre-equilibrated solutions	-	-	0.02	7-10 days	0.03	increases with decreasing C/S ratio	
C-S-H1.5		~7·10 ⁻⁷ -0.6						0.01		
HCP CEM I mortar CEM V mortar	9.5-12.2	Variable	Pre-equilibrated with CEM I and CEM V			1.25-5	7 days - 9 months	10 ⁻³ -20	K _d increases with decreasing C/S ratio; 2 surface sites on C-S-H, competing with Na & Ca	[7]
SRPC (CEM I)	12.5-13.2 11.5	1·10 ⁻⁹	Pre-equilibrated	0.38		0.14-1	15 days	2.5·10 ⁻³ ~0.1		[8]
OPC	≥12.5	10 ⁻³ - 1	Cs ₂ SO ₄ solution	0.42 (28 days)	0.18-1	0.006	900 days (const. < 7 days)	2·10 ⁻⁴		[9]

[1] Sarott, Bradbury et al. (1992) [2] Bradbury and Sarott (1994) [3] Jakob, Sarott et al. (1999) [4] Aggarwal, Angus et al. (2000) [5] Poinneau, Marmier et al. (2001)

[6] Viailis-Terrisse, Nonat et al. (2002) [7] Ochs, Poinneau et al. (2006) [8] Poinneau, Coreau et al. (2008) [9] Papadokostaki and Savidou (2009)

4 Methodology

4.1 Starting Material

4.1.1 Cement Clinker

Two similar Portland cement clinkers were used in experiments: Sulfadur and Holcim-1. Sulfadur is a sulphate resisting type I Portland Cement (CEM I 52.5 N/SR). We ground clinker nodules shortly after receiving using a Retsch Planetary ball mill with agate balls. Particle size distribution was measured with a Malvern Mastersizer 2000 at the Institut de Ciències de la Terra Jaume Almera - CSIC, giving the following distribution: $d_{10} = 2 \mu\text{m}$, $d_{50} = 19 \mu\text{m}$, $d_{90} = 78 \mu\text{m}$. The powdered clinker was sealed in plastic bags and stored dry. Holcim-1 is a sulphate resisting type I Portland Cement (CEM I 42.5 R/SR). Holcim-1 was received as already ground clinker and hydrated by the Fundació CTM Centre Tecnològic. XRD diffractograms of both clinkers and corresponding HCPs before use in experiments can be found in annex 10.5, Figure 86 and Figure 17. The elemental compositions were analysed by XRF and are given in Table 14 (chapter 5.1).

4.1.2 Hardened Cement Paste

Holcim-1 cement clinker was cured by the Technological Centre of Manresa in the following manner: It was mixed at a water to cement ratio of 0.4 l/kg with deionised water and allowed to set in cylindrical polypropylene containers during 24 hours before demoulding and hardening for 28 days at 25 °C immersed in deionised water in a closed container without additional measures regarding the contacting atmosphere (following the ASTM C190-90a procedure, American Society for Testing and Materials (1990)). Then the hardened cement paste was dried at 105°C until constant weight during seven days before storage in ambient air. Two years later it was crushed to grain size < 250 μm using a ball mill. Eighteen months later the ground HCP was used in experiments.

We hydrated Sulfadur clinker as described above, but cured and hardened in 100 % relative humidity atmosphere in a closed container, but without additional measures regarding the contacting atmosphere. The hardening time extended to 55 days allowing for more complete hydration. The HCP was dried at 35 °C during 48 hours, then crushed, milled in a planetary ball mill and finally passed entirely through a 250 μm mesh. Surface area of the sieved HCP was measured with a Quantachrome Autosorb Automated Gas Sorption System using 5-point N_2 adsorption isotherms, giving 10.6 m^2/g . The powder was stored in sealed plastic bags that were kept in closed containers until its use in experiments within the following months.

4.1.3 Solutions

We prepared artificial granitic groundwater following a recipe used by Vuorinen and Snellman (1998) who described the preparation of ‘modified Allard’ water in equilibrium with atmospheric CO₂. Stock solutions were prepared from CaCl₂·2H₂O, NaHCO₃, NaCl, KCl, MgCl₂·6H₂O (Scharlau, reagent grade), MgSO₄·7H₂O (Sigma, minimum 99.0%), Na₂SiO₃·9H₂O (Alfa Aesar, minimum 98 %) and HCl (Scharlau, trace analysis grade). The modified Allard water (Table 8) was supposed to have pH 8.4 in at equilibrium with log₁₀(pCO₂) = -3.5, corresponding to 316 ppm. However, CO₂ partial pressure was higher at our laboratory conditions (500 - 600 ppm CO₂). Measured pH in GG water was 8.17±0.05. We tested that the GG water was stable for at least one week. This solution was slightly undersaturated with respect to calcite and no formation of precipitate was observed.

Table 8 Chemical composition of artificial granitic groundwater as added from the reactants, prepared according to a recipe by Vuorinen and Snellman (1998). In laboratory atmosphere pH was stable at 8.17.

Element	Si	Na	K	Ca	S(VI)	Cl*	Mg	HCO ₃ ⁻
Concentration (mol/l)	5.0·10 ⁻⁵	2.3·10 ⁻³	1.0·10 ⁻⁴	2.5·10 ⁻⁴	1.0·10 ⁻⁴	ca. 1.3·10 ⁻³	1.1·10 ⁻⁴	2.0·10 ⁻³

*small variation due to dependence of the amounts used to adjust pH of Si stock solution

All experiments were performed using deionised water (18.2 MΩcm resistivity), produced with a Millipore system. Deionised solution equilibrated with the atmosphere was produced freshly by the Millipore system and bubbled for a couple of hours with filtered air. Then it was allowed to equilibrate overnight in the laboratory.

For CO₂ ‘free’ experiments under nitrogen atmosphere in a glove box deionised solution was previously boiled in ambient atmosphere for at least 10 minutes and bubbled with bottled N₂ gas during cooling in a 2 l glass bottle. When cooled the bottle was closed firmly, sealed with Parafilm and immediately transferred into the glove box.

4.2 Degradation Experiments

4.2.1 Batch Experiments

A weighed quantity of Sulfadur HCP powder was filled into polypropylene containers of different size, mixed with solution and sealed with Parafilm. All containers were initially shaken by hand before their placement in mixing devices.

Batch experiments were performed at two liquid to solid (L/S) ratios: 0.1 and 2 m³/kg. These ratios were chosen to equilibrate cement and solution at different stages of cement degradation allowing for comparison with flow-through experiments. Extrapolating findings from Sugiyama and Fujita (2006), we expected chosen ratios to approximately correspond to the second and third degradation stage (pH 12.5 and ~11, respectively). For both L/S ratios one half of experiments was performed with atmosphere equilibrated DI water and the other half with GG water. Smaller samples (B1 through B8 and B17

through B24) were placed on a horizontal mixing table while larger samples (B9 through B16) of 2000 ml volume were mounted into an end-over-end rotating device (1 rpm). The latter device had to be stopped after one week and equilibration continued without further agitation. During the first hours on the mixing devices all containers were periodically mixed end-over-end by hand to avoid agglomeration of particles. After 26 to 27 days all experiments were terminated. We filtered aliquots for analyses using 0.2 μm nylon filters and acidified solutions after filtration with HNO_3 to avoid adsorption of metals to the containers. Possible bias of analytical results due to colloids was analysed and excluded (chapter 6.2.4). To recover the solid for detailed analysis the remaining, unfiltered suspensions were filtered on Büchner funnels using 0.45 μm nylon filters. The larger filter size in this case was chosen to prevent clogging during filtration process. Filter cakes were dried in an oven at 35 °C during 2 days before storage in small and sealed containers. Detailed information on experimental conditions and measurement results are given in Table 30, annex 10.1.

4.2.2 Flow-Through Experiments

A continuous flow-through reactor, presented by Bruno, Casas et al. (1991) was modified, tested and employed in this study for the first time with HCP. The main feature of this reactor is that it uses only tiny amounts of solid material, as shown in the setup scheme in Figure 16. At the beginning the reactor had to be adapted for the needs of this study compared to the one presented by Bruno, Casas et al. (1991) which used a smaller diameter of filter papers and only monocrystalline material. First, we performed several tests to assemble the whole setup and proof its reliable functioning.

Second, we conducted a pilot study with Holcim-1 HCP to estimate necessary amounts of cementitious material in the reactor and feasible pump rates (chapter 6.2.1). Third, we analysed the evolution of major and minor phases during HCP degradation in CO_2 -‘free’ DI water (chapter 6.2.2 and 6.2.5). Fourth, we performed experiments with Sulfadur HCP with DI water containing varying $\text{CO}_2(\text{aq})$ concentration and different types of solution while pump rate and cement mass were kept constant (chapter 6.2.3 and 6.2.5).

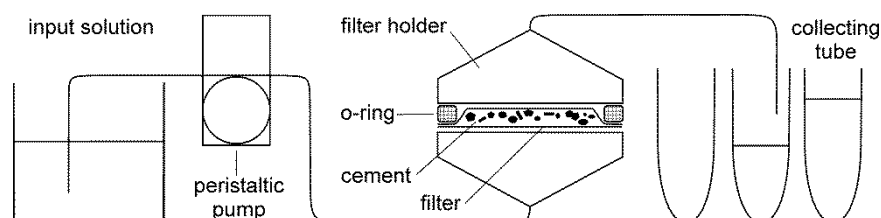


Figure 16 Scheme of the employed thin-layer flow-through reactor (not to scale).

In our thin-layer flow-through reactor a peristaltic pump directs stock solution from a container upwards through the vertically orientated reactor. This orientation provides best conditions for homogeneous flow through the reactor, i.e. avoiding any dripping, accumulation of bubbles, pulse or gravity effects. The transparent polycarbonate housing allows to monitor bubble accumulation in the

reactor at the beginning of experiments and bubbles could be removed by gentle tilting of the reactor. We satisfactorily tested water- and gas-tightness of the whole setup from inlet to outlet before starting experiments. The solution leaving the reactor outlet was collected continuously in subsequently exchanged test tubes or bottles for time-resolved analyses.

We estimated the volume of the reactive zone in the reactor to be 0.7 ml, considering the cement monolayer and both filter papers. Thus, the L/S ratio was approximated for each experiment and the residence time t_r in the reactor was obtained from equation (11).

$$t_r = \text{reactor volume} / \text{flow rate} \quad (11)$$

We placed two nylon filter sheets (diameter 47 mm, Sartorius) in a commercial polycarbonate filter holder (Whatman Swin Lok), maintaining a single layer of sieved HCP in the interstice. Nylon filters were preferred over common cellulose filters due to their potential decomposition at highly alkaline pH, generating the complexing agent isosaccharinic acid (e.g., Glaus and Van Loon (2008)). The filter pore size had to be adapted according to employed solutions. Nylon filters of 0.2 μm pore size performed well when DI water was used. For GG water, the 0.2 μm filters did not allow for homogenous flow through the reactor. This was tested in quintuplicate, with and without cement powder in the interstice. By increasing filter pore size to 0.45 μm we established homogeneous flow conditions through the reactor also in this case. However, for analysis of solution compositions samples were also filtered using 0.2 μm syringe filters.

In all the experiments pH was measured immediately after sampling. In experiments performed outside the glove box the sampling tubes were to the greatest possible extent sealed with Parafilm during sample collection and pH measured immediately after sample collection, also in sealed tubes. In this way we minimised posterior carbonation of outflow solution and avoided biased results of pH measurement that would not have been representative for the pH inside the reactor. Further, precipitation of carbonates from outflow solution was avoided which would have biased measured aqueous concentrations.

The degraded HCP, remaining between the filter sheets after each experiment, was transferred into storage containers immediately after termination of an experiment and dried under flowing nitrogen atmosphere for several hours. Then containers were closed tightly and sealed with Parafilm for storage until further analysis by XRD and SEM.

All experiments with Holcim-1 HCP were conducted in a Jacomex glove box filled with Argon and $\text{CO}_2(\text{g})$ concentration < 2 ppm. The experimental parameters of these tests are given in Table 9 and more detailed parameters, including sampling are presented in Table 31, annex 10.1.

Table 9 Conditions of flow-through experiments with Holcim-1 HCP. Two CO₂-‘free’ input solutions were used: pure deionised water and 0.1 mol/l NaClO₄ solution.

Experiment	Solution	Atmosphere	Initial HCP mass (mg)	Pump rate (ml/min)	L/S ratio (m ³ /kg)	Residence time (s)	Cumulated flow (ml)
FL 4 I=0M	DI	N ₂ , glove box	50.5	1.47	0.013	27	180.5
FL 5 I=0M	DI	N ₂ , glove box	47.2	1.03	0.014	39	307
FL 7 I=0M	DI	N ₂ , glove box	39.6	0.72	0.017	55	918
FL 8 I=0.1M	0.1M NaClO ₄	N ₂ , glove box	28.8	1.08	0.023	37	292.5
FL 9 I=0.1M	0.1M NaClO ₄	N ₂ , glove box	35.0	0.68	0.019	58	844.5

One degradation experiment with Sulfadur HCP was performed in the glove box with CO₂-‘free’, deionised solution as used in the study with Holcim-1 HCP. Another two experiments with Sulfadur HCP were conducted in ambient air, but N₂ was bubbled continuously through stock- and outflow-solutions. Measurements of outflow solution pH were done immediately and N₂ bubbling continued until termination of pH measurements. DI water used in these experiments was prepared as described in chapter 4.1.3 to remove CO₂. The remaining experiments with Sulfadur HCP were conducted open to the atmosphere and solutions allowed to equilibrate before experiments (‘open system’) as described above. Experimental conditions of experiments with Sulfadur HCP are summarised in Table 10 and include experiments with added contaminants which are explained in more detail in the following chapter. Detailed parameters including sampling can be found in Table 32, annex 10.1.

Table 10 Experimental parameters in flow-through experiments with Sulfadur HCP.

Name	Solution	Atmosphere	Initial HCP mass (mg)	Pump rate (ml/min)	L/S ratio (m ³ /kg)	Residence time (s)	Cumulated flow (ml)
FLS1	DI CO ₂ -free	N ₂ , glove box	55.9	1.05	0.013	40	1522
FLS2	DI CO ₂ -low	N ₂ bubbled, air	56.5	1.04	0.012	41	1425
FLS3	DI CO ₂ -low	N ₂ bubbled, air	55.3	1.03	0.013	41	1371
FLS4	DI, air	air	54.9	0.98	0.013	43	1290
FLS8	GG water, air	air	57.5	1.04	0.012	40	66
FLS9	DI, air	air	55.1	0.97	0.013	43	1400
FLS10	DI, air	air	55.8	1.02	0.013	41	1451
FLS11	GG water, air	air	55.9	0.96	0.013	44	1459
FLS12	GG water, air	air	55.6	0.98	0.013	43	1497
FLS13	GG water, air	air	55.2	0.98	0.013	43	1441
FLS15	GG water, air	air	56.0	0.99	0.013	42	1468

The thin-layer flow-through setup was tested for adsorption of contaminants. It showed no adsorption of Cs and Se(VI) on any part of the setup, including filter sheets. However, Ni did get retained in the setup and could not be studied under flow-through conditions.

4.2.3 Thermodynamic Data

To model cement degradation we used the US Geological Survey software Phreeqc Version 3 (Parkhurst and Appelo 2013). Thermodynamic data for cement phases was taken from Cemdata07

database (Lothenbach, Matschei et al. (2008), Matschei, Lothenbach et al. (2007b), Lothenbach and Winnefeld (2006), Babushkin, Matveyev et al. (1985), Hummel, Berner et al. (2002), Thoenen and Kulik (2003), Möschner, Lothenbach et al. (2008), Schmidt, Lothenbach et al. (2008)) in a version translated to Phreeqc format by Diederik (2009). Diederik translated version 7.2, including data for thaumasite which was officially added in the later Cemdata07 version 7.3. Auxiliary thermodynamic data in Cemdata07 comes from the Nagra/PSI-thermodynamic database. Activity coefficients are calculated using the extended Debye-Hückel equation in the Truesdell-Jones form.

We choose the Cemdata07 database for this study due to its widespread and successful use in the cement community. The Cemdata07 database was set up specifically for cement systems and contains all major solid phases, as well as a variety of minor phases. It has been employed in several studies relating experimental and modelling results, for the case of clinker hydration, as well as HCP degradation (e.g., Lothenbach and Winnefeld (2006), Loser, Lothenbach et al. (2010)). Other thermodynamic databases also include cement phases. The probably most up-to-date one is ThermoChimie database (Giffaut, Grivé et al. 2014). This database is not restricted to cement systems and also contains, e.g. radionuclides and solid phases for other systems like clay minerals. Regarding major and most minor phases Cemdata07 and ThermoChimie databases are similar with respect to cementitious systems, even though some additional phases are contained in the latter. The most important one is probably Friedel's salt ($\text{Ca}_4\text{Al}_2(\text{OH})_{12}\text{Cl}_2 \cdot 4\text{H}_2\text{O}$), an AFm phase which may form at high aqueous Cl⁻ concentrations. Performing benchmark calculations Damidot, Lothenbach et al. (2011) showed that ThermoChimie and Cemdata07 give very similar results for cement systems, with the exception of hydrogarnet and monosulphoaluminate stability (see chapter 6.3.1). A practical advantage of using Cemdata07 database is reduced calculation time with Phreeqc due to limitation to the cement system. This study does not intend to perform a benchmark between databases.

We replaced the implemented C-S-H model of Cemdata07 database⁵ by the CSH3T model from Kulik (2011). Both are ideal solid-solution models, but the original model uses two ideal solid-solutions with two end-members each, while the CSH3T model bases on one solid-solution with three end-members. End-members are classified by the mean chain-length of their *Dreierketten* which have dimeric jennite-like composition ('T2C'), pentameric composition ('T5C') and polymeric tobermorite-like composition ('TobH') (Table 11).

⁵ Note that with recent updates, available in GEMS format, also the original C-S-H model was replaced in the Cemdata07 database.

Table 11 CSH3T model with 4 bridging tetrahedral interlayer sites as suggested by Kulik (2011). Dissolution reactions according to Table 12.

End member	Bulk formula (per Dreierkette)	G ^o kJ / mol	Log ₁₀ K
T2C (=C-S-H1.5)	(CaO) ₃ (SiO ₂) ₂ ·5H ₂ O	-4934.16	-12.43
T5C (=C-S-H1.0)	(CaO) _{2.5} (SiO ₂) _{2.5} ·5H ₂ O	-5037.32	-13.94
TobH (=C-S-H0.67)	(CaO) ₂ (SiO ₂) ₃ ·5H ₂ O	-5123.06	-12.40

We consider the CSH3T solid-solution model more versatile than the original C-S-H model of Cemdata07 for several reasons. The original model uses amorphous silica as one end-member, allowing for representation of wider C/S ratios, but no experimental investigation proved that silica is an end-member of C-S-H phases (Kulik 2011). Amorphous silica was included in Cemdata07 for mathematical fitting, but has no physical meaning. The CSH3T model not only reproduces aqueous concentrations of Ca, Si and OH⁻ according to literature solubility data, but also takes into account realistic microstructural changes of C-S-H phase. This model permits variation of C/S ratios in C-S-H from 0.67 to 1.5. Moreover, due to the realistic stoichiometry it allows for modelling the structural uptake of other cations into the C-S-H lattice (Kulik 2011) in future.

Where necessary we recalculated formation constants of species and solubility constants of end-members used in the CSH3T model to be consistent with thermodynamic data of Cemdata07 database. We modified the recalculated solubility constant of T2C (log₁₀K -25.09), naming it T2Cmod (Table 12) to better match results from modelling with those from batch experiments. As Kulik (2011) did not optimize the solubility constants in his model we regard this modification as non-critical. The solid-solution model for C-S-H still remains within the range of solubility data from literature.

Table 12 CSH3T model, recalculated and adapted for consistency with Cemdata07 in Phreeqc format.

End member	Dissolution reaction in water	Log ₁₀ K
T2Cmod (=C-S-H1.5)	(CaO) ₃ (SiO ₂) ₂ ·5H ₂ O ⇌ 2 SiO(OH) ₃ ⁻ + 3Ca ²⁺ + 4 OH ⁻	-25.80
T5C (=C-S-H1.0)	(CaO) _{2.5} (SiO ₂) _{2.5} ·5H ₂ O ⇌ 2.5 SiO(OH) ₃ ⁻ + 2.5 Ca ²⁺ + 2.5 OH ⁻	-23.27
TobH (=C-S-H0.67)	(CaO) ₂ (SiO ₂) ₃ ·5H ₂ O ⇌ 3 SiO(OH) ₃ ⁻ + 2 Ca ²⁺ + 1 OH ⁻	-18.39

4.2.4 Thermodynamic Equilibrium Approach

When enclosing together specified amounts of HCP and pure water or groundwater in an isolated system at standard conditions of 25 °C and 1 atm pressure the paste degrades until equilibrium conditions are established. Therefore, we define degradation as a function of liquid to solid ratio in our model.

This thermodynamic equilibrium approach is employed for modelling batch experiments where the driving parameter, liquid/solid ratio, was increased from 0.1 to 2 m³/kg. Our model allows varying the liquid/solid ratio. Using the Cemdata07 database, which includes the relevant cement phases, we calculate equilibrium phase assemblages at each liquid / solid ratio.

4.2.5 Kinetic Degradation Approach

According to the experimental design of the thin-layer flow-through setup we model degradation of the HCP powder as a one-dimensional problem. In our model we do not consider diffusion related processes due to the fast flow through the very thin layer of HCP powder. Further, we suppose laminar flow of solution through the reactor, neglecting any effects from possible imperfect mixture.

A solid containing HCP particles degrading in a fast flowing solution is complex due to the large variety of different solid phases and parallel reactions (Taylor 1997). The kinetically controlled degradation or dissolution of each solid phase has to be addressed individually, e.g. by defining rate equations for each mineral (Steeffel and Lichtner 1998).

In our kinetic degradation approach we use the same starting composition as employed for modelling batch experiments. We choose a general dissolution equation (equation (12)), based on transition state theory (Lasaga 1998), to model kinetic dissolution of all cement hydrate phases.

$$Rate_i = A_i \cdot \frac{m_i}{m_{i,0}} \cdot k_i \cdot \left(1 - \frac{Q_i}{K_i}\right) \quad (12)$$

In the equation subscript *i* denotes a certain solid phase. *A*, *m* and *m*₀ are phase related surface area (m²), actual moles present and the initial moles (mol) of phase *i*, respectively. The rate constant is *k* (mol / (m² s)); and the quotient of *Q*, the actual solubility product in solution and *K*, the thermodynamic solubility product, gives the saturation rate. We evaluated dissolution rate constants from literature and fitted missing data to our experimental results (Table 24 in chapter 6.3.3).

The saturation rate distinguishes dissolution from precipitation and is evaluated in each modelling step. In case of equality of *Q*_{*i*} and *K*_{*i*} the phase *i* is in equilibrium and numerically does neither dissolve nor precipitate. The coefficient *m* / *m*₀ accounts for decreasing surface area with decreasing amount of solid phase during dissolution. For specific mineral habitus this quotient might be exponentiated to better reproduce changes in surface area according to simplified geometric relations. However, this extension neglects features like pitting, etc. Also strong and fine intermixture of cement phases may bias such geometric relations. For minerals with relatively robust geometry, gypsum and calcite we tested to introduce an exponent of 2/3 which ideally represents a cube or sphere. Results show more deviation from experiments than those with the more simple equation. Consequently, we assume the exponent to be unity for all phases.

A challenge in kinetic modelling studies is the integration of solid-solutions. In the equilibrium approach Phreeqc allows using an ideal solid-solution model of C-S-H phases. However, in the case of kinetic modelling no rates can be assigned to the transient solid-solution compositions. Alternatively, several authors suggest to define as many as desired/required virtual phases with intermediate compositions between end-members. These discrete phases may be defined with fixed solubility constants that are consistent with more sophisticated solid-solution models (Lichtner and Carey 2006). Moreover,

this allows assigning dissolution rate constants to each composition. This approach was followed successfully for C-S-H phases by different authors (e.g. Grandia, Galíndez et al. (2010), Trapote-Barreira, Cama et al. (2014)). However, dissolution constants of C-S-H phases with intermediate C/S ratios have not been experimentally measured, yet.

Owing to these aspects we tried to limit the number of arbitrary intermediate compositions. Therefore, we used only three kinetically dissolving fixed C-S-H end-members (shown in Table 11) to describe degradation of C-S-H.

4.3 Contaminant Retention experiments

Ni, Se(VI) and Cs retention on Sulfadur HCP at batch conditions were studied by performing experiments as described for the degradation study in chapter 4.2.1. Experimental conditions and analytical results from batch experiments are given in Table 30 in the annex 10.1. The same was done for studying retention in flow-through conditions. Blank measurements are described in the corresponding chapters on Ni (7.1.1.2), Se(VI) (7.2.1.2) and Cs (7.3.1.2) retention.

To study contaminant retention under flow-through conditions experiments were performed as described in chapter 4.2.2. Referring experimental conditions at different Cs(I), Ni(II) and Se(VI) concentrations and with both types of solutions are given in Table 10 and Table 13. Detailed parameters including sampling can be found in Table 31, annex 10.1. Analytical results including blank measurements of these flow-through retention experiments are given in chapters 7.1.2, 7.2.2 and 7.3.2.

For both, batch and flow-through experiments we added Cs(I), Ni(II) and Se(VI) to input solution directly before starting. In some cases elements were combined and added simultaneously if no mutual interaction of one with the other was expected at the applied concentrations. Salts used for preparation of stock solutions were CsCl (Aldrich, 99.9 %), Na₂SeO₄ (Fluka, purum p.a.), Ni(NO₃)₂·6H₂O (Scharlau, purissimo) for high concentration of 5·10⁻⁴ mol/l, and NiCl₂·6H₂O (Scharlau, para analisis) for lower concentrations.

All vials used in batch experiments were previously leached for one week in diluted nitric acid, turned upside down in the meantime and afterwards rinsed several times with deionised water. Before each flow-through run all parts of the setup were thoroughly cleaned, leached in diluted nitric acid for at least one night and rinsed repeatedly. Vials of stock solutions and sampling vials of flow-through experiments were acid-leached for at least two days, in the meantime turned upside down and finally rinsed repeatedly.

Table 13 Overview on flow-through experiments with Sulfadur HCP in which Cs(I), Ni(II) or Se(VI) were added to input solution.

Element	DI water			GG water		
	Experiment	Spike concentration (mol/l)	atmosphere	Experiment	Spike concentration (mol/l)	atmosphere
Ni(II)	FLS 9	10^{-7}	air	FLS 15	10^{-7}	air
				FLS 12	10^{-8}	air
				FLS 13	10^{-8}	air
Se(VI)	FLS 10	10^{-4}	air	FLS 11	10^{-4}	air
				FLS 13	10^{-6}	air
				FLS 15	10^{-7}	air
Cs(I)	FLS 3	10^{-3}	N ₂ -bubbled			
	FLS 4	10^{-3}	air			
				FLS 12	10^{-4}	air
				FLS 13	10^{-6}	air

4.4 Analytical Methods

4.4.1 Analysis of Solid Phases

HCP and clinkers were analysed by X-Ray powder diffraction XRD in Bragg-Brentano geometry. The device (Philips PW1700/10/00/12) was equipped with a copper filament and a secondary graphite monochromator, eliminating reflections from Cu-K β radiation from the sample. Most diffractograms were recorded with a counting time of 2 s on each step of 0.02 °2- θ (Cu-K α). Exceptions are indicated in the text. Directly before analysis samples were taken from N₂-gas flushed, Parafilm sealed containers and hand-ground in a mortar until disappearance of tangible grains. We analysed samples from flow-through experiments in a zero-background silicon sample holder. For clinkers, Sulfadur HCP, Holcim-1 HCP as well as for samples from batch experiments we used a conventional aluminium sample holder that was back-loaded to avoid preferential orientation. The software EVA (Bruker AXS) and X Powder12 were employed for data treatment and phase identification, based on the pdf-2 database (ICDD).

We further analysed sane HCPs by coupled thermogravimetric analysis-differential scanning analysis TG-DSC (Mettler Toledo TGA/DSC 1). The device was equipped with an alumina crucible and the applied heating rate was 10 °C/min from room temperature up to 1000 °C. Weighed sample volumes were between 40 and 50 mg.

For Scanning Electron Microscopy SEM analyses three different devices were employed: Zeiss FESEM Ultra Plus with Oxford instruments X-Max EDS detector, FEI Quanta 200 EDAX with a Centaurus detector and FEI Quanta 400 with a Gatan detector. SEM samples embedded in epoxy resin were finally polished with 0.25 μ m diamond powder and sputtered with carbon while rough samples with texture were sputtered with gold. We chose a relatively low beam current of 15 keV due to the sensitivity

of most hydrate phases in cement to higher acceleration voltage. Lower energy also improves the lateral and vertical resolution of point analysis as the excited volume in the sample decreases with lower energy. Unfortunately, backscattered electron yield decreases with lower current. Best quantitative results are obtained for elements whose electron transition occurs at energies lower than about one third to half of the incident beam.

Total elemental compositions of the clinkers were evaluated by duplicate X-ray fluorescence analysis XRF (AXIOS Advanced) with pressed (200 kN) powder for trace elements and with pills of with Li-tetra borate fused powder for major elements.

4.4.2 Analysis of Aqueous Solutions

We filtered each liquid sample (0.2 μm syringe filters, nylon) and always acidified an aliquot of the filtrate with nitric acid (Scharlau 65 % suprapur). For filtration we tested Al-oxide syringe filters (Anopore) with 0.02 μm mesh size on GG water and outflow solutions from flow-through experiments. Due to severe contamination of analysed solutions with dissolved Al from the filter, these filters were abandoned. Nylon filters instead were stable in the analysed solutions and finally chosen.

Acidified solutions were analysed for several components with the estimated error given within brackets: Ca (5 %), S(VI) (8 %), Mg (8 %), Na (5 %) and K (5 %) by Ion Chromatography (Dionex ICS-2100 RFIC with Ulti Mate 3000 autosampler column compartment) and Si (5 %), Al (10 %), Ni (5 %), Se(VI) (5 %), Cs (4%) by Inductively Coupled Plasma-Mass Spectrometry ICP-MS (Agilent 7500cx), equipped with an helium collision cell.

Separate aliquots were taken to measure pH immediately after sampling, using combined electrodes (CRISON 50 10, 50 14, 50 21 and 52 22). Electrodes were calibrated daily at approximately 25 °C with four to five (exceptionally three) buffers, depending on the pH of samples: pH 4.01 (Potassium hydrogen phthalate), pH 7.00 (potassium and di-sodium phosphate), pH 9.21 (borax), pH 10.90 (boric acid/sodium hydroxide/potassium chloride), pH 11.88 (di-sodium hydrogen phosphate/sodium hydroxide) and pH 12.83 (potassium chloride/sodium hydroxide). Uncertainty of pH measurement was estimated to be 0.05 pH units, five times higher than the manufacturers declared accuracy. This was due to varying ionic strength between different samples which was not explicitly taken into account for pH measurements.

Redox measurements were either made after pH measurements in the same aliquot or with separate aliquots, depending on the sample volume. A Pt electrode with Ag/AgCl reference was used (CRISON 52 62) and calibrations made with buffers at 220 and 468 mV (CRISON). For stabilisation of the measurement at least one hour was given.

Electric conductivity was measured with a CRISON Multimeter MM41, equipped with CRISON conductivity cell 50 70 and temperature sensor Pt1000.

5 Results on Starting Material Properties

5.1 Composition of Cement Clinker

The two cement clinkers, Holcim-1 and Sulfadur are similar with respect to main elements Ca and Si, but differ in Mg, S, Fe and Al contents (Table 14). The oxide compositions of both clinkers were determined according to the Bogue calculation (ASTM C 150 as described in Thomas and Jennings (2013)). Two different sets of equations were used, depending on the A/F ratios of oxide compositions. For Holcim-1 clinker A/F ratio is above 0.64 while for Sulfadur clinker it is below this threshold value (Table 14). Both cements have a relatively high content of aluminoferrite C₄AF.

Table 14 Cement composition from duplicate XRF analysis. Results are given in wt.% of the oxides, referring to the ignited mass which was determined from TGA. Results for Na (*narrowed*) are below calibration limit of 0.5 wt.%. The given mineralogical compositions were determined according to the (modified) Bogue-method.

	SiO ₂	Al ₂ O ₃	Fe ₂ O ₃	CaO	MgO	SO ₃	Na ₂ O	K ₂ O	Sum	A/F	C ₃ S	C ₂ S	C ₃ A	C ₄ AF	Sum
Holcim-1 clinker	19.71	3.78	4.67	64.72	0.88	3.84	0.06	0.25	98.38	0.8	68.6	4.8	2.1	14.2	89.7
Sulfadur clinker	20.46	2.63	6.82	64.82	2.26	1.42	0.04	0.38	98.82	0.4	73.1	3.5	0.0	17.1	93.7

5.2 Composition of Hardened Cement Paste

Both HCPs mainly consist of C-S-H and portlandite, but differ significantly in carbonate content (Table 15). Holcim-1 HCP, which was submitted to prolonged storage was carbonated before experiments, while recently hydrated Sulfadur HCP contains only a small fraction of carbonate, according to quantitative Differential Thermogravimetric analysis (Figure 18). The XRD diffractogram in Figure 17 indicates a significant amount of calcite in three years stored Holcim-1 HCP. Reduced weight loss of Holcim-1 HCP below about 200 °C, but a regular portlandite content, similar to the one of Sulfadur HCP, indicates that carbonation occurred mostly at expenses of C-S-H. Thermodynamically it would be expected that portlandite carbonates preferentially in comparison with C-S-H. However, recent experimental studies show that during carbonation dense calcite layers may form on portlandite surfaces, thereby protecting it from further transformation (Morandeu, Thiéry et al. 2014, Galan, Glasser et al. 2015).

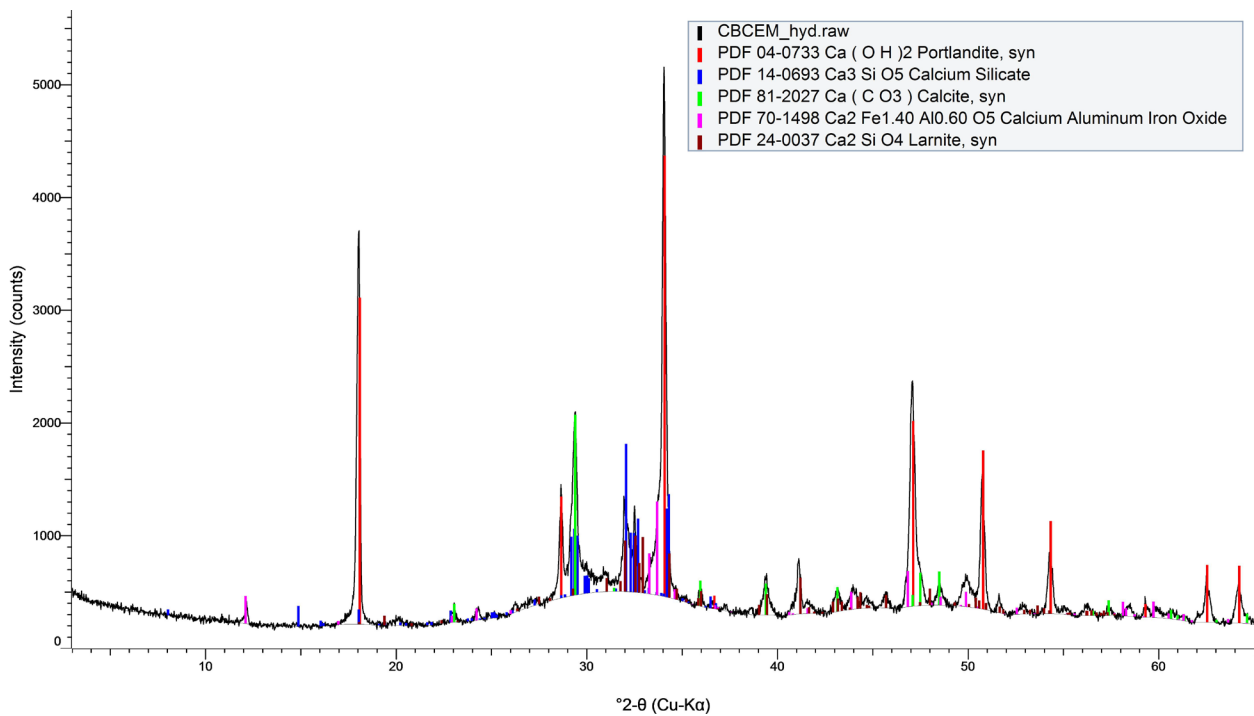


Figure 17 X-ray diffractogram of Holcim-1 HCP after 3 years of dry storage in air. Ca(OH)_2 , CaCO_3 , aluminoferrite, Ca_3SiO_5 and Ca_2SiO_4 (orthorhombic and hexagonal modifications) were identified.

For Sulfadur HCP a calcium carbonate content of 1 wt.% was determined based on weight loss at the decomposition temperature range of calcite. However, in TG-analysis the temperature where calcite decomposes overlaps partly with decomposition of C-S-H and amorphous monocarboaluminate. Consequently, we regard 1 wt.% as the maximum possible calcium carbonate content. Moreover, X-ray analysis of shelved, non-reacted Sulfadur HCP after completion of all experiments still did not reveal calcium carbonate reflections, neither from calcite, aragonite or vaterite. Due to the generally high crystallinity of calcite, which makes it well detectable in XRD diffractograms, we assumed that calcite content in stored Sulfadur HCP cement was below 1 wt.-% throughout the experimental study.

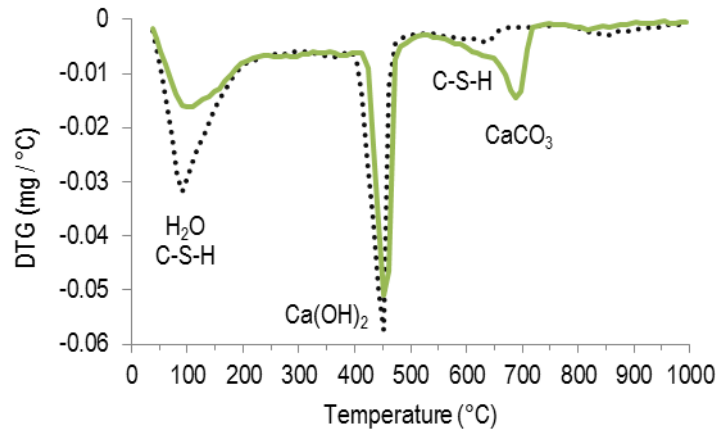


Figure 18 Differential thermogravimetric analyses results from Sulfadur (stippled line) and Holcim-1 HCP (solid line). Only major phases responsible for peaks are indicated in the figure.

Clinker minerals are still present in both hydrated cement pastes, even in 8 weeks hardened Sulfadur HCP samples. Persistent clinker phases consist of aluminoferrite and small calcium silicate fractions, observed by SEM and XRD analysis. Diffractograms of Sulfadur and Holcim-1 HCP are included in Figure 19 and annex 10.5, respectively.

We did not identify any typical sulphate and/or aluminium bearing hydrate phases (e.g. ettringite, monosulphoaluminate or hydrotalcite) by XRD in neither of the two hardened pastes. Regarding Holcim-1 HCP this might be due to the intensive drying procedure at 105°C which certainly led to dehydration and probably amorphisation of any present aluminate-sulphate-hydrate phase. For ettringite, e.g., water loss starts already at 50 °C in ambient atmosphere (Taylor 1997). In the case of Sulfadur HCP it is unlikely that the employed more gentle drying procedure caused a similar effect on sulphate phases. However, we identify three other factors that may be responsible for their absence. First, sulphate content is inferior in Sulfadur HCP which reduces the absolute amount of sulphates that may potentially form. Second, according to Taylor (1997), ettringite may become X-ray amorphous upon extensive drying (which he did not further specify) at room temperature. Finally, in this study we found that especially aluminoferrite hydrated sluggishly. Persistence of this phase, also throughout experiments, reduces availability of Al for formation of aluminosulphate phases.

Table 15 Mineralogical composition of HCPs. Where determined by TG analysis, mineral content is given in wt.-% referring to the mass of HCP at laboratory conditions. For details on the indicated calcium carbonate content in Sulfadur HCP see explanations given in text.

Holcim-1 HCP	Sulfadur HCP
C-S-H	C-S-H
Portlandite 21.5	Portlandite 21.8
Calcium carbonate 7.3	(Calcium carbonate <1.0)
Tri-/dicalcium silicate, aluminoferrite	Tri-/dicalcium silicate, aluminoferrite

6 Results on HCP Degradation

6.1 Batch Experiments

6.1.1 Solid Phases

Evolution of crystalline cement phases from sane over moderately to severely degraded Sulfadur HCP was followed systematically by XRD and SEM analysis of the solid. All diffractograms were recorded with the same sample preparation and instrument settings ($0.02^\circ 2\text{-}\theta$ step width, 2 s accumulation time) so that changes in reflection intensity between different samples provide relative information on phase abundance. Identified phases from XRD and SEM analyses are summarised in Table 16. In Figure 87 of annex 10.5 detailed assignment of XRD reflections to precipitated phases is given. In the following, we present phase characteristics, their relations and development with increasing degree of degradation for experiments with GG and DI water.

Table 16 Phase assemblies formed during batch experiments with Sulfadur HCP in GG and DI water.

L/S ratio	DI water	GG water
0.1 m ³ /kg	C-S-H	C-S-H
	Portlandite	Portlandite
	Calcite	Calcite
	Ettringite	Ettringite
	Hydrotalcite/monocarboaluminate	Hydrotalcite/monocarboaluminate
	Aluminoferrite	Brucite
	Di-/tricalcium silicate	Aluminoferrite Di-/tricalcium silicate
2 m ³ /kg	C-S-H	C-S-H
	Calcite	Calcite
	Hydrotalcite/monocarboaluminate*	Brucite
	Aluminoferrite	Aluminoferrite
	Di-/tricalcium silicate	Di-/tricalcium silicate

Portlandite is the most abundant crystalline phase of Sulfadur HCP (Figure 19). Reflection intensities of portlandite in Figure 19 show its subsequent dissolution from sane HCP over low L/S ratio to high L/S ratio in DI and GG water. In this order the degree of degradation increases. At 0.1 m³/kg L/S ratio starting dissolution of portlandite is accompanied by precipitation of scalenohedral calcite (Figure 20), indicating transformation of portlandite to calcium carbonate and thus carbonation. Diffractograms of HCP degraded in GG and DI water are almost identical at this stage. At 2 m³/kg L/S ratio portlandite completely dissolves and precipitation of calcite continues. According to diffraction intensities, calcite becomes the major crystalline phase in the system at this second experimental degradation step (Figure 19).

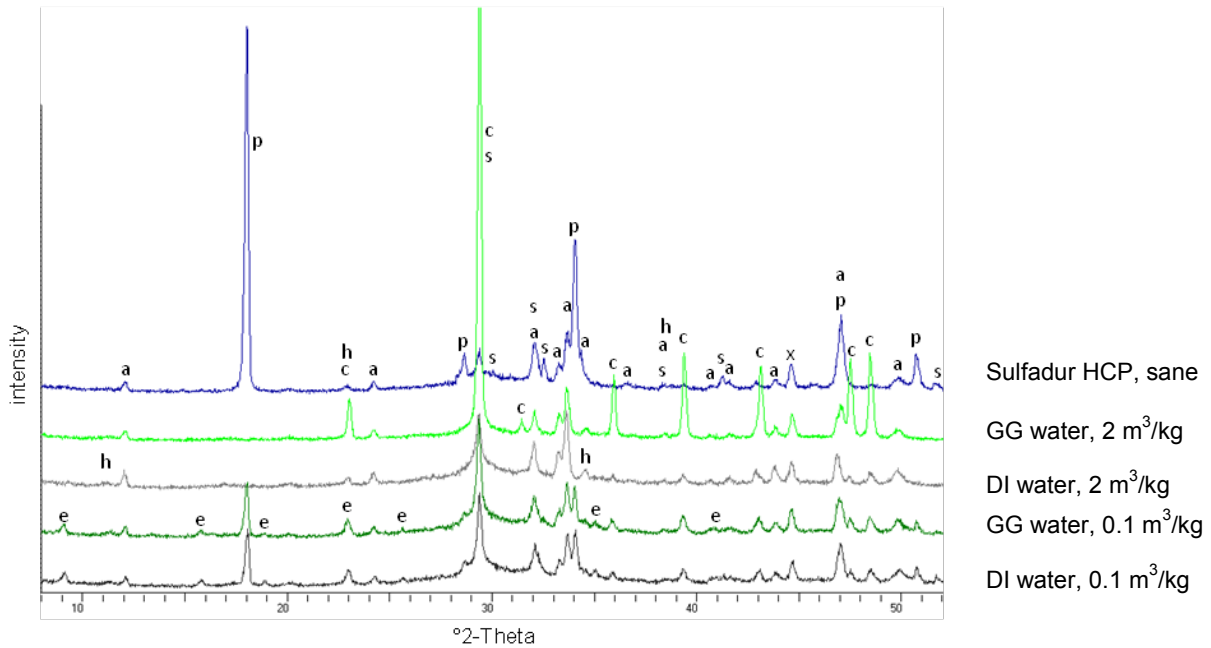


Figure 19 Representative XRD patterns of the different states of degraded HCP, from freshly hydrated and sane (top pattern) to severely degraded HCP. The legend indicates the type of solution used and the L/S ratio. Reflections were assigned to phases: a aluminoferrite, c calcite, p portlandite, s bi-/tricalcium silicate, e ettringite, h hydrotalcite, x artefact (aluminium sample-holder).

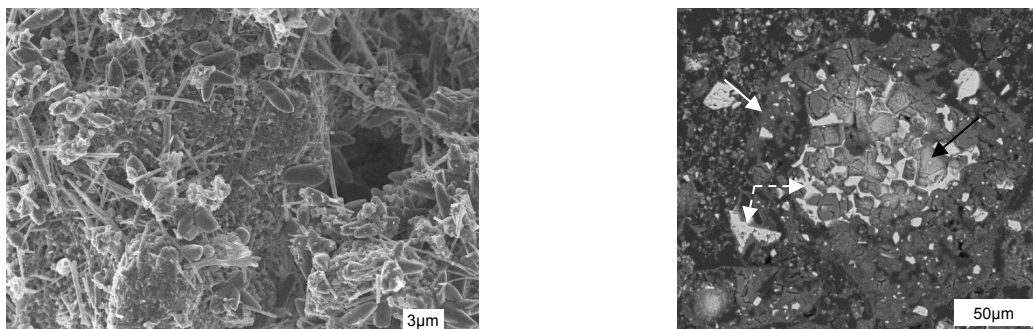


Figure 20 SEM images of HCP after batch experiments with GG water at low L/S ratio. In metal sputtered powder (left, SE image) ettringite needles are present, together with scalenohedral darker grains which are calcite and irregular shaped C-S-H. In the polished and carbon coated section of epoxy embedded grains (right, BSE image) inner and outer C-S-H (black and white arrow, respectively) and aluminoferrite (stippled arrows) are identified.

In GG water degraded HCP shows even higher calcite reflection intensities, demonstrating larger carbonation potential of GG water over DI water, as expected. Since portlandite is already absent at this stage, increased precipitation of calcite indicates fostered dissolution of C-S-H, the principal Ca source in the system. Reduced background from amorphous C-S-H in the range from 28 to 35 $^{\circ}2\theta$ in diffractograms (Taylor 1997) further proves that in GG water more C-S-H phase from the HCP reacts compared to DI water (Figure 21).

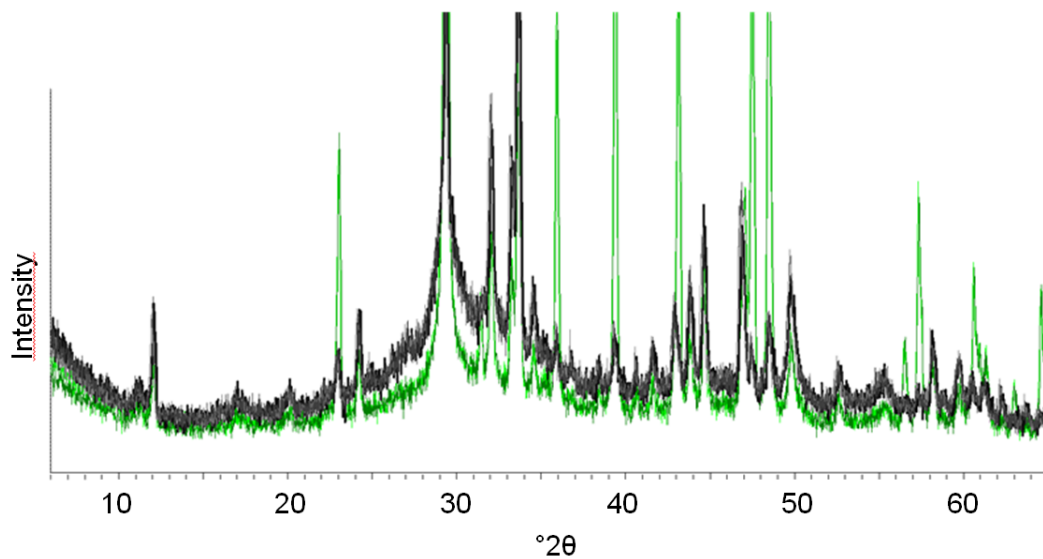


Figure 21 XRD diffractograms recorded after batch experiments with GG water at high L/S ratio (two almost identical patterns in green tones) and DI water (three almost identical patterns in grey tones). Notice the higher amorphous hump of the grey patterns from DI water, caused by amorphous C-S-H.

SEM analysis revealed that in GG water at high L/S ratio, calcite precipitates mainly in form of idiomorphic rhombohedra without recognisable preferential physical contact to other cement phases or distribution at grain boundaries (Figure 22). At low L/S ratio C-S-H composition is similar to jennite with C/S ratio of 1.4 ± 0.1 . After degradation with GG water at high L/S ratio C/S ratio decreases to 0.8 ± 0.1 (Table 17).

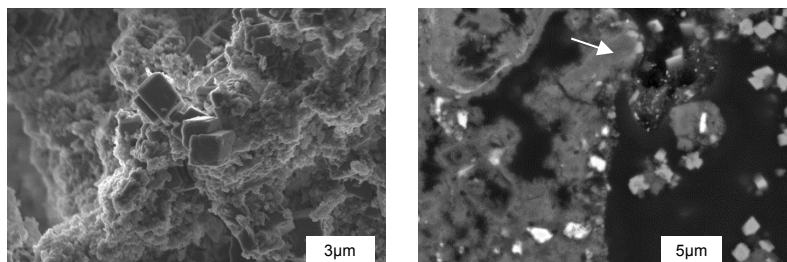


Figure 22 SEM images of cement after batch experiments at high L/S ratio with GG water. In metal sputtered powder (left, SE image) idiomorphic calcite rhombohedra are surrounded by irregular shaped C-S-H. In the polished and carbon coated section of epoxy embedded grains (right, BSE image) the rhombohedral shape of calcite crystals, which are randomly dispersed in the epoxy resin (black), can still be recognised. The white arrow points to inner C-S-H which is surrounded by fibrillar outer C-S-H. Brightest spots are aluminoferrite.

In the first experimental degradation step at $0.1 \text{ m}^3/\text{kg}$ L/S ratio, besides calcite precipitation, crystalline ettringite and a minor amount of hydrotalcite and/or monocarboaluminate form. In the second experimental degradation step at $2 \text{ m}^3/\text{kg}$ L/S ratio ettringite is unstable in both solution systems,

indicated by absence of reflections from diffractograms (Figure 19). In contrast, hydrotalcite is found in HCP equilibrated with DI water at high L/S ratio, but not in GG water.

Table 17 Compositions of C-S-H phases from HCP degraded in GG water at both L/S ratios. Mean concentrations and standard deviations from semi-quantitative SEM-EDX analysis of 14 individual points and corresponding C/S ratios are given.

L/S ratio	2 m ³ /kg	0.1 m ³ /kg
Element	At.-%	
Al	1.6±0.2	2.2±1.0
Ca	16.2±1.8	20.2±2.4
Fe	1.2±0.4	3.8±2.8
Mg	1.8±0.5	2.1±1.0
O	60.4±0.9	57.9±0.4
Si	19.3±0.9	14.0±1.4
C/S ratio	0.8±0.1	1.4±0.1

Identification of the corresponding phases was difficult for the following reasons: First, presence of ettringite disturbs unambiguous differentiation of hydrotalcite and monocarboaluminate from XRD diffractograms since it overlaps with the second characteristic reflection of hydrotalcite. Second, differentiation of carbo- and sulphoaluminate phases is moreover complicated as main reflections of both may appear in the range from 10 to 12 °2-θ (Cu-Kα) (Johnson and Glasser 2003, Matschei, Lothenbach et al. 2007a, Lothenbach, Le Saout et al. 2008) and minor reflections also overlap with other phases. The variability of the main reflection is due to loosely incorporated water molecules which, depending on the drying procedure, extensively affect interlayer distance. Third, in this 2-θ range monocarboaluminate might also overlaps with the present reflection of persistent, non-hydrated aluminoferrite. Even though not unambiguously determinable from diffractograms, we assume that of the three phases monocarboaluminate, monosulphoaluminate and hemicarboaluminate only the first may coexist with portlandite, calcite and ettringite. This was shown by Matschei, Lothenbach et al. (2007a) and also confirmed by our thermodynamic equilibrium calculations (c.f. chapter 6.3.2).

We did not observe formation of brucite Mg(OH)₂ in any diffraction patterns after experiments. However, brucite was identified by SEM-EDX in single spots after experiments with GG water at both, low and high L/S ratio. Due to its absence from XRD patterns we estimate the abundance of brucite in the degraded HCP to be inferior to 1-2 wt.%. As brucite is typically present in crystalline form it is unlikely to overlook amorphous phase.

In all diffractograms (c.f. Figure 19) aluminoferrite reflections remained almost unchanged with respect to the sane HCP. We expected aluminoferrite in the HCP to hydrate secondarily during degradation experiments, at least partly. Nevertheless, no indications for secondary hydration of aluminoferrite were found in either of the two types of solutions or at the different L/S ratios. At the spatial resolution achievable by SEM, rims of aluminoferrite always appear sharp without any indications for dissolution.

Moreover, SEM analyses indicate two morphologically different types of aluminoferrite: one appearing as massive, single grains without visible internal porosity and another one which forms characteristic aggregates of smaller crystals. The latter has an open porosity in between (Figure 23) and forms networks around other phases, basically C-S-H (Figure 20). From this observation we suggest that these spaces were originally filled by calcium silicate oxides in the clinker before hydration. The chemical composition of both aluminoferrite types does not differ measurably; they have an A/F ratio of 0.48 ± 0.07 (standard deviation from 20 analysed spots). This ratio further coincides with the aluminoferrite phase identified by XRD, having an A/F ratio of 0.4.

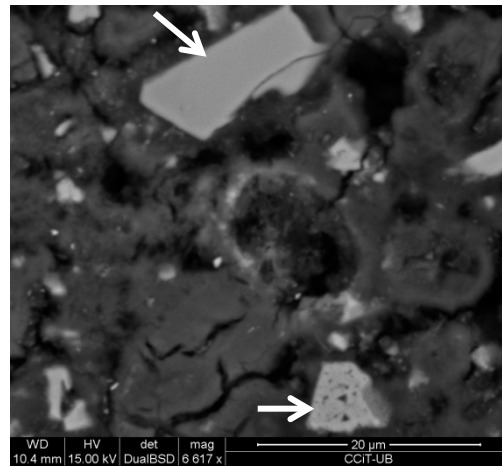


Figure 23 Polished section of a Sulfadur HCP sample after a batch experiment at $L/S = 0.1 \text{ m}^3/\text{kg}$ in GG water. Indicated are the two distinct morphologies of sluggishly reacting aluminoferrite.

6.1.2 Solutions

Aqueous major ions concentrations at $0.1 \text{ m}^3/\text{kg}$ L/S ratio are almost identical in both, GG water and DI water except for alkali elements (Table 18 and Figure 24). They are more concentrated in experiments with GG water since the solution itself contributes alkalis which are not solubility limited and only minor fractions partition to HCP. At $2 \text{ m}^3/\text{kg}$ L/S ratio aqueous elemental concentrations are significantly affected by the type of contacting solution. Different Ca and Si concentrations indicate distinct degradation states of the cementitious material in the two solutions. We measured slightly higher Si, but slightly lower Ca concentrations in experiments with GG water compared to DI water. This indicates fostered degradation of C-S-H in GG water and consequently fostered degradation of HCP.

At low L/S ratio alkali elements Na and K from the HCP dissolve readily so that at this first degradation stage pH is already buffered by portlandite to 12.50 ± 0.05 , independently of the starting solution. At high L/S ratio portlandite dissolves entirely in DI water and pH decreases by approximately one unit to 11.65 ± 0.05 . As expected, dissolution of portlandite is accompanied by significantly increased

mobilisation of most elements from HCP when quantitatively more solid dissolves than reprecipitates. At high L/S ratio the system becomes more susceptible to the type of starting solution than at low L/S ratio.

Table 18 Solution composition after batch experiments with Sulfadur HCP. Values are means from 2 to 6 individual experiments and errors give corresponding standard deviation. Only S(VI) concentrations at low L/S ratio are from single analyses and give analytical errors. Concentrations are given in $\mu\text{mol/l}$ (10^{-6} mol/l) for all elements.

L/S ratio, solution m^3/kg , -	pH	Eh mV, SHE	Ca $\mu\text{mol/l}$	Si	Al	Mg	S(VI)	Na	K
0.1, DI water	12.50 ± 0.05	215 ± 9	24500 ± 200	7.57 ± 0.7	5.02 ± 0.3	<3.7	49 ± 4	<311	741 ± 9
0.1, GG water	12.51 ± 0.05	221 ± 2	23500 ± 100	7.59 ± 0.5	4.62 ± 0.4	<3.7	54 ± 4	2789 ± 124	870 ± 23
2, DI water	11.65 ± 0.05	248 ± 15	2160 ± 200	181 ± 7	23.6 ± 0.7	<43	40 ± 10	<46	29.0 ± 1.1
2, GG water	11.55 ± 0.05	248 ± 15	1210 ± 20	305 ± 0.8	16.4 ± 0.7	<43	144 ± 0.3	1964 ± 857	133 ± 1.0

Apart from the alkalis, Ca is the element, which most importantly dissolves from HCP at low L/S ratio, i.e. one quarter of its inventory is released with both solutions (26 and 25 at.-% with DI and GG water, respectively). Ca ions present in GG water do not significantly affect Ca dissolution from HCP as the initial concentration of $2.5 \cdot 10^{-4}$ mol/l is low compared to Ca concentration in equilibrium with portlandite which is approximately two orders of magnitude higher. At high L/S ratio considerable decalcification is attained with DI water where almost 50 at.-% of the Ca inventory dissolve from HCP, calculated from an aqueous equilibrium concentration of $2.5 \cdot 10^{-3}$ mol/l (Table 18 and Figure 24). In the equilibrated GG water system however, only 20 at.-% of the HCP's Ca inventory are dissolved, calculated from $1.2 \cdot 10^{-3}$ mol/l Ca in solution (Table 18 and Figure 24). As expected, referring Ca concentrations are about one order of magnitude lower than at pH 12.5.

In the case of Si the equilibrium concentration is $7.6 \cdot 10^{-6}$ mol/l in both solutions (Table 18 and Figure 24) at low L/S ratio. It is controlled by metastable C-S-H with C/S ratio 1.4 ± 0.1 (see chapter 6.1.1 and chapter 6.3.2), in equilibrium with portlandite. This low Si concentration implies dissolution and precipitation of Si in trace amounts with DI and GG water, respectively. As expected, aqueous Si concentrations increase when going from low to high L/S ratio which is due to incongruent dissolution of C-S-H. At high L/S ratio GG water causes removal of 19 at.-% Si ($3.1 \cdot 10^{-4}$ mol/l) from the inventory while in DI water only 13 at.-% Si ($1.8 \cdot 10^{-4}$ mol/l (Table 18 and Figure 24)) are dissolved.

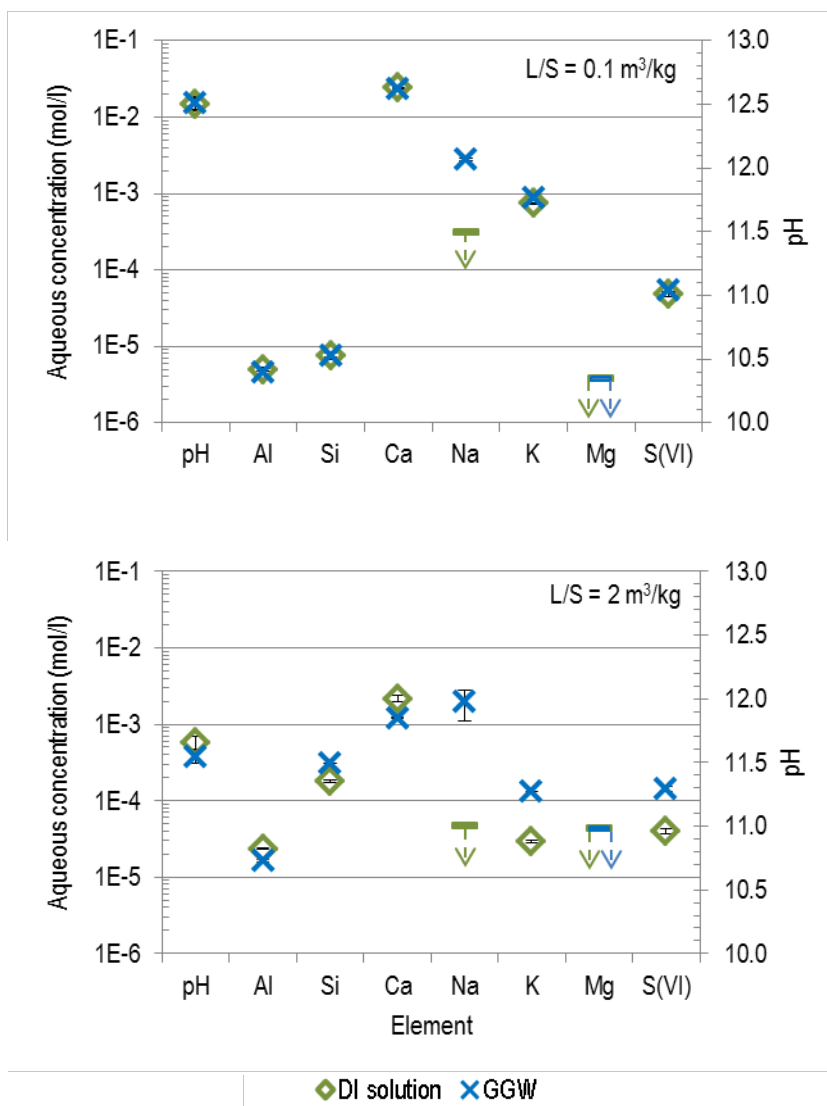


Figure 24 Solution composition after batch experiments as given in Table 18. Dashes with arrows indicate maximum concentrations with concentrations below detection limit.

Similar to Ca and Si, concentrations of Al and S(VI) are equal in both solutions at low L/S ratio (Table 18 and Figure 24). This suggests that also these elements are solubility controlled, presumably by the same phase in both systems. In experiments with DI water 3.5 at.-% of the solid-bound sulphate inventory is dissolved at equilibrium concentration (Figure 25). In contrast, in GG water there is no net solubilisation of sulphate from the HCP as it precipitates from solution until equilibrium concentration is reached. Ettringite is the only identified sulphate phase forming at low L/S ratio. We therefore conclude that this phase controls S(VI) equilibrium concentrations in both solutions. In the more degraded system the higher L/S ratio significantly affects sulphate repartition. We measured about three times higher S(VI) concentration in GG water equilibrated systems than in DI water. However, adding the initial S(VI) concentration of GG water to the measured aqueous sulphate concentration after equilibrating HCP in DI water, we almost obtain the measured concentration in equilibrated GG water at high L/S ratio (Table 18 and Figure 24). This translates to the mass balance of HCP's S(VI) inventory: Around 56 at.-% of the inventory dissolve in DI water and a similar amount, 62 at.-%, dissolves in GG water. Consequently, in

this degradation stage solubility is not controlling S(VI) concentrations, even though around 40 at.-% of the sulphate inventory are still bound to the solid. These observations suggest that the remaining S(VI) inventory of HCP in both systems is either physically protected from mobilisation, or adsorbed to another phase. In the latter case sorption sites for S(VI) would have been already saturated in DI water.

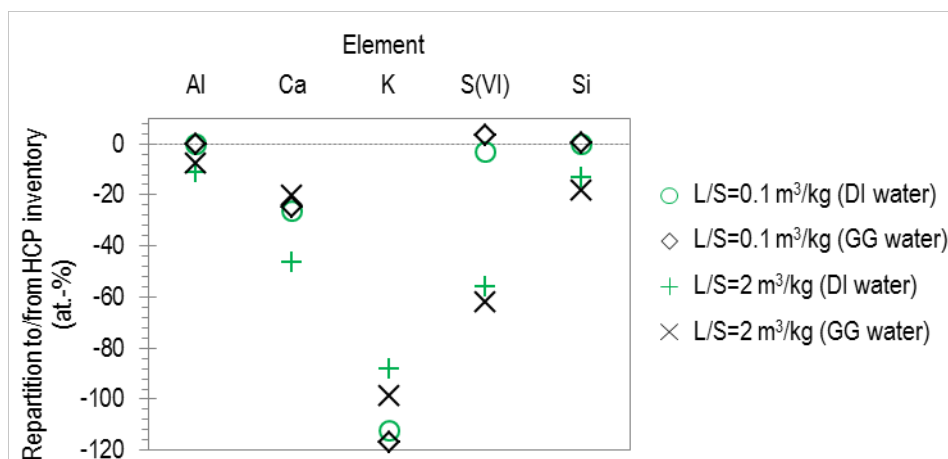


Figure 25 Diagram visualising repartition of HCP inherent elements after degradation at both L/S ratios (negative values indicate diminution). For experiments with GG water (black symbols) the yielded contribution of elements from GG water was subtracted from the measured concentrations before calculating repartitions. Each data point was derived from 2 to 4 individual experiments.

Aqueous Al concentrations of both solution systems at low L/S ratio are equal within analytical range of error. Synthesised GG water is not a source of Al. Therefore, the low aqueous concentration of about $5 \cdot 10^{-6}$ mol/l (Table 18 and Figure 24) entirely stems from HCP. This corresponds to 0.1 at.-% of Al inventory dissolved from HCP in both types of solutions. We therefore suppose that Al is solubility limited in this degradation stage. The three phases ettringite, hydrotalcite or monocarboaluminate may control its dissolution at various stages. With increasing degradation ettringite disappears at higher L/S ratio, as described in chapter 6.1.1. With ettringite dissolution, Al mobilisation increases to 11 at.-% and 8 at.-% of Al inventory with DI and GG water, respectively. Since we did not identify Al hydrate phases in GG water, we assume that Al dissolution is restricted by aluminoferrite. In contrast, a small amount of hydrotalcite still binds Al in DI water. Nevertheless, a significant quantity of aluminoferrite remains in degraded HCP, indicating that in DI water most Al is retained by aluminoferrite.

In all equilibrated solutions Mg concentrations are below the detection limit of $3.7 \cdot 10^{-6}$ and $4.3 \cdot 10^{-5}$ mol/l, for low and high L/S ratio, respectively. Therefore, we use the lowest calibrated concentration of the analytical method to calculate the maximum amount of Mg that possibly dissolves from HCP in DI water, i.e. less than 0.1 at.-% at low L/S ratio. In experiments with GG water, Mg precipitates and its aqueous concentration decreases from initially $1.1 \cdot 10^{-4}$ mol/l to below $3.7 \cdot 10^{-6}$ mol/l. Similarly, at high L/S ratio Mg concentrations in solutions are below $4.3 \cdot 10^{-5}$ mol/l. Calculating from the lower calibration concentration we deduce that at least 60 % of added Mg from GG water partitions to HCP at high L/S ratio and even 96 % at low L/S ratio. The presence of Mg containing hydrotalcite and/or

brucite in the degraded HCPs indicates that Mg does not simply adsorb to HCP, but precipitates from GG water.

6.2 Flow-Through Experiments

6.2.1 Role of Cement Type and Mass

For all flow-through degradation experiments performed at CO₂-‘free’ conditions results are similar for both cement types, Holcim-1 and Sulfadur HCP, regarding solid analyses and solution compositions. An exception is the evolution of Al concentrations in outflow solution which is discussed in chapter 6.2.5.2.

The amount of HCP placed in the reactor is crucial for the reproducibility of experiments. When HCP mass is inferior to 28 mg results scatter due to sample heterogeneity. Therefore, the reported results only include those experiments with representative HCP mass, above 28 mg. To present and discuss experimental data with varying flow rate and/or HCP mass in the reactor, results are regarded as function of degree of leaching (volume / mass). In doing so results are comparable. Degree of leaching is defined as the amount of solution (l) that passed the reactor, divided by the initial HCP mass (g) in the reactor. Analytical results are appended in annex 10.3, Table 33, including experimental time, cumulated flow and individual sample volumes.

6.2.2 Degradation of Major HCP Phases in CO₂-‘free’, deionised water

6.2.2.1 Dissolution of Portlandite and C-S-H

In all degradation experiments performed under CO₂-‘free’ conditions portlandite reacts to completion. SEM analyses of degraded HCP after flow-through experiments do not show any portlandite, neither for lower nor for higher degree of leaching. Moreover, XRD analyses of degraded HCP confirm complete dissolution of portlandite in experiments that were discontinued between 3.6 and 27.1 m³/kg degree of leaching (Figure 26).

C-S-H phases dissolve during experiments, thereby changing their compositions. Therefore, we used SEM-EDX analysis to characterise C/S ratios. After 6.5 m³/kg degree of leaching C-S-H phases show C/S ratios between 1.3 and 1.4 while after 24.1 m³/kg they range from 0.4 to 1.1. We assume that if HCP had degraded in a homogeneous manner, C/S ratios of C-S-H after experiments would have decreased rather homogeneously in the entire solid. Although the flow-through setup contains only a single layer of HCP powder, C/S ratios scatter with increasing duration of experiments. This indicates heterogeneities in the degraded HCP. Locally calcite and small amounts of dolomite as well as dicalcium silicate were identified by SEM. Further, persistent and non-hydrated dicalcium silicate indicates that the solid does not react homogeneously, as indicated by the evolution of C/S ratios.

Apart from degraded C-S-H with lower C/S ratio, we found a phase consisting of Si, Ca, Al and Fe with untypical stoichiometry, probably a C-A-S-H gel as described by Hidalgo, Petit et al. (2007) which may also incorporate Fe during degradation (Faucon, Adenot et al. 1998).

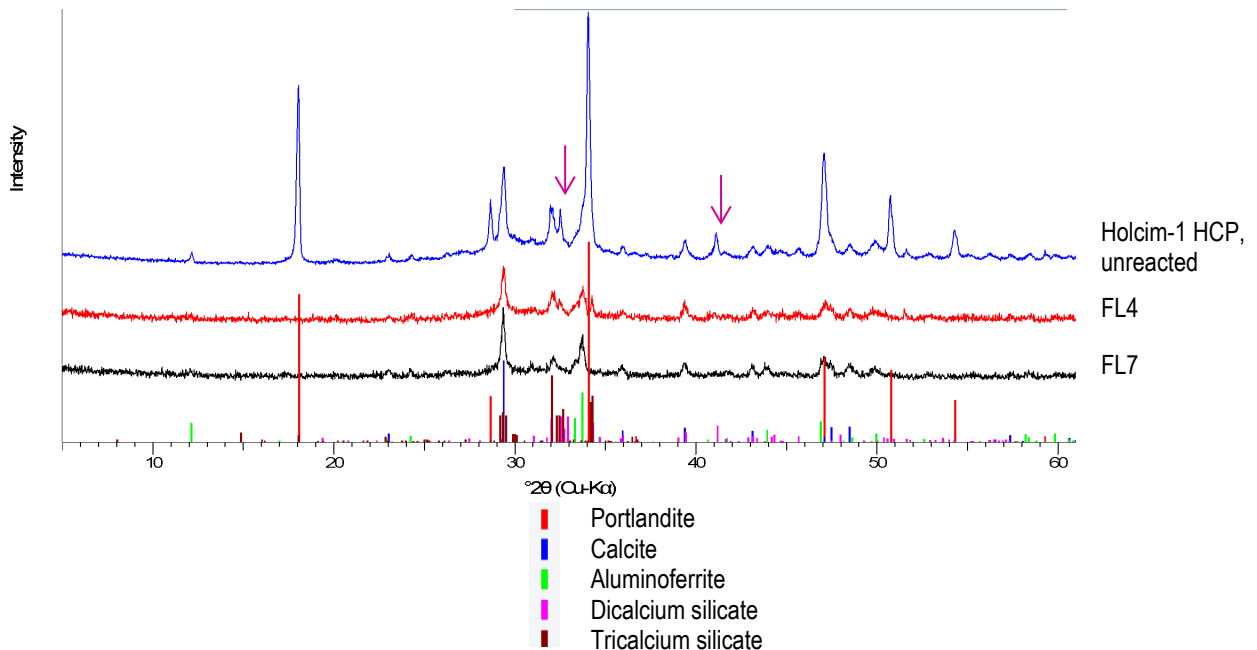


Figure 26 XRD diffractograms of sane Holcim-1 HCP and of degraded HCPs after short FL4, as well as after long flow-through experiment FL7. Since measurement conditions were different in each case, diffractograms are offset in y-direction and rescaled for comparability. Note that portlandite (red bars) is absent from diffractograms of both degraded HCPs. Reflections of dicalcium silicate are most important in sane HCP (highlighted by arrows) and decrease significantly in HCP from experiment FL4 until they disappear in experiment FL7 (discussed in chapter 6.2.5.1).

6.2.2.2 Evolution of Outflow Solution pH

At the beginning of experiments measured pH in outflow solutions (11 - 50 ml) have maximum values of around pH ~ 11.9. These high values first decrease rapidly, then more slowly approach ‘steady state’ values (Figure 27). This slowing down of pH decrease in outflow solution occurs at around 1.5 m³/kg degree of leaching.

At degree of leaching above 20 m³/kg, reached in experiments FL 7, FL 9 and FLS1, pH scatters within pH 9.8±0.2. Nevertheless, even over these last samples pH measurements still indicate a slowly decreasing trend. The lowest measured pH value is considerably higher than the neutral pH around 7 of the input solution (‘CO₂-free’ DI water). This proves that throughout experiments pH is always conditioned by alkaline buffering of the HCP, i.e. alkalinity does not get depleted.

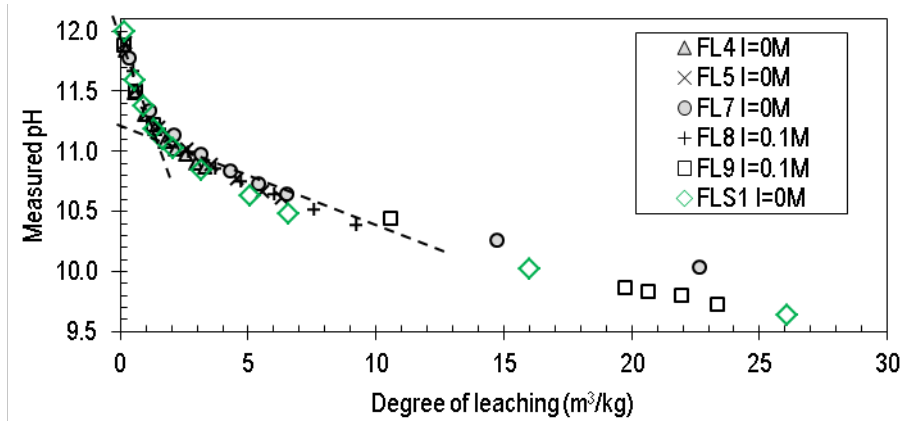


Figure 27 Evolution of pH, measured in outflow solutions of flow-through experiments with Sulfadur (FLS1) and Holcim-I HCP. Size of symbols corresponds to the error of pH measurement. Dashed lines highlight changing trend in pH decrease at around 1.5 m³/kg degree of leaching.

6.2.2.3 Evolution of Outflow Solution Ca Concentration

In contrast to solid phase characterisation the evolution of the compositions of outflow solutions was assessed in each experiment over the whole course. Of all elements mobilised from HCP, Ca reaches highest concentrations in outflow solutions. Measured Ca concentrations in outflow solutions have maximum values around $5 \cdot 10^{-3}$ mol/l at the beginning of all experiments (Figure 28). At the same time pH is also high with values around ~11.9 (chapter 6.2.2.2). This shows that portlandite always is thermodynamically undersaturated in these experiments.

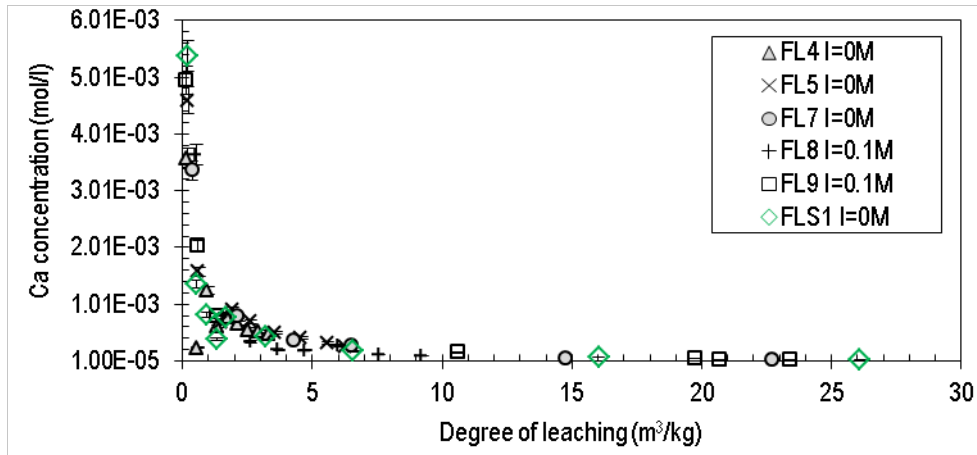


Figure 28 Evolution of Ca concentration, measured in outflow solutions of flow-through experiments with Sulfadur (FLS1) and Holcim-I HCP. Four last samples above 20 m³/kg have a mean Ca concentration of $3.6(\pm 0.7) \cdot 10^{-5}$ mol/l.

Similar to pH evolution, high Ca concentrations first decrease rapidly, then more slowly approach ‘steady state’ concentrations (Figure 28). This slowing down of Ca concentration decrease in solution occurs at around 1.5 m³/kg degree of leaching, simultaneously to the change in pH evolution. Ca concentrations of $3.6(\pm 0.7) \cdot 10^{-5}$ mol/l are attained for high degree of leaching from 20 m³/kg until 26.10 m³/kg. However, as for pH in this degradation stage, concentrations still have a slowly decreasing trend.

6.2.2.4 Evolution of Outflow Solution Si Concentration

Silicate mobilisation evolves differently compared to Ca mobilisation. At the beginning Si concentration in outflow solution increases up to 1.5 m³/kg degree of leaching (Figure 29). Here, maximum concentrations are around $1.7 \cdot 10^{-4}$ mol/l in pure DI water and around $2.4 \cdot 10^{-4}$ mol/l in 0.1 mol/l NaClO₄ solution. In continuation, Si concentration starts to decrease. Similar to the evolution of pH and Ca (chapters 6.2.2.2 and 6.2.2.3, respectively), at high degree of leaching Si concentration decreases more slowly. From 20 to 26 m³/kg degree of leaching the mean concentration of outflow solutions is $3.4(\pm 0.7) \cdot 10^{-5}$ mol/l. However, as for pH and Ca concentration the trend is still slightly decreasing.

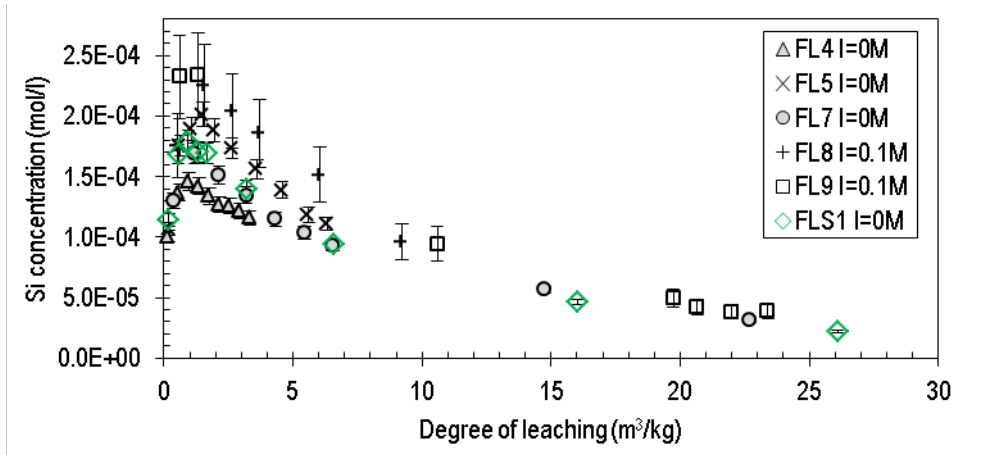


Figure 29 Evolution of Si concentration, measured in outflow solutions of flow-through experiments with Sulfadur (FLS1) and Holcim-I HCP.

Silicate is the only analysed species mobilised from Holcim-1 HCP which is affected by the addition of 0.1 mol/l NaClO₄ to DI water. At the beginning Si concentrations are lower in DI water. However, the gap of measured ion concentrations decreases continuously until 10 - 15 m³/kg degree of leaching are reached. At higher degree of leaching Si concentrations measured in both solutions tend towards similar values (Figure 29). According to Hong and Glasser (1999) higher Si concentrations might be caused by introduction of alkali elements into solution, increasing Si solubility. They attributed this effect to either higher ionic strength or modified C-S-H solubility due to replacement of Ca through Na.

6.2.2.5 Evolution of Outflow Solution Ca/Si Ratio

In all experiments the Ca/Si ratios in solution converge towards unity with increasing degree of leaching (Figure 30). When aqueous Ca/Si ratio equals 1 we assume that degraded C-S-H phase has a C/S ratio around 1 and is dissolving congruently. The observed evolution of Ca/Si ratio reflects the Ca depletion of C-S-H phases during HCP degradation.

In short experiments, attaining only 4 m³/kg degree of leaching, portlandite gets exhausted (chapter 6.2.2.1) while Ca/Si ratio in solution remains around 4. Consequently, C-S-H phases dissolve incongruently throughout these experiments. In longer experiments Ca/Si ratios approach 1, pointing out progressed degradation and congruent dissolution of C-S-H. We assume that also in short experiments (FL 4 and FL 5) Ca/Si ratios would reach unity if experiments had not been terminated before reaching higher degree of leaching.

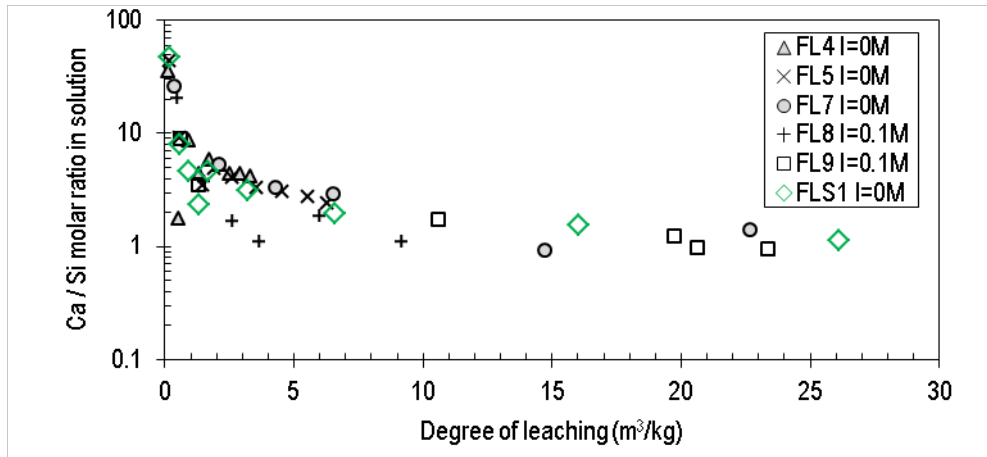


Figure 30 Ratio between measured Ca and Si concentrations in outflow solutions of flow-through experiments with Sulfadur (FLS 1) and Holcim-I HCP.

For further validation, we tested this explanation by crosschecking the relationship between measured Si concentration and pH. We calculate pH basing on congruent dissolution of C-S-H phase (‘C-S-H1.0 dissolution model’) and by supposing that all Si in solution stems from hydrolysis of C-S-H. Release of Si and Ca is thus stoichiometrically. Assuming a C/S ratio of 1, C-S-H dissolves according to equation (13).



If this is the pH controlling reaction, pH may be calculated from equation (14) by replacing measured Si concentration for hydroxyl concentration (equation (15)).

$$pH = 14 - pOH = 14 + \log_{10}\{OH^-\} \cong 14 + \log_{10}[OH^-] \quad (14)$$

$$pH \cong 14 + \log_{10}[Si] \quad (15)$$

This balance is in accordance with speciation of Ca and Si over nearly the whole range of measured pH values in outflow solutions (pH ~9.8 to ~11.9, chapter 6.2.2.2). Only at less alkaline conditions, approaching pH 9.8, Si speciation changes according to reaction (16).



Speciation changes as function of pH, calculated with Phreeqc, are illustrated in Figure 31.

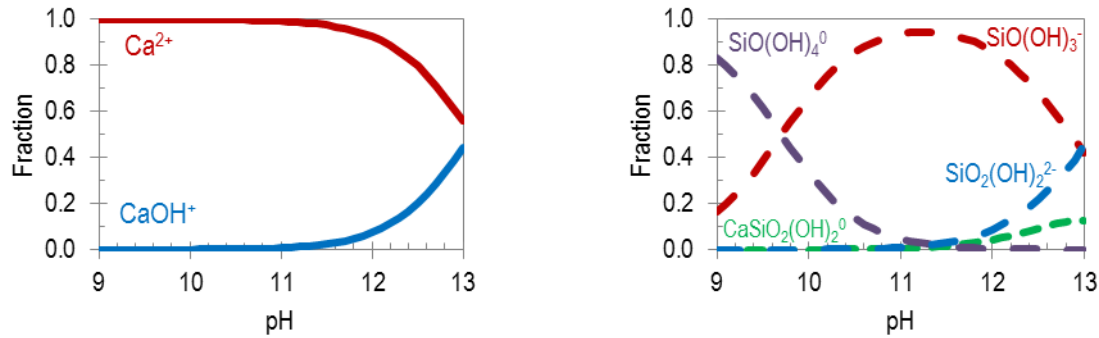


Figure 31 Aqueous speciation of Ca and Si as function of pH, calculated with the Cemdata07 database. Total Ca and Si concentrations are constant at 10^{-4} mol/l and 10^{-6} mol/l, respectively, and ionic strength is 0.1 mol/l. Species with fractions < 0.001 are omitted in the figures.

The calculations reproduce satisfactorily the measured pH for degrees of depletion higher than $20 \text{ m}^3/\text{kg}$ of the longest experiment FL 9. Calculated pH values for experiments ending at lower degree of leaching follow the same trend as FL 9 (shown in Figure 32), but do not attain measured values.

In calculations basing on Si concentrations only the $\text{SiO}(\text{OH})_3^-$ species is used. Not taking into account changes of speciation at low pH leads to slight deviation of calculated pH towards lower values. For lowest measured pH values we included corresponding mixed speciation of Si in calculations. The implied generation of additional hydroxyl ions improves the match between calculation and measurement.

Another way of calculating pH is based on the assumption that portlandite is the major pH controlling solid phase (' $\text{Ca}(\text{OH})_2$ dissolution model'). In this case portlandite dissolves according to equation (17).



Consequently, measured concentrations of Ca are used to calculate pH (equation (18)).

$$\text{pH} \approx 14 + \log_{10}(2 \cdot [\text{Ca}]) \quad (18)$$

With the $\text{Ca}(\text{OH})_2$ dissolution model measured and calculated pH agree at pH values higher than ~ 11 which is when portlandite and C-S-H would start to dissolve simultaneously (chapter 6.2.2.1). At more degraded stages the Ca based pH calculation gives similar results compared to measurements, but they deviate slightly to higher values. Results obtained with this $\text{Ca}(\text{OH})_2$ dissolution model are plotted together with results from the C-S-H1.0 dissolution model (Figure 32).

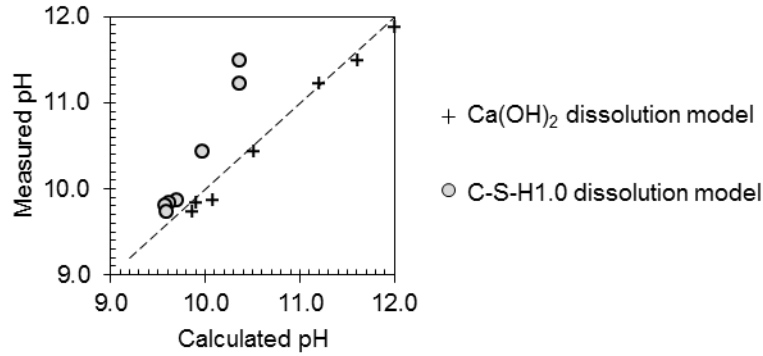


Figure 32 Calculated pH based on Ca and Si concentrations versus experimentally measured pH (FL9).

6.2.2.6 Mass Balances of Calcium and Silicate

The total amount of Ca and Si mobilised during HCP degradation is calculated from measured elemental concentrations and related to the initial inventory, giving the relative loss of elements from HCP (Table 19).

In some experiments single samples were not analysed (experiment FL 5 (1 of 10 samples) and FL 9 (1 of 8 samples) for Ca, FL 8 (2 of 8 samples) and FL 9 (1 of 8 samples) for Si). This missing data is evaluated by linear interpolation between nearest analysed samples. To determine the associated error we applied concentrations equal to the measured concentration in the antecedent and precedent sample. This shows maximum errors of +4/-2 at.-% on the total loss of elements from HCP. This method is not appropriate for balancing Ca loss in FL 7 since 3 samples of the series (9 samples) were not analysed. Therefore, in this case missing concentrations were interpolated by regression to all measured concentrations. Comparing all experiments shows that at 10 m³/kg degree of leaching more than 60 at.-% of the initial inventory of Ca and Si are removed from HCP. Moreover, Ca and Si losses are slowing down with increasing degree of leaching. Both observations point out the advanced stage of HCP degradation achieved in flow-through experiments.

Table 19 Cumulated loss of Ca and Si mobilised from Holcim-1 and Sulfadur HCP during degradation experiments with CO₂-‘free’ DI water , referred to the sane HCPs.

Experiment	FL 4	FL 5	FL 8	FL 7	FL 9	FLS1
Degree of leaching (m ³ /kg)	3.6	6.5	10.2	23.2	24.1	27.2
Total loss of Ca (at.-%)	37	62	68	71	69	69
Total loss of Si (at.-%)	17	37	60	67	82	66

6.2.3 Degradation of Major HCP Phases in Different Solutions

6.2.3.1 Dissolution of Portlandite and C-S-H and precipitation of calcite

To analyse the impact of CO₂ on dissolution of HCP phases we compare experiments with Holcim-1 HCP, performed under ‘CO₂-free’ conditions, with experiments performed with Sulfadur HCP under conditions of varying CO₂(aq) activity. For this we use atmosphere equilibrated DI and GG water. Moreover, we compare results from experiments with both HCPs, performed under ‘CO₂-free’ conditions.

Under all experimental conditions and for all attained degree of leaching portlandite dissolves completely and is not detected by XRD in any of the degraded HCP powders posterior to experiments (Figure 33). Even in the shortest experimental run, performed with GG water (FLS8) and lasting until 0.98 m³/kg degree of leaching results confirm that portlandite entirely dissolves from HCP already at the very early stages of flow-through runs.

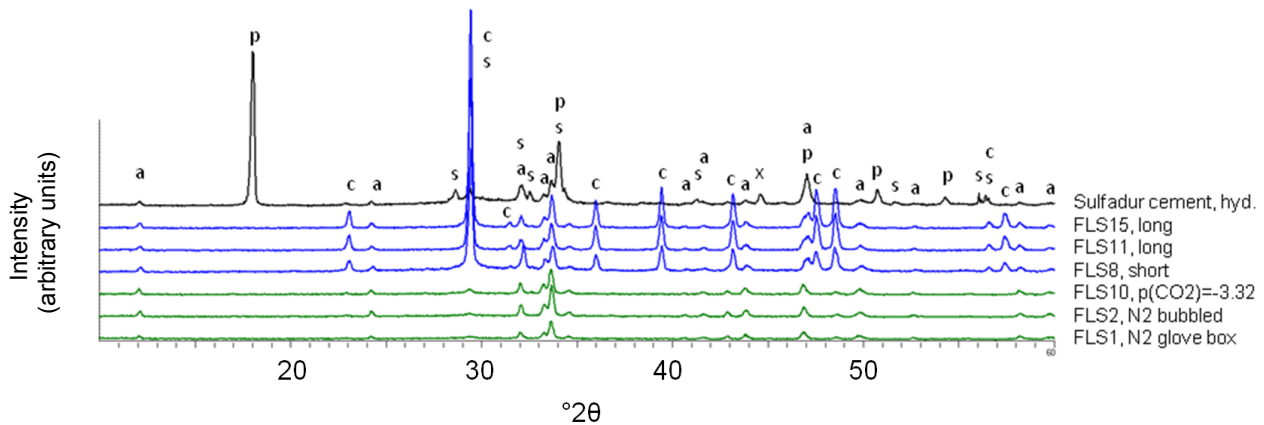


Figure 33 XRD pattern stack from degraded Sulfadur HCP samples after flow-through experiments. All patterns were recorded at the same conditions. The ordinate scale is measured intensity, but patterns were offset from zero. Experiments with DI water are shown in green. Blue tones are used for GG water and sane Sulfadur HCP is shown in black. FLS 1 has lower relative intensity as the sample holder could not be entirely filled. Peaks are assigned as follows: c calcite, p portlandite, a aluminoferrite and s di-/tricalcium silicate. Sane HCP was analysed with a different sample holder and the reflection marked ‘x’ is an artefact from this sample holder.

Dissolution of C-S-H is observed by comparing diffractograms in the region of the amorphous hump of C-S-H phases between 28 and 35 °2-θ. The short experiment FLS 8 (using GG water) shows a significantly higher hump compared to long experiments FLS 11 and 15 (using GG water), resulting from continued dissolution of C-S-H with increasing degree of leaching (Figure 34).

Similar to experiments with Holcim-1 HCP we used SEM-EDX analysis to assess C/S ratios, referring to changing C-S-H compositions due to degradation. High C/S ratios of C-S-H in Sulfadur HCP decrease significantly to values between 0.4 and 1.0 in experiments with DI water equilibrated with ambient air. Furthermore, C-S-H is enriched in Al and Fe, as already observed with Holcim-1 HCP

(chapter 6.2.2.1). The composition of remaining C-S-H phases after long experiments indicates an advanced degree of degradation, according to Figure 4 in chapter 3.2.1. The relatively large span of C/S ratios suggests that Sulfadur HCP, like Holcim-1 HCP, degrades heterogeneously.

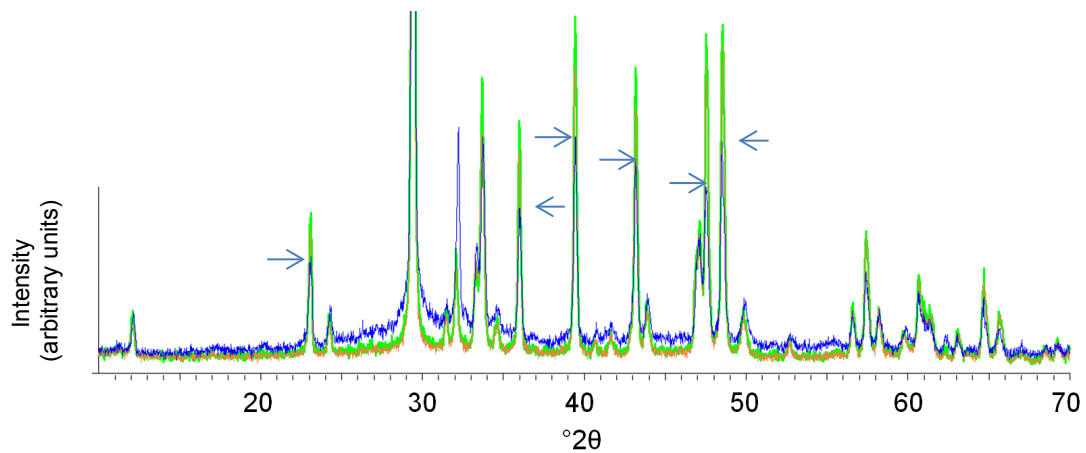


Figure 34 Flow-through experiments FLS 8 (blue), FLS 11 (orange) and FLS 15 (green) with GG water. Experiment FLS 8 which has higher background intensities was stopped after short time (see text). Notice the higher amorphous hump in the diffractogram from FLS8, alongside with lower intensity of calcite reflections (highlighted by arrows), compared to the two longer experiments.

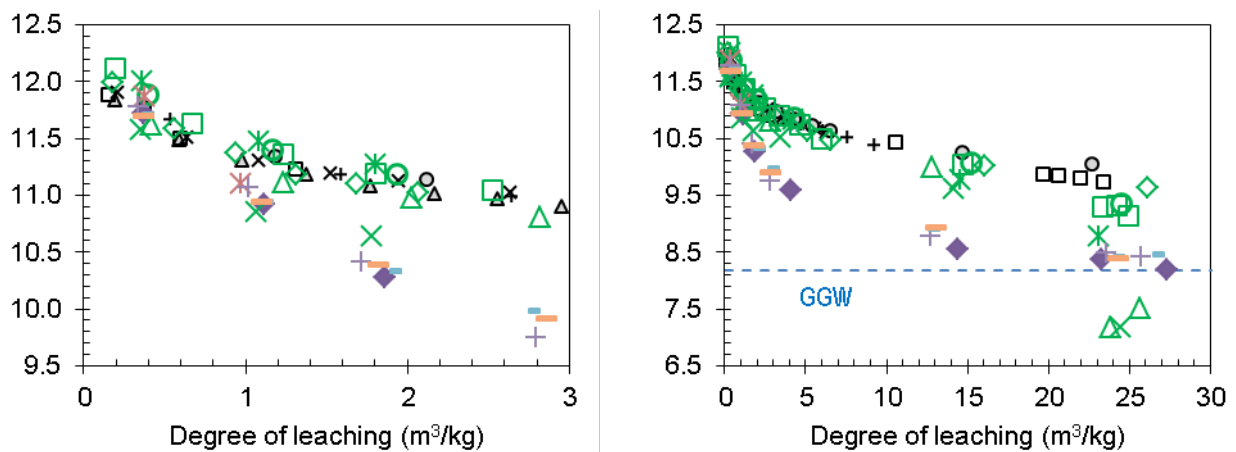
During experiments with CO₂-‘free’ DI water in N₂ atmosphere no secondary precipitates are found in degraded Sulfadur HCP. This observation equals the observations made with Holcim-1 HCP. In contrast, we observed precipitation inside the reactor after HCP degradation in DI water equilibrated in ambient air. X-ray powder diffraction identified small amounts of precipitated calcite in the HCP. Identification of calcite was difficult as the intensity of reflections is low and the main reflection at 29.4 °2-θ from {104} layers unfortunately overlaps with a typical reflection from C-S-H (FLS 10 in Figure 33). Still, comparing the diffractogram with the one from degraded Sulfadur HCP in degassed DI water (FLS 1) shows that in this case the small calcite reflection at ~23 °2-θ is absent and the reflection at 29.4 °2-θ is weaker and broader. Both support the identification of calcite in FLS 10. The calcite may either stem from initially present calcite in sane Sulfadur HCP, or it may precipitate during the experiment.

For experiments in GG water the diffractogram of the final residue shows that after the short run (FLS 8, 0.98 m³/kg degree of leaching) already a significant amount of calcite precipitates. Consequently, dissolving portlandite is the main source of Ca from the solid during very first stages of flow-through experiments. As the diffractograms of samples from experiments FLS 8, 11 and 15 were recorded at identical conditions we are able to directly compare calcite reflection intensities. Comparability is corroborated by equal intensities of reflections from persistent aluminoferrite which barely reacts in experiments. After longer runs with GG water (FLS 11 and 15, around 25 m³/kg degree of leaching) the amount of calcite further increases, illustrated by higher intensities in diffractograms (Figure 34). As described above, Portlandite has already been depleted and C-S-H dissolution continues at higher degree

of leaching. Consequently; dissolution of C-S-H phases becomes the main Ca source for calcite precipitation in GG water after disappearance of portlandite until the end of experiments when HCP is severely degraded.

6.2.3.2 Evolution of Outflow Solution pH

Varying concentration of aqueous $\text{CO}_2(\text{aq})$ in flow-through experiments performed with DI water shows that slight differences already affect pH of outflow solutions. As explained in chapter 4.2.2 we performed two experiments with degassed DI water where the setup was not installed in a glove box. In this case we minimised $\text{CO}_2(\text{g})$ ingress from ambient air by bubbling N_2 gas through the container of input solution and through the sample collection tubes of outflow solution. Under such conditions (experiments FLS 2 and FLS 3 in Figure 35) pH evolution is more acidic than in CO_2 -‘free’ conditions in the glove box (FLS 1 and all FL experiments). From 10 to 15 m^3/kg degree of leaching onwards pH evolution starts to deviate to slightly lower values. At the end of experiments at around 25 m^3/kg degree of leaching, pH of the outflow solutions is about 0.3 pH units lower than in corresponding CO_2 -‘free’ experiments.



Symbols:

DI water	Holcim-1 HCP	\triangle FL4	\times FL5	\circ FL7	$+$ FL8 (I=0.1M)	\square FL9(I=0.1M)	
	Sulfadur HCP	\diamond FLS1					
Low $\text{CO}_2(\text{aq})$		\square FLS2	\circ FLS3				
Air-equilibrated		\times FLS4	\times FLS9	\triangle FLS10			
GG water		\diamond FLS5	\times FLS8	$+$ FLS11	$-$ FLS12	$-$ FLS13	\diamond FLS15

Figure 35 Evolution of pH versus degree of leaching in course of flow-through experiments. On the left hand side only results from the initial stages of reaction up to 3 m^3/kg are shown to highlight differences between the individual series. On the right hand side all data is shown. Symbols: grey - experiments with Holcim-1 HCP and CO_2 -‘free’ DI water, green - experiments with Sulfadur HCP and varying $\text{CO}_2(\text{aq})$ concentration in DI water, coloured - experiments with Sulfadur HCP and GG water. Errors correspond to or are smaller than symbols. The blue, stippled line gives pH of pure GG water as a reference.

When aqueous $\text{CO}_2(\text{aq})$ concentration of DI water was further increased by equilibration with ambient air (experiments FLS 4, FLS 9 and FLS 10) pH values drop significantly at the end of

experiments. Here, HCP is no longer capable to buffer the input solution efficiently in the alkaline milieu so that pH drops by more than 2 units to almost neutral pH (Figure 35).

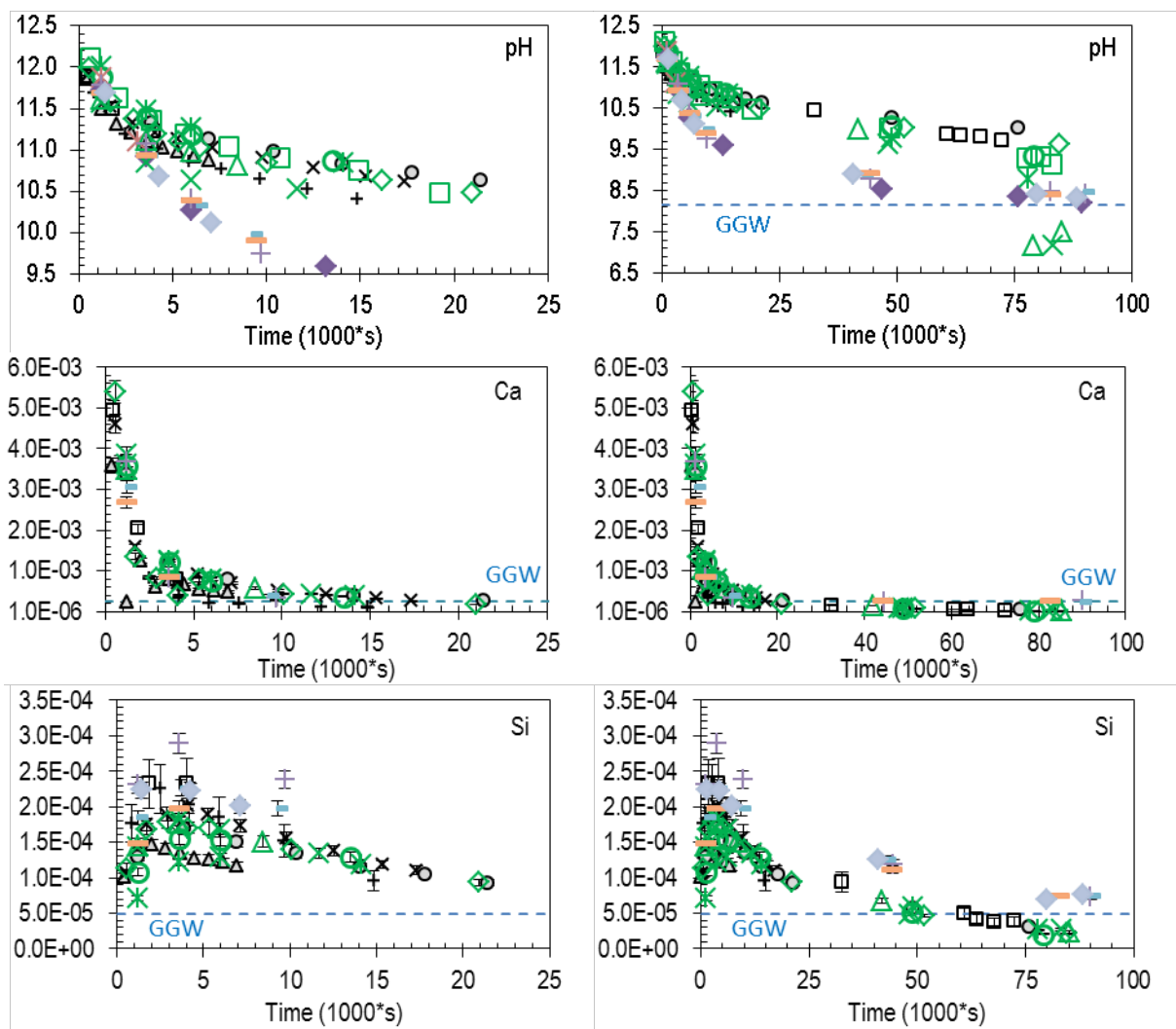
From all solutions GG water has the highest aqueous $\text{CO}_2(\text{aq})$ concentration, mainly as hydrogen carbonate. It contains about two orders of magnitude higher aqueous $\text{CO}_2(\text{aq})$ concentrations than DI water in equilibrium with ambient air. In experiments with GG water significant decrease of pH starts already at early degradation stages. This deviation increases with ongoing degradation, but is limited by pH of the input solution. At the end of experiments pH of outflow solution is about pH 8.4, only slightly higher than the one of GG water stock-solution.

6.2.3.3 Evolution of Outflow Solution Ca and Si Concentrations

In contrast to pH of outflow solutions neither Ca nor Si concentrations are affected by varied $\text{CO}_2(\text{aq})$ concentrations of DI water (Figure 36).

With GG water highest Ca concentrations in outflow are measured initially, as with all other types of studied solutions. Concentrations also decrease rapidly, but when using GG water Ca concentrations in outflow solutions are slightly lower than in DI water at the beginning of experiments, despite the additional Ca load. Then Ca concentration in outflow approaches input concentration which it equals at the latest when half of the GG water has passed the HCP. This shows ceasing Ca mobilisation with time in experiments with GG water (Figure 36) while in DI water Ca mobilisation continues at a low level (chapter 6.2.2.3).

In contrast to Ca, measured Si concentrations are higher than in DI water. However, after subtraction of the Si fraction from GG water, no measurable net increase of Si occurs, neither while portlandite is dissolving, nor after depletion of portlandite. At the end of experiments Si concentrations in outflow solutions attain an apparent steady state. Here, subtracting the Si concentration of GG water, only $2.4(\pm 0.3) \cdot 10^{-5}$ mol/l Si are mobilised from HCP compared to $3.1(\pm 0.2) \cdot 10^{-5}$ mol/l in DI water. Hence, mobilisation of Si is slightly weaker under the influence of GG water at the final stage of experiments.



Symbols:

DI water	Holcim-1 HCP	CO ₂ -'free'	△ FL4	× FL5	○ FL7	+ FL8 (I=0.1M)	□ FL9 (I=0.1M)			
	Sulfadur HCP	Low CO ₂ (aq)	◇ FLS1	□ FLS2	○ FLS3					
GG water		Air-equilibrated	* FLS4	× FLS9	△ FLS10	◇ FLS5	* FLS8	+ FLS11	- FLS12	- FLS13

Figure 36 Evolution of pH, Si and Ca concentrations in outflow solutions with time. Measured concentrations are all given in mol/l. Black symbols: Experiments with Holcim-1 HCP in DI water. Green symbols: experiments with Sulfadur HCP in DI water, coloured symbols: experiments with Sulfadur HCP in GG water. Concentrations in GG water input solution are indicated by blue, stippled lines. Where helpful, results are split into two graphs, from 0 to 25·10³ s in the left column and the full experimental length in the right column.

With DI water of varying CO₂(aq) content the evolution of Ca/Si ratios in the outflow solution is exactly as in experiments under CO₂-'free' conditions, i.e. with increasing degradation the ratio approaches unity. In contrast, the evolution of Ca/Si ratio evolves differently if GG water is used to degrade the HCP. GG water contains Ca and Si in a molar ratio of 5 : 1 which influences the Ca/Si ratio in experiments. Initially, when portlandite dissolution provides high Ca concentrations evolution of the Ca/Si ratio is similar to experiments with DI water (Figure 37), but when portlandite diminishes the Ca/Si

ratio in GG water decreases faster than in DI water experiments. However, the Ca/Si ratio rises again with increasing degradation and finally reaches a ratio of 3.5.

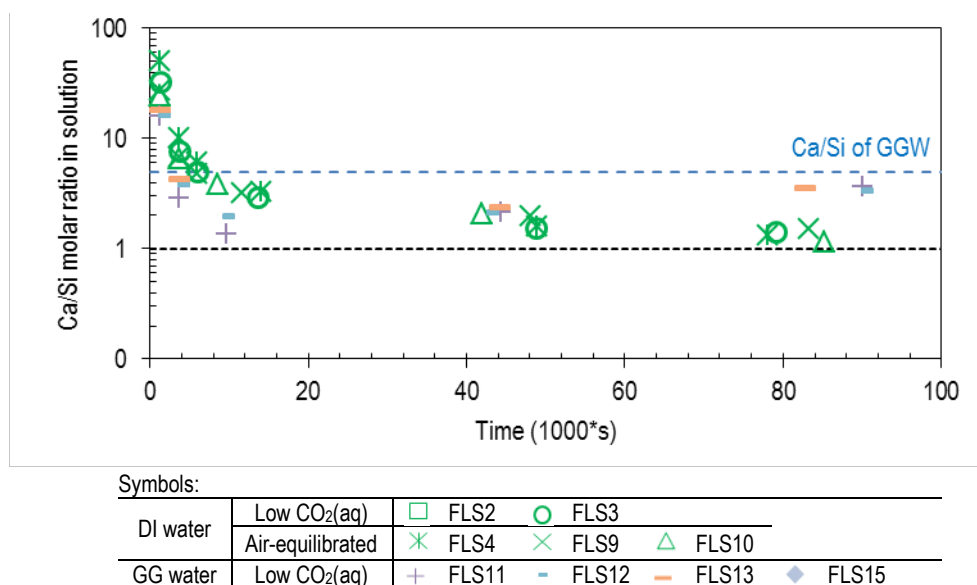


Figure 37 Ratio between measured Ca and Si concentrations in outflow solutions of flow-through experiments with DI water of varying CO₂(aq) content and GG water. The black line indicates Ca/Si ratio of unity.

6.2.3.4 Mass balances of Calcium and Silicate

Mass balances of the Ca and Si inventory of HCP before and after experiments show the effect of the solution type. While DI water mobilises almost 80 % of total Ca inventory (Table 19), GG water mobilises only about 34 % from HCP (Table 20) after comparable degree of leaching. Silicate depletion in both types of solutions is similar or slightly fostered by GG water, attaining 72 % removal compared to 65 % in DI water.

Table 20 Cumulated loss of Ca and Si mobilised from Sulfadur HCP during degradation experiments with GG water and varying CO₂(aq) content in DI water, referred to the same HCP. 'Air equilibrated' is abbreviated 'air eq.'.

Experiment	FLS1	FLS3	FLS4	FLS9	FLS10	FLS11	FLS12	FLS13	FLS15
Solution	DIW	DIW	DIW	DIW	DIW	GG water	GG water	GG water	GG water
CO ₂ (aq) content	'free'	Low	air eq.	air eq.	air eq.	very high	very high	very high	very high
Degree of leaching (m ³ /kg)	27.2	24.8	23.5	25.4	26.0	26.1	26.9	26.1	26.2
Total loss of Ca (at.-%)	69	78	77	78	85	33	35	34	
Total loss of Si (at.-%)	66	65	62	61	71	73	72		71

6.2.4 Colloid Generation During Experiments

Colloid stability is inversely related to ionic strength and colloidal metastability is enhanced at low ionic strength values (Wieland, Tits et al. 2004). The composition of colloids generated in HCP/mortar

systems is similar to that of C-S-H phases (Wieland, Tits et al. 2004). Influence of possibly generated colloids on measured Ca and Si concentrations in outflow has to be controlled, due to very low ionic strength of DI water and the applied filter size (0.2 μm). At this filter size colloids may not have been entirely retained. To exclude influence of colloids selected aliquots were filtered with factor 10 smaller filters (0.02 μm), giving identical Ca and Si concentrations.

Moreover, between experiments with CO_2 -free DI water and those with 0.1 mol/l NaClO_4 solution Ca concentrations do not differ. In contrast, the Si concentration in outflow is influenced by the 0.1 mol/l NaClO_4 solution (described in chapter 6.2.2.4). We observe higher Si concentration with higher ionic strength. However, in the event of colloid formation the effect would be the opposite. Due to these observations we conclude that potential bias induced by colloid formation is negligible under the studied experimental conditions.

6.2.5 Degradation of Minor Hardened Cement Paste Phases

6.2.5.1 Behaviour of Minor Cement Phases

For both sane HCPs XRD and TGA analyses only identify calcium carbonate / crystalline calcite and clinker minerals (calcium-silicates and aluminoferrite) as minor phases. The only observed secondary phase which forms during flow-through experiments is calcite (as described in chapter 6.2.3.1). Under no experimental conditions formation of Al, S(VI) or Mg bearing phases in the degraded solid is confirmed by direct methods after flow-through experiments. Consequently, we were first not able to directly follow dissolution of amorphous minor phases such as AFm and AFt, which commonly control S(VI), Al and Mg in cementitious systems. Second, we also did not observe formation of minor secondary phases incorporating Al, S(VI) or Mg during flow-through experiments.

Calcite is present in very low concentration in sane Sulfadur HCP and it is not encountered after experiment FLS1 (CO_2 -free) by XRD. In sane Holcim-1 HCP calcite is abundant and also after flow-through experiments under CO_2 -free conditions it is present after experiments (Figure 26 in chapter 6.2.2.1). Carbonates are naturally expected to dissolve under CO_2 -free conditions. Two explanations for persistence are therefore possible: kinetic limitation of complete dissolution and physical protection from solution contact, probably by surrounding solid material. However, unfortunately it is also quite possible that it formed during storage posterior to experiments. The analysed samples from flow-through experiments with Holcim-1 HCP were kept in closed plastic vials, but were stored for one year in air before XRD analysis.

Regarding the behaviour of clinker minerals evidence was found from XRD and SEM analyses. In the case of calcium-silicates reflections in XRD diffractograms disappear in all experiments with one exception. In the very short experiment FL4 there is still a small fraction of dicalcium silicate present, in contrast to longer experiment FL7 which is highlighted in Figure 26.

Consequently, the small fraction of calcium-silicate clinker minerals, present in sane Sulfadur HCP, hydrates during flow-through experiments.

In the case of clinker mineral aluminoferrite behaviour during experiments is different to calcium silicates. Like in batch experiments, the honeycomb-like aluminoferrite structure remains stable and does not show microscopic signs of dissolution/hydration or reaction-rims after flow-through experiments. In Figure 38 a SEM image of aluminoferrite is shown which has similar morphology to aluminoferrite encountered after batch experiments (Figure 20).

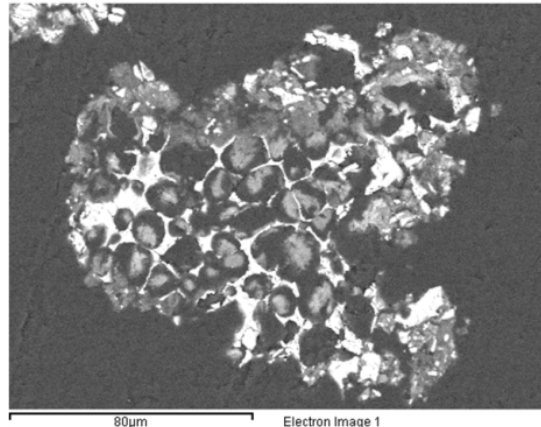


Figure 38 SEM backscattered electron image of epoxy embedded and polished HCP grain after a flow-through experiment using DI water equilibrated in ambient air. Aluminoferrite's honeycomb structure (bright in image) is maintained while C-S-H, formerly filling the voids, is partly dissolved.

In contrast to batch experiments, epoxy-filled 'holes' in the aluminoferrite structures indicate that in this case, formerly enclosed phases, mainly C-S-H, widely dissolve in flow-through experiments. After batch experiments these spaces are still completely filled by solid phases, as depicted in Figure 20. Enhanced mobilisation of C-S-H during flow-through experiments from these holes proves that aluminoferrite comes in contact with solution during experiments. These observations from SEM analyses are in line with findings from XRD diffractograms which also proof severe degradation of the cement in flow-through experiments while aluminoferrite, unexpectedly, appears to be largely resistant to dissolution/hydration (Figure 33).

6.2.5.2 Evolution of Outflow Ion Concentrations in Deionised Water

As it has been previously discussed, the aluminium-oxide filters contaminated the filtrate of the experiment using Sulfadur HCP in CO₂-'free' DI water with Al (chapter 4.4.2.). In contrast to Ca and Si the mobility of Al and S(VI) is not controlled by the content of aqueous CO₂(aq) in input solution. In the following we therefore consider the experimental series with Sulfadur HCP and varying CO₂(aq) content where nylon filters were used to compare results of both cement types.

Values of measured Al concentrations in outflow solutions are double and initially three times higher from Holcim-1 HCP compared to those from Sulfadur HCP. Since the latter was dried more gently (as explained in chapter 6.2.5) we suppose that intact crystal structure was maintained, thus dissolution behaviour of minor hydrate phases was not affected. In all experiments with Sulfadur HCP the highest Al concentrations, up to $\sim 6 \cdot 10^{-6}$ mol/l, are measured at low degree of leaching. Values decrease slightly to $\sim 3 \cdot 10^{-6}$ mol/l at the end of experiments. Aluminium concentrations in experiments with varying carbonate content are almost identical (Figure 39), indicating that the dissolving and Al liberating phase(s) is not significantly affected by carbonation

In the case of S(VI), outflow concentrations are only slightly higher in experiments with Holcim-1 HCP and moreover, concentrations converge with increasing progress of dissolution. This shows that the drying procedure affected both, Al and S(VI) which often appear together in cement phases. However, the effect on mobility of Al is stronger compared to S(VI).

Mg concentrations in outflow DI water are low. In experiment FLS4 we measured concentrations exemplarily which always remain below detection limits. Depending on the sample dilution detection limits were $2.5 \cdot 10^{-5}$ mol/l during the initial degradation stage and even below $4.1 \cdot 10^{-6}$ mol/l during the last third of the experiment.

Aqueous Fe concentration was measured in the first and in the last samples of experiment FL 5 by UV-VIS using the ferrozine method. The measured concentrations were below the detection limit of $3 \cdot 10^{-7}$ mol/l, indicating the immobility of Fe under these conditions.

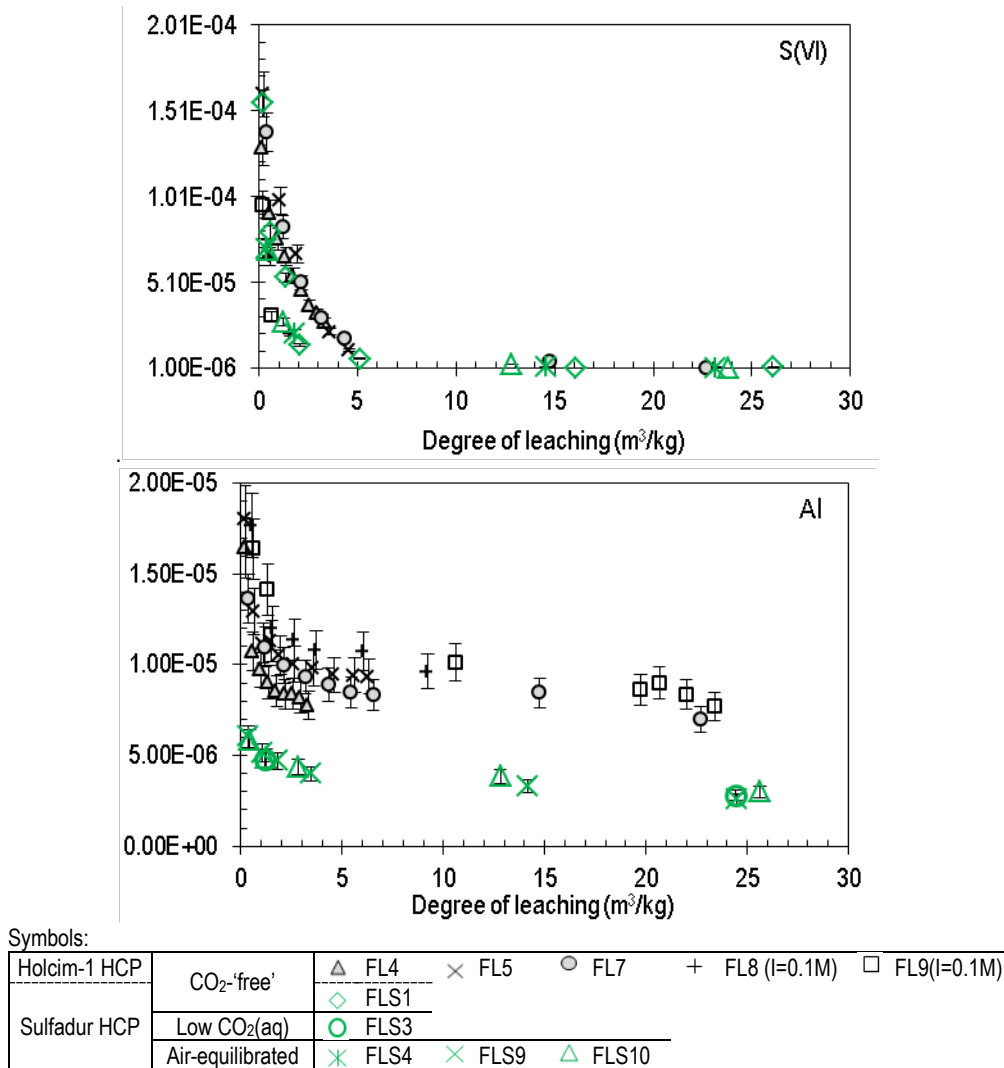
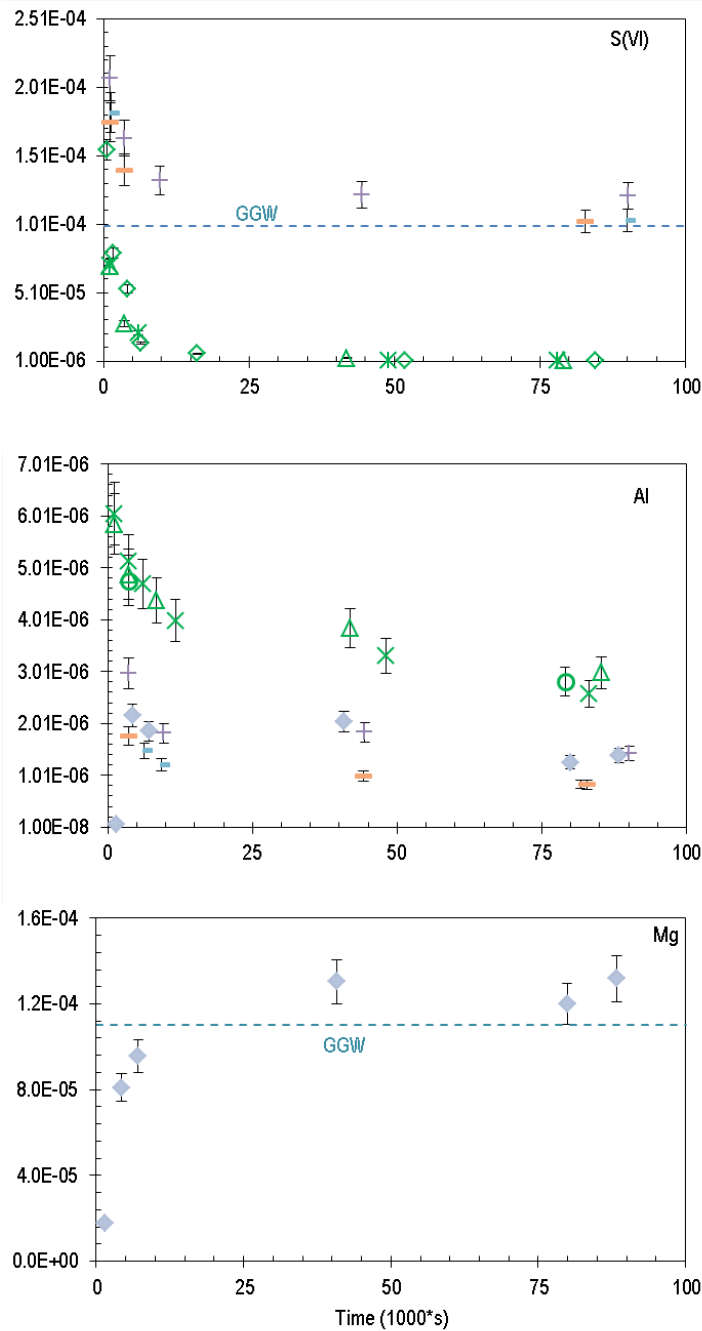


Figure 39 Evolution of S(VI) and Al concentrations in outflow solutions with time. Measured concentrations are all given in mol/l. Black symbols: Experiments with Holcim-1 HCP in CO₂-free' DI water. Green symbols: experiments with Sulfadur HCP in DI water with varying CO₂ content.

6.2.5.3 Evolution of Outflow Ion Concentrations in Granitic Groundwater

The behaviour of Al is significantly altered by using GG instead of DI water. At the beginning of experiments with GG water Al concentrations in outflow solutions are below detection limit except for experiment FLS 15 where Al concentration reaches $5.9 \cdot 10^{-8}$ mol/l (Figure 40), almost equal to the detection limit. In continuation Al concentrations rise abruptly to their maximum values around $(2 - 3) \cdot 10^{-6}$ mol/l which is when pH approximates 11. Towards the end of experiments Al concentrations slightly decrease and finally attain values of $(1.1 \pm 0.3) \cdot 10^{-6}$ mol/l which is the mean from all experiments with GG water above $75 \cdot 10^3$ s ($23 \text{ m}^3/\text{kg}$ degree of leaching). Compared to DI water, all measured Al concentrations in outflow are significantly lower in GG water.



Symbols:

DI water	CO ₂ -free	◇ FLS1				
	Low CO ₂ (aq)	○ FLS3				
GG water	Air-equilibrated	✱ FLS4	✱ FLS9	△ FLS10		
		✱ FLS11	✱ FLS12	✱ FLS13	◆ FLS15	

Figure 40 Evolution with time of Al, S(VI) and Mg concentrations in outflow solutions. Measured concentrations are given in mol/l. Green symbols: experiments with Sulfadur HCP and DI water. Coloured symbols: experiments with Sulfadur HCP and GG water. Base load concentrations in GG water input solution are indicated by blue, stippled lines.

In the case of S(VI) outflow concentrations are significantly higher in GG water compared to DI water. With around $2.1 \cdot 10^{-4}$ mol/l they are highest in the initial outflow in experiments with GG water. Then S(VI) concentrations decrease fast until they equal the concentration of the input GG water.

Approximately all mobilised sulphate from Sulfadur HCP adds to the S(VI) load of the input solution, shifting the evolution of sulphate concentrations on the ordinate towards higher concentrations if compared with DI water experiments (Figure 40). Consequently, there is no effect of GG water on sulphate retention or mobilisation. The high hydrogen carbonate content of GG water does not affect sulphate evolution, as experiments with DI water of varying CO₂(aq) content.

For Mg concentrations we analysed the outflow solutions from FLS15, an experiment with GG water. Mg from the input solution is initially retained in the reactor, but retention ceases when pH reaches values below 10. Then, at lower pH, Mg partitioning is inverted, i.e. it is removed at constant rate from the solid (Figure 40).

6.2.5.4 Mass Balances of Aluminium and Sulphate

The total amount of Al and S(VI) mobilised during HCP degradation is calculated from measured elemental concentrations and related to the initial inventory, giving the relative loss of elements from HCP (Table 21). In the case of Al depletion from HCP is stronger with DI water than with GG water. Mass balances show that GG water reduces the depletion of Al inventory from ~23 % to ~9 %.

In the case of sulphate the whole inventories of both HCP types are mobilised by DI water, independent of its CO₂(aq) content. Only in experiments FL4 and FL5 fractions of S(VI) inventory remain in HCP, due to the short length of these experiments. Also with GG water there is no net conservation of the HCP's S(VI) inventory in the reactor at the end of experiments (Table 21). Note that in the case of S(VI) mobilisation in experiments with GG water two experiments indicate unreasonably high mobilisation from the inventory. However, this overshoot may be due to the high content in GG water which is much more important than the inventory of the cement. Calculated mass balance takes the measured S(VI) concentration in GG water into account. Measured concentrations of GG water in these two experiments are $1.0(\pm 0.1) \cdot 10^{-4}$ mol/l in both cases. If we assume the concentration was a bit higher, around $1.4 \cdot 10^{-4}$ mol/l, the mass balance in both cases would indicate 100 at.-% mobilisation of S(VI) from the HCP. Therefore, mass balance of S(VI) in GG water systems should not be stressed.

Table 21 Cumulated loss of Al and S(VI) mobilised from Holcim-1 HCP during degradation experiments, referred to the same HCP. For mass balances of S(VI) in GG water systems see explanation in the main text.

Experiment Solution CO ₂ (aq) content	FL4	FL5	FL8	FL7	FL9	DI water			GG water			FLS15		
	'free'					low		air equilibrated			very high			
Degree of leaching (m ³ /kg)	3.6	6.5	10.2	23.2	24.1	27.2	24.8	23.5	25.4	26.0	26.1	26.9	26.1	26.2
Total loss of Al (at.-%)	6	11	18	34	38	*	*	*	21	24	11	8	6	12
Total loss of S(VI) (at.-%)	57	78	n.m.	98	n.m.	165	n.m.	124	n.m.	121	97	830	763	n.m.

* measurements contaminated with Al

n.m. not measured

6.3 Modelling of Chemical HCP Degradation

6.3.1 Starting Point

We have used the analytical results from the phase analyses (chapter 5.2, Table 15) and the measured elemental inventory of the cement clinker (chapter 5.1, Table 14) as constraints to derive the mineralogical composition of Sulfadur HCP for modelling (Table 22).

Table 22 Composition of sane Sulfadur HCP used for modelling.

Phase	Composition	Abundance wt.-%
Calcite	CaCO ₃	1.00
Ettringite	Ca ₆ Al ₂ (SO ₄) ₃ (OH) ₁₂ ·26H ₂ O	3.34
Gypsum	CaSO ₄ ·2H ₂ O	1.00
Hydrotalcite	Mg ₄ Al ₂ (OH) ₁₄ ·3H ₂ O	1.00
Potassium hydroxide	KOH	0.37
Sodium hydroxide	NaOH	0.04
Portlandite	Ca(OH) ₂	21.80
C-S-H1.5	(CaO) ₃ (SiO ₂) ₂ (H ₂ O) ₅	58.00
Aluminoferrite	Ca ₂ Fe _{1.35} Al _{0.65} O ₅	13.45

Analytical results of fresh and degraded HCP show that a considerable amount of aluminoferrite does not react. Moreover, analysis of unreacted Sulfadur HCP does not reveal pure sulphate phases (chapter 5.2). However, we assume that S(VI) is incorporated in mineral phases which became X-ray amorphous upon grinding. To derive a mineralogical composition for modelling additional considerations and assumptions are necessary. In a modelling attempt we introduced clinker in form of its oxides (Table 14) and equilibrated it with pure water at w/c ratio of 0.4 l/kg, as used in experiments. However, we reduced the content of Al₂O₃ and Fe₂O₃ in the clinker compared to the measured composition (see explanations later in this chapter). The resulting hydrate composition comprises C-S-H1.5 (T2Cmod), portlandite, ettringite, hydrotalcite, hematite and calcite. We derived the model composition of HCP from this phase assemblage, quantitatively measured mineral content as well as oxide composition, maintaining minimal mass balance deviations between modelled and measured chemical compositions.

Portlandite and calcite proportions in the solid phase assembly are based on TGA measurements of Sulfadur HCP. In accordance with measured Ca and Si inventories we assigned an average C-S-H content from literature (Table 3). C-S-H was included in the hydrated cement as C-S-H1.5 (T2C) only. This end-member has the highest C/S ratio and is representative for sane HCP.

In all batch experiments crystalline ettringite is the first sulphate phase that forms (chapter 6.1.1), corroborating ettringite formation from oxides in the model. Therefore, we included ettringite in the model assemblage of Sulfadur HCP. A small amount of gypsum is further added to the initial phase assembly to account for the missing S(VI) in mass balance.

Similar to sulphate, no pure Mg bearing phase is identified in sane HCP. Diffractograms of degraded HCP after batch experiments in most cases indicate presence of Mg bearing AFm phase

hydrotalcite. This also corroborates hydrotalcite formation from oxides in the model. Hydrotalcite is known to be often poorly crystalline and hence can be easily overlooked or confounded in XRD patterns. Since we did not find hydrotalcite in unreacted HCP and observed low degree of carbonation, a small amount (1 wt.-%) is introduced in the model which would not be recognisable by XRD. Likewise, only a small amount of calcite was assigned. In our model we use hydrotalcite as the only Mg source among solid phases.

Iron concentrations were measured in selected samples and are very low, under the detection limit of $3 \cdot 10^{-7}$ mol/l. Fe concentrations were therefore not systematically measured in experiments. Al end-members of solid-solutions in HCP are more frequent than Fe end-members. The ratio of Al^{3+}/Fe^{3+} in hydrated phases is higher than in non-hydrated aluminoferrite which is the major Al and Fe mineral in cement clinker. This is due to higher mobility of Al^{3+} compared to Fe^{3+} which is bound by different (amorphous) Fe-oxyhydroxide phases (Hewlett 2004). Therefore, we do not expect any significant perturbation of modelling results due to omission of Fe. Moreover, experimental validation of modelling results on Fe is not possible, since concentrations were below detection limit. Redox potential in the model is controlled by oxygen from the air.

Cemdata07 database does not include Na and K in any solid phase. As alkali metals from HCP are not solubility limited and dissolve almost entirely in contact with water, we include them as completely dissolving hydroxides achieved by giving them high solubility constants.

The elemental inventory used for modelling widely agrees with the measured elemental inventory of Sulfadur HCP (Table 23). Only Mg inventories deviate significantly.

Table 23 Compliance of modelled with measured elemental inventories of sane Sulfadur HCP.

Compliance in at.-%							
Al	Ca	Fe	K	Mg	Na	S	Si
107	95	104	99	20	103	96	111

In the case of Mg all measurements are below detection limit in batch experiments, as well as in flow-through experiments with DI water. Only in one experiment with GG water outflow concentrations are quantified. Therefore, we made no efforts to optimise compliance of Mg inventories.

Achieving 100 % match of all element inventories between modelled and measured composition would require taking into consideration all possible solid-solutions and phase impurities occurring in HCP. However, in this study we focus on the evolution of major phases and neglect phase impurities as well as solid-solutions other than C-S-H, e.g., C-A-S-H phases, alkali uptake by C-S-H and a variety of carbonate-sulphate / hydroxide or Fe-Al solid-solutions

We set up our model including all phases listed in Cemdata07 database allowing them to precipitate, except for C-S-H phases which are replaced by the CSH3T model and hydrogarnet. The latter is excluded as its stability is known to be largely overestimated by this database while in HCP of CEM I type it is rarely encountered at 25 °C (Lothenbach, Pelletier-Chaignat et al. 2012).

Experimental results show that a fraction of aluminoferrite persists during curing and – unexpectedly - even during degradation of HCP. The mechanisms responsible for this persistence are out of the scope of this study. The quantity of aluminoferrite in the hydrate assemblage is the remainder to 100 wt.-% after summation of the other phases. It is very unlikely that aluminoferrite is entirely inert in contact with aqueous solution. Since we could not quantify the amount of aluminoferrite that reacts during experiments, in a very simplifying approach we arbitrarily assume that only one fifth of aluminoferrite is soluble in our model, i.e. this fraction is introduced in soluble form in the model.

6.3.2 Batch Degradation Model

6.3.2.1 Solid Phases

Modelling of batch experiments using the thermodynamic equilibrium approach (chapter 4.2.4) reproduces the observed solid phase evolution during Sulfadur HCP degradation in the experiments. Results are given for HCP degradation in DI and GG water (Figure 41). Corresponding input files can be found in annex 10.2.

At low L/S ratio of 0.1 m³/kg portlandite is still controlling pH in DI as well as GG water (Figure 41). However, at this stage portlandite is already considerably dissolved in both solutions which is in accordance with experimental results (Figure 19). Beyond this L/S ratio the remaining absolute quantities of portlandite decrease rapidly. Modelling results therewith show that small variations of either sample homogeneity (portlandite content) or of solution volume would strongly affect the absolute amount of remaining portlandite.

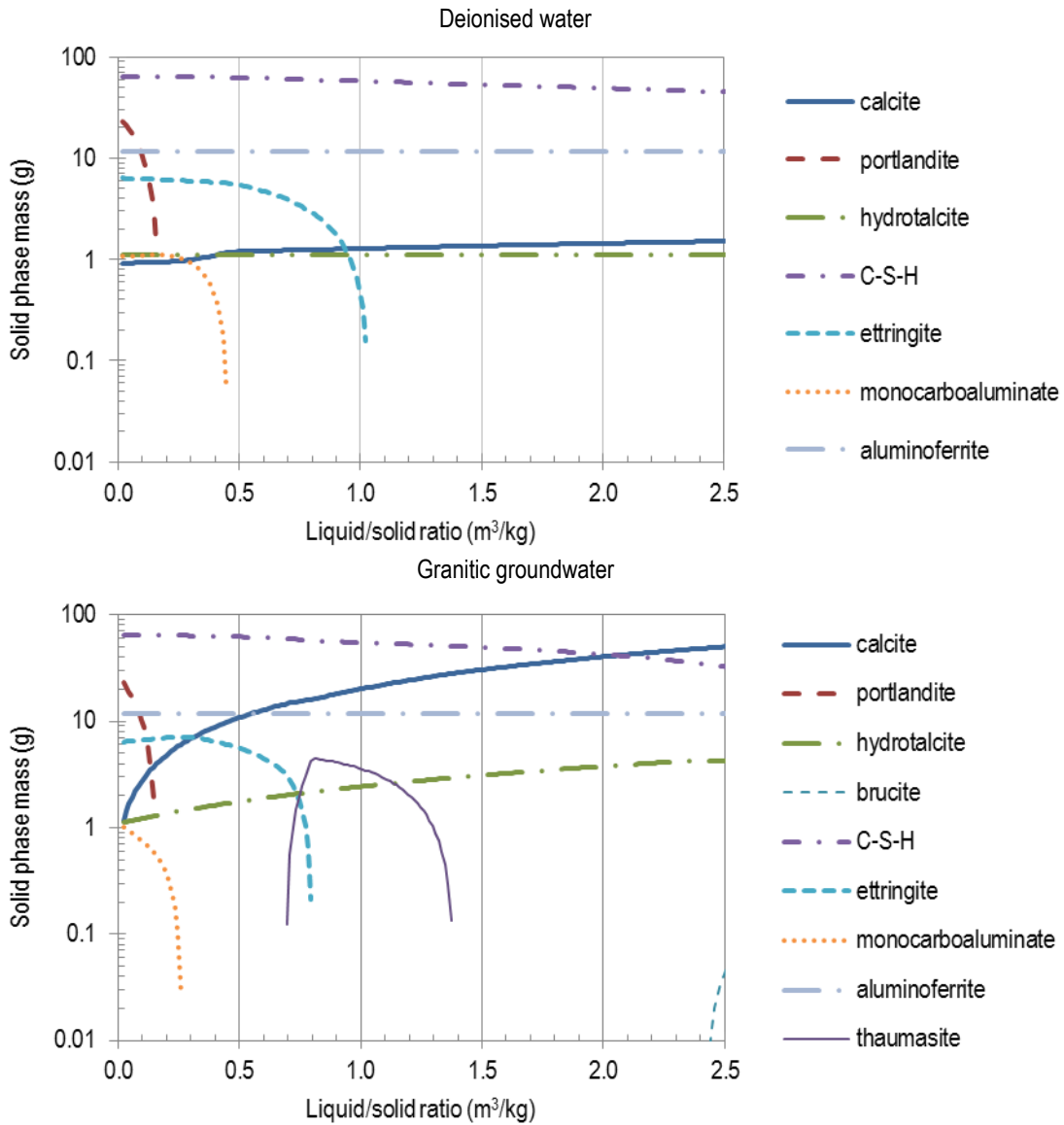


Figure 41 Computed evolution of solid phases as a function of added DI (top figure) and GG water (bottom figure) volumes, expressed as L/S ratio.

C-S-H is stable at low L/S ratio and the solution type does not show any influence on it as long as portlandite is buffering the system. According to modelling the C/S ratio corresponds to the high C/S end-member (C-S-H1.5) of the CSH3T model in both solution types at low L/S ratio (Figure 42). Once portlandite is dissolved, C-S-H dissolution depends on solution type. At the same L/S ratio in GG water more C-S-H dissolves compared to DI water. According to the model, at 2 m³/kg L/S ratio only 63 wt.-% of initially present C-S-H remain in GG water, while still 76 wt.-% remain in DI water. Corresponding C/S ratios are 1.14 and 1.02 in DI and GG water, respectively.

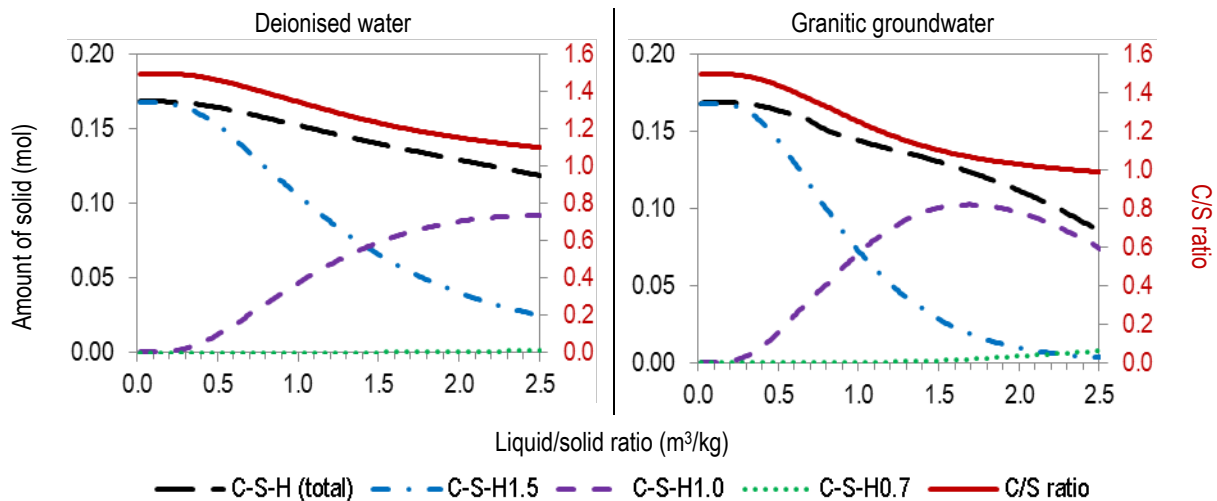


Figure 42 Computed evolution of C-S-H amount and composition as function of added solution in batch experiments, expressed as L/S ratio. Figures show the influence of the solution that is used by comparing DI water (left) with GG water (right).

A small amount calcite precipitates in the HCP reacting with DI water in the range of 0.1 m³/kg L/S ratio and also in the more severely degraded stage initial calcite content (1 wt.-%) not even doubles. In contrast, calcite content doubles in GG water already at 0.1 m³/kg and at 2 m³/kg even increases by factor 34 compared to DI water. Consequently, carbonation withdrawing Ca from solution fosters dissolution of C-S-H in GG water at equilibrium conditions.

According to model results hydrotalcite is stable under all tested conditions. In DI water almost no precipitation or dissolution is predicted, while in GG water it continuously precipitates from low to high L/S ratio (Figure 41). Hydrotalcite thereby controls Mg concentration in solution at low levels (10⁻⁸ - 10⁻⁷ mol/l) until brucite becomes oversaturated (see later in this chapter).

We were not able to distinguish between present hydrotalcite and monocarboaluminate from diffractograms. Model calculations suggest the presence of both phases at low L/S ratios, but monocarboaluminate – which has formed in the initial equilibration step from aluminoferrite and gypsum - dissolves relatively fast. Moreover, in GG water ettringite is more stable and precipitates the released Al so that monocarboaluminate is exhausted earlier than in DI water (Figure 41). In both solutions dissolution of monocarboaluminate is succeeded by dissolution of ettringite. In GG water the model additionally predicts formation of thaumasite, destabilising ettringite. Ettringite dissolution is therefore completed at lower L/S ratio in GG water compared to DI water. The model predicts precipitation of thaumasite at around 0.7 m³/kg L/S ratio and dissolution at about 1.3 m³/kg. This range is bracketed by our experimental study investigating 0.1 and 2 m³/kg L/S ratios, but no samples were prepared at these specific points. Therefore, intermediate occurrence of thaumasite in GG water is not experimentally confirmed or excluded. However, formation of thaumasite is rather rare in CEM I due to relatively low SO₃/Al₂O₃ ratio and favoured formation at lower temperature, around 8 °C (Schmidt, Lothenbach et al.

2008). Deactivating thaumasite in the model does not influence the solid and solution compositions at experimentally investigated L/S ratios.

Since GG water contains additional Cl⁻ the possible formation of Friedel's salt (not contained in the Cemdata07 database) in equilibrated systems is investigated thermodynamically, even though not observed by XRD or SEM. Employing the solubility data from Blanc, Bourbon et al. (2010) Friedel's salt is strictly undersaturated ($SI < -4$) in all systems.

During degradation of Sulfadur HCP small amounts of brucite form in GG water experiments at both L/S ratios, while none is detected in DI water systems (chapter 6.1.1). In contrast, the model predicts brucite formation only above L/S ratio of 2.4 m³/kg. Mismatch between model and experiments is related to underestimated Mg inventory of HCP composition in the model (Table 23).

6.3.2.2 Solutions

Modelling of batch experiments using the thermodynamic equilibrium approach (chapter 4.2.4) reproduces the evolution of measured ion concentrations during Sulfadur HCP degradation in experiments. Model results are presented for HCP degradation in both, DI and GG water and can be compared in Figure 43. Corresponding input files are given in annex 10.2.

All in all, the main parameters pH, Ca and Si concentrations are satisfactorily reproduced by both models. Similar to experimental results, when L/S ratio rises the pH decreases more significantly in GG water compared to DI water while Si increases to a larger extent. This is due to fostered dissolution of C-S-H phase from HCP, as described in chapter 6.3.2.1.

Ca concentration at low L/S ratio is about 20 % higher in experiments than in calculations. Ionic strength may influence solubility of Ca concentration controlling portlandite. In both, experiments as well as in modelling ionic strength is below 0.1 mol/l at this stage. Therefore, we conclude that ionic strength does not cause any bias in this case. Instead, Portlandite solubility is possibly slightly increased due to traces of dissolved NaCl and KCl in experiments, an effect observed by Duchesne and Reardon (1995).

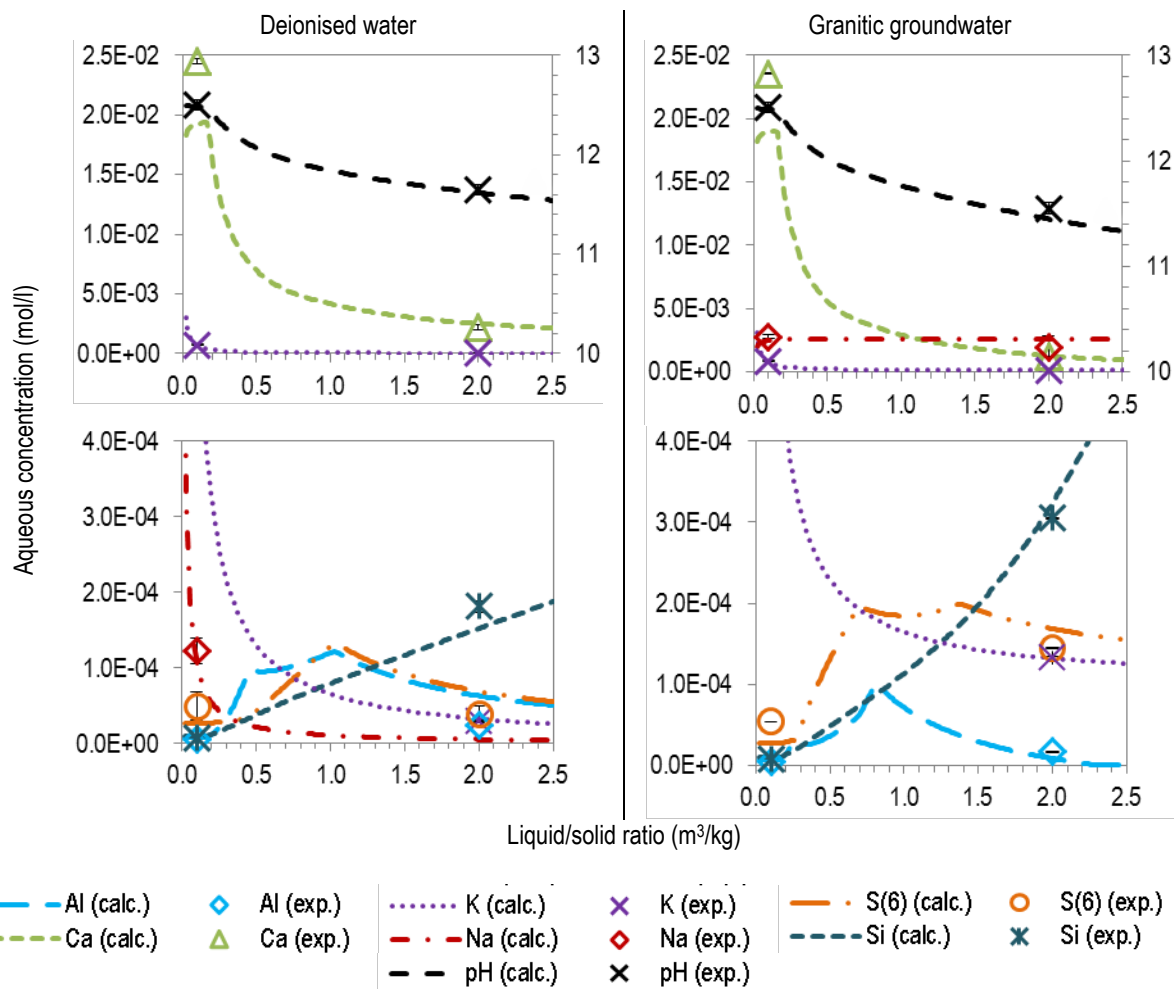


Figure 43 Comparison between computed (lines) and measured (points) ion concentrations and pH from batch experiments with DI water (left column) and GG water (right column), plotted as a function of L/S ratio. Due to large differences in concentrations and keep decimal scale the top figures give elements at higher concentrations while the bottom figures give elements at lower concentrations.

Sulphate concentrations are similar in both solutions at low L/S ratio, but increase significantly with increasing L/S ratio in GG water while in DI water concentrations remain similar. This evolution is alike in experiments and in the models of both systems (Figure 43). According to modelling results ettringite is the S(VI) concentration controlling phase in both solutions at low L/S ratio (Figure 41) and added sulphate from GG water precipitates prominently as ettringite. However, in our model no sulphate retaining phase is stable above 1 and 1.3 m³/kg in DI and GG water, respectively. This matches with analytically identified phases in degraded HCP at both L/S ratios and explains higher S(VI) concentrations with GG water.

The largest deviation between modelling and experimental results arises in the case of Al. Computed concentration is over-predicted by factor 2.7 at high L/S ratio in DI water. At all other experimental conditions and for all elements deviation between calculations and experimental results is lower, from 0.5 to 1.7 (Figure 43). Similar to S(VI), computed Al concentration changes significantly in between experimentally investigated L/S ratios. According to the model this is due to subsequent

dissolution of monocarboaluminate and ettringite. However, at the experimentally investigated L/S ratios Al concentrations are similar at both L/S ratios.

The calculated Na and K concentrations in DI water are only controlled by the solution volume, i.e. they get diluted with increasing L/S ratio. Evolution of K and Na is similar in DI and GG water, but alkali concentrations approach their concentrations in GG water. The modelled evolution reproduces the observed evolution of the alkali metals, but the Na evolution in DI water cannot be compared between model and experiment because it is below detection limit.

Calculating mass balances of HCP elemental inventories from modelling results at low L/S ratio gives similar loss of Ca in DI and GG water, 21 at.-% and 20 at.-%, respectively (Figure 44). This is in line with mass balances from measured Ca concentrations. However, the proportions are higher: 26 at.-% and 25 at.-% (in DI and GG water, respectively). The release of Ca is slightly higher in the experiments (chapter 6.1.2) due to the underestimation of Ca concentrations in our model.

The above described deviation between computed and measured concentrations of elements related to ettringite, S(VI) and Al, is less pronounced in the mass balance of the inventory at low L/S ratio. The reason is that at this stage both elements are mainly in the solid. The model predicts slight mobilisation of HCP inherent Al in both solutions at low L/S ratio, as well as for S(VI) in DI water. In GG water in contrast, precipitation of ettringite leads to an increase of the S(VI) inventory (Figure 44) at this stage. The depletion / enrichment of the Al and S(VI) inventory hence agrees with experimental measurements.

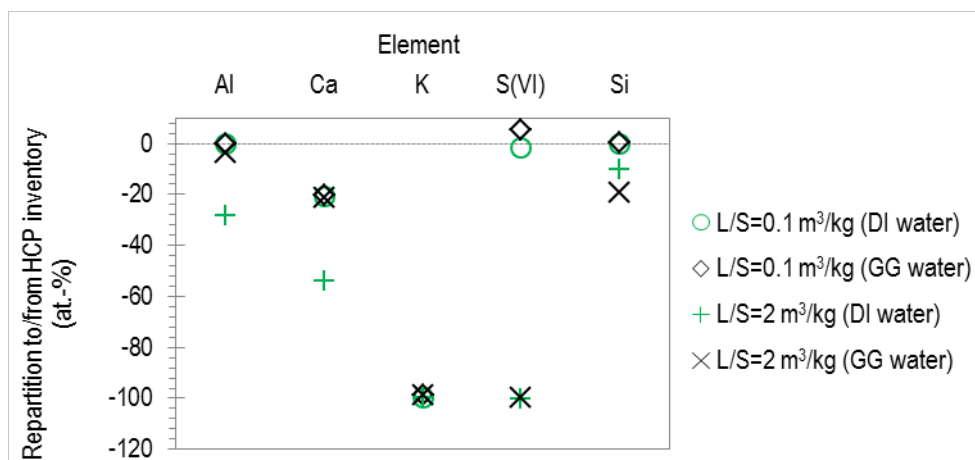


Figure 44 Diagram visualising calculated repartition of HCP inherent elements after degradation at both experimental L/S ratios (negative values indicate diminution). For experiments with GG water (black symbols) the yielded contribution of elements from GG water was subtracted from the measured concentrations before calculating repartitions. The diagram is analogous to Figure 25 giving mass balances from experiments.

At high L/S ratio of 2 m³/kg results of Ca and Si agree well between experiment and model as can be seen from concentrations (Figure 43) and mass balances (Figure 25 and Figure 44) In the case of Ca the high L/S ratio with DI water leads to significant depletion of its inventory. In contrast, in GG water the massive precipitation of calcite effectively conserves Ca in the solid which quantitatively agrees

between experiments and modelling. Moreover, model results and experiments both indicate fostered degradation of HCP in GG water by stronger depletion of the HCP Si inventory.

The mass balance for S(VI) diverges between modelling and experimental results at high L/S ratio. According to modelling the entire S(VI) inventory would get mobilised in both solutions whereas in experiments only about 60 at.-% of the inventory is mobilised. However, as discussed in chapter 6.1.2 in experiments the behaviour of S(VI) is as if the complete inventory was mobilised. Therefore, we assume that the in the solid remaining 40 at.-% of S(VI) inventory are not retained by a solubility limiting phase in experiments, but by another mechanism which is not addressed in the model.

The computed over-prediction of Al concentrations in DI water at high L/S ratio is reflected in mass balance. Computed mobilisation of the Al inventory accounts for about 30 at.-% while experimentally only about 10 at.-% is mobilised. Modelling results predict that hydrotalcite is the only thermodynamically stable Al containing phase at this stage. Since solubility data of hydrotalcite from the applied Cemdata07 database is only an estimate we made no effort to improve results for Al at high L/S ratio. Nevertheless, according to modelling results also in GG water hydrotalcite is the only thermodynamically stable Al containing phase. Computed mass balance of Al is closer to the experimentally measured low mobilisation of 8 at.-%.

6.3.3 Flow-Through Degradation Model

6.3.3.1 Thermodynamic Equilibrium Model

To evaluate the necessity of a kinetic model describing the performed flow-through experiments a simple one-dimensional flow-through model is set up. In this model reaction steps are portions of solution volume passing through the reactor. Equilibrium state is calculated for each step and cell where solid phases may dissolve or precipitate according to their saturation states. The starting composition of HCP in the flow-through model is consistent with the one used for modelling batch experiments. However, due to the short experimental time of flow-through experiments aluminoferrite is regarded as non-reactive in our model.

For comparability with results from experiments and kinetic models shifts of solution volume are transformed to time-equivalent steps (Figure 45).

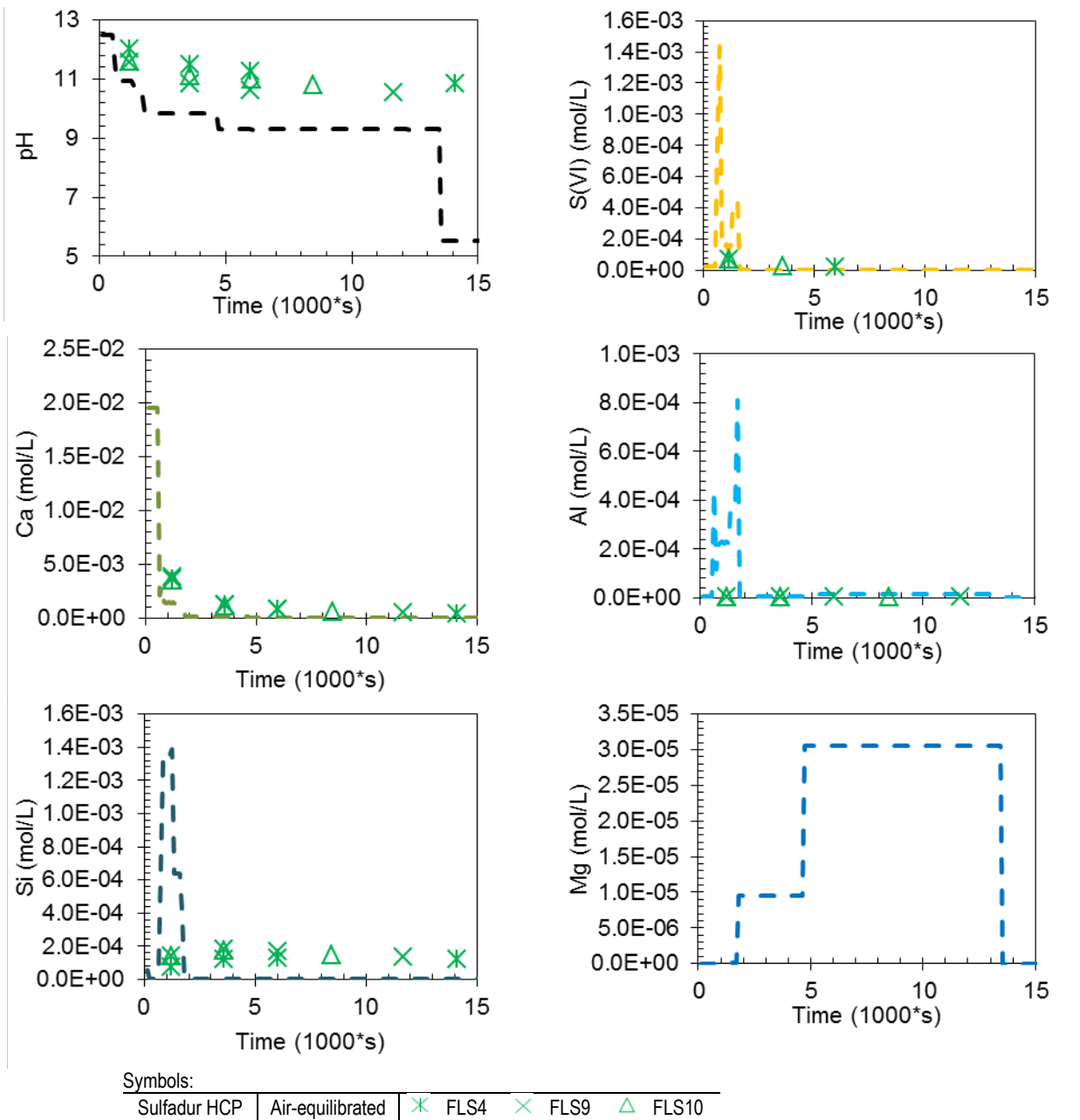


Figure 45 Comparison between computed (lines) and measured (points) ion concentrations and pH from flow-through experiments with air-equilibrated DI water, plotted versus time. Computed values base on the thermodynamic equilibrium approach.

Using the thermodynamic equilibrium approach results in complete dissolution of HCP after exchange of about 320 reactor volumes with fresh DI water, corresponding to about 13000 s. In contrast, during experiments about seven times more reactor volumes are exchanged with new solution, but HCP still remains in the reactor. Figure 45 illustrates the disagreement between the equilibrium model results and experiments, indicating that the model does not take into account relevant processes of the reactions occurring in experiments. The equilibrium approach would simulate degradation of the HCP powder faster than it is observed in flow-through experiments. Hence, kinetic limitations for the dissolution of the solid phases are needed to explain our experimental data.

6.3.3.2 Kinetic Degradation Model

6.3.3.2.1 Specific Assumptions and Parameters

To model the kinetically controlled degradation of Sulfadur HCP we use the mean flow rate of experiments (Table 10), the residence time defined by the reactor geometry and the solid mass as well as the liquid to solid ratio (chapter 4.2.2). To account for distinct dissolution rates of each mineral they are treated individually in rate equations. We take dissolution rate constants and specific surface areas of the solid phases mostly from literature (Table 24). Collected values show a large span for both parameters. We tested different values in our model and selected those that fitted best with experimental results.

Table 24 Surface area and kinetic dissolution rate constants used for modelling flow-through experiments.

Phase	Surface area	Sources	Best fit	Dissolution rate	Sources	Best fit
	Range			Range		
	m ² /g		m ² /g			mol/(m ² s)
Brucite	0.1 - 0.2	[9]	not specified	2·10 ⁻¹¹ - 10 ⁻⁹ 10 ⁻⁸	[9] [10]	1·10 ⁻¹⁰
Calcite	0.1 - 5	[6]	0.50	7.5·10 ⁻⁷ (with 0.5 m ² /g) 6.5·10 ⁻⁷	[6] [10]	7.5·10 ⁻⁷
Ettringite	10	[8]	10	1·10 ⁻¹² -1·10 ⁻⁸ 1·10 ⁻¹¹ (with 10 g/m ²)	[8]	2·10 ⁻⁹
Gypsum	0.5	[4] [5]	0.5	2·10 ⁻⁵ - 1·10 ⁻⁴ 1·10 ⁻⁸	[3] [4] [5] [10]	5·10 ⁻⁶
Hydrotalcite	103 (BET-N ₂)	[2]	25	~1·10 ⁻⁸	[10]	2·10 ⁻¹⁰
KOH	not specified		1.7	instantaneous		1·10 ⁻³
NaOH	not specified		1.7	instantaneous		1·10 ⁻³
Portlandite	1	[1]	7.0	1·10 ⁻⁸	[3]	1.3·10 ⁻⁶
	14	[11]		7.2·10 ⁻⁶		
C-S-H1.5	250 (BET-H ₂ O)	[13]		3.2·10 ⁻¹⁰	[13]	
C-S-H1.0	12 - 64 (BET-N ₂)	[1] [15]	13	1·10 ⁻⁸	[1]	4·10 ⁻⁹ / 7·10 ⁻⁹
	~150 - 290 (BET-H ₂ O)	[14] [8] [12]		9·10 ⁻¹² - 4·10 ⁻¹¹	[7] [8]	
C-S-H0.7	30 - 203 (BET-N ₂)	[12] [1] [7]	142	3.1·10 ⁻¹¹	[1] [8]	3.1·10 ⁻¹¹
	290 (BET-H ₂ O)	[12]		3·10 ⁻¹¹ - 2·10 ⁻¹⁰	[7]	
Thaumasite	30 - 142 (BET-N ₂)	[12] [1]	142	3.1·10 ⁻¹¹	[1]	3.1·10 ⁻¹¹
	-	-	not specified	-	-	1·10 ⁻¹²

[1] Trapote-Barreira, Cama et al. (2014), [2] Châtelet, Bottero et al. (1996), [3] Bullard, Enjolras et al. (2010), [4] Jeschke, Vosbeck et al. (2001), [5] Niemann (2005), [6] Chou et al 1989, [7] Schweizer (1999), [8] Baur, Keller et al. (2004), [9] Pokrovsky and Schott (2004), [10] Steefel and Lichtner (1998), [11] Regnault, Lagneau et al. (2009), [12] Pointeau (2000), [13] Matschei and Glasser (2011), [14] Odler (2003), [15] Thomas, Chen et al. (2004).

The right discretisation is crucial for computing meaningful modelling results, despite of the small dimensions of the reactor, especially in the longitudinal direction of flow. A first, simple model considering the reactor as a single cell is numerically unstable. The code converges numerically, but does not reiterate sufficiently due to the number of kinetic reactions that have to be solved simultaneously. Results are therefore chemically meaningless, e.g. during one single transport step some phases are computed to be oversaturated, but in fact dissolve and vice versa. Discretising the reactor into more cells

improves this problem substantially. We find that already 10 cells are sufficient to resolve inconsistencies. To verify the validity of this grid for numerical model results we tested discretisation with up to 100 cells. Results from finer discretisation deliver almost identical results, why we consider the 10 cells based model as sufficient.

Instead of many intermediate C-S-H compositions we use three end-members of fixed composition to model HCP degradation under flow-through conditions (chapter 4.2.5). We tested the influence of variations in the initial C-S-H composition in our thermodynamic equilibrium model. There is no difference in modelling results if up to 10 wt.-% of HCP are constituted by C-S-H with lower C/S than C-S-H1.5. Models of batch and flow-through experiments start with the same C-S-H content of 58 wt.-% in sane HCP, but when modelling flow-through experiments 7.45 wt.-% are C-S-H0.67 and only 50.55 wt.-% C-S-H1.5. With this composition the initial C-S-H C/S ratio decreases to 1.4. This allows for better fitting of model results with the measured evolution in flow-through degradation experiments.

6.3.3.2.2 Degradation of Major HCP Phases in CO₂-‘free’ DI Water

Modelling of flow-through experiments using the kinetic degradation approach (chapter 4.2.5) reconfirms experimental results (chapters 6.2.2.1 and 6.2.5.1) on solid phase evolution during Sulfadur HCP degradation with DI water at CO₂-‘free’ conditions (Figure 46). Corresponding input files can be found in annex 10.2.

The model illustrates the fast dissolution of portlandite, so within 5000 s to 10000 s ($\sim 1 - 2 \text{ m}^3/\text{kg}$ degree of leaching) its amount decreases already by more than factor ten. This corroborates experimental observations, where portlandite is not detected in XRD diffractograms at this degradation stage. Simultaneously, C-S-H starts dissolving slowly, but steadily according to modelling results. The C/S ratio decreases from 1.4 down to 1.1. After flow-through experiments we observe large heterogeneity of C-S-H C/S ratios so that we cannot validate the computed evolution. Nevertheless, the trend of this evolution is the same as indicated by experimental observations. According to modelling results 27 wt.-% of the initial C-S-H mass remain in the reactor after $88 \cdot 10^3 \text{ s}$, corresponding to the duration of long experiments. A discussion on the heterogeneity is included in chapter 6.4.2.2.

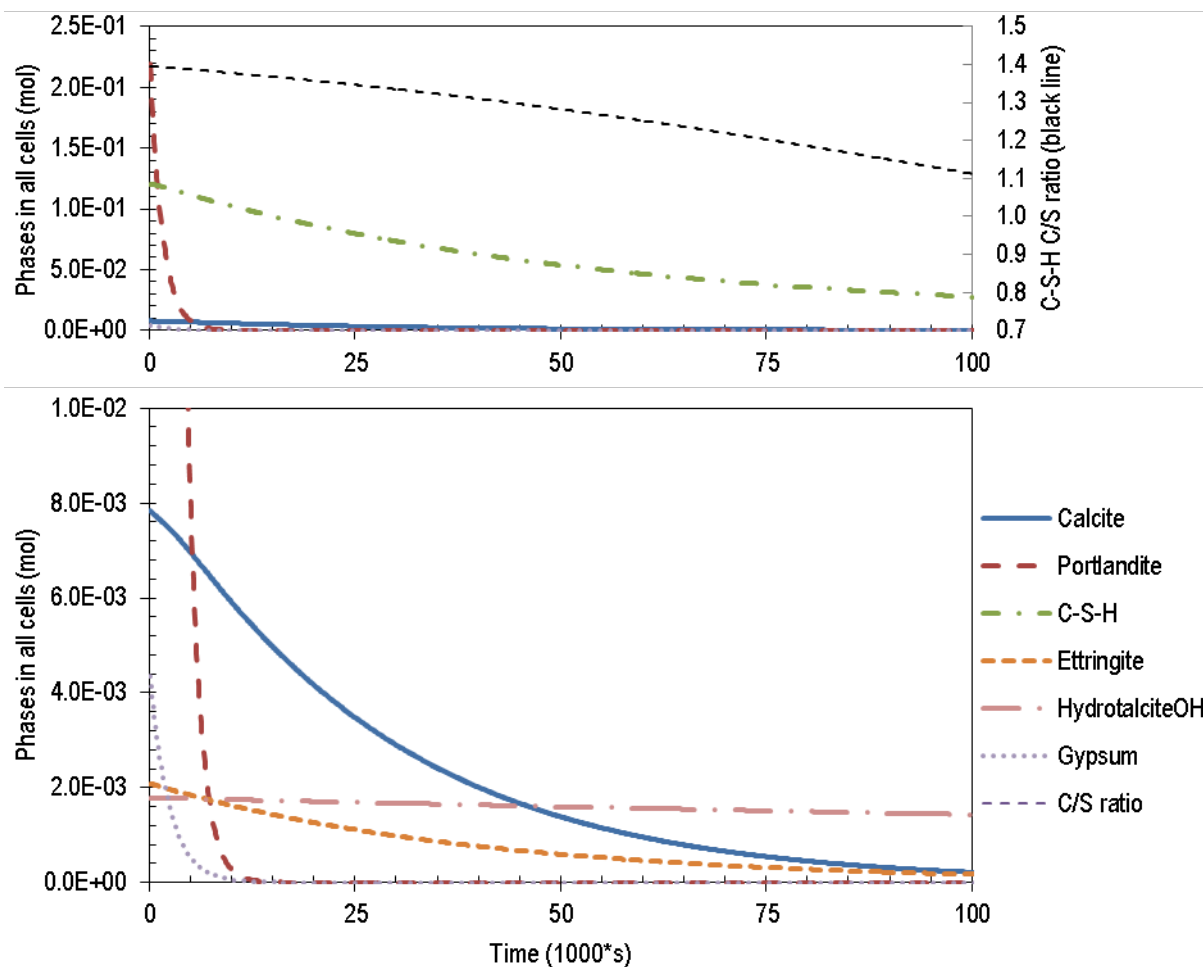


Figure 46 Kinetic degradation model: Computed evolution of solid phases during degradation of cement in the flow-through reactor using CO₂-free DI water. Phases are shown in two plots for major (top) and minor (bottom) phases to avoid logarithmic scale.

The modelled results for the three major solution parameters pH, Ca and Si concentrations fit satisfactorily with the experimental results for HCP degradation in CO₂-‘free’ DI water (Figure 47). Also according to the model Si concentrations increase initially, due to two reasons. First, C-S-H dissolves in some modelled cells at the column inlet. At the same time C-S-H_{1.5} precipitates in cells at the column outlet as long as portlandite conditions prevail with high pH and large Ca concentration. This has a retaining effect on Si in the HCP. Second, initially high pH and Ca concentration in solution (Figure 47) caused by portlandite dissolution (Figure 46) decrease the driving force for C-S-H dissolution and thus the dissolution rate in the model. Calcite is dissolving throughout the whole duration of the model with DI water ‘free’ of CO₂. Dissolution slows down as its content decreases, controlled by the dissolution rate equation. A number of kinetic dissolution models exist for calcite. However, we use the same simple rate equation for calcite as for all other phases. Dissolution of calcite was compared with different rate equations, e.g. from Appelo, Verweij et al. (1998) and Subhas, Rollins et al. (2015), giving qualitatively similar results.

At the late stages of flow-through experiments release of Ca and Si continues while pH remains almost constant in alkaline regime, indicating continued dissolution of C-S-H. Modelling results confirm

that C-S-H dissolution controls solution composition at this stage. According to the model at the end of long runs only 27 wt.-% of the initial HCP mass remain in the degraded HCP of which 47 wt.-% are C-S-H and 49 wt.-% aluminoferrite.

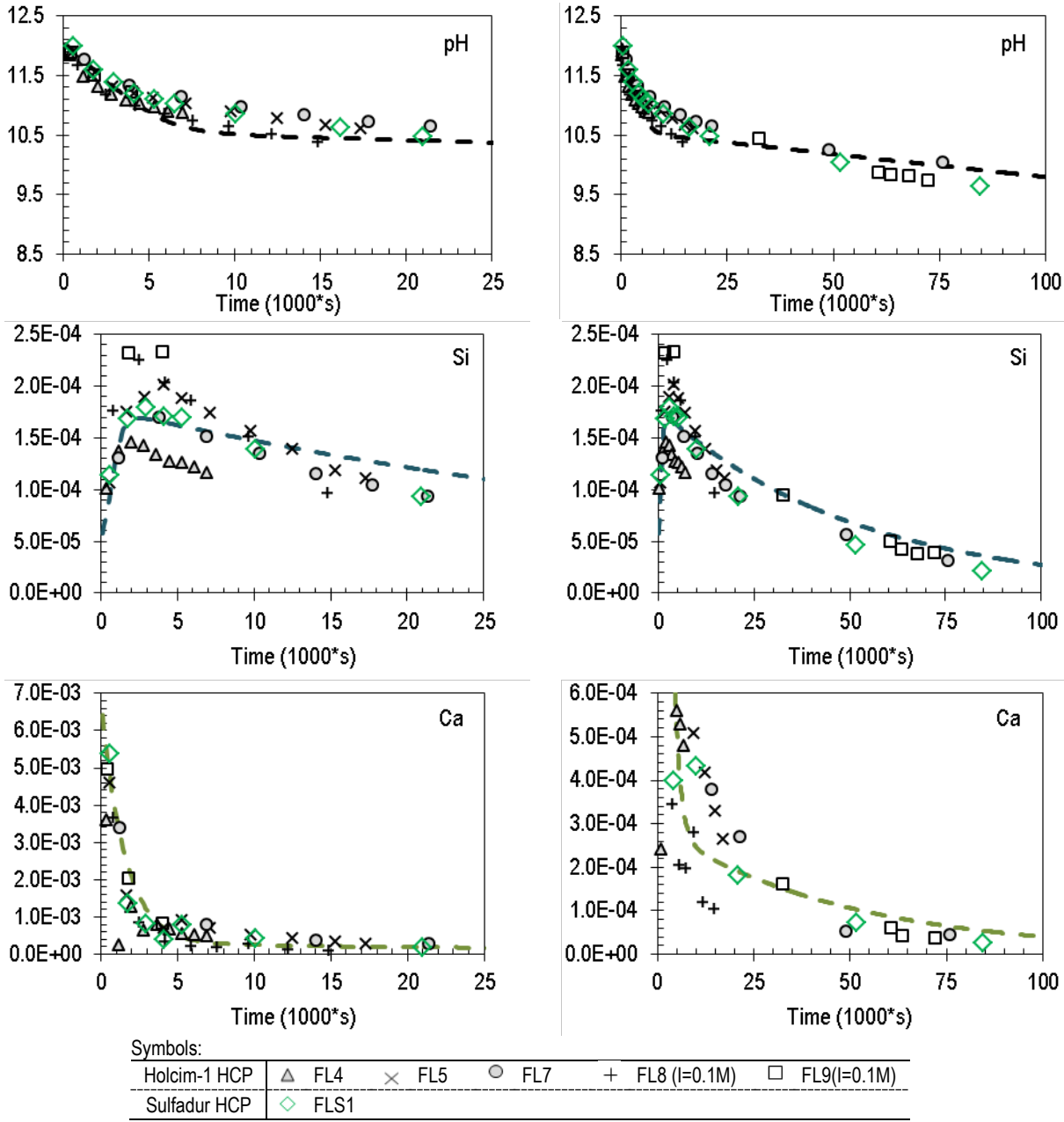


Figure 47 Kinetic degradation model: Comparison between computed (lines) and measured (points) ion concentrations (in mol/l) as well as pH from flow-through experiments with CO₂-‘free’ DI water, plotted versus time. To represent data in decimal scale two diagrams are shown per element, representing only the initial phase (left column) and the entire length of experiments (right column).

In the course of modelling HCP degradation we find that under the influence of CO₂ the model is only capable to reproduce experimental results if we assume that not all C-S-H reacts with water. Experimentally observed large variability of C/S ratios in C-S-H phases after flow-through experiments indicates heterogeneous reactivity of C-S-H phases (chapter 6.2.2.1 for DI water and chapter 6.2.3.1 for

GG water) and support the validity of our assumption. Heterogeneity is probably due short length of experiments, as well as finite size and geometry of HCP particles (see chapter 6.3.3.2.3). In the modified model, we regard only part of the C-S-H in the reactor as accessible to solution. In Figure 48 results from three calculations with 25 %, 50% and 75 % of reactive C-S-H are compared. In further calculations the amount is fixed at 50 % (explanations later in this chapter). To stay consistent with initially measured Si concentrations we slightly increased the dissolution rate constant of C-S-H1.5, from $4 \cdot 10^{-9}$ mol/(m²s) to $7 \cdot 10^{-9}$ mol/(m²s), i.e. closer towards the value suggested by Trapote-Barreira, Cama et al. (2014) for jennite-like C-S-H.

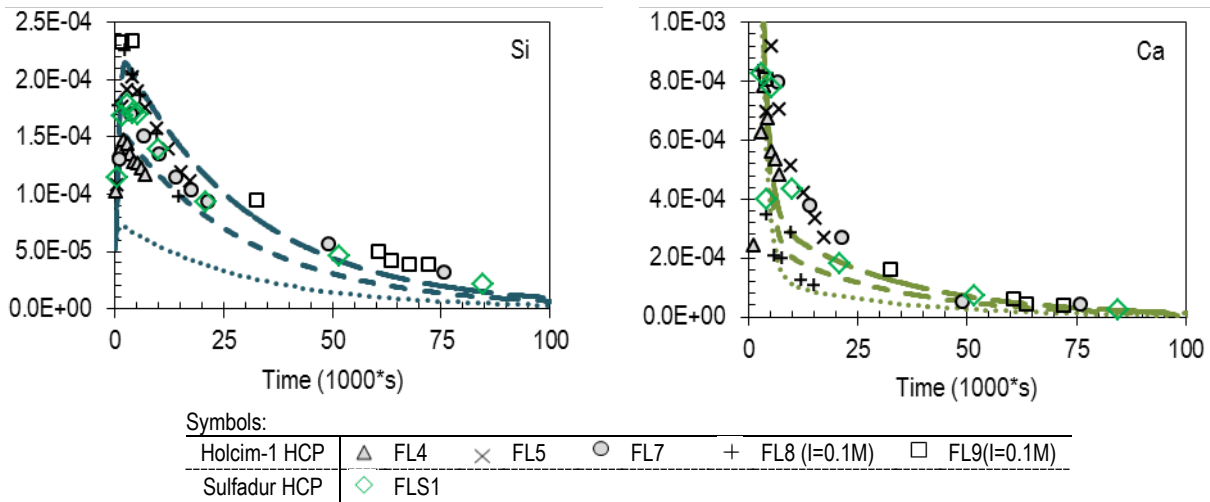


Figure 48 Kinetic degradation model with reduced amount of water-accessible C-S-H: Comparison between computed (lines) and measured (points) ion concentrations (in mol/l) with CO₂'free' DI water, plotted versus time. The dotted line represents calculation results obtained with 25 % C-S-H reactive, the dashed line 50 % and the long-dashed line 75 %.

Also results of the modified model fit satisfactorily with experiments, even though in this case the modelled pH and Si concentrations are slightly lower than mean experimental values (Figure 49). Evolution of Ca concentration, in contrast, fits even better. However, computed results according to this modified assumptions differ regarding the composition of the degraded solid. At the end of long runs still 68 wt.-% of the degraded HCP is constituted by C-S-H of which only 9 wt.-% are 'reactive' C-S-H. Aluminoferrite constitutes 29 wt.-% of degraded HCP mass.

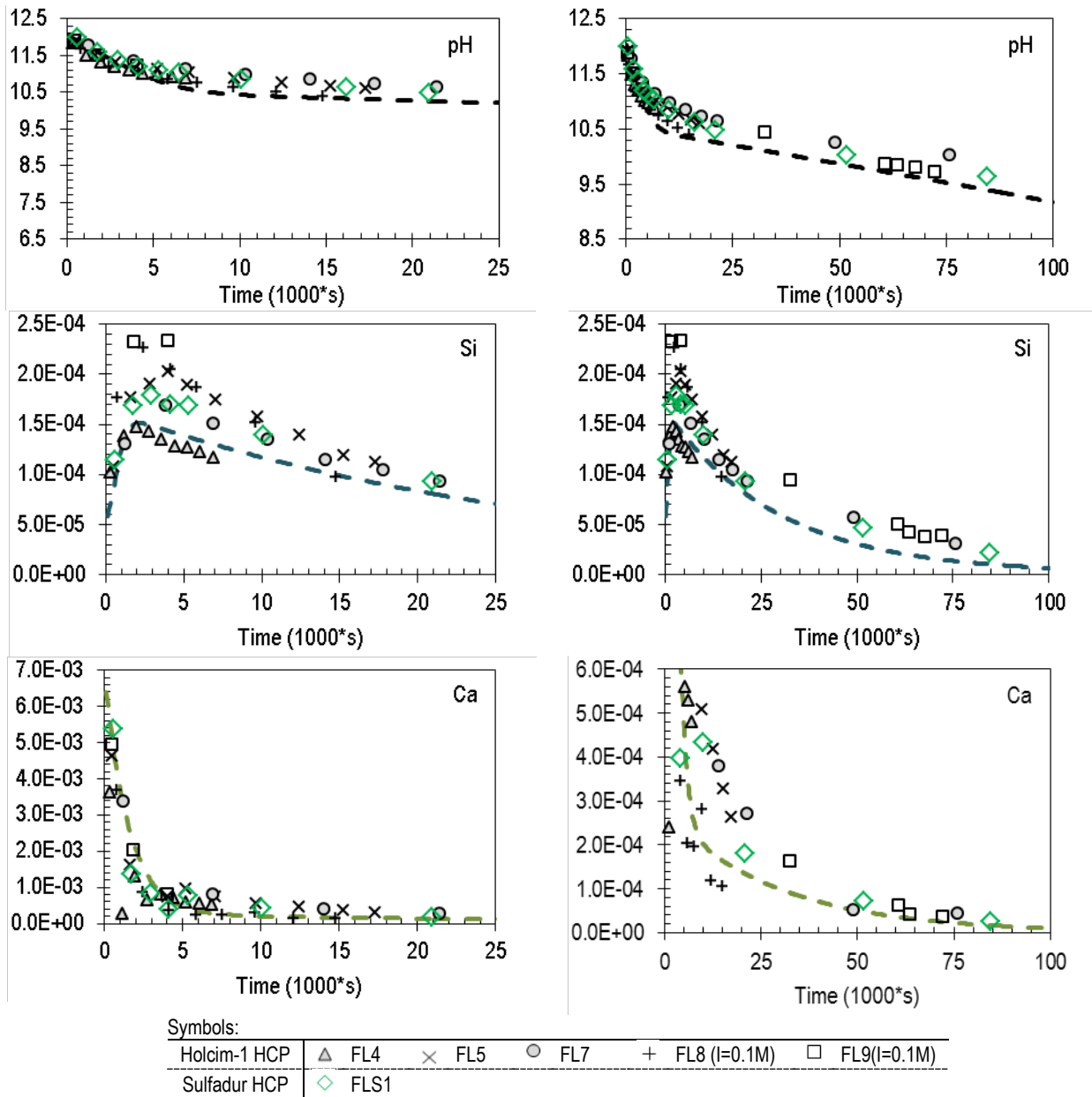


Figure 49 Kinetic degradation model with reduced amount of water-accessible C-S-H: Comparison between computed (lines) and measured (points) ion concentrations (in mol/l) as well as pH from flow-through experiments with CO₂'free' DI water, plotted versus time. To represent data in decimal scale two diagrams are shown per element, representing only the initial phase (left column) and the entire length of experiments (right column).

6.3.3.2.3 Degradation of Major HCP Phases in Air-Equilibrated DI Water

Results from modelling flow-through experiments with ambient air equilibrated DI water are in line with experimental observations (chapter 6.2.3.1). The evolution of solid phases is unaffected by the introduction of CO₂ into the model, except for calcite. It initially precipitates as long as portlandite dissolution provides sufficiently high Ca concentrations (Figure 50). In the model without CO₂ calcite mainly dissolves (Figure 46).

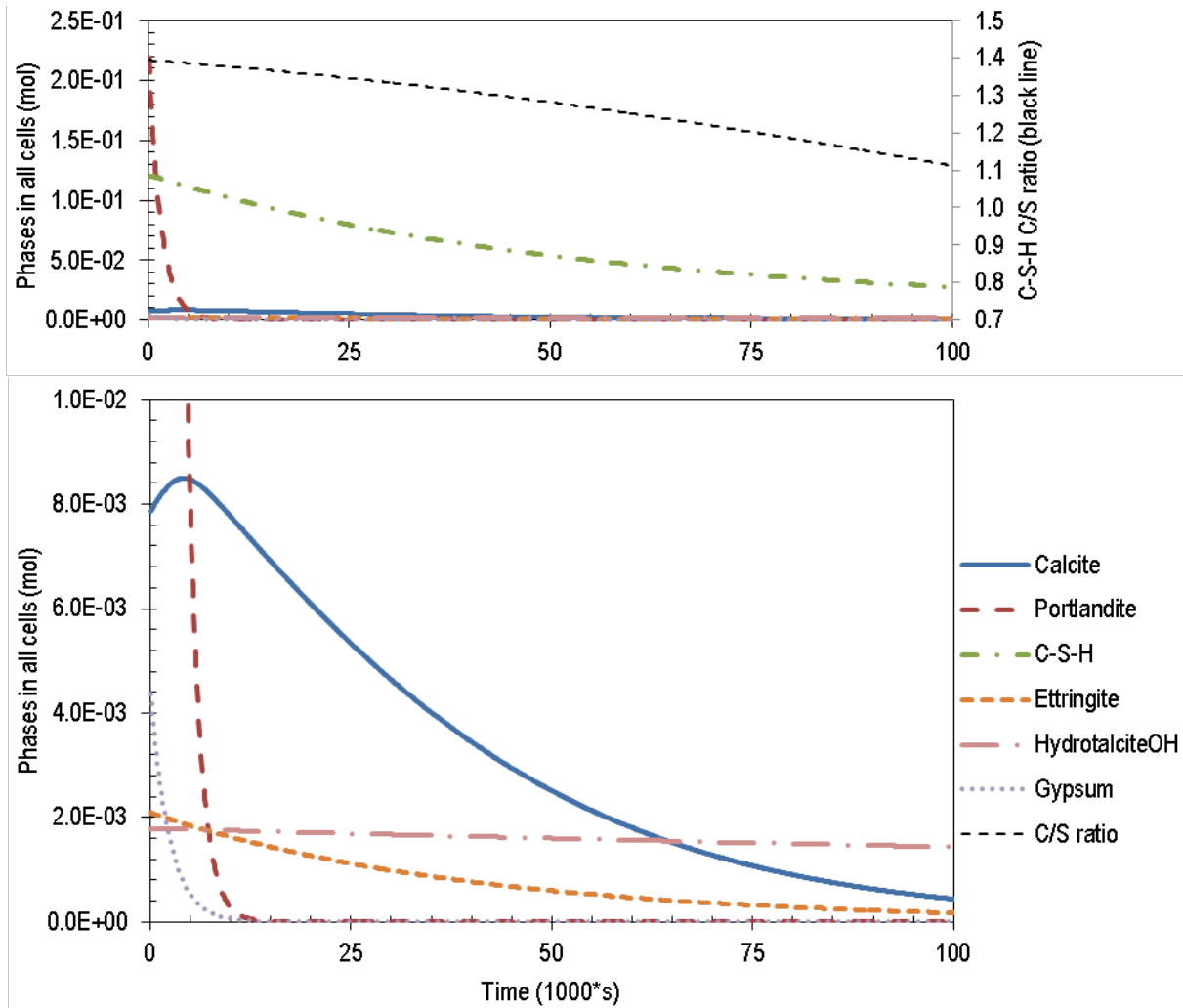


Figure 50 Kinetic degradation model: Computed evolution of solid phase dissolution and precipitation during degradation of cement in the flow-through device, reacting with ambient air (CO₂) equilibrated DI water. Phases are shown in two plots for major (top) and minor (bottom) phases to avoid logarithmic scale.

Lowering the amount of reactive C-S-H results in stronger decalcification of this C-S-H fraction. Towards the end of experiments the computed C/S ratio decreases to about 0.9 (Figure 51), compared to 1.1 (Figure 50). Degraded C-S-H hence coexists with sane C-S-H in the model. Evolution of solid phases other than C-S-H remain unchanged by the decrease of reactive C-S-H compared to the previous model in which C-S-H reacts entirely. The modelled C/S ratio agrees with measured ratios of degraded C-S-H between 0.4 and 1.0 (chapter 6.2.3.1).

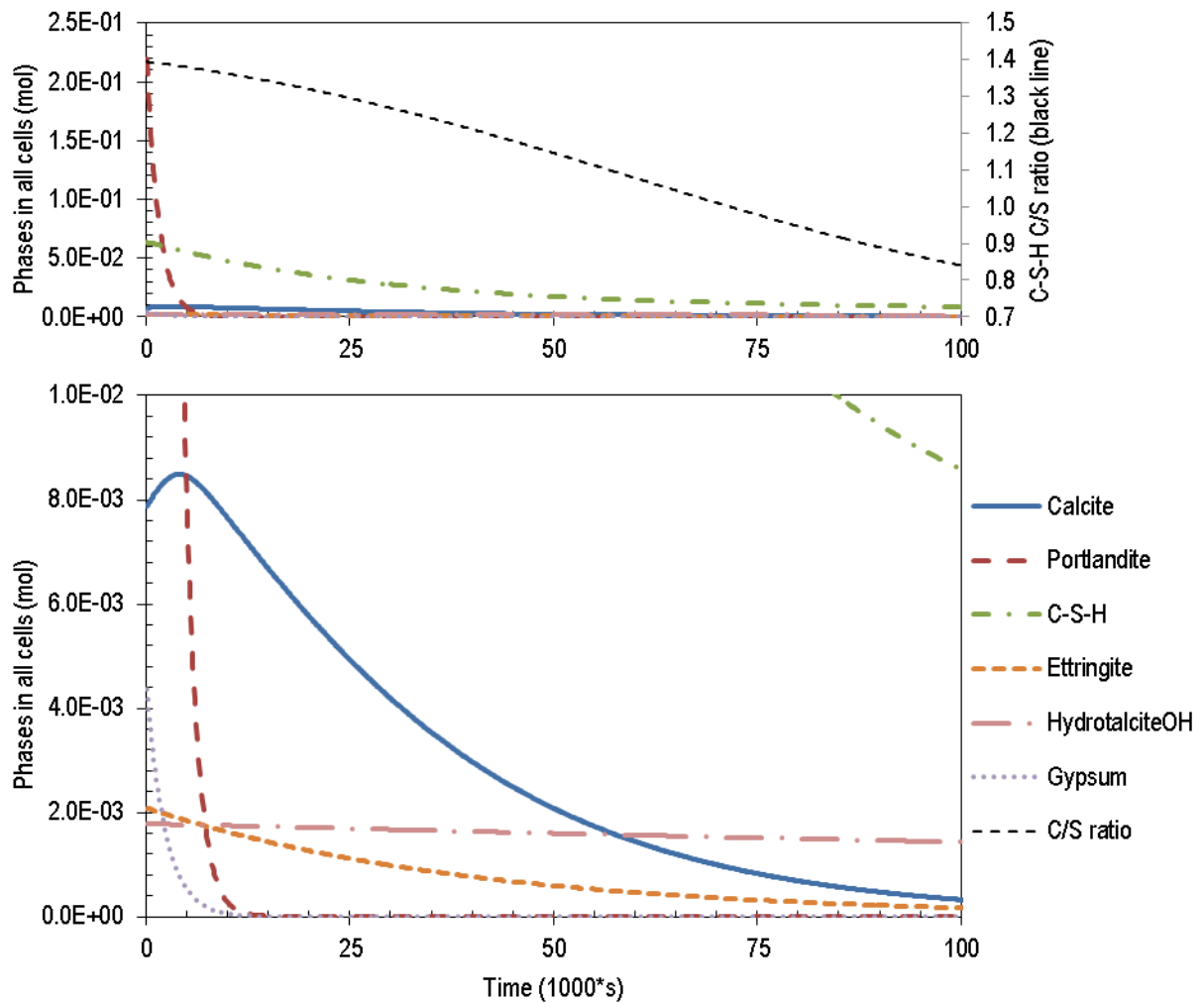
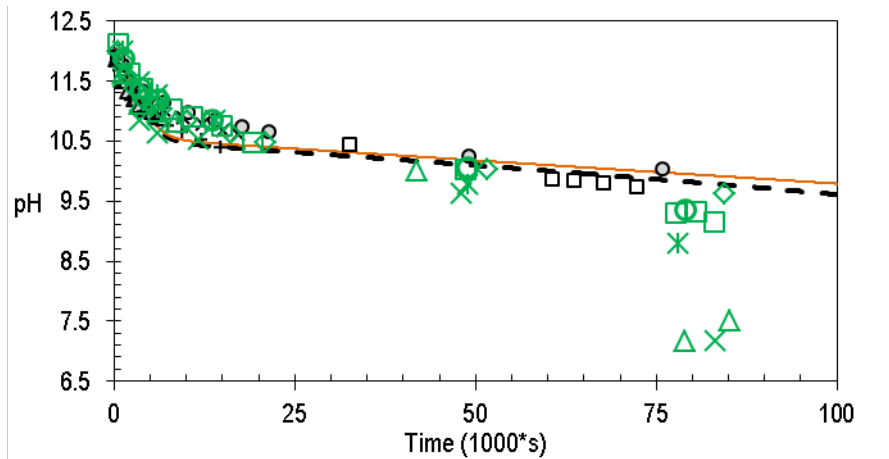


Figure 51 Kinetic degradation model with reduced amount of water-accessible C-S-H: Computed evolution of solid phase dissolution and precipitation during degradation of cement in the flow-through device, reacting with ambient air (CO_2) equilibrated DI water. Phases are shown in two plots for major (top) and minor (bottom) phases to avoid logarithmic scale.

Regarding the evolution of ion concentrations the introduction of CO_2 into the model with DI water delivers almost identical results as the CO_2 free model with fully reactive C-S-H inventory. Only pH decreases slightly, about 0.1 to 0.2 pH units, in the second half of the flow-through model (Figure 52).



Symbols:

Holcim-1 HCP	CO ₂ -'free'	△ FL4	× FL5	○ FL7	+ FL8 (I=0.1M)	□ FL9(I=0.1M)
		◇ FLS1				
Sulfadur HCP	Low CO ₂ (aq)	□ FLS2	○ FLS3			
	Air-equilibrated	* FLS4	× FLS9	△ FLS10		

Figure 52 Kinetic degradation model: Comparison between computed evolution of pH in flow-through experiments with CO₂-'free' DI water (orange line), with ambient air (CO₂) equilibrated DI water (black line) and measured pH (points). Notice that both model results do not reproduce the sudden pH drop after 75·10³ s which is observed experimentally with ambient air equilibrated DI water.

In contrast, the experimentally observed effect of CO₂ from ambient air is significant, i.e. pH in the last stages of experiments drops below 8 while it remains around 10 under CO₂-'free' conditions. As mentioned before, this is why we modified the model by reducing the amount of C-S-H that may react with water.

As explained above, results from three calculations with 25 %, 50 % and 75 % reactive C-S-H are compared (Figure 53). With 75 % reactive C-S-H the pH drop still is not reproduced. In contrast, with 25 % reactive C-S-H the computed pH in outflow solution is significantly lower than measured values and the pH drop is reproduced too early. With 50 % reactive C-S-H the evolution of pH is in the range of measured values and the pH drop is reproduced in this case, even though slightly delayed.

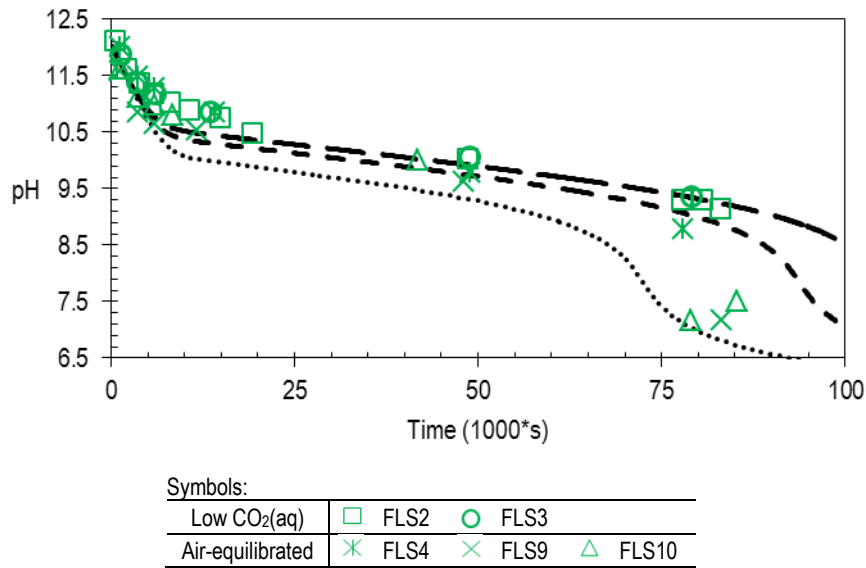


Figure 53 Kinetic degradation model with reduced amount of water-accessible C-S-H: Comparison between computed (lines) and measured (points) pH with air (CO₂) equilibrated DI water, plotted versus time. The dotted line represents calculation results obtained with 25 % reactive C-S-H, the dashed line 50 % and the long-dashed line 75 %.

The model with less reactive C-S-H is qualitatively able to explain the experimentally observed drop of pH, caused by dissolved atmospheric CO₂(aq) (Figure 54). According to the modified model reactive C-S-H is still present and dissolving in the reactor when pH drops, but it cannot provide sufficient alkalinity to buffer the slightly acidic DI water. Evolutions of Ca and Si concentrations are not affected under the influence of CO₂. This is in line with experimental results (chapter 6.2.5.2).

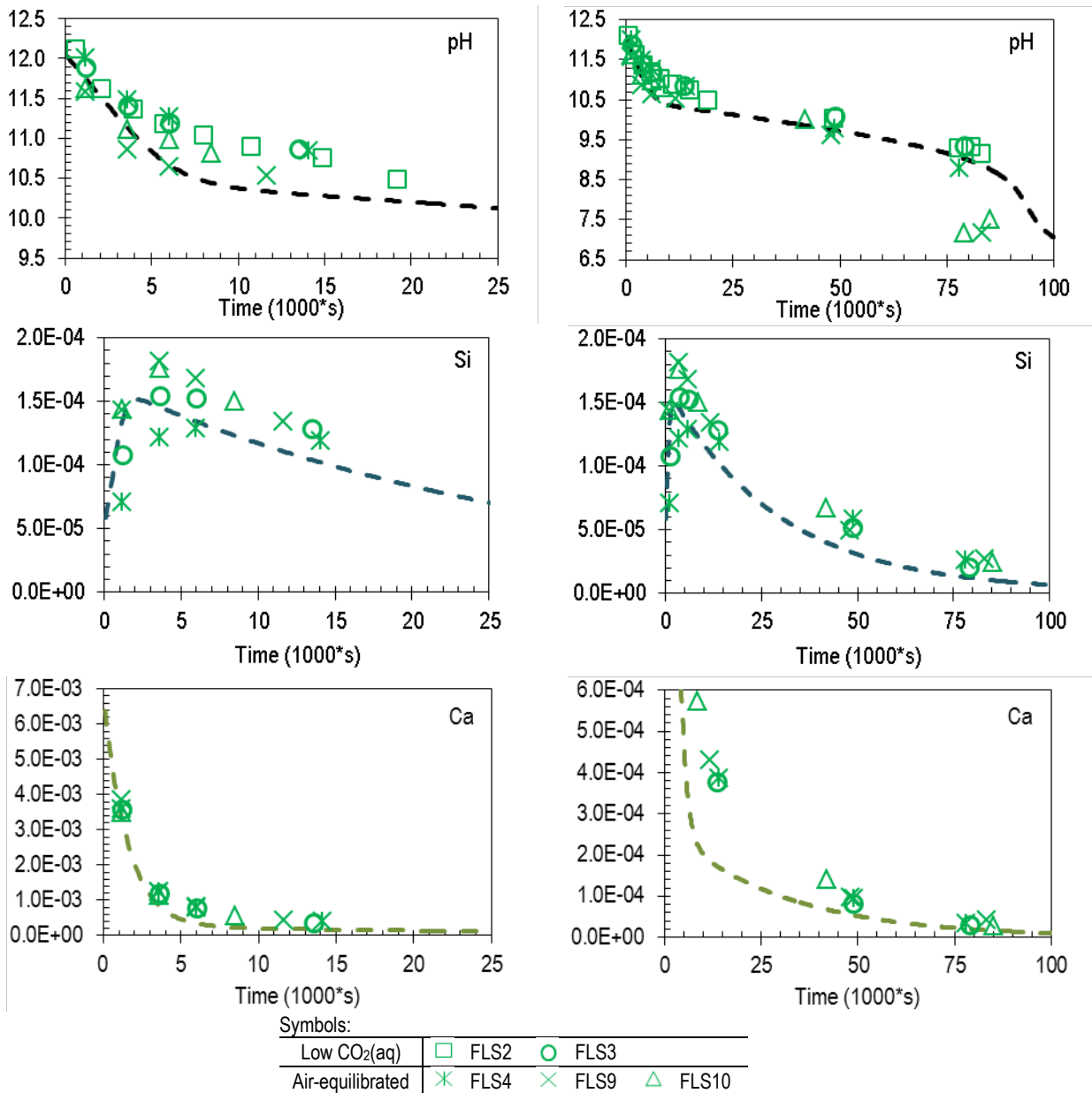


Figure 54 Kinetic degradation model with reduced amount of water-accessible C-S-H: Comparison between computed (lines) and measured (points) ion concentrations (in mol/l) as well as measured pH from flow-through experiments with ambient air (CO₂) equilibrated DI water, plotted versus time. To represent data in decimal scale two diagrams are shown per element, representing only the initial phase (left column) and the entire length of experiments (right column).

6.3.3.2.4 Degradation of Major HCP Phases in GG Water

For modelling degradation of HCP with GG water both models, with full and with reduced C-S-H inventory, are applied. The composition of GG water is given in Table 8 (chapter 4.1.3). Results from modelling flow-through experiments agree with experimental observations (chapters 6.2.3.1 and 6.2.5.1) and differ from results on HCP degradation in DI water.

According to modelling results calcite precipitates in great amounts so that after about 5000 s it becomes the main component of the degraded HCP. Once portlandite has disappeared calcite formation

decelerates, but continues throughout the whole time (Figure 55), in line with experimental observations. When GG water is introduced instead of DI water neither dissolution of portlandite, nor does dissolution of C-S-H show any response.

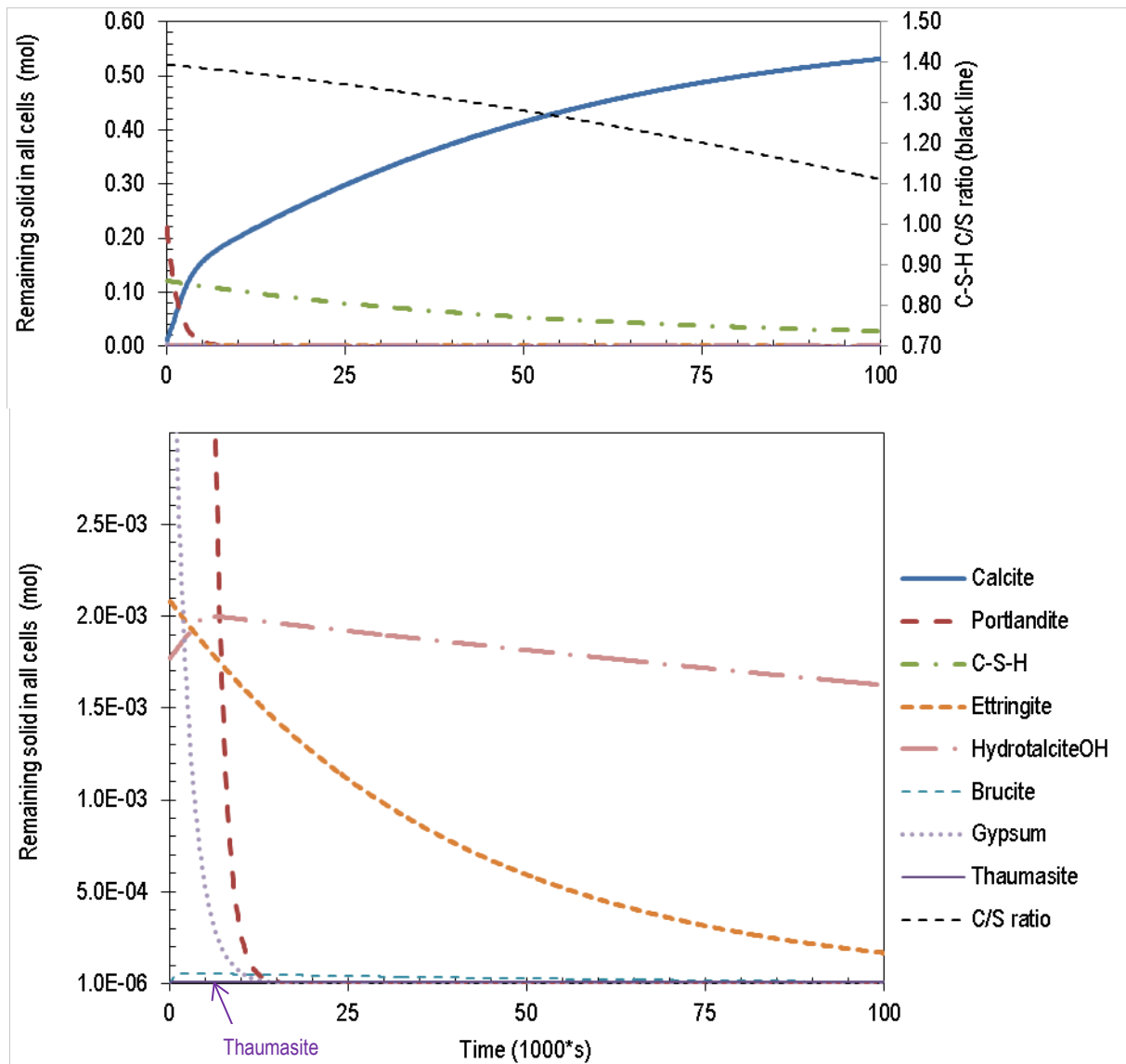


Figure 55 Kinetic degradation model: Computed evolution of solid phase formation and dissolution during degradation of Sulfadur HCP in the flow-through experiments due to reaction with GG water. Results for major and minor phases are split into two diagrams for visibility and plotted versus time.

Lowering the amount of reactive C-S-H results in stronger decalcification of the C-S-H fraction. Similar to the influence of lower C-S-H amount in modelling flow-through experiments with DI water, the computed C/S ratio decreases to about 0.9 (not shown), compared to 1.1 (Figure 55) towards the end of experiments. Apart from C-S-H also the fate of calcite differs compared to the previous model in which C-S-H reacts entirely. From reduced C-S-H less Ca is liberated, leading to precipitation of about 30 % less calcite towards the end of experiments. Nevertheless, calcite also rapidly becomes the main solid phase in the degraded HCP and never ceases to precipitate in modelling. Evolutions of all other phases remain unchanged by the decrease of reactive C-S-H.

Regarding the evolution of ion concentrations and pH results from the model with original C-S-H content (Figure 56) reflect the experimentally observed effects arising with the use of GG water instead of DI water. Modelling shows that with GG water pH in outflow solutions is lower than with DI water due to the superior buffering capacity of the solution. As described above; dissolution of C-S-H is not affected by GG water in the model. Therefore, higher Si concentrations in the model with GG water are caused by additional Si from the solution itself. Modelling results for Ca slightly underestimate concentrations in outflow solution compared with experimental measurements. While in experiments Ca concentrations are similar for both solutions during the portlandite dissolution period, the model indicates more efficient Ca removal from solution due to increased precipitation of calcite under the influence of GG water (Figure 56). The overestimation of calcite precipitation ceases towards the end of experiments, indicated by converging values of measured and computed Ca concentrations.

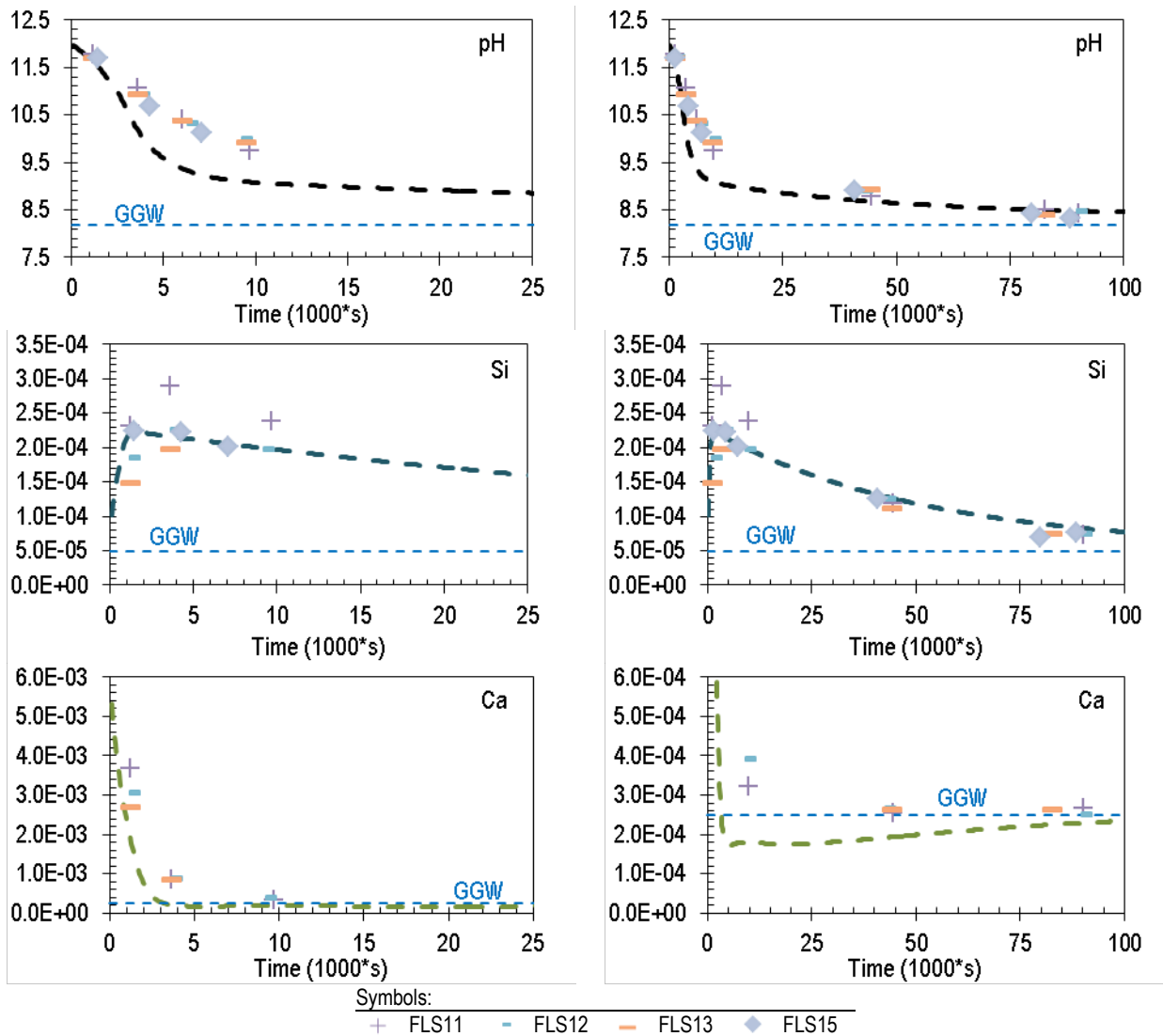


Figure 56 Kinetic degradation model: Comparison between computed (thick lines) and measured (points) ion concentrations (in mol/l) as well as measured pH from flow-through experiments with GG water, plotted versus time. To represent data in decimal scale two diagrams are shown per element, representing only the initial phase (left column) and the entire length of experiments (right column).

Lowering the amount of reactive C-S-H again gives comparable results to the original model. Computed ion concentrations from the modified model (Figure 57) even slightly better agree in the case of Ca, while concentrations initially deviate towards lower values in the case of Si. At the late stage computed and measured values approach each other. Computed evolution of pH gives values slightly lower than the original model which better matches with experimentally measured values.

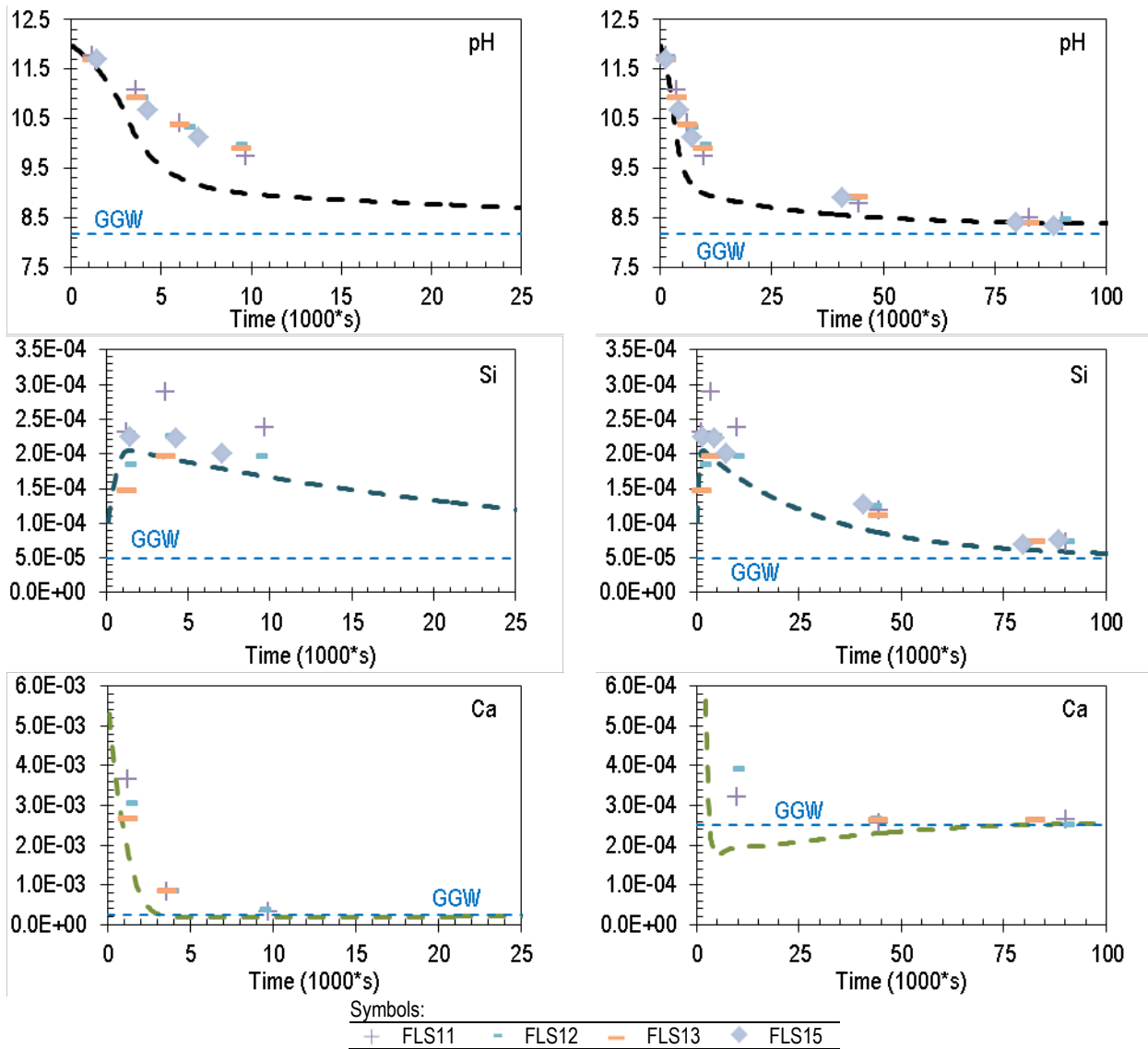


Figure 57 Kinetic degradation model with reduced amount of water-accessible C-S-H: Comparison between computed (thick lines) and measured (points) ion concentrations (in mol/l) as well as measured pH from flow-through experiments with GG water, plotted versus time. To represent data in decimal scale two diagrams are shown per element, representing only the initial phase (left column) and the entire length of experiments (right column).

6.3.3.2.5 Degradation of Minor HCP Phases in DI Water

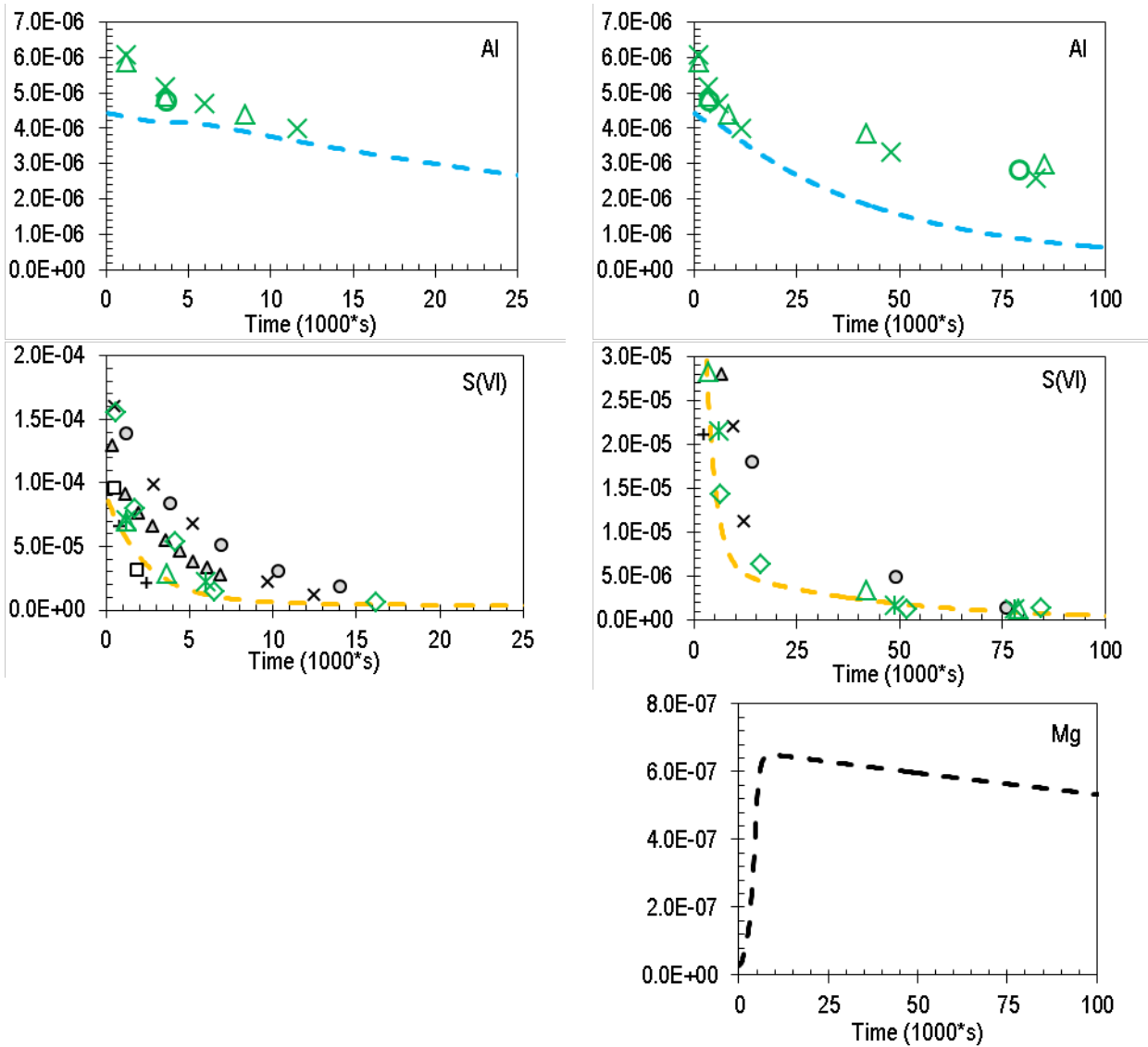
Modelling results of HCP degradation in flow-through experiments with DI water qualitatively reproduce the experimentally observed dissolution and precipitation processes of minor phases. Moreover, they reveal minor phase evolutions which we do not observe in experiments due to their amorphous character or low proportion in HCP.

The computed evolution of minor phases is shown in previous chapters for CO₂-free DI water (Figure 46, chapter 6.3.3.2.2) and DI water equilibrated with ambient air (Figure 50, chapter 6.3.3.2.3). The only difference for minor phases due to changing CO₂ conditions is that calcite initially precipitates if

CO₂ is provided by the water while in the CO₂-free model calcite only dissolves. In both cases, a significantly decreased fraction of the initial calcite inventory persists until the end of flow-through runs. In the CO₂-free model only 4 wt.-% of the initial calcite inventory remain, while 9 wt.-% remain when air-equilibrated DI water is used. This computed evolution of calcite in DI water is qualitatively in line with experimental observations, described in chapters 6.2.2.1 and 6.2.3.1. Regarding hydrotalcite, modelling results show that it dissolves slowly during HCP degradation, so that finally about 80 wt.-% of the initial inventory persist in the reactor. Ettringite in contrast dissolves faster, i.e. finally only about 10 wt.-% of the initial inventory remain. Both, ettringite and hydrotalcite are not identified from XRD diffractograms after any flow-through experiment with DI water.

As we did not find adequate kinetic data for dissolution of aluminoferrite in literature, we tested different dissolution rate constants for aluminoferrite. However, considering a rate constant allowing for dissolution of aluminoferrite during flow-through runs, does not improve model results. Therefore, we assume no mobilisation of Al from aluminoferrite during short flow-through experiments. This is in agreement with experimentally observed inert behaviour of aluminoferrite. Still, during longer batch experiments the equilibrium model requires dissolution of one fifth of the aluminoferrite fraction to match measured concentrations (chapter 6.3.1).

In the model different CO₂ concentrations in DI water do not influence Al, Mg and S(VI) outflow concentrations. Also from experiments we find unchanged evolution of Al and S(VI) concentrations (Mg was not measured). Therefore, calculation results on Al, Mg and S(VI) evolutions are plotted together with experiments performed at different CO₂ partial pressure (Figure 59).



Symbols:

Holcim-1 HCP	CO ₂ -'free'	△	FL4	×	FL5	○	FL7	+	FL8 (I=0.1M)	□	FL9 (I=0.1M)
		◇	FLS1								
Sulfadur HCP	Low CO ₂ (aq)	□	FLS2	○	FLS3						
	Air-equilibrated	✱	FLS4	×	FLS9	△	FLS10				

Figure 58 Kinetic degradation model with reduced amount of water-accessible C-S-H: Comparison between computed (thick lines) and measured (points) ion concentrations (in mol/l) from flow-through experiments with DI water, plotted versus time. To represent data in decimal scale two diagrams are shown per element, representing only the initial phase (left column) and the entire length of experiments (right column).

In the model evolution of S(VI) mobilisation in DI water is controlled by dissolution of ettringite and gypsum. The latter gets depleted very fast when at the same time S(VI) concentrations decrease rapidly. This is in line with experimental observations, even though measured concentrations during the initial stage are slightly higher. At later stages of flow-through experiments S(VI) concentrations are very low. The model indicates that S(VI) stems from continued dissolution of remaining small amounts of ettringite. In contrast, Al concentrations only agree during the initial phase, approximately during the first 10⁴ s of flow-through experiments. In later stages computed values decrease significantly faster than

experimentally measured concentrations (Figure 58). Nevertheless, model and experimental results are well within the same order of magnitude, i.e. in the worst case Al concentration deviates by factor three between experiment and model.

In the case of Mg experiments show that concentrations stays below detection limits of $2.5 \cdot 10^{-5}$ mol/l and $4.1 \cdot 10^{-6}$ mol/l during the initial and final degradation stages, respectively. Modelling results illustrate initially rising concentrations (Figure 58). This is due to two aspects: First, hydrotalcite dissolves during this stage at the column inlet while it precipitates towards the outlet. Second, dissolution of portlandite initially rises pH and Ca concentrations so that hydrotalcite dissolves more slowly due to the saturation ratio relationship in the kinetic equation. The result of these effects is that Mg concentration rises until hydrotalcite becomes undersaturated in all modelled cells of the reactor. In continuation Mg concentration in the outflow slowly decreases throughout the run. Peak Mg concentration of $6.5 \cdot 10^{-7}$ mol/l in the model is below detection limits in experiments.

6.3.3.2.6 Degradation of Minor HCP Phases in GG Water

Modelling results of HCP degradation in flow-through experiments with GG water qualitatively reproduce experimentally observed dissolution and precipitation processes of minor phases. Moreover, they reveal minor phase evolutions which we did not observe in experiments due to their amorphous character or low share in HCP.

The computed evolution of minor phases is shown in the previous chapter for GG water (Figure 55, chapter 6.3.3.2.4). Evolution of calcite is described in chapter 6.3.3.2.4 as it becomes a major phase during degradation of HCP. According to modelling results the evolution of ettringite is identical in DI and GG water. It dissolves continuously until finally only about 10 wt.-% of the initial content in HCP remain. In the case of hydrotalcite modelling results show different evolutions in DI and GG water. While in DI water a small fraction dissolves, in GG water it first precipitates from solution as long as pH is above ~ 9.3 . Hydrotalcite then starts dissolving until finally still about 94 wt.-% of the initial content remain in the HCP. Brucite is not contained in sane Sulfadur HCP, but is oversaturated initially in the model. It therefore precipitates until pH falls below 10.5 in computations. However, only a small amount forms, not even summing up to 0.01 wt.-% of the HCP. Also thaumasite is not contained in the sane HCP, but the model predicts a similar evolution compared to brucite: The amount of precipitated thaumasite is even smaller than the one of precipitated brucite. Neither of the phases are identified from XRD diffractograms of degraded HCP after flow-through experiments. We did not find measured dissolution rates or surface area for thaumasite in literature. Hence, the outcome of the modelling results is uncertain and the fitted values have to be taken as tentative.

Evolution of Al and S(VI) concentrations changes when using GG water instead of DI water, according to modelling and experimental results, illustrated in Figure 59. Al is released from dissolution of ettringite, but a fraction of it initially precipitates with hydrotalcite. This causes the lower Al concentration in GG water at the beginning which is also observed in our experiments. As the pH decreases and the release of Al from ettringite diminishes, hydrotalcite precipitation slows down. After

some 6000 s when pH falls below 9.3 hydrotalcite becomes undersaturated and starts to dissolve. Here, Al concentrations rise to maximum values in the model, as well as in experiments. In contrast to results with DI water, in late stages of flow-through runs computed values agree well with measured concentrations. In this case, Al is mainly released from dissolving ettringite, but an important fraction also stems from the dissolving hydrotalcite.

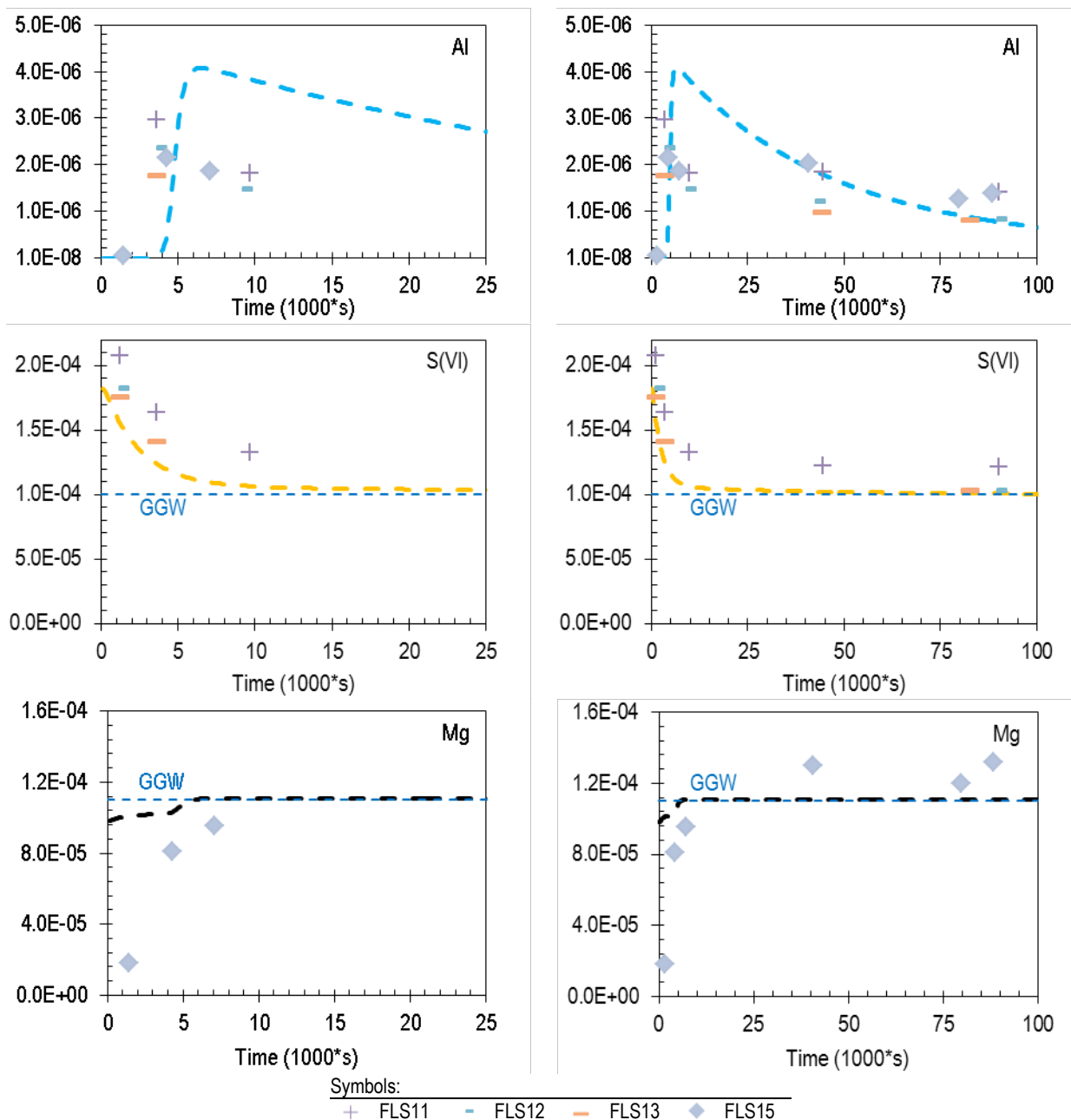


Figure 59 Kinetic degradation model with reduced amount of water-accessible C-S-H: Comparison between computed (thick lines) and measured (points) ion concentrations (in mol/l) from flow-through experiments with GG water, plotted versus time. To represent data in decimal scale two diagrams are shown per element, representing only the initial phase (left column) and the entire length of experiments (right column).

The modelled evolution of S(VI) concentrations in GG water resembles the one in DI water. Only the levels of computed values differ due to the higher S(VI) content in GG water. This agrees with experimental observations in both systems.

In the case of Mg observations from experiments with GG water would indicate that it is initially retained in the HCP. The Mg concentration rises until a constant level is measured in outflow solution which is slightly above GG water's Mg concentration. Modelling results also show initial retention of Mg which is caused by precipitation of brucite and hydrotalcite. However, Mg coming from GG water is not

as strongly retained as in experiments. As the dissolution proceeds, in experiments as well as modelling results constant Mg concentration in the outflow solution establishes which is slightly higher than the one of GG water (Figure 59). Computed concentrations in this stage underestimate the measured outflow concentrations to some degree. According to modelling the sources for Mg during the constant release stage are dissolving brucite and hydrotalcite which are not accessible experimentally due to their low quantities.

6.4 Discussion and Conclusions from the Degradation Experiments

6.4.1 Practicability and Limitations of the Methodology

Degradation studies with two setups, i.e. batch- and thin-layer flow-through experiments, show satisfactory reproducibility at all conditions. Even though the HCP degradation in the thin-layer flow-through experiments is controlled by the kinetics of dissolution and phase abundance, the evolution of the constituting major solid phases is qualitatively in line with the classical degradation scheme (chapter 3.2.1, Figure 4). In contrast, for the minor phases kinetic control causes deviation from the expected behaviour (chapter 3.2.2).

Due to the kinetic control of dissolution and precipitation reactions in flow-through experiments a thermodynamic equilibrium approach, as used for modelling batch experiments, is unable to give comparable results. Instead, we apply a kinetic degradation approach even though necessary data for cement phases is rather limited. However, model and experimental results reasonably match for different applied solution compositions. Due to assumptions relying on experimental observations the model only applies to similar physical and flow conditions as used in experiments.

Commonly used methods to test steady state dissolution rates of single phases, independent of flow velocity, are not adequate for dissolution of complex multi-phase material like HCP since they are not able to differentiate the potential overlap of the various phases. Instead, we have normalised the results of outflow solution analysis obtained from different flow rates to the mass/volume ratio of HCP mass in the reactor and volume of passed solution. This helps to merge the evolution of concentrations from different experiments and demonstrates independency of dissolution rates from flow velocity.

The thin-layer flow-through reactor allows performing reproducible degradation experiments using only little amount of solid. Its use therefore accelerates experiments compared to other flow-through setups. However, experiments using less than 28 mg HCP did not give reproducible results, but those using between 28 and 51 mg performed well. Hence, for further experiments it was therefore decided to use around 50 mg of HCP.

We did not vary particle size of HCP powder. Particle size may influence leach rates as it affects the reactive surface area of the material and its constituting phases. Large grains may not fully equilibrate with the solution at short experimental time. In this case the 'identified' steady state may represent stages in that fast reactions are completed and further changes of the system depend on, e.g., diffusion of ions

through reacted layers of grains. To avoid such processes smaller particle size could be used, but this would not necessarily help and also it entrains other disadvantages. More discussion on this issue is provided in chapter 6.4.2.2.

Continuous monitoring of outflow solution compositions help in identifying dissolution and precipitation processes which analysis of the remaining degraded HCP alone cannot indicate. The advantage of solution analysis is that certain parameters, Ca and Si concentration as well as pH are sensitive to the degradation of HCP. However, results show that the choice of control parameters depends on the inlet solution. More discussion on this issue is provided in chapter 6.4.2.1.

6.4.2 Major Cement Phases

6.4.2.1 Successive Stages of Degradation

We discern and interpret several successive stages of degradation in flow-through experiments which are characterised for CO₂-‘free’ DI water by I_{F1}) presence of dissolving portlandite and incongruently dissolving C-S-H, II_{F1}) incongruently dissolving C-S-H after depletion of portlandite and III_{F1}) congruently dissolving C-S-H, possibly coexisting with neoformed C-A-S-H (Figure 60). The different stages can be distinguished by analyses of outflow solutions. In stage I_{F1} concentrations of Si rise while Ca and pH decrease rapidly, stage II_{F1} is characterised by moderate decrease of Ca, Si and pH, while in stage III_{F1} ‘steady state’ is established, expressed by nearly constant pH, Ca and Si concentrations.

In the case that input solution contains aqueous CO₂(aq), hydrogen carbonate buffering leads to sudden pH drop while the release of Ca and Si concentration continues. In which stage pH drop occurs mainly depends on the concentration of CO₂(aq), i.e. it overlaps with stages I_{F1}, II_{F1} or III_{F1}. The suffix ‘a’ therefore indicates the stages before pH drops and suffix ‘b’ stages after pH drop. The subscript ‘_{F1}’ is added to avoid confusion with respect to the classical nomenclature, used in cement degradation for equilibrated systems.

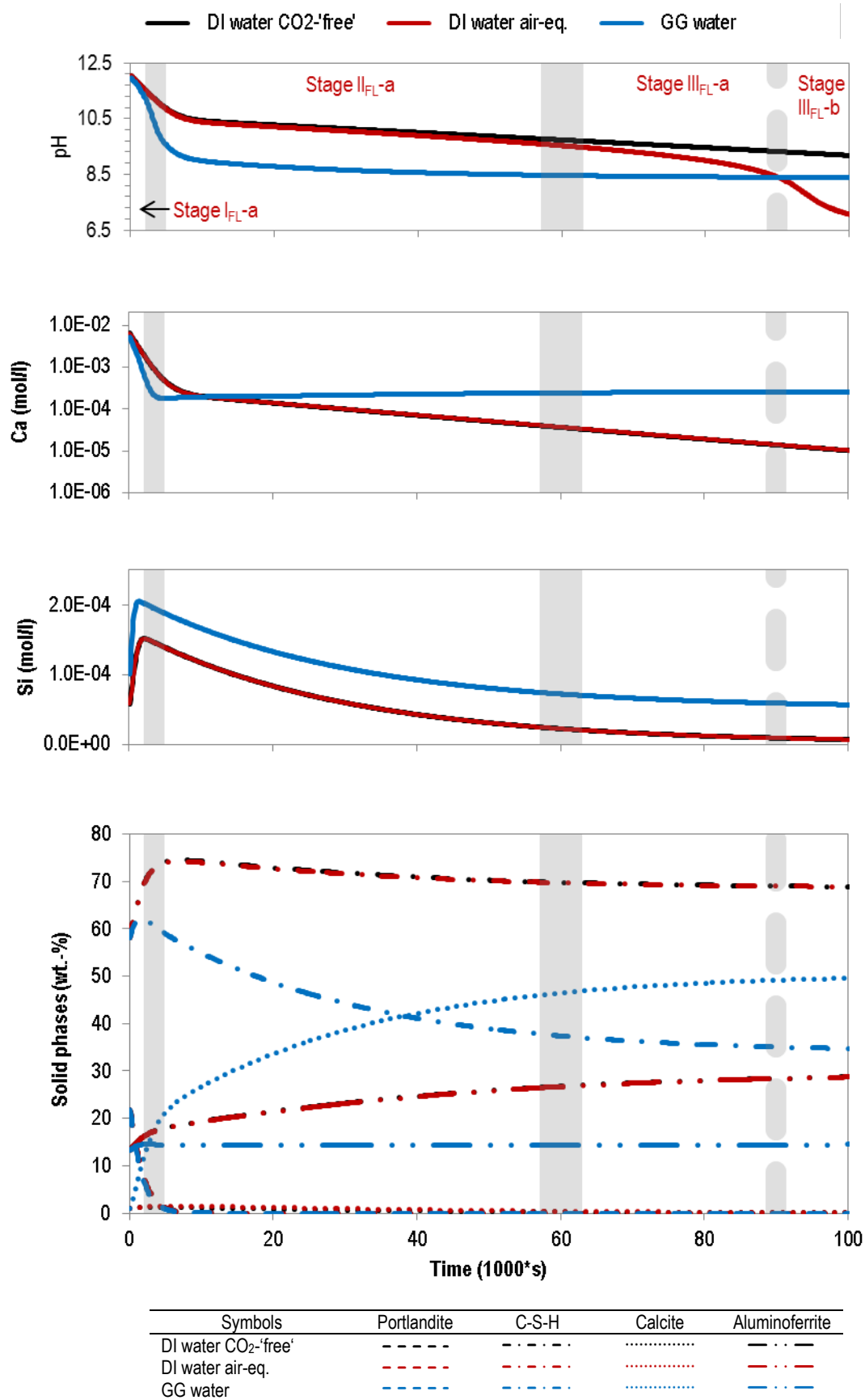


Figure 60 Characteristic evolution of HCP degradation under the investigated conditions. Different stages are indicated in the figure and refer to a system of air-equilibrated DI water (red). In all solutions stages (I_{FL} – III_{FL}) establish, but stage (b) only applies for CO₂(aq) containing water, indicating the moment when carbonate buffering leads to drop of pH.

In all flow-through experiments Ca concentrations and pH initially drop to lower values, giving indications of the conditions inside the reactor. First, it shows that portlandite dissolves far from equilibrium. Second, it shows that the amount of portlandite and its absolute surface area in contact with solution decrease. High pH and Ca concentration in solution from dissolving portlandite decrease the driving force for C-S-H to dissolve. Thus, with diminishing Ca the release from portlandite, more C-S-H dissolves leading to the initial rise of Si in outflow solutions in all experiments (Figure 36) and modelling (Figure 47, Figure 54 and Figure 56). Moreover, modelling results indicate that during stage I_{F1} C-S-H dissolves at the column inlet while it precipitates at the outlet (chapter 6.3.3.2.2). The result of both effects is that Si concentration rises until all C-S-H end-members become undersaturated in all modelled cells of the reactor which occurs when the portlandite content is largely depleted. In stage II_{F1} concentration in the outflow solution then slowly decreases.

In stage II_{F1} after around 1.5 m³/kg degree of leaching C-S-H starts to control pH while Si begins to decrease (Figure 36). The pH decrease becomes more slowly in this stage which is due to the greater abundance and the higher specific surface area of C-S-H compared to portlandite. We therefore conclude that dissolving C-S-H has greater ability to control pH than portlandite in our experiments with short residence time of solution in the reactor. Further, we conclude that experimentally observed transient conditions after complete dissolution of portlandite are due to both, decreasing dissolution rates of C-S-H with lower C/S ratios (Bullard, Enjolras et al. 2010, Trapote-Barreira, Cama et al. 2014) and decreasing amount of the dissolving phases, as integrated in the model. After this transition stage, during which Ca and Si concentrations decrease, finally almost constant pH, Ca and Si concentrations establish in stage III_{F1}. A Ca/Si ratio around unity indicates that here already degraded C-S-H is dissolving congruently. However, in the case that Ca and Si are contained in input solution the Ca/Si ratio being approached will be that of the input solution.

If the inlet solution contains CO₂(aq) we observe a second drop of pH, discerning between stages before I_{F1}-a - III_{F1}-a and after I_{F1}-b - III_{F1}-b this drop. We find that in this case hydrogen carbonate containing solution buffers pH more efficiently than C-S-H dissolution consumes protons. However, the current modelling and experiments show that C-S-H dissolution is not affected by this. When pH drop occurs in course of experiments depends on the buffering capacity of the solution. With ambient air equilibrated DI water we observe two clearly separated pH drops while with GG water they overlap, leading to very low pH values in outflow solution. In this sense we find that under fast flowing conditions without CO₂(aq) in solution pH is a sensitive indicator for degradation of HCP. It is thus suited as an easily accessible parameter for real-time monitoring of the HCP degradation process during experiments. In contrast, with CO₂(aq) in solution, pH is only sensitive for degradation during stage a, before carbonate buffering becomes effective. Afterwards pH is not controlled by HCP anymore. In this case Ca and Si concentrations are better suited to discern the actual degradation state of HCP.

6.4.2.2 Dissolution of C-S-H

Measured pH and C/S ratios of C-S-H in batch experiments at two distinct degradation stages are in line with solubility experiments of pure, synthetic C-S-H by Chen, Thomas et al. (2004). According to their data C/S ratio of C-S-H in our less degraded system in DI water at pH 12.50 is expected to be about 1.5 while it is expected to be around 1 in the more degraded system at pH ~11.65 with 2 m³/kg L/S ratio (Figure 61). We measured ratios of 1.4 ± 0.1 and 0.8 ± 0.1 at low and high L/S ratio, respectively. These results therefore confirm equilibration of the system at low L/S ratio. They further demonstrate the control of C-S-H over pH, Ca and Si concentrations and thereby equilibration of the degraded and carbonated HCP at high L/S ratio.

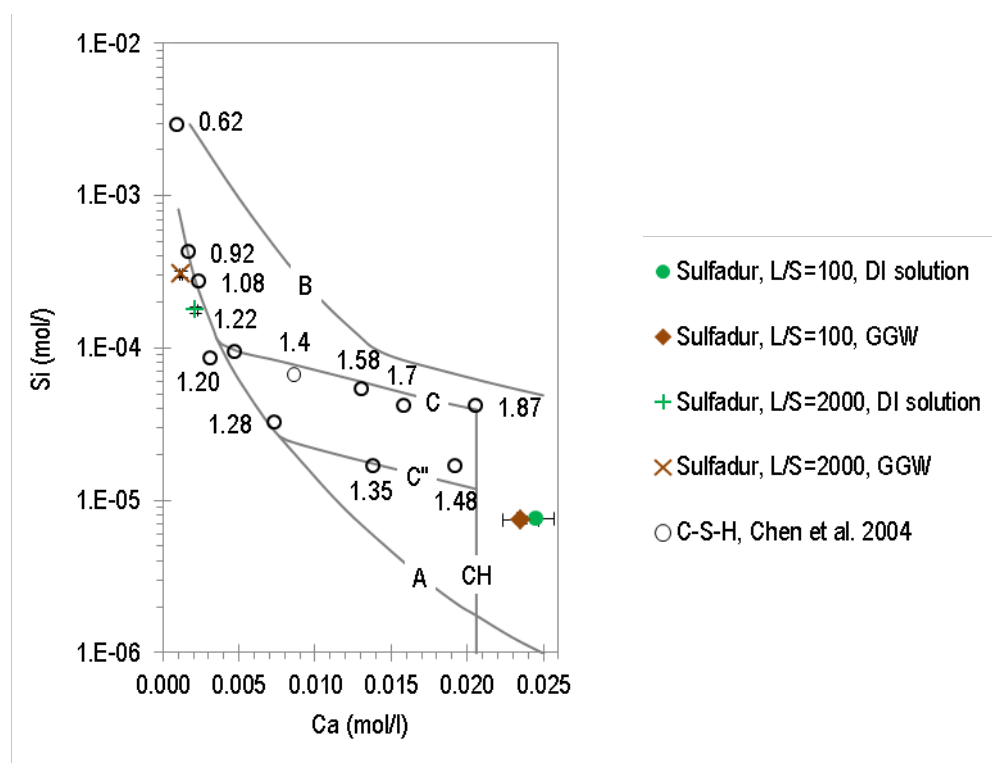


Figure 61 Plot of mean measured aqueous concentrations of Si versus Ca after batch experiments.

Experimental results from degradation of Sulfadur HCP (coloured points) are compared with data from solubility measurements of pure C-S-H phases by Chen, Thomas et al. (2004). They assigned C/S ratios to corresponding C-S-H phases and indicated dissolution behaviour of different types of C-S-H by lines. The vertical line 'CH' gives the thermodynamic solubility limit of portlandite. Lines A and B border the range of possible Ca and Si concentrations in equilibrium with C-S-H. Lines C and C'' indicate different trends of solubility for C-S-H phases synthesised in different ways.

In batch experiments with GG water measured aqueous concentrations of Ca are lower compared to those in DI water while Si concentrations are higher, indicating fostered decalcification of C-S-H. Further, at high L/S ratio measured pH is lower in GG water (pH 11.55) than in DI water (pH 11.65), also indicating fostered C-S-H degradation. Difference of 0.1 pH-units is about the resolution limit due to measurement error. Nevertheless, modelling results confirm these trends and fostered degradation of HCP

under the influence of GG water. In the severely degraded stage quantitatively more C-S-H dissolves in GG water, resulting in lower C/S ratio (Figure 42) and pH 11.45 compared to pH 11.62 in DI water.

In contrast to batch experiments, flow-through experiments do not indicate fostered degradation of C-S-H under the influence of GG water, neither in measured nor in computed results. There is no difference in XRD diffractograms of degraded HCP from both solutions regarding the amorphous hump of C-S-H and also mass balance of Si mobilisation gives similar values for GG and DI water. Moreover, kinetic modelling results show that C-S-H in GG water degrades exactly as it does in DI water. We suggest, the difference between findings from batch and flow-through systems is due to kinetic limitation of the dissolution process in flow-through experiments and consequently that HCP dissolves at maximum rate at the employed experimental conditions. This is also the reason for identical evolution of C-S-H with both solution types under flow-through conditions.

When comparing results of each first outflow sample of flow-through experiments with solubility data from Chen, Thomas et al. (2004), measured Ca and Si concentrations indicate saturation of C-S-H with C/S ratio around 1.0 - 1.2. Modelling results allow assessing saturation states of phases independent of experimental sampling intervals. Computations indicate that during this initial phase (stage I_{F1}) C-S-H dissolves at the inlet while at the outlet C-S-H precipitates (chapter 6.3.3.2.2). Consequently, we have to assume the possibility that C-S-H might have dissolved and reprecipitated inside the reactor during stage I_{F1} of degradation. Also at later stages modelling results and experimental observations are consistent. The model is only able to reproduce the pH drop in stage III_{F1} due to carbonate buffering with air-equilibrated DI solution if part of the C-S-H in HCP is assumed to be non-reactive. Moreover, this assumption is in line with the experimentally observed heterogeneity of degraded C-S-H composition.

This heterogeneity of C-S-H composition might be attributed to the finite size of cement particles (< 250 µm), entraining regions that are better or worse hydraulically connected by porosity. Limited water access and diffusion processes may lead to regions that degrade more slowly. Even if every single mineral phase was in ideal contact with solution, still there would have been limited recrystallisation due to the dense structure of inner C-S-H and short experimental time. Also persistent calcium silicate clinker minerals after flow-through experiments, still protected from hydration by a micrometre-scale thin layer of inner C-S-H, indicate limited water contact.

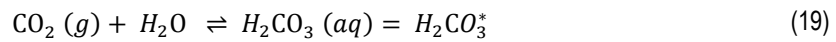
At ambient temperature solid phases can only dissolve or be replaced at the solid-liquid interface. As C-S-H is an incongruently dissolving solid-solution its kinetic dissolution inevitably entails non-equilibrium states when considering finite particle. Finer grinding might reduce the extent of heterogeneity. However, Trapote-Barreira, Cama et al. (2014) used one order of magnitude smaller particle size than the one we have used and they still identified heterogeneity in the degraded C-S-H after flow-through dissolution experiments of significantly longer duration. Taking into account their and our observations we conclude that it is practically impossible to exclude solid phase heterogeneities in flow-through experiments with crushed HCP. Therefore, smaller grain size cannot completely eliminate

heterogeneity in a kinetic study involving solid-solutions. Moreover, apart from the benefits, finer grinding could also bring other experimental difficulties, e.g. amorphisation or filter clogging.

6.4.2.3 Buffering Effects

In flow-through experiments pH of outflow responds sensitively to different CO₂(aq) content of input solutions (Figure 35). As pH is a key indicator for HCP constitution in equilibrated systems it might be assumed that lower pH in outflow solution with higher CO₂(aq) content indicates accelerated degradation of HCP. Our observations show much faster decrease of pH with GG water. However, we consider two alternatives to explain the observed pH decrease without implying accelerated degradation of HCP: brucite precipitation (chapter 6.4.3.3) and pH buffering through dissolved CO₂.

At the beginning of flow-through experiments pH rises to very alkaline conditions, around pH 12. Here, the major carbonate species in GG and DI water, hydrogen carbonate as well as aqueous H₂CO₃, neutralise the solution by reacting according to equations (19) - (21), resulting in formation of the CO₃²⁻ species. Equation (19) gives the content of free carbon dioxide, present as CO₂ and carbonic acid, which together are abbreviated H₂CO₃^{*} according to what is proposed in Stumm and Morgan (1996).



To quantify the effect of this buffer mechanism we calculate it for a simplified case in that alkaline solutions of different pH are regarded and CO₂(aq) is added, corresponding to concentration and speciation in GG water and atmosphere equilibrated DI water (Figure 62). Influence of dissolving solid phases is neglected here, as well as precipitation of carbonates as calcite. In the case of DI water, the later but strong pH decrease with higher CO₂(aq) concentration in air-equilibrated solution (Figure 35) occurs when pH is around 10 (Figure 62). The pH decrease derived by calculated carbonate buffering therewith coincides with the observed drop of pH. Ca and Si release are not affected by the pH drop in experiments, indicating that C-S-H continuously dissolves. We therefore conclude that C-S-H is not exhausted, but its amount decreased until CO₂ bearing DI water controls pH at the end of flow-through experiments (stage III_{F1}-b).

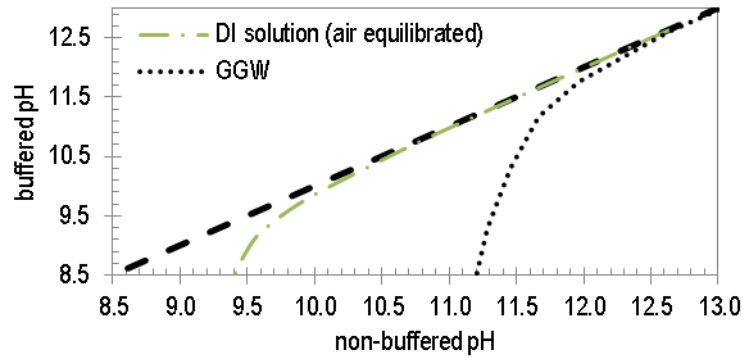


Figure 62 Plot showing the dependence of pH on different concentrations of dissolved $\text{CO}_2(\text{aq})$, derived with Phreeqc and the Cemdata07 database. The abscissa gives the pH of alkaline solution free of CO_2 and the ordinate gives pH of the same solution after addition of $\text{CO}_2(\text{aq})$ concentrations corresponding to GG water and atmosphere ($p(\text{CO}_2) = -3.26$) equilibrated DI water. Black, dashed line has slope 1 and is inserted only for comparison.

In the case of GG water the effect of carbonate buffering on outflow solution pH establishes earlier than in DI water. Taking a CO_2 -‘free’ solution at pH 11.5 as reference, addition of hydrogen carbonate in concentration equivalent to GG water decreases pH of the solution to pH 10.3 (Figure 62). The experimentally observed initial pH drop with GG water in stage I_{F1} is similar to the calculated buffering effect shown in Figure 62. In experiments with GG water, when pH approaches pH 8.2, continuously dissolving C-S-H attenuates this effect.

We conclude that high aqueous $\text{CO}_2(\text{aq})$ content of the flowing, attacking solution on the one hand does apparently alter alkalinity of flowing water that degrades HCP. On the other hand this does not affect the net dissolution rate of C-S-H at conditions that are most of the time far-from equilibrium.

As described above, the comparison between batch and flow experiments suggests that in equilibrium conditions granitic groundwater is more detrimental to HCP than deionised water at equal L/S ratio. GG water effectively buffers cement alkalinity far-from equilibrium dissolution conditions in flow-through experiments. However, the buffering effect has no kinetic influence on the dissolution- and degradation-rate of C-S-H at the studied flow conditions.

6.4.2.4 Carbonation

In many real occasions in-situ carbonation occurs, e.g. in concrete structures which are carbonated by atmospheric CO_2 . However, our observations indicate that dissolution of Ca host phases and precipitation of calcite can also be a spatially decoupled process. A coupled dissolution-precipitation mechanism would imply physical contact of host and product phase (Putnis 2009). In this scheme dissolved carbonate would directly attack portlandite or C-S-H and transform the phase in-situ, or on the surface, to calcium carbonate. Several studies with monoliths suggest such a coupled dissolution-

precipitation mechanism which is also often applied in modelling, e.g. by applying the shrinking-core model of Fujii and Kondo (1974).

We find rather large formation of calcite in degraded HCP, but neither under flow-through nor under batch conditions we could observe the formation of a surface covering or protecting layer from in-situ carbonation around HCP particles. In contrast, we observed the formation of randomly dispersed idiomorphic calcite crystals in batch experiments (Figure 22) which rather indicates nucleation and growth of calcite crystals from solution.

These observations are interesting when considering carbonation in the context of pore clogging in real cementitious systems. Pore clogging may affect degradation of HCP and hydrodynamic transport parameters. If the mechanisms of dissolution and precipitation are not spatially coupled to the surface of HCP particles it is possible that formation of calcite, and therewith carbonation, occurs, but without leading to extensive pore clogging. However, according to our experiments kinetics of calcite formation is fast, allowing for its precipitation inside the reactor within 40 seconds mean residence time. This is illustrated by diffractograms (Figure 33) and mass balance of Ca mobilisation (Table 20) from degradation experiments with GG water.

6.4.3 Minor Phases

6.4.3.1 Incomplete Clinker Hydration

In the performed experiments using two different but similar Sulphate Resisting Portland Cements we observed incomplete cement clinker hydration for both curing procedures, lasting 28 and 55 days. During all experiments a comparably small fraction of calcium silicate clinker contained in HCP dissolved, but is unlikely to significantly affect the results. Slow kinetics of clinker mineral hydration, especially in the case of dicalcium silicate, is long-known, but has mostly been included in models addressing the process of clinker mineral hydration (e.g., Garrault and Nonat (2001), Lothenbach, Matschei et al. (2008)). In studies focusing on cement degradation, presence of non-hydrated clinker is commonly neglected or they report remaining clinker minerals in HCP to dissolve upon degradation (Lothenbach, Winnefeld et al. 2007).

In contrast to calcium silicate clinker, we found considerable amounts of aluminoferrite in both HCPs. There is no indication for further aluminoferrite hydration or dissolution, neither in several weeks lasting batch experiments, nor in thin-layer flow-through experiments where cement is severely degraded. In our study we were not able to identify the mechanisms leading to inhibited hydration of aluminoferrite. Theoretically, grinding of HCP implies creation of new surfaces and thereby facilitates further hydration of aluminoferrite during degradation experiments. However, this is not confirmed experimentally in our study.

Presence of persistent aluminoferrite after clinker hydration is occasionally reported in hydration studies or encountered when real cementitious structures are analysed (Taylor 2002). However, to our

knowledge there is no evidence in literature for persistent aluminoferrite after degradation studies comparable to ours, using powdered HCP and up to 4 weeks immersion time or performing flow-through experiments. Yet, we assume that persistence of aluminoferrite is only important in cement with relatively high content of aluminoferrite. Here, mass balance of available Al and Fe in the system can be altered. Therefore, the evolution of a ‘real’ system and its model may diverge, especially with increasing degree of degradation which is when elemental inventories of the HCP start affecting calculations. To reproduce experimental results we consider persistence of aluminoferrite by limiting the amount of reactive aluminoferrite in the model.

Especially elements that usually appear in trace concentrations in groundwater like Fe and Al would be affected by mass balance issues in a real engineered cement barrier since cementitious material may be a considerable source of these elements. This affects Al and Fe incorporating cement phases like hydroxalite, AFm or AFt phases which often have considerable sorption capacity for radionuclides. We therefore recommend to study the mechanisms hindering aluminoferrite hydration during curing and hardening, as well as during degradation experiments in future.

6.4.3.2 Evolution of AFm and AFt Phases

Regarding Al and S(VI) phases in sane HCP we observed absence of XRD reflections from Al-S(VI)-hydrates, AFm or AFt. AFm and AFt minerals may be invisible for XRD analysis due to cryptocrystalline form, or due to amorphisation during grinding in the planetary ball mill. Comparison between release of Al in flow-through experiments with Sulfadur and Holcim-1 HCP indicates that the latter is probably affected by the prolonged drying procedure at 105 °C before experiments. This may also have caused amorphisation of the phases. Consequently, experimental results from flow-through experiments regarding Al and S(VI) behaviour are only comparable among experiments performed with the same HCP type. For modelling we supposed presence of common ettringite in sane Sulfadur HCP to accommodate Al and S(VI).

Batch experiments in DI and GG water show precipitation of ettringite at pH 12.5, proving that sufficient S(VI) and Al are available to form AFt minerals in HCP. However, at high L/S ratio (pH ~ 11.6) ettringite is absent in both solutions. Moreover, in this stage higher concentration of S(VI) with GG water compared to DI water indicates that there is no solid phase limiting S(VI) at measured concentration of $1.5 \cdot 10^{-4}$ mol/l. This observation is corroborated by thermodynamic modelling, showing that all sulphate phases from Cemdata07 database are strongly undersaturated. We therefore conclude that complete dissolution of ettringite at high L/S ratio is due to limited availability of S(VI). However, mass balance shows that still about 40 % of the S(VI) inventory are retained in experiments (Figure 25). The retained S(VI) fraction can either be physically excluded from water contact or co-precipitated / adsorbed with another phase, e.g. C-S-H. Nevertheless, S(VI) only weakly associates with C-S-H, especially in degraded states when surface charge of C-S-H is negative and therefore repulsive for aqueous S(VI).

Consistently with results from batch and flow-through experiments we assume that non-mobilised S(VI) is physically trapped in HCP which is not addressed by our model.

Batch experiments show that Al concentrations are controlled by a solid phase at all conditions. Our thermodynamic calculations suggest ettringite, hydrotalcite and monocarboaluminate to be the Al containing phases while the system is in equilibrium with portlandite. This is in accordance with results from XRD analysis. In HCP equilibrated with DI water at high L/S ratio XRD only identifies hydrotalcite or monocarboaluminate, while in GG water no Al-hydrate or -carbonate phase is detected.

Successful reproduction or prediction of aqueous Al and S(VI) concentrations as a function of degradation by thermodynamic modelling is known to be difficult (e.g. Sugiyama and Fujita (2006)). Computed results of the present study do not entirely reproduce the experimentally observed solid phase assemblage at 2 m³/kg L/S ratio with GG water. Compared to other elements, computed Al mobilisation deviates most from measured mobilisation. It is overestimated by (up to) factor three with DI water and underestimated by almost factor two with GG water. However, considering the complexity of our experimental system, e.g. formation of C-A-S-H phases, modelling results can still be regarded as reasonably satisfying. According to the model only hydrotalcite is thermodynamically stable and precipitates in GG water at high L/S ratio in batch systems (chapter 6.3.2). Here, from the model excluded hydrogarnet would be oversaturated, but its precipitation is unlikely according to Lothenbach, Le Saout et al. (2012) and it is absent in our XRD diffractograms. Thus, we have no experimental observation regarding the Al limiting phase in equilibrium with tobermorite like C-S-H in GG water, while modelling indicates hydrotalcite.

For flow-through experiments we infer evolution of the solid Al and S(VI) phases from modelling which is fitted to the observed aqueous concentrations. Results suggest that formation of hydrotalcite also explains strong, initial retention of Al during stage I_{F1} which is mobilised from dissolving ettringite in flow-through experiments with GG water. Also in stage II_{F1} and III_{F1} it is mainly hydrotalcite, now dissolving, which controls Al concentrations in outflow solution, matching well with experiments. With DI water evolution of Al can be explained by kinetically controlled dissolution of ettringite, even though match is not as good as in the GG water system. In the case of S(VI), a fraction of S(VI) is released too fast during stage I_{F1} to be explained by ideally dissolving ettringite. It is possible that a fraction of weakly bound S(VI) in the columns of ettringite is mobilised preferentially upon dissolution. However, we lack experimental proof for the source of S(VI) in HCP. In our model we therefore include a small fraction of gypsum in sane HCP. For the later stages II_{F1}-III_{F1} our model explains the evolution of S(VI) concentrations by kinetically controlled evolution of ettringite.

We do not see any effect of carbonate content of the solution on the behaviour of Al or S(VI) in batch or flow-through experiments.

As explained in section 3.2.2, several of the S(VI) containing AFm and AFt phases might be thermodynamically stable in severely degraded HCP at 'lower' pH, i.e. down to pH 10.5-11. However, in our study we observe and reconfirm by modelling much earlier exhaustion of such phases, due to limited

inventory of S(VI). This is the case with DI water, as well as with GG water which even supplies additional S(VI) to the system. These findings demonstrate the limited applicability of generalised degradation stages to estimate radionuclide retention potential of degraded HCP and the need for site-specific reactive transport models to predict the evolution of individual cement phases in safety assessment studies.

6.4.3.3 Buffering Effect of Brucite Precipitation

From the pronounced initial Mg retention in GG water in flow-through experiments we suspected precipitation of brucite as a mechanism contributing to faster decrease of pH. Equilibrium calculations show that portlandite dissolution in GG water with associated rise of alkalinity above approximately pH 10.5 creates conditions in that brucite becomes oversaturated. Brucite precipitation consumes OH⁻ from solution which decreases the high initial pH in flow-through experiments following the precipitation reaction of brucite shown in equation (22).



However, balancing this reaction with the measured amount of retained Mg from GG water during stage I_{F1} shows that its influence is negligible. Under the experimental conditions brucite precipitation may only decrease pH by 0.07 pH units. Influence of brucite precipitation on pH in flow-through experiments can therefore be neglected with all employed solutions. This is because the higher amounts of the alkali and alkali-earth elements contained in HCP and their significantly stronger influence on pH.

7 Results on Contaminant Retention by HCP

7.1 Nickel

7.1.1 Retention in Batch Conditions

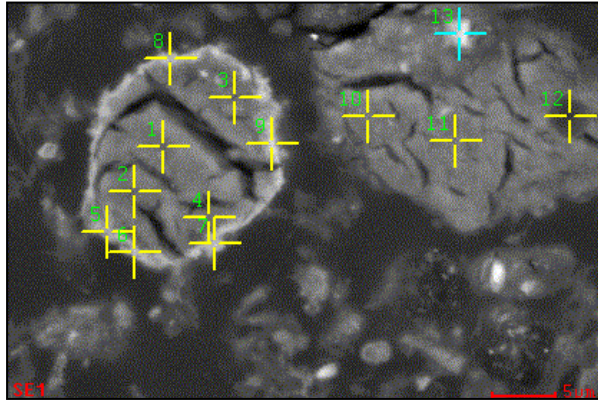
7.1.1.1 Ni Solid Phases

The Ni content of Sulfadur HCP quantified by XRF is 59.1 mmol/kg (34.7 mg/kg), referred to air-dried HCP mass. All samples were analysed by XRD to characterise the degraded, Ni-loaded product and a selection was further characterised by SEM. For the two investigated L/S ratios we identify different nickeliferous phases, forming during equilibration.

XRD diffractograms of degraded HCP, equilibrated at low L/S ratio in both solutions with high Ni load do not differ from diffractograms of samples without Ni addition. This can be attributed to the small amount of total Ni in the system, corresponding to < 0.3 wt.-% of the HCP. Due to the low Ni content, diffractograms cannot reliably prove absence or presence of crystalline Ni phases in HCP.

At low L/S ratio of 0.1 m³/kg SEM analysis identifies a Ni(II) phase that precipitated in GG water as a rim around another hydrate mineral (Figure 63). Considering initial Ni(II) concentration of $5 \cdot 10^{-4}$ mol/l and the applied L/S ratio gives a maximum Ni load of 2935 µg/g HCP for these experiments. Due to this low Ni load any formed phase would be sparsely distributed within the sample. We found a nickeliferous rim (here called 'Ni-rim') in one single spot of degraded HCP at pH 12.5 in this study.

The phase in the centre of the rim resembles C-S-H in textural appearance (Figure 63). In the same image we analysed another grain of similar composition which does not show a nickeliferous rim. According to chemical analyses both contain mostly Si and Ca while other elements are minor components. C/S ratio of 0.5 indicates severely degraded C-S-H (Figure 63, for details see Table 35 and Figure 83 in annex 10.4). However, this low C/S ratio is unexpected for the degradation stage, at pH 12.5 and in equilibrium with portlandite.



Element	Core n = 5 At%	Ni-rim n = 5 At%
Al	1.2±0.1	4±1
Ca	12±2	9±1
Fe	1.3±0.3	1.5±0.3
Mg	2.4±0.7	3.6±0.8
Ni	-	15±3
O	61.3±0.8	57±1
S	0.2±0.1	1.1±0.2
Si	21.6±1.5	10±3

Experimental conditions:	Solution	L/S ratio	pH	Ni load
	GG water	0.1 m ³ /kg	12.5	5·10 ⁻⁴ mol/l

Figure 63 SEM-BSE image and analysed spots of Sulfadur HCP sample B6 after equilibration. The bright rim surrounding the left grain is the Ni bearing phase, here called ‘nickel-rim’. The enclosed C-S-H like phase and the other grain on the right hand side are identical in composition. Experimental conditions and mean compositions of the phases, obtained from SEM-EDX, are given in the tables. Individual analyses can be found in Table 35 of annex 10.4.

The Ni-rim itself is relatively thin of about 1 μm maximum diameter. As SEM uses an electron beam, the excited volume in the sample measures about 1-2 μm lateral extension and around 5 μm in depth. Results from spot analyses of the Ni-rim (Figure 63, for details see Table 35 and Figure 83 in annex 10.4) therefore contain information from adjacent phases which cannot be subtracted quantitatively. This bias is probably negligible on the outer side of the rim, being mostly epoxy resin, but is considerable for the inner side with C-S-H like phase. When comparing element quantities of Ni-rim and C-S-H like phase we find that Al, Ni, S and Mg are significantly higher in the Ni-rim, taking into account the statistical error of SEM-EDX analysis. Our observations and the physical similarity with Ni Al LDH described by Vespa et al (2006a) (Figure 13) suggest that the Ni-rim might be a Ni(II)-Al(III) LDH.

At high L/S ratio of 2 m³/kg we added high absolute amounts of Ni, summing to 58.69 mg/g HCP). We do already optically note that high Ni concentration affects HCP (Figure 64). Degraded HCP in systems without Ni addition and with only low concentration consists of dark grains that rapidly sediment to the ground once agitation is stopped. At high Ni concentration most of these dark grains disappear. Instead, most of the solid turns into a flaky, greenish product which sediments considerably slower than HCP grains do in all other experiments.

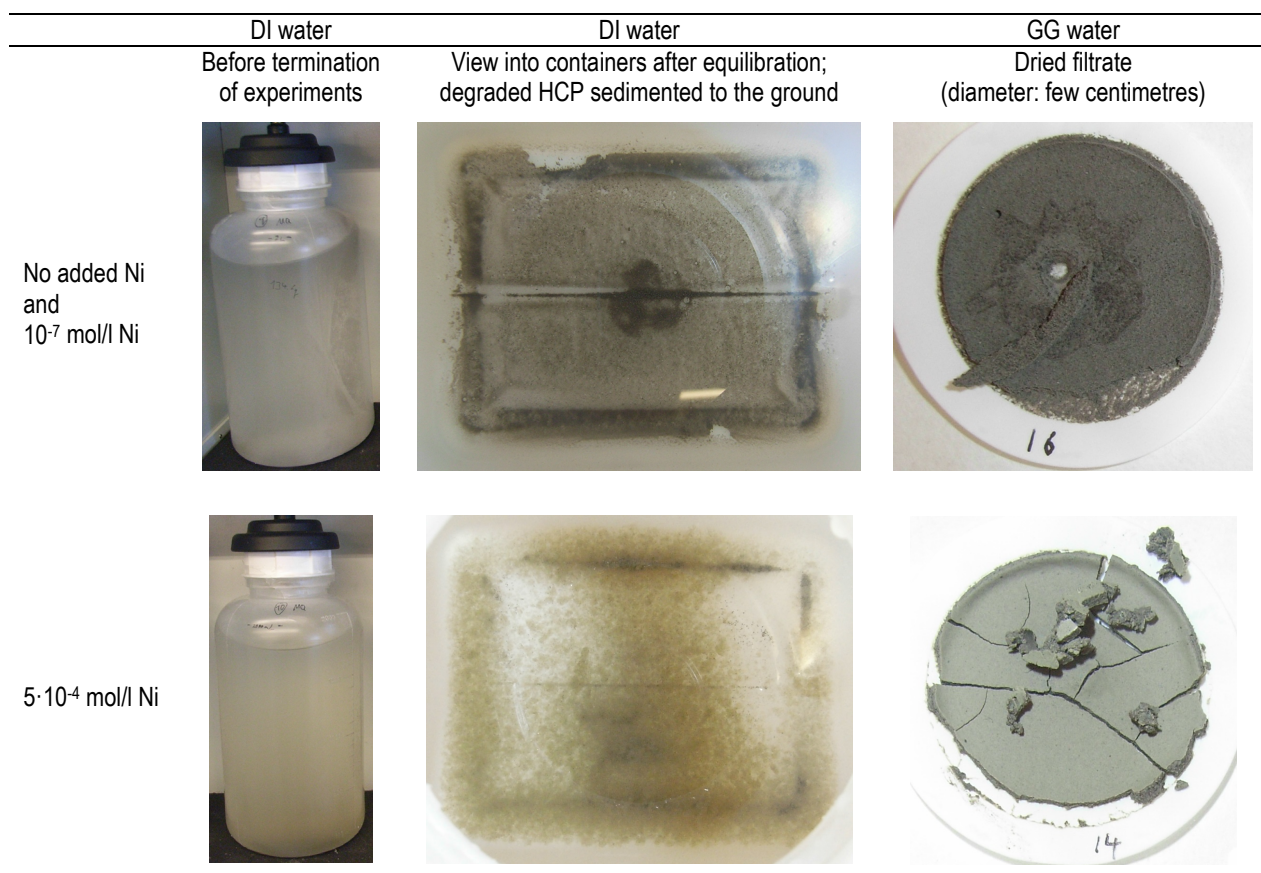


Figure 64 Photographs (not colour edited) of HCP after batch experiments with $2 \text{ m}^3/\text{kg}$ L/S ratio. Added Ni concentrations are indicated in the figure. Images from experiments with DI water show HCP in contact with solution and images of HCP from experiments with GG water shows the dried filtrate. Note the solids change in appearance with high Ni concentration. Images were made from duplicate experiments and better quality images selected (therefore round and rectangular containers for DI water experiments).

We analysed samples of dried, degraded HCP from experiments with high Ni loading, equilibrated at high L/S ratio in two series of X-ray diffraction analyses: one directly after experiments and another one after two years of storage, during which the powder was kept at dry conditions in closed plastic vials. Unfortunately, due to instrument difficulties and accessibility, analyses performed directly after experiments used a not properly focused X-ray beam, resulting in loss of signal below $\sim 8^\circ 2\theta$ and generally reduced intensity at low diffraction angles. Moreover, for the second series of analyses another diffractometer was used with different geometries and settings. Diffractograms from the two series can only be compared qualitatively.

XRD diffractograms of blank experiments and of experiments with high Ni load, both performed with DI water and analysed shortly after experiments, do not show any significant difference that would indicate formation of a Ni-phase (Figure 65). This suggests that any Ni precipitate is likely to be amorphous or cryptocrystalline.

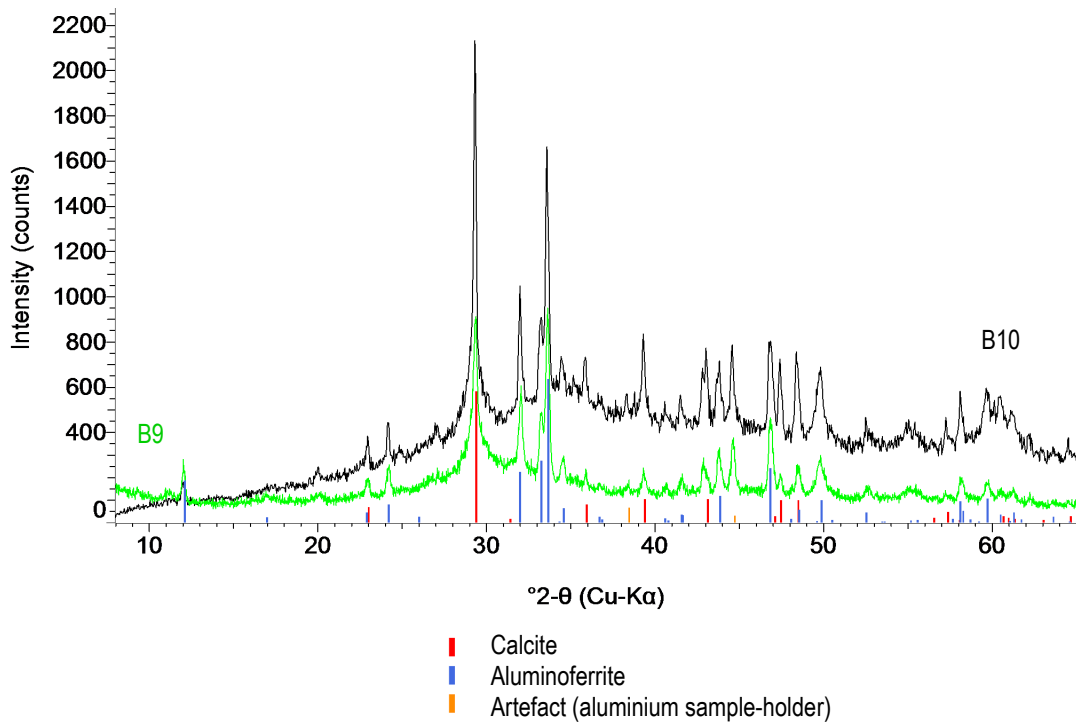


Figure 65 Comparison of XRD diffractograms from blank experiment B9 (bottom, step size 0.02 ° and count time 2 s) and experiment B10 (bottom, step size 0.008 ° and count time 5 s) with high Ni load, both equilibrated with DI water at 2 m³/kg L/S ratio. Note that the diffractogram of HCP from experiment B10 was recorded with an X-ray beam not properly focused.

In the case of GG water the same XRD analysis scheme as for DI water was followed. Similar to experiments with DI water, diffractograms did not show any reflections that would indicate precipitation of Ni-phases. Diffractograms of degraded HCP from a blank experiment show the same reflections as of degraded HCP from an experiment with high Ni-load (Figure 66).

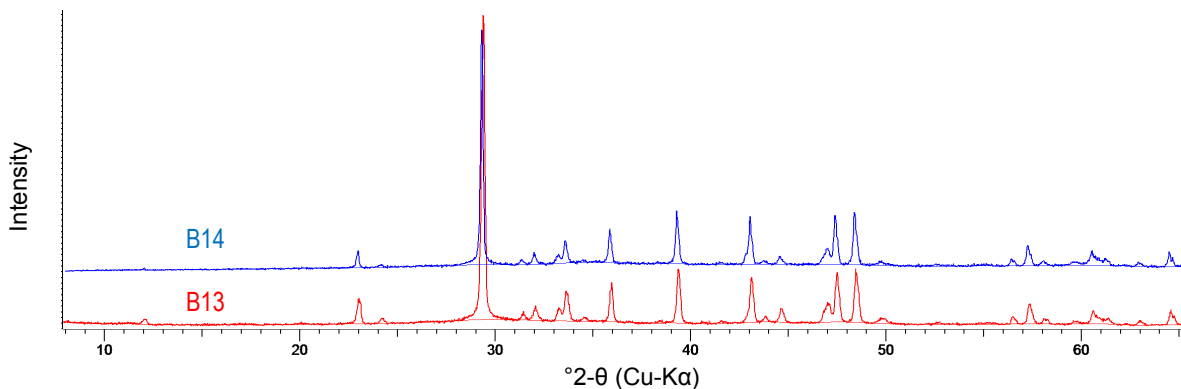


Figure 66 Comparison of XRD diffractograms (step size 0.02 ° and count time 2 s) from blank experiment B13 (bottom) and experiment B14 with high Ni load, both equilibrated with GG water at 2 m³/kg L/S ratio. Note that diffractogram of HCP from experiment B14 was recorded with not properly focused X-ray beam.

The second series of analyses, after two years storage, was performed with the samples presented in Figure 65 and Figure 66, as well as with additional samples from duplicate experiments. Comparing diffractograms of degraded HCP from experiments with DI water, equilibrated at high Ni load shows

formation of aragonite during two years storage (Figure 67), indicating carbonation of HCP. Additionally, a new reflection appears after storage in one of both samples at $18.58^\circ 2-\Theta$, corresponding to 4.77 \AA lattice spacing, (Figure 67). In the duplicate experiment this reflection is absent or very weak.

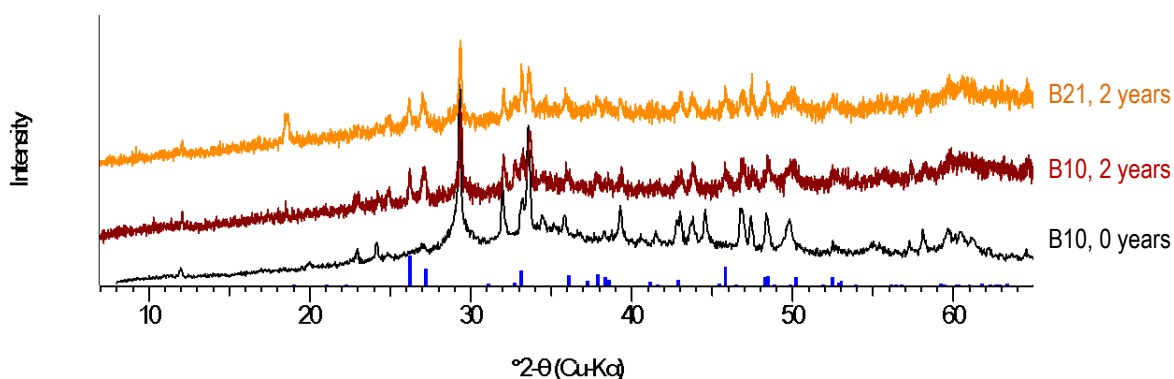


Figure 67 Comparison of XRD diffractograms from the same degraded HCP sample measured directly after experiments (black) and after two years storage (red), as well as from a duplicate experiment after two years storage (orange). Aragonite reflections are indicated by blue sticks. Samples are from experiments with DI water and high Ni load at high L/S ratio. Note that diffractogram of HCP from experiment B10 (bottom) was recorded with not properly focused X-ray beam.

In the case of GG water, after two years storage, we also observe formation of aragonite in degraded HCP from experiments at high L/S ratio and with high Ni load (Figure 68). Similar to diffractograms from the DI water system, the additional reflection from a phase with lattice spacing of 4.77 \AA appears in both diffractograms of HCP.

The interlayer distance 4.77 \AA overlaps to some degree with the main reflection of $\beta\text{-Ni(OH)}_2$, but since other major reflections from this phase are absent, we cannot assign this reflection to $\beta\text{-Ni(OH)}_2$. Thereby, the observed reflection could not be assigned to any existing Ni phase listed in the ICDD pdf-2 database.

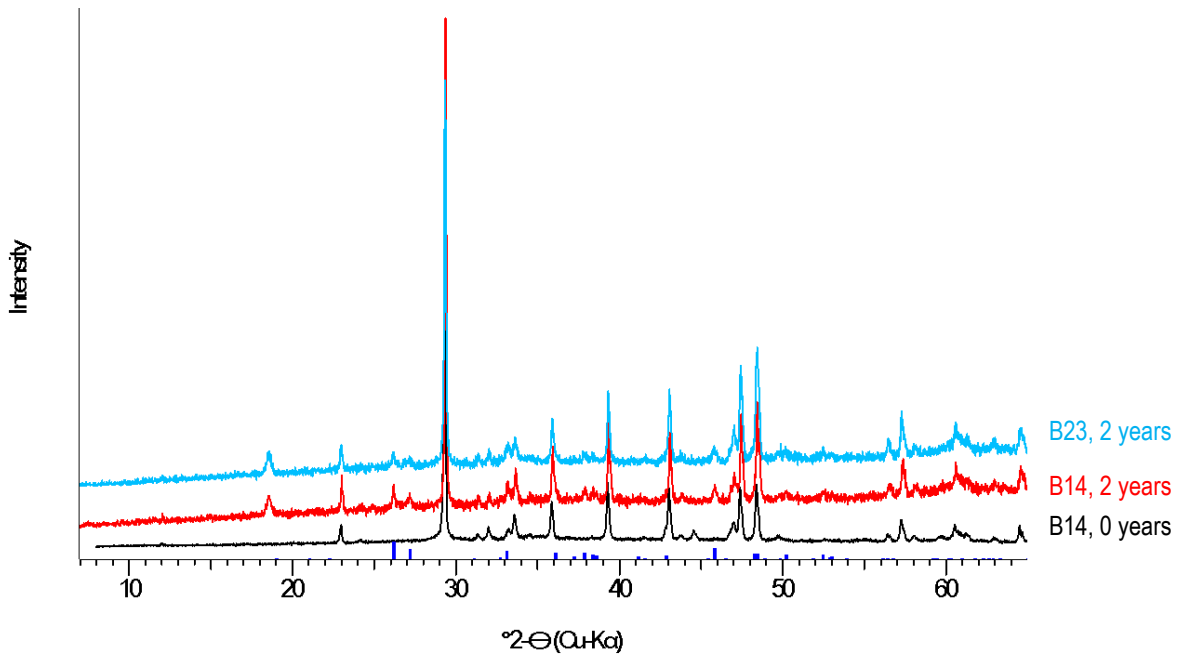


Figure 68 Comparison of XRD diffractograms from the same degraded HCP sample measured directly after the experiment (black) and after two years storage (red). Additionally, a diffractogram from a duplicate experiment after two years storage is shown (blue). Aragonite reflections are indicated by blue sticks. Samples are from experiments with GG water and high Ni load at high L/S ratio. Both upper diffractograms were recorded with step size 0.015° and count time of 5 s/step while the measurement shortly after the experiment was made with 0.02° step size and count time of 2 s/step.

Apart from experiments with high Ni concentration we also analysed samples of degraded HCP from experiments without Ni addition and with low Ni concentration after two years storage under identical conditions. XRD diffractograms show a reflection corresponding to 4.77 \AA interlayer distance in only one of these four samples, degraded in DI water (Figure 69). In the other three diffractograms the reflection is absent.

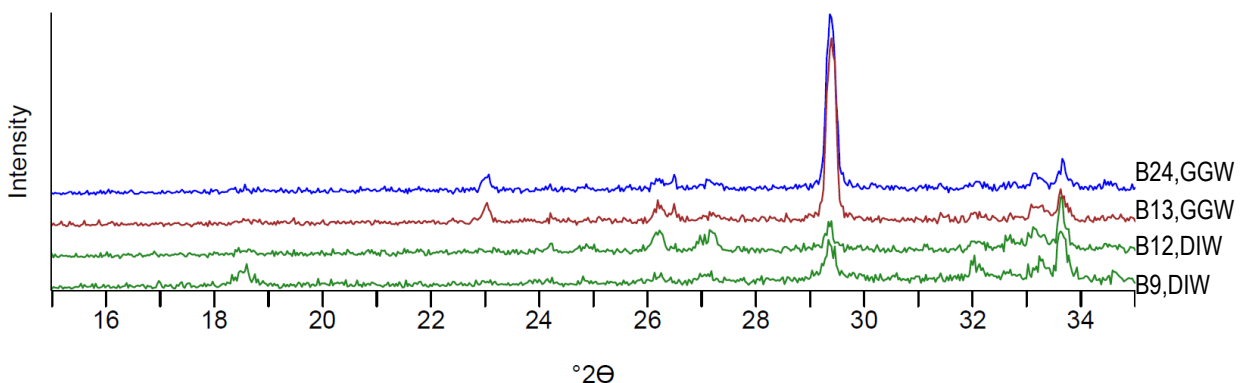
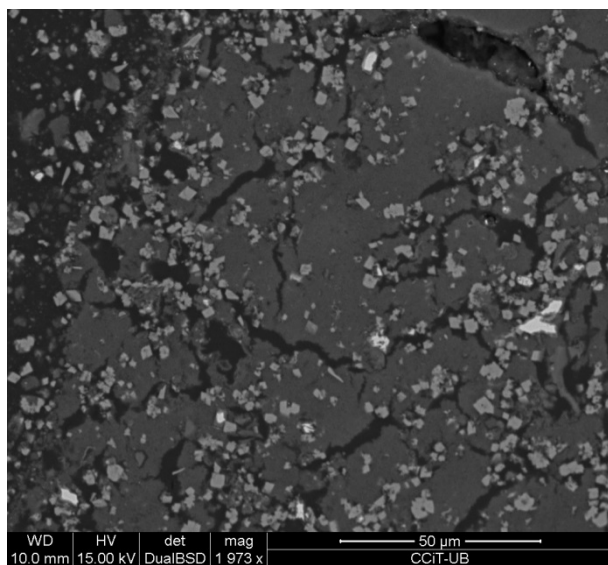


Figure 69 XRD diffractograms recorded after two years storage in air of degraded HCP at high L/S ratio. Samples B9, B12 and B13 were not doped with Ni while sample B24 was equilibrated with 10^{-7} mol/l Ni in GG water. Note the reflection occurring at $18.58^\circ 2-\Theta$ in sample B9.

Detailed information on textural aspects, composition and phase relations of nickeliferous phases and other cement phases are obtained from SEM analysis. In HCP degraded in GG water at high L/S ratio

and with high Ni load we find a nickeliferous phase that is different to the Ni-rim, observed at low L/S ratio conditions. This second nickeliferous phase is spread over large areas of the polished section with diameters of grains exceeding 150 μm (one is shown in Figure 70). It contains similar amounts of Ni as the Ni-rim which is observed at low L/S ratio (summarised results are given in Figure 70, for details see Table 36 in annex 10.4.). The Ni containing phase resembles C-S-H in grey level, texture and dissemination within HCP grains. Further, it also resembles C-S-H in chemical composition with the main difference that to the benefit of Ni it is severely depleted in Ca (Figure 70 and Figure 85 in annex 10.4). Therefore, we will call this phase ‘Ni-S-H’ in this text.



Ni-S-H composition n = 11	
Element	At%
O	59.3 ± 1.6
Al	2.5 ± 0.4
Ca	3.6 ± 1.8
Fe	2.1 ± 0.2
Mg	4.9 ± 0.8
Ni	13.2 ± 1.7
Si	15.0 ± 1.3
Sum	100.7

Experimental conditions:	Solution	L/S ratio	pH	Ni load
	GG water	2 m ³ /kg	11.49	5·10 ⁻⁴ mol/l

Figure 70 SEM-BSE image from polished powder after experiment B14. Very bright phases are aluminoferrite, dispersed medium-bright minerals are calcite and the grey matrix is Ni-S-H. Experimental conditions and the mean composition of Ni-S-H, obtained from SEM-EDX analyses of 11 individual spots, are given in the tables. Individual analyses can be found in annex 10.4.

SEM analysis shows small amounts of C-S-H with Ca/Si ratio ~ 0.8 in contact with Ni-S-H (Figure 71). We see idiomorphic, bright calcite crystals which are apparently completely surrounded by Ni-S-H in several spots in Figure 70 and Figure 71. This suggests that at least a fraction of calcite crystals has formed prior to or simultaneously with Ni-S-H. It may indicate that Ca liberated from formerly sane C-S-H is captured immediately by precipitation when Ni is incorporated. Further, we observe large cracks pulling through Ni-S-H grains (Figure 71), similar to cracks in C-S-H which open due to shrinking upon sample drying. We take this as an indication that Ni-S-H is a hydrate phase with high amount of water in its structure, comparable to C-S-H.

Grey-levels in SEM images from backscattered electrons reflect to a certain degree the chemical compositions of the solid since brightness is directly related to the atomic number of atoms hit by the electron beam. Ni-S-H shows a homogenous grey-tone without any zoning from inside to outside or rim structures. We therefore assume that its composition is rather homogeneous.

Ni-S-H is darker than bright calcite crystals although from its chemical composition the Ni phase may be expected to appear brighter than calcite due to greater mass of Ni. However, energy-emission spectra from EDX analysis prove that precipitation of Ni is unambiguous (Figure 85 in annex 10.4). Assuming that Ni-S-H is a hydrate, a high content of structural water may be the reason for less dense packing of heavier atoms in the structure, hence causing lower X-ray density which gives lower backscattered electron density. Calcite does not bear any water in its structure and has comparatively a more dense atomic packing. Further, calcite crystals are well crystalline, proven by clear and narrow XRD-reflections and also indicated by well-defined facets in SEM images, whereas XRD analysis of samples containing Ni-S-H indicate that this phase is amorphous or cryptocrystalline.

Apart from Ni-S-H we find another nickeliferous precipitate by SEM in one spot of sample B14 (Figure 71, for details see Figure 84 in annex 10.4). Morphologically it resembles very much the Ni-rim observed in the less degraded system (Figure 63,). In chemical composition it also resembles the Ni-rim, taking into account the described difficulties of quantification. However, to distinguish both phases, we call this second phase which forms at high L/S ratio 'Ni-ring'. The inner volume of the Ni-ring seems to be void or filled by resin, but analysis of that area indicates presence of a solid phase. From the composition it can be described as a low-density C-S-H phase which generally is known as Hadley grain which appear as voids in SEM (Scrivener and Gartner 1987). Due to the wide similarity between Ni-rim and Ni-ring we assume that both phases actually represent the same phase. Further, we observe the phase at pH 12.5 and at pH 11.6, i.e. in moderately and severely degraded HCP, respectively. We therefore conclude that this Ni phase is stable over wide ranges of conditions regarding cementitious environments.

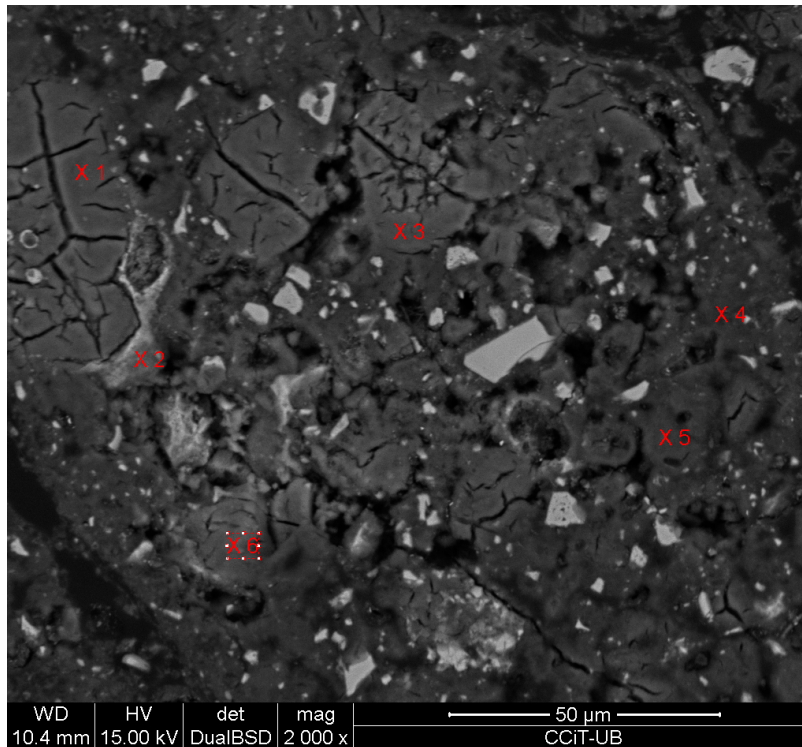
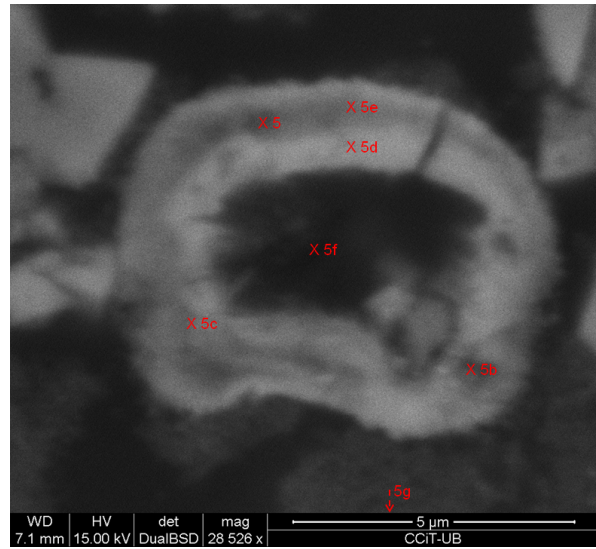
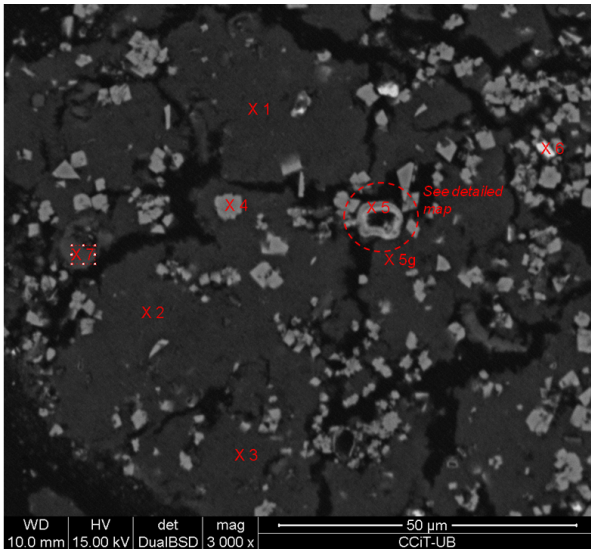


Figure 71 Upper left: SEM-BSE image of sample B14, equilibrated at 2 m³/kg L/S ratio with GG water. The grey matrix (analysis spots 1, 2 and 3) is Ni-S-H phase. The red circle indicates the Ni-ring which is shown enlarged in the upper right image. C-S-H with C/S ratio 0.8 is indicated by analysis spot 7. Bottom: SEM-BSE image of sample B6, equilibrated at 0.1 m³/kg L/S ratio with GG water. Analysis spots 1,3,4,5 correspond to C-S-H phase. Notice similarity of cracks in C-S-H from sample B6 compared to cracks in Ni-S-H phase from sample B14.

As we do not have conclusive structural information of the different nickeliferous phases, Ni-S-H, Ni-rim and Ni-ring, from XRD, we try to narrow the possible phases by semi quantitative SEM-EDX analysis. A multitude of point analyses of the Ni phases is used to identify possible known mineral phases, based on the stoichiometry of their chemical compositions. We exclude C from quantification

since samples were coated with C. There is no proof that Ni precipitated as a carbonate phase, but we cannot exclude the opposite. Charge balance is calculated and hydroxide used to balance composition where necessary. This method is quite rough and does not account for possible hydration of a phase. Formulas are calculated basing on whole-numbered silicate contents (Table 25).

Table 25 Possible mineral compositions of the different Ni phases, based on SEM-EDX analyses and charge-balance. Since we do not have information on contents of water in the lattice, H₂O is omitted in molar weights

Name	Exp.	Composition	MW (g/mol)
Ni-S-H (B14)	B14 (mass)	Ca _{0.24} Mg _{0.33} Ni _{0.88} Fe _{0.14} Al _{0.17} SiO ₄ ·nH ₂ O	for n=0: 174 g/mol
Ni-ring	B14 (ring)	Ca _{0.9} Mg _{0.4} Ni _{6.2} Al _{0.6} Fe _{0.3} (SiO ₄) ₄ ·(OH) _{2.8} ·nH ₂ O	for n=0: 859 g/mol
Ni-rim	B6 (rim)	Ca _{0.9} Mg _{0.4} Ni _{1.5} Al _{0.4} Fe _{0.2} (SO ₄) _{0.1} SiO ₄ (OH) _{1.5} ·nH ₂ O	for n=0: 191 g/mol
Ni-Al LDH		[(Ni _{0.8} Al _{0.2} (OH) ₂) ^{+0.2} (SO ₄) _{0.1}]·nH ₂ O	for n=0: 132 g/mol

In the case of the Ni-rim (B6) we assign two distinct compositions, considerably different from another. The reason is the uncertainty with regard to which elements are associated to the Ni-rim and which come from the neighbouring phase in the core. As discussed earlier, this is due to the small diameter of the rim. By excluding the main elements measured in the core from the measured composition of the Ni-rim (Figure 63) while maintaining molar ratios of Ni, Al and S(VI), we obtain a stoichiometry matching Ni-Al LDH.

Mass balances of the different possible nickeliferous phase compositions show that precipitation of these phases in the degraded system at 0.1 m³/kg L/S ratio would only result in fractions each contributing less than 1 wt.-% to total HCP mass (Table 26). These low shares would, even if phases were perfectly crystalline, hardly be visible by XRD and difficult to find by spatially limited techniques like SEM. Thus, identification of the Ni-rim by SEM was owed to favourable circumstances.

Table 26 Maximum amounts of Ni phases that may form if all added Ni (0.5 mmol/l) precipitates as one of these phases. Molar weight used for calculations is specified in Table 25

L/S ratio (m ³ /kg)	Maximum wt.-% formed, referred to initial cement mass			
	Ni(OH) ₂	Ni-LDH·2H ₂ O	Ni-S-H	Nickel-ring (B14)
0.1	0.8	0.5	0.9	0.7
2	17	9	17	14

Mass balance of nickeliferous phases, obtained from SEM-EDX analyses of polished sections, supports the observation that Ni-S-H is abundant in severely degraded HCP at 2 m³/kg L/S ratio. Basing on the Ni-S-H composition obtained from SEM-EDX analysis, this phase may constitute up to 17 wt.-% of the HCP. If Ni-S-H had crystalline structure, such an important share in the solid would have been recognised by our XRD analyses. Absence of any X-ray reflection consequently indicates amorphous character of Ni-S-H after four weeks equilibration.

7.1.1.2 Ni Solutions

Within four weeks equilibration of Sulfadur HCP powder at high aqueous Ni concentrations, ranging from $1 \cdot 10^{-7}$ mol/l to $5 \cdot 10^{-4}$ mol/l, Ni concentrations in DI and GG water decrease below detection limits in all experiments. Quantifiable detection limits are $1.5 \cdot 10^{-8}$ mol/l in experiments at 0.1 m³/kg L/S ratio and $2.6 \cdot 10^{-7}$ mol/l at 2 m³/kg L/S ratio. In both solutions high Ni concentrations are effectively scavenged at the different experimental degradation stages, characterised by pH ~11.6 and pH 12.5. Only in the case of low initial Ni concentration at high L/S ratio we cannot analytically prove Ni retention due to limitations by the detection limit.

Blank experiments were performed with DI and GG water at the same conditions as experiments, but without addition of HCP in order to test retention to container walls. In DI water Ni remains within 2 % of the spiked concentration ($1 \cdot 10^{-7}$ mol/l). In GG water a decrease by 14 % of aqueous Ni compared to the spiked concentration ($1 \cdot 10^{-8}$ mol/l) occurs, so that a minor contribution of Ni adsorption to the walls has to be assumed.

According to the analysis of equilibrated solutions from experiments with high initial Ni concentrations we find that precipitation of nickeliferous phases affects aqueous Al and Si concentrations as well. At 0.1 m³/kg L/S ratio aqueous Al concentrations - in GG water as well as in DI water - are more than 30 % lower compared to blank experiments. Aqueous Si concentrations in DI and GG water, which are similar to Al concentrations at this degradation stage, are identical in experiments with high Ni load and blank experiments (Table 27). Considering only the difference of aqueous Al concentration between blank and high Ni-load experiments is not sufficient to explain precipitation of Ni-Al LDH because mass balances between solution and solid phase do not match for the given amount of Ni. Nevertheless, changes in Al concentrations with high initial Ni concentration at low L/S ratio indicate that Al is involved in the formation of nickeliferous phase(s).

Table 27 Comparison of experiments without Ni and with high initial Ni concentration of 0.5 mmol/l, equilibrated at high and low L/S ratio with DI and GG water.

Solution	L/S m ³ /kg	Al			Si		
		mol/l blank	mol/l Ni added	% difference	mol/l blank	mol/l Ni added	% difference
DI water	0.1	$5.02 \cdot 10^{-6}$	$3.34 \cdot 10^{-6}$	-33	$7.57 \cdot 10^{-6}$	$7.24 \cdot 10^{-6}$	-4
GG water	0.1	$4.62 \cdot 10^{-6}$	$2.84 \cdot 10^{-6}$	-39	$7.59 \cdot 10^{-6}$	$7.12 \cdot 10^{-6}$	-6
DI water	2	$2.36 \cdot 10^{-5}$	$2.26 \cdot 10^{-5}$	-4	$1.81 \cdot 10^{-4}$	$1.40 \cdot 10^{-4}$	-23
GG water	2	$1.64 \cdot 10^{-5}$	$1.37 \cdot 10^{-5}$	-16	$3.05 \cdot 10^{-4}$	$2.23 \cdot 10^{-4}$	-27

At 2 m³/kg L/S ratio we observe formation of Ni-S-H, which according to SEM analyses (chapter 7.1.1.1) is abundant and different to the Ni-rim observed at low L/S ratio. Formation of this phase at high Ni concentrations apparently affects aqueous concentrations. Measured concentrations are given in Table 27 and Figure 72. In this system with severely degraded HCP, at lower pH around 11.6, Si concentration is significantly lower compared to blank experiments, 23 and 27 % in DI and GG water,

respectively. In contrast, Al concentration is not affected by Ni addition in DI water while in GG water it is 16 % lower than in blank experiments.

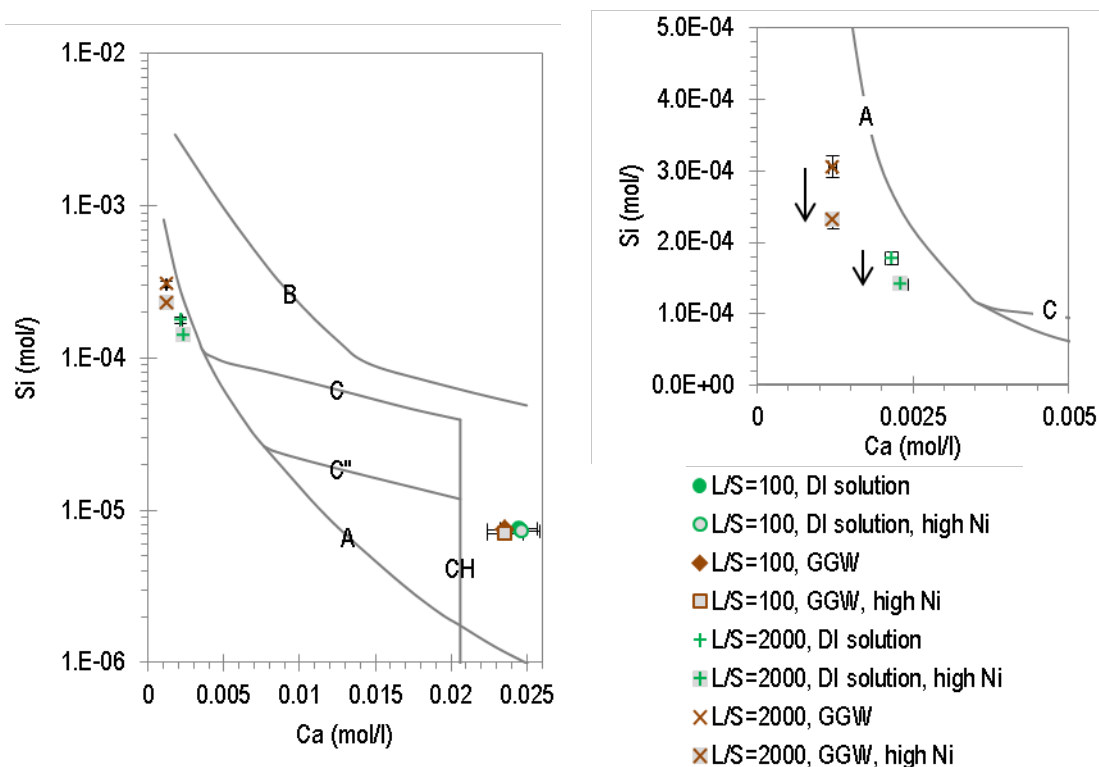


Figure 72 Plot of mean measured aqueous concentrations of Si versus Ca after batch experiments without and with $5 \cdot 10^{-4}$ mol/l Ni. Results from both degradation stages of Sulfadur HCP (coloured points) are compared in the solubility diagram of pure C-S-H phases by Chen, Thomas et al. (2004) which is already shown in Figure 61. The right figure is a zoom on results from high L/S ratio which is also included in left figure. Arrows indicate lower concentrations in high Ni concentration experiments compared to blank experiments.

Influence of different aqueous carbonate concentrations on Ni retention is not observed in batch experiments. According to SEM and XRD measurements in both equilibrated solutions Ni concentrations fall below detection limit, suggesting that the formed Ni phases are sparingly soluble, independent of calcite precipitation and carbonate content. We only observe one case where results from GG and air-equilibrated DI water differ. This concerns slightly lower Al equilibrium concentration in granitic groundwater at high L/S ratio. However, decreased Al concentration by 4 % in DI water and by 16 % in GG water compared to blank experiments makes a difference between GG and DI water which is at the limit of measurement significance.

7.1.2 Retention in Flow-Through Conditions

7.1.2.1 Ni Solid Phases

The concentration of Ni in flow-through experiments is low with a maximum load of 10^{-7} mol/l in input solution. However, we made mappings and single-point analyses by SEM of recovered HCP powder and of the filter. Both samples were taken from experiment FLS9 with highest Ni load in flow-through series. No Ni was detected, neither in the HCP, nor on the filter.

7.1.2.2 Ni Solutions

We performed three experiments with the flow-through reactor in which we added Ni to DI water and GG water. Ni concentrations in the outflow show erratic values.

We performed a ‘blank’ experiment without HCP to test influence of filters, tubing, the reactor cask and filter support on the evolution of Ni concentrations. DI water was used as input solution, adjusted to pH 11.4 with NaOH and spiked with $1 \cdot 10^{-8}$ mol/l Ni. The pump rate was the same as in all flow-through experiments with Sulfadur HCP. We collected two outflow samples of 32 ml representing the initial phase of experiments. Measured concentrations in outflow solutions decrease and fall below detection limit of 10^{-9} mol/l. Consequently, adsorption on parts of the experimental setup biases experimental results for Ni which we discarded and do not present here.

7.1.3 Discussion and Conclusions

We observe formation of nickeliferous phases during batch experiments at both investigated degradation stages in GG water. At low L/S ratio a phase (called ‘Ni-rim’) that we identify as Ni-Al LDH precipitates which also is proven to be present at high L/S ratio (called ‘Ni-ring’). Moreover, at high L/S ratio another nickeliferous phase forms which resembles Ca-exchanged C-S-H (in analogy called ‘Ni-S-H’).

Ni is scavenged effectively in all batch experiments. After equilibration Ni concentration drops below detection limits of $\sim 10^{-8}$ and $\sim 10^{-7}$ mol/l at pH 12.5 and 11.6 in all equilibrated solutions from experiments with DI and GG water to which Ni was added. XRD analysis of all degraded solid samples from DI and GG water systems do not show additional reflections of Ni phases. Due to the low amount of added Ni at low L/S ratio even perfectly crystalline Ni-Al LDH would not be detectable by XRD. Contrarily, at high L/S ratio the amount of added Ni is very high and if the Ni controlling solid phase was crystalline, it would have been detectable. As this is not the case we conclude that the Ni-S-H precipitate is amorphous.

Ni-rim and Ni-ring show similarities with SEM images of Ni-Al LDH from Vespa, Dähn et al. (2006a). While they distinguish between inner- and outer-C-S-H as neighbouring phases, we only identify C-S-H in the core. However, differences may be due to other experimental methods of their study

compared to ours. At low L/S ratio reduced Al concentration indicates that Al is involved in the formation of the nickeliferous phase. Taking into account bias due to neighbouring phases in detailed SEM analyses of Ni-ring and Ni-rim the compositions of both phases are alike (Table 25), suggesting that both phases are the same solid phase. Both, Ni-rim and Ni-ring were encountered in singular spots which raises the question if the phases incorporated Ni from the background content of Sulfadur cement, or if they formed from added aqueous Ni. From SEM images we observe that the phases are embedded in epoxy resin which indicates that during experiments they were in contact with the solution (Figure 63 and Figure 71). Therefore, it can be assumed that each phase is stable at the corresponding experimental conditions. In this case it is not relevant if incorporated Ni stems from the HCP or was added to the solution. Due to small size of phases analysis of the compositions is hampered. Excluding those elements more importantly present in neighbored phases gives a composition consisting mainly of Ni, Al and S. For the above reasons we conclude that both, Ni-rim and -ring are a Ni-Al LDH. In contact with HCP Ni-Al LDH has so far only been observed experimentally above pH 12.5 (see chapter 3.3.2), but this study indicates that it still is stable in severely degraded HCP at pH ~ 11.6.

We identify X-ray amorphous Ni-S-H at high L/S ratio by SEM analysis. In appearance it resembles C-S-H and extends over large areas in polished sections of HCP grains. We therefore assume it is the main Ni retaining phase at pH ~ 11.6. Due to the observed abundance in the solid it can be excluded that this phase is an artefact from the Ni background content of HCP. We find indications for fostered dissolution of C-S-H in presence of high Ni concentration and disintegration of C-S-H by exchange of Ca with Ni.

At high L/S ratio Si concentrations decrease compared to blank experiments when high concentrations of Ni are added and Ni-S-H forms. In these systems degradation of HCP is fostered, indicated by disintegration of HCP particles and formation of voluminous, greenish flocks. Moreover, we observe Ni to promote decalcification of C-S-H. Consequently, we would expect that more C-S-H gets dissolved, resulting in higher aqueous Si concentrations compared to Ni free experiments. We suggest that C-S-H may not be the Si controlling phase in these experiments, but Ni-S-H may control Si concentrations in the equilibrated solution instead.

We conclude that Ni fostered HCP degradation may become an important issue with regard to the longevity of cementitious barrier materials. A focussed study would allow to estimate the risk of wastes with high Ni inventories to potentially accelerate degradation of cementitious material. However, the detrimental effect is probably overestimated since we used Ni concentrations orders of magnitudes higher than solubility limits at high pH of cementitious conditions. Nevertheless, in the case of solubility limited concentrations Ni enhanced HCP degradation may play a role on the long term if considerable amounts of Ni bearing solution are expected to come in contact with cementitious barriers.

To evaluate whether Ni-S-H is precipitating from solution or forming by replacement of Ca in C-S-H we compare parameters of Ca-Ni exchange with Ca-Mg exchange. The charge of Ca, Mg and Ni is +2 and Ca has largest ionic radius, followed by Mg and Ni. Recent investigations show that there exists

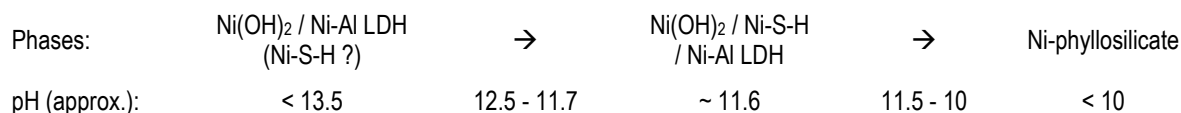
no solid-solution series between M-S-H and C-S-H, but two distinct phases form in Ca-Mg-Si-H₂O systems (Lothenbach et al. 2014). Since Ni is even smaller than Mg a solid-solution between a Ni end-member and C-S-H is unlikely. Moreover, this is also supported by presence of degraded C-S-H in direct contact with Ni-S-H after four weeks equilibration. Due to the similarity with C-S-H and high Si concentration of Ni-S-H we assume that its formation follows a dissolution- and reprecipitation process of C-S-H. However, for verification synthesis experiments free of HCP would be required, allowing for derivation of thermodynamic data of Ni-S-H and elucidation of its relation to C-S-H.

XRD diffractograms made after two years storage of samples from high L/S ratio experiments reveal changes in the solid phases. First, reflections from aragonite appear in all samples, from experiments with and without Ni, in DI as well as in GG water. The formation of aragonite is probably due to carbonation by CO₂ from the air (Black, Breen et al. 2007). Second, an additional reflection from lattice spacing of 4.77 Å appears in experiments with high Ni load which could neither be indexed by cement phases, nor by known Ni-phases. However, only 3 out of 4 samples (1 in 2 from DI water and 2 in 2 from GG water) develop this reflection. Appearance of the same reflection in 1 out of 4 analysed samples from experiments with no or low added Ni concentration puts into question if this reflection does originate from a nickeliferous phase. Consequently, we cannot certainly assign the reflection to Ni-S-H or Ni(OH)₂.

Our observations regarding the role of calcite precipitation on Ni retention are in accordance with findings by Van Gerven, Cornelis et al. (2006) and Aggarwal, Angus et al. (2000) who found that the influence of limestone on Ni sorption to HCP and release from it is negligible. Referred to our SEM-EDX analysis Ni is not associated with calcite after batch experiments while nickeliferous precipitate is abundant. We conclude that the effect of carbonate on Ni retention at the employed conditions is negligible.

According to findings from natural systems the Ni-S-H phase may be considered as a precursor of Ni-phyllosilicate type minerals which are stable at and below pH 9-10, somewhat lower than experimental pH 11.6 from this study.

Considering our observations and findings from the cited studies in chapter 3.3.2 we suggest the following sequence of Ni solubility controlling solid phases during degradation of cementitious systems:



To our knowledge there are no kinetic studies of Ni(OH)₂ precipitation, but in analogy to other divalent hydroxides it can be assumed that it is a relatively fast process. Precipitation of a more complex phase like Ni-S-H and probably referring disintegration of C-S-H by a dissolution-precipitation reaction is expected to be significantly slower. Considering the observations by Vespa and co-workers (chapter 3.3.2) it is likely that Ni-S-H formation is preceded by precipitation of Ni(OH)_{2(am)}. However, in our study we did not vary contact time and cannot observe kinetic sequences from batch experiments.

Up to now discussion on Ni solubility at alkaline conditions mainly argues about the degree of hydrolysis of aqueous Ni and whether Ni(OH)_{2(am)} or Ni-Al LDH is the solubility limiting solid phase. Ni-Al LDH has so far only been observed experimentally above pH 12.5. Our study shows that it is stable at pH 12.5 and also at pH 11.6 in degraded HCP. Further, here identified Ni-S-H extends the discussion on the fate of Ni in case of severely degraded cementitious barriers. To our knowledge Ni-S-H has not been described, yet. As Ni-S-H is amorphous it might have been overlooked in previous studies. Studies investigating Ni in HCP by Scheidegger, Wieland et al. (2000), Vespa, Dähn et al. (2006a) and Wieland, Tits et al. (2006), for example, did not publish measured pH, aqueous Si concentrations or C/S ratio of C-S-H. These are parameters which would allow to evaluate possible formation of Ni-S-H in these studies.

7.2 Selenium

7.2.1 Retention in Batch Conditions

7.2.1.1 *Se Solid Phases*

The Se content of Sulfadur HCP quantified by XRF is 4.76 µmol/kg (376 µg/kg), referred to air-dried HCP mass. None of the experiments in which Se(VI) was added show any difference compared to samples from blank experiments regarding their XRD diffractograms. The composition of degraded HCP is the same as given in chapter 6.1.1

Analyses of the Se(VI) doped solutions after equilibration with HCP in batch experiments prove retention of Se(VI) only at low L/S ratio, i.e. in equilibrium with portlandite. By SEM-EDX we did not find any Se(VI) hot spot or quantifiable X-ray signature in samples from experiment B6 in which highest Se(VI) concentration was applied. We assume this is due to the little amount of the Se(VI) which was used. According to mass balance the load of Se(VI) adsorbed to HCP is 0.04 wt.%. Nevertheless, by SEM and XRD identified solid phases of HCP which may adsorb Se(VI) at low L/S ratio are ettringite, hydrotalcite / monocarboaluminate and C-S-H.

7.2.1.2 *Solutions*

We investigate Se(VI) retention by Sulfadur HCP at Se(VI) concentrations from 1·10⁻⁶ mol/l to 2·10⁻⁴ mol/l. Since these concentrations are below known solubility limits of Se(VI) phases in cementitious systems we exclude precipitation as a retention mechanism. Background concentrations in experiments without Se(VI) addition are below detection limit of 1·10⁻⁸ mol/l. We therefore regard HCP inherent Se(VI) as negligible for results of our sorption study.

Blank experiments were performed with DI and GG water at the same conditions as experiments, but without addition of HCP in order to test retention to container walls. In DI and GG water concentration remains within 3 % of the spiked concentration ($7.6 \cdot 10^{-5}$ mol/l).

At low L/S ratio of $0.1 \text{ m}^3/\text{kg}$ and pH 12.5 about 50 % of Se(VI), added to DI and GG water, are retained by HCP. Measured redox potentials in both types of solutions are equal at 220 ± 4 mV (SHE), indicating that Se(VI) is the stable redox species in the systems. We assess sorption isotherms for these experiments, based on six individual experiments at two different initial Se(VI) concentrations (Figure 73). Though only two initial Se(VI) concentrations are given, sorption results can be interpreted in terms of a Freundlich isotherm since linear regression of results gives slopes of 1.01 and 1.03 for DI and GG water, respectively. This indicates that only linear sorption processes account for removal of Se(VI) from solution. Analytic results thereby reconfirm that precipitation of Se(VI) phases does not occur at the investigated conditions.

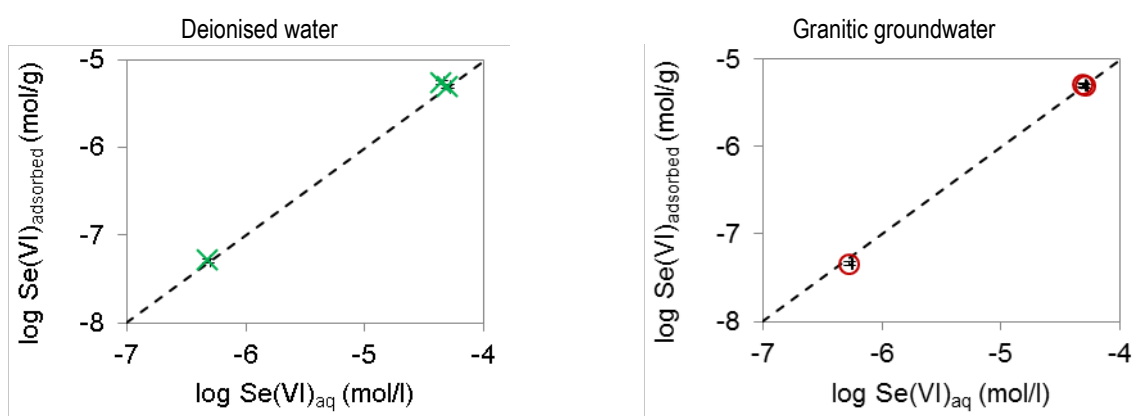


Figure 73 Sorption isotherms of Se(VI) on Sulfadur HCP after equilibration at $0.1 \text{ m}^3/\text{kg}$ L/S ratio and pH 12.5. With each solution three sorption experiments were performed at initial concentrations of $9.95 \cdot 10^{-7}$ and $9.95 \cdot 10^{-5}$ mol/l. Stippled lines indicate slope of 1.

From experimental results on repartitioning of Se(VI) between HCP and DI water at low L/S ratio we derive a distribution coefficient K_d of $0.11 \pm 0.01 \text{ m}^3/\text{kg}$. At the same conditions, but in GG water, we derive a K_d of $0.095 \pm 0.009 \text{ m}^3/\text{kg}$, i.e. slightly lower than in DI water considering that the standard deviations are similar.

For experiments at high L/S ratio of $2 \text{ m}^3/\text{kg}$ and pH ~ 11.6 we directly dissolved Na_2SeO_4 salt in the starting solutions to obtain the same aqueous Se(VI) concentrations as in experiments at low L/S ratio. Measured redox potentials in both types of solutions are equal, as expected, at 255 ± 25 mV (SHE) and indicate that Se(VI) is the stable redox species in the systems. After four weeks of equilibration measured remaining Se(VI) concentration in GG water as well as DI water show no deviation from the initially added concentrations. In contrast to low L/S ratio, we do not observe adsorption of Se(VI) when HCP is severely degraded. However, it is possible that sorption occurs within analytical error. More precisely, adsorption that might have occurred in any case would have been below $0.1 \text{ m}^3/\text{kg}$.

In one experiment at high L/S ratio with GG water and high Se(VI) addition of $2 \cdot 10^{-4}$ mol/l, we observe by factor 10 lower Ca concentration ($1.1 \cdot 10^{-4}$ mol/l), compared to blank experiments. Contrarily, aqueous Si concentration remains unchanged and Se(VI) is not retained measurably. Therefore, we assume that a calcium selenate precipitates and interaction of Se(VI) with C-S-H is unlikely. Moreover, we evaluate the stability of Se(VI) phases by computing saturation indices for the measured solution composition using thermodynamic data from the OECD-NEA review (Olin, Noläng et al. 2005). For this we also include Mg to be present in solution at concentration of the detection limit and consider carbonate to be in equilibrium with calcite. Results indicates that any Se(VI) phase is undersaturated at these conditions. Hence, we regard this Ca measurement as an outlier.

7.2.2 Retention in Flow-Through Conditions

7.2.2.1 *Se Solid Phases*

To identify Se(VI) association with solid phases we analysed degraded HCP by SEM. Samples were taken from a flow-through experiment with air-equilibrated DI water and Se(VI) concentration of $7.6 \cdot 10^{-5}$ mol/l (FLS10). We made single-spot analyses and element-mapping on epoxy-embedded, polished surfaces and on loose powder which we gently pressed onto carbon-tape.

On the polished surfaces we do not detect Se in the sample, neither by element mapping, nor in chemical analyses of single spots. In polished surfaces minerals are cut-through which reduces areas of rims and adsorbed Se(VI), potentially present on grain surfaces. In contrast, element mapping of loose powder on undamaged surfaces shows a relatively broad dissemination of Se over degraded HCP grains (Figure 74).

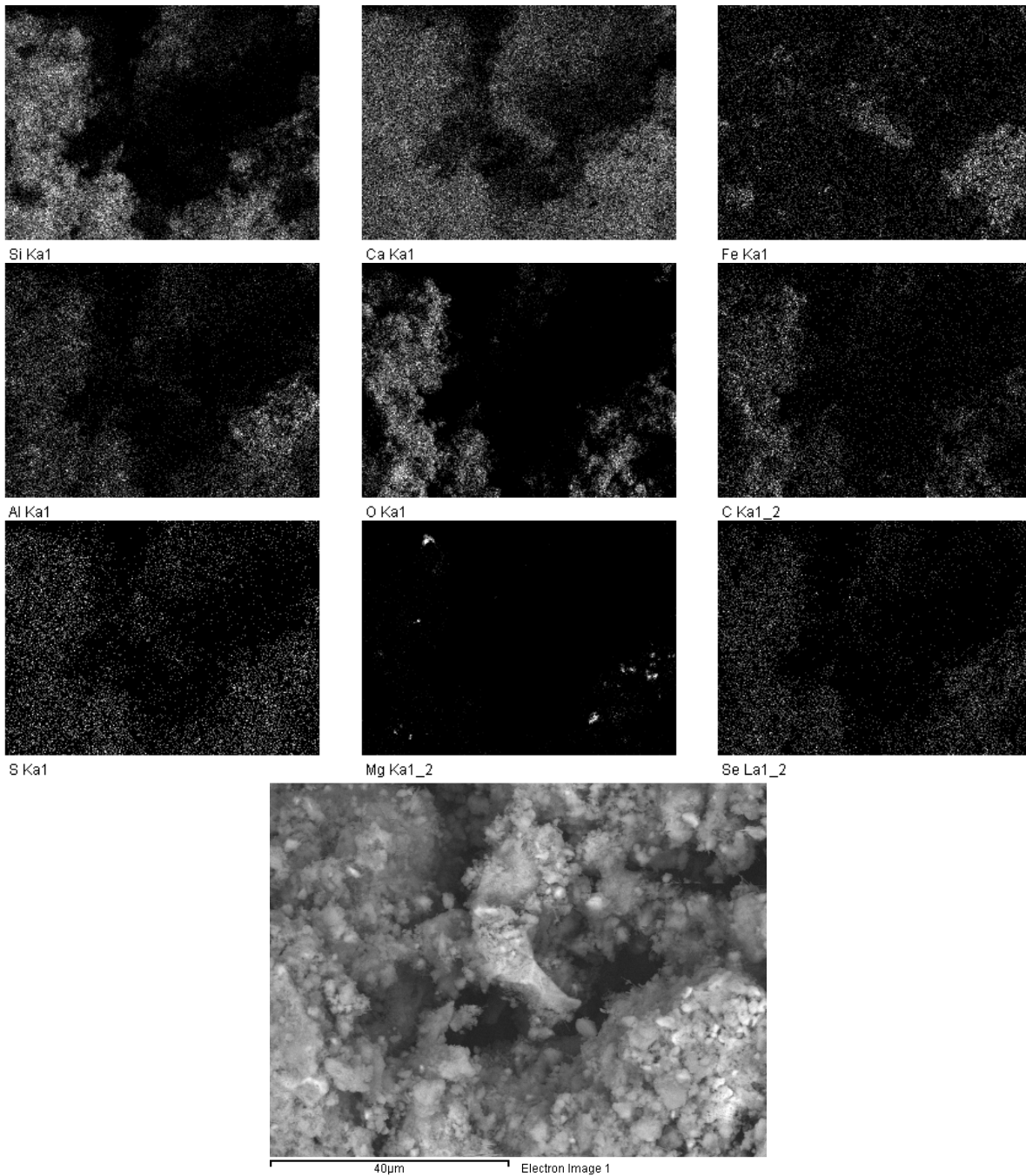


Figure 74 SEM-EDX element maps of loose Sulfadur HCP powder from a flow-through experiment with air-equilibrated DI water and $7.6 \cdot 10^{-6}$ mol/l Se(VI) concentration (FLS10). At the bottom is an SE image of the area corresponding to elemental maps. Note that distributions of Al, Ca, S and Si show similar patterns.

According to elemental distributions, Se occurs together with Al, Ca, S and Si (Figure 74). The SEM-SE image illustrates that most grains are much smaller than the areas of Se accumulation. We do not find any Se(VI) adsorbing AFm or AFt phase after flow-through experiments, but fine particles, basically C-S-H, covering most parts of larger grains and filling interstices. We assume that Se(VI) which is retained until completion of the experiment is associated to C-S-H.

7.2.2.2 Se Solutions

Of the studied elements, Se(VI) is the one with lowest inventory in the utilised Sulfadur HCP. Similar to batch experiments, Se(VI) mobilisation from HCP in flow-through experiments without added Se(VI) is below detection limit. In other words, there is no quantifiable bias by Se(VI) released from HCP in our retention study. To analyse Se(VI) retention we spiked DI water input solution with $7.8 \cdot 10^{-5}$ mol/l and GG water with $1.4 \cdot 10^{-7}$ mol/l, $1.1 \cdot 10^{-6}$ mol/l and $7.8 \cdot 10^{-5}$ mol/l Se(VI).

During degradation stage I_{FI}-a a comparatively high fraction of Se(VI), up to 17 % of inflowing Se(VI), is retained by the thin layer of HCP powder at all experimental conditions. To illustrate Se(VI) 'breakthrough' in outflow solution we relate measured Se(VI) concentrations to input concentrations, plotted versus time (Figure 75). During degradation stage II_{FI} and III_{FI}, where pH decreases more slowly due to C-S-H dissolution, a smaller fraction of Se(VI) is retained. In two out of four experiments with high Se(VI) concentration retention ceases completely towards the end of flow-through runs, but Se(VI) concentration never exceeds the input concentration. This indicates that once retained Se(VI) is not remobilised later on during flow-through experiments. We therefore assume that Se(VI) is still adsorbed to HCP.

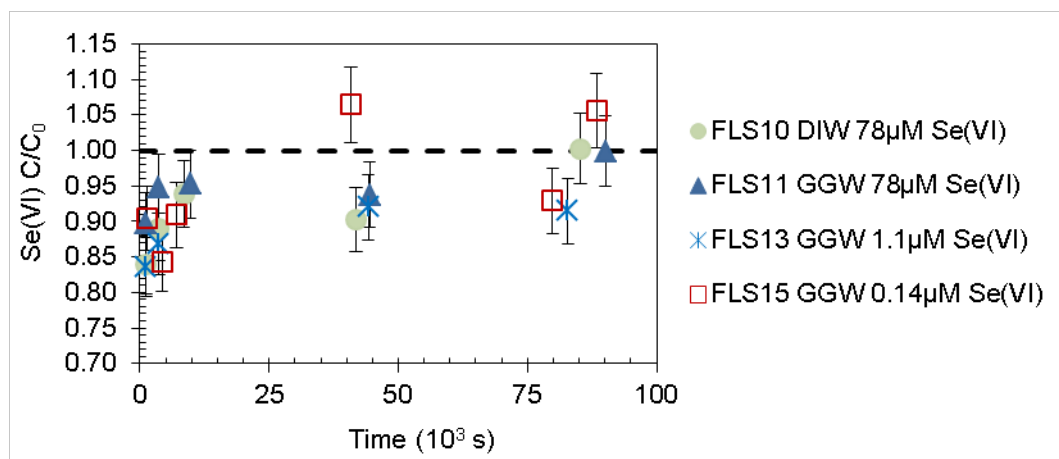


Figure 75 Breakthrough plot of Se(VI), giving the ratio of measured outflow solution concentration (C) and spiked input solution concentration (C₀) for flow-through experiments with DI and GG water and varying Se(VI) concentration.

To understand the underlying mechanism of Se(VI) retention under flow-through conditions we compare parameters of different experimental runs. In the two experiments at high Se(VI) concentration retention ceases with DI and GG water, while in experiment FLS13 with almost two orders of magnitude lower Se(VI) concentration retention continues. This indicates that at this degradation stage the number of available sorption sites has decreased and / or sorption sites are saturated at high Se(VI) concentration. In experiment FLS15 with lowest Se(VI) concentration Se(VI) is initially retained similar to experiments with higher concentrations. However, in degradation stages II_{FI} and III_{FI} we observe scattering Se(VI) concentrations in outflow solution. Due to very low input concentrations in this experiment it is possible

that Se(VI) bias is an analytical problem. Mass balance supports this conclusion since taking into account the measured concentrations Se(VI) would significantly exceed the total added amount of Se(VI).

We tested whether Se(VI) is retained on filters, tubing, the reactor cask or filter support by performing a ‘blank’ experiment without HCP in the reactor (as described in chapter 7.1.2.2). DI water was adjusted with NaOH to pH 11.4, spiked with $1.24 \cdot 10^{-6}$ mol/l Na_2SeO_4 and pumped at the same rate as in retention flow-through experiments. In two samples, representing the initial stage I_{FI} -a of flow-through experiments, which is where most Se(VI) retention occurs, we measured Se(VI) concentrations of $1.21(\pm 0.06) \cdot 10^{-6}$ and $1.26(\pm 0.06) \cdot 10^{-6}$ mol/l, i.e. identical to input concentration. Consequently, we exclude adsorption of Se(VI) on parts of the experimental setup during experiments.

To evaluate the influence of aqueous S(VI) concentration on Se(VI) retention we compare experiments with equal concentrations of Se(VI) performed with DI and GG water (Figure 76). Even though S(VI) concentration is significantly higher in GG water than in DI water, Se(VI) retention is equal in both solutions. Therefore, results suggest that under the tested conditions S(VI) has no influence on the retention of Se(VI).

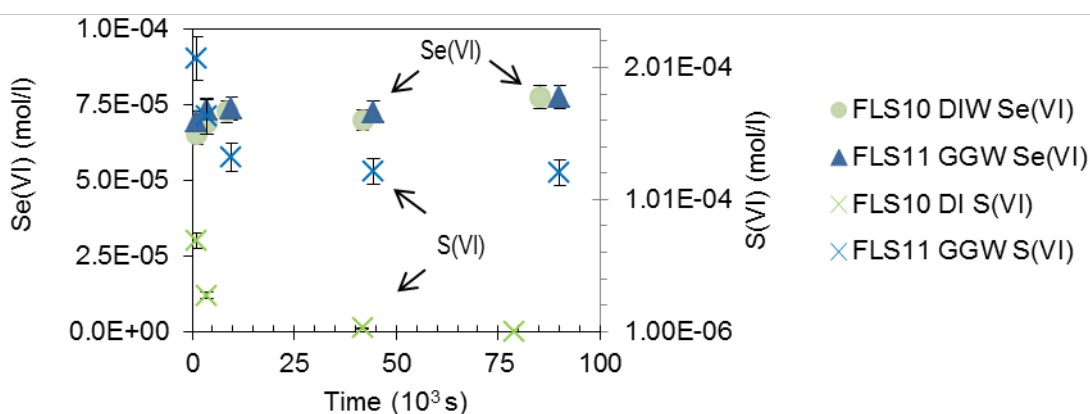


Figure 76 Concentrations of Se(VI) and S(VI) in outflow solution from two experiments with equal initial Se(VI) concentration of $7.75 \cdot 10^{-5}$ mol/l. Note that S(VI) concentration in GG water is always higher than Se(VI) concentration.

We roughly estimate the initial retardation factor of Se(VI) by plotting the evolution of initial Se(VI) concentrations versus time and fitting to the experimental data (Figure 77). For the four Se(VI) retention experiments we obtain retardation factors around 24 - 36, corresponding to an average distribution coefficient of less than $0.02 \text{ m}^3/\text{kg}$. The observed K_d in equilibrated systems at pH 12.5 is almost an order of magnitude higher. Moreover, for the weak retention of Se(VI) during stage II_{FI} to III_{FI} (after about $4 \cdot 10^3$ s), we calculate an ‘apparent distribution coefficient’ of roughly $9 \cdot 10^{-4} \text{ m}^3/\text{kg}$ when assuming a mean density of $1600 \text{ kg}/\text{m}^3$ (Gluth 2001) for HCP and a porosity of 0.95 in the reactor cell which is derived geometrically from the parameters given in (chapter 4.2.2). Due to continuous degradation of the HCP, the high pump rate and therewith fast renewal time of solution in the reactor of

about 40 seconds, partitioning to the cement does not represent equilibrium conditions. That retention does occur under these conditions indicates that adsorption of Se(VI) to HCP is a fast process.

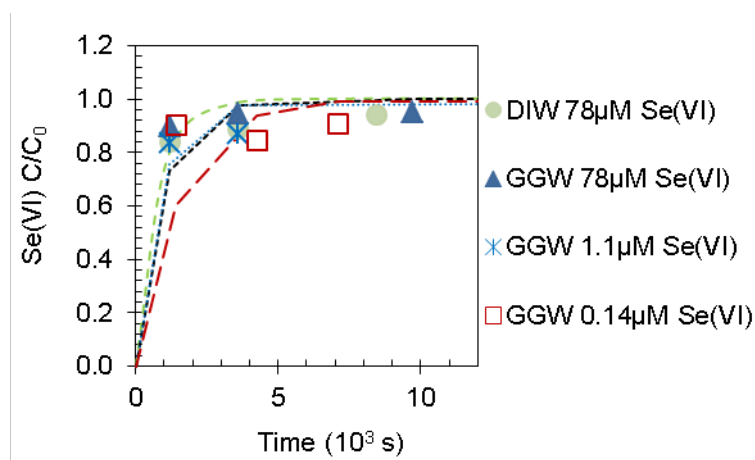


Figure 77 Fitting of retardation factors to experimentally measured Se(VI) concentration in outflow solution at the beginning of experiments. To obtain the stippled lines retardation factor was varied between 24 and 36. Only initial, stronger Se(VI) retention is considered, why computed lines approach $C/C_0 = 1$ very fast.

7.2.3 Discussion and Conclusions

In batch experiments determined K_d values for adsorption of Se(VI) on HCP, equilibrated at 0.1 m³/kg L/S ratio, are similar in DI and GG water (0.11 ± 0.01 m³/kg and 0.095 ± 0.009 m³/kg, respectively). Further, Freundlich sorption isotherms with slopes of almost unity suggest sorption and not precipitation being the retention mechanism.

Similar to blank experiments, XRD analyses of HCP degraded in both solution types with Se(VI) at low L/S ratio identifies ettringite and hydrotalcite/monocarboaluminate in the solid. Since these phases are favourable for Se(VI) adsorption (chapter 3.3.3) it is likely that Se(VI) is mainly retained by adsorption on or ion exchange with at least one of these phases. Mass balance and modelling indicate precipitation of a small amount of ettringite at low L/S ratio in GG water. According to modelling, here 6 % more ettringite is present compared to the DI water systems. This may explain the slightly lower sorption of S(VI) in GG water. We therefore conclude that the type of solution has no or little effect on Se(VI) retention at low L/S ratio for the investigated conditions.

S(VI) concentrations are solubility controlled by ettringite in both systems at low L/S ratio and are equal in both solutions types after equilibration, as described in chapter 6.1. This explains the similar distribution coefficients measured in both solutions, even though experiments with GG water were starting with high S(VI) concentration while in DI water initially there was no S(VI) in solution.

For systems reaching equilibrium conditions where S(VI) concentration is solubility controlled we find that the initial S(VI) concentration does not influence Se(VI) adsorption. It is the equilibrated S(VI) concentration which influences Se(VI) retention. However, initial S(VI) concentration may to a low extent influence sorption since it controls precipitation / dissolution of Se(VI) adsorbing phases like

ettringite. These aspects are important to consider when evaluating Se(VI) sorption on engineered barriers if water is expected to flow sufficiently slow to equilibrate with cementitious material.

In severely degraded HCP at 2 m³/kg L/S ratio ettringite, the major Se(VI) retaining phase with surface sites appropriate to bind and retain Se(VI), dissolves in DI water, as well as in GG water. In the case of hydrotalcite modelling indicates its formation in GG water, but as explained in chapter 6.1.1 presence of a small amount is only confirmed by XRD analysis for DI water. In this degradation stage present C-S-H is less favourable since decalcification and lower pH lead to increasingly negative surface charge and hence more repulsion of Se(VI) anion.

Our results from solution analysis are in line with absence of Se(VI) adsorbing phases. In experiments we do not see any diminution of aqueous Se(VI) concentrations at high L/S ratio. Results show that sorption of Se(VI) to severely degraded HCP at pH ~ 11.6 is minor than sorption to less degraded HCP at pH 12.5. As described in chapter 6.2.5, S(VI) concentrations at high L/S ratio is $4.0 \cdot 10^{-5}$ mol/l in DI water which is in the range of added high Se(VI) concentrations. S(VI) and Se(VI) may therefore compete for sorption sites. In GG water competition is even stronger due to significantly higher S(VI) concentration of $1.4 \cdot 10^{-4}$ mol/l.

According to solubility studies, AFt and AFm phases may be suspected to be stable in degraded cementitious systems at equilibrium pore water pH around 11.6 (see chapter 3.2.2). However, our batch experiments with DI and GG water indicate that sulphate phases are unlikely to be stable at these conditions due to their limited amount and the high quantity of solution required to decalcify C-S-H until solution pH of 11.6 or lower. For generalised considerations about Se(VI) sorption on cementitious materials during degradation, presence or absence of sulphate phases is crucial. According to our results it is valid to assume their presence in less degraded systems during approximately the first high-pH stage and the second, portlandite controlled stage of cement degradation at equilibrium conditions. In more degraded systems presence of sulphate phases cannot generally be assumed and depends on their initial inventory, groundwater composition and L/S ratio.

During flow-through experiments we observe retention of Se(VI) on HCP. Results indicate the existence of at least one adsorption mechanism with fast kinetics, capable to retain Se(VI) at a residence time of only ~40 s in the reactor. Retention of Se(VI) is strongest in degradation stage Ia when portlandite is still present and C-S-H is dissolved and reprecipitated, but retention is still significantly lower compared to batch conditions.

Different to batch experiments, concentrations of S(VI) are not solubility controlled under flow-through conditions. Therefore, with GG water S(VI) concentrations are significantly higher than with DI water, in the starting solution, as well as in the outflow. We find no influence of different S(VI) concentrations on Se(VI) retention, indicating that the sorption mechanism is not affected by S(VI) competition and possibly selective for Se(VI).

Measured Se(VI) outflow concentrations never exceed input concentrations, proving that retained Se(VI) remains bound to the solid throughout experiments. Moreover, we find by SEM analysis Se after

flow-through experiments to be associated with C-S-H particles. This indicates that adsorption and retention of Se(VI) are controlled by C-S-H. However, according to literature Se(VI) sorption on C-S-H does not occur or is weak (chapter 3.3.3). We therefore also discuss retention on alternative phases in the following.

Ettringite may be responsible for pronounced initial Se(VI) retention. Our derived initial K_d values are similar to the ones determined by Rojo, Rovira et al. (2007) who identified ettringite as the Se(VI) retaining phase in their model. However, our kinetic degradation model shows that ettringite dissolves almost entirely, meaning that Se(VI) would be released again which is not observed experimentally. We conclude that strong initial retention is not caused by ettringite. Experimental and modelling results indicate precipitation of hydrotalcite during stage I_{F1}-a of flow-through experiments with GG water, but slow dissolution in experiments with DI water. Since Se(VI) retention is equal in DI and GG water we conclude that hydrotalcite is not involved in the retention of Se(VI) during flow-through experiments. Finally, we suggest that stronger retention during degradation stage I_{F1}-a is caused by sorption to dissolving and reprecipitating C-S-H. According to literature (see chapter 3.3.1), surface charge of C-S-H may be positive or neutral during degradation stage I_{F1}-a with high pH. Positive surface charge is favourable for adsorption of negatively charged Se(VI).

During degradation stages II_{F1} and III_{F1} pH is lower than 11.5 and surface charge is expected to be negative. Although these conditions do not favour Se(VI) retention, we do observe it at these stages. We give two different explanations. First, C-S-H not simply dissolves, but polymerises to longer chains while increasing its surface area up to an order of magnitude from jennite to tobermorite composition (Trapote-Barreira, Cama et al. 2014). In other words, dissolving C-S-H not simply decreases the number of available surface sites for adsorption, but undergoes transitions that even may increase available surface sites. Second, and more hypothetical, surface charge of C-S-H may be reversed during dissolution in flow-through conditions. To our knowledge, for such conditions no measurements of surface charge have been made. Accumulation of massively released Ca at the surface of incongruently dissolving C-S-H might lead to reversal of surface charge, thereby favouring electrostatic retention of Se(VI) anions.

During stage III_{F1}-a to III_{F1}-b when reactive C-S-H is depleted retention of Se(VI) ceases. We therefore conclude that lack of available C-S-H surface in contact with the solution is responsible for this behaviour.

7.3 Caesium

7.3.1 Retention in Batch Conditions

7.3.1.1 Cs Solid Phases

The Cs content of Sulfadur HCP quantified by XRF is 37.5 $\mu\text{mol/kg}$ (4.98 mg/kg), referred to air-dried HCP mass.

In batch experiments on Cs retention initial concentrations are low and few Cs is removed from solution during equilibration (chapter 7.3.1.2). Hence, the adsorbed amount of Cs on HCP is too low to be detectable by SEM. Therefore, we only analysed Cs concentrations in solutions.

7.3.1.2 Cs Solutions

At low L/S ratio of 0.1 m³/kg the amount of Cs released from Sulfadur HCP reaches values as high as the added concentration of 1·10⁻⁷ mol/l Cs (Figure 78). Results regarding sorption of Cs on HCP therefore have to be interpreted differently than in the case of Se(VI) which is not released from HCP.

Blank experiments with DI and GG water at the same conditions as experiments, but without addition of HCP additionally confirmed that no sorption of Cs to container walls occurs. In DI and GG water concentration remains within 4 % of the spiked concentration (1.0·10⁻⁶ - 1.0·10⁻³ mol/l). We determine the degree of Cs mobilisation from HCP by measured Cs concentrations in the equilibrated solutions of blank experiments. Relating the amount of dissolved Cs in solution to total Cs content of HCP (37.5 μmol/kg) gives 29 ± 1 % mobilisation of Cs inventory at low L/S ratio for DI and GG water (Table 28). Equal Cs concentrations in all experiments where Cs has not been added shows that mobilisation of HCP inherent Cs is not affected by addition of Ni or Se(VI).

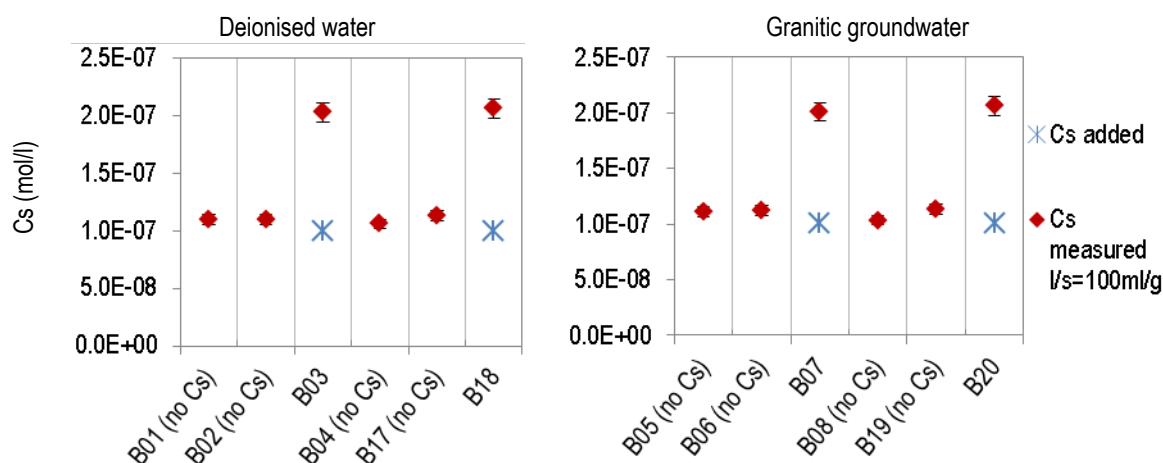


Figure 78 Measured Cs concentrations from batch experiments equilibrated at 0.1 m³/kg L/S ratio with DI water (left) and GG water (right). Blank experiments without Cs addition and experiments with 1·10⁻⁷ mol/l added Cs are compared.

At high L/S ratio of 2 m³/kg the aqueous background concentration of Cs in blank experiments is more than an order of magnitude lower than at low L/S ratio (Figure 79). However, in DI water 39 ± 3 % of Cs inventory are mobilised from HCP while we find 45 ± 5 % in GG water (Table 28) which is more than at low L/S ratio.

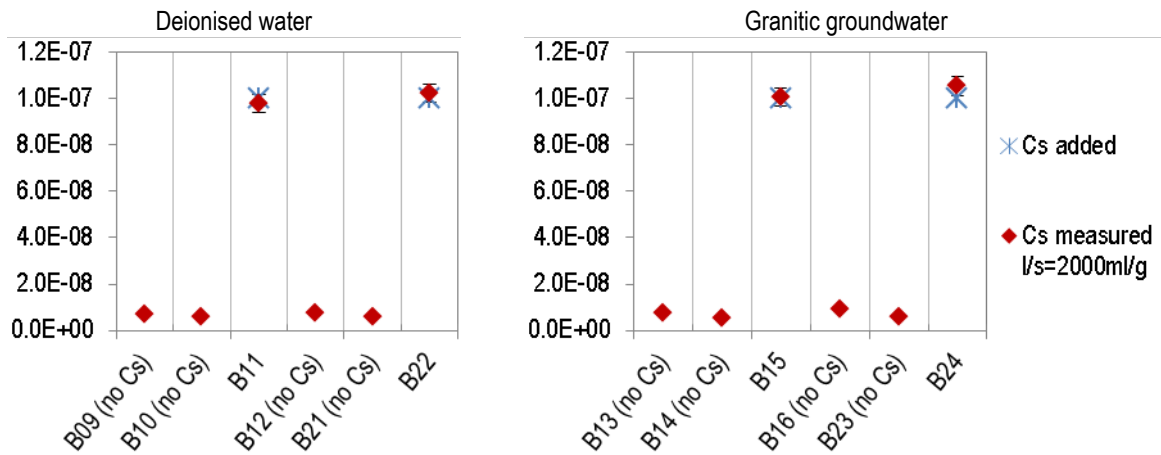


Figure 79 Measured Cs concentrations from batch experiments equilibrated at 2 m³/kg L/S ratio with DI water (left) and GG water (right). Blank experiments without Cs addition and experiments with 1·10⁻⁷ mol/l added Cs are compared.

Different to low L/S ratio, we observe influence of Ni addition on Cs mobilisation from HCP at high L/S ratio. With high Ni concentration of 5·10⁻⁴ mol/l, measured Cs concentrations are lower so that mobilisation of Cs from the inventory decreases to 32±0.3 and 30±1.5 % in DI and GG water, respectively. As described before, we find that C-S-H degradation is fostered and a Ni-S-H like phase precipitates in the case of initially high Ni concentrations (chapter 7.1.3). Less mobilisation of Cs with high Ni concentration therefore indicates that Cs either more strongly adsorbs to C-S-H with lower C/S ratio which would be in accordance with more negative surface charge, or it preferentially adsorbs to Ni-S-H.

Table 28 Measured Cs concentrations in equilibrated solutions and mobilised Cs from Sulfadur HCP inventory, all from experiments where Cs was not added. Results are given for different L/S ratios, solution types, and Ni concentrations.

L/S ratio	Solution	Ni concentrations	Mean measured Cs concentration	Mean mobilised Cs from inventory \pm standard deviation	Numbers of experiments
m ³ /kg		mol/l	mol/l	at.-%	
0.1	DIW	From 0 to $5 \cdot 10^{-4}$	$(1.10 \pm 0.03) \cdot 10^{-7}$	29 ± 0.8	4
	GGW	From 0 to $5 \cdot 10^{-4}$	$(1.10 \pm 0.03) \cdot 10^{-7}$	29 ± 0.9	4
	DIW & GGW	From 0 to $5 \cdot 10^{-4}$	$(1.10 \pm 0.04) \cdot 10^{-7}$	29 ± 1	8
2	DIW	No Ni added	$(7.4 \pm 0.6) \cdot 10^{-9}$	39 ± 3.0	2
		$5 \cdot 10^{-4}$ mol/l Ni	$(6.03 \pm 0.04) \cdot 10^{-9}$	32 ± 0.3	2
		From 0 to $5 \cdot 10^{-4}$	$(6.7 \pm 0.7) \cdot 10^{-9}$	36 ± 4	4
2	GGW	No Ni added	$(8.4 \pm 0.98) \cdot 10^{-9}$	45 ± 5	2
		$5 \cdot 10^{-4}$ mol/l Ni	$(5.6 \pm 0.3) \cdot 10^{-9}$	30 ± 2	2
		From 0 to $5 \cdot 10^{-4}$	$(7.0 \pm 1.5) \cdot 10^{-9}$	38 ± 8	4
2	DIW & GGW	No Ni added	$(7.9 \pm 0.8) \cdot 10^{-9}$	42 ± 4	4
		$5 \cdot 10^{-4}$ mol/l Ni	$(5.8 \pm 0.2) \cdot 10^{-9}$	31 ± 1	4
		From 0 to $5 \cdot 10^{-4}$	$(6.9 \pm 1.2) \cdot 10^{-9}$	37 ± 6	8

Due to release of Cs from Sulfadur HCP we determine distribution coefficients for Cs by taking determined background concentration into account. In doing so we assume that mean Cs release from HCP is not influenced by addition of Cs to the solution. Consequently, we subtract background concentration from measured concentration in doped experiments and calculate the corrected distribution coefficient $R_{d,bc}$ according to equation (23).

$$R_{d,bc} = \frac{C - C_{add} - C_{bg}}{C} \cdot \frac{V}{m} \quad (23)$$

C , C_{add} , C_{bg} are measured, added and background Cs concentrations (mol/l), respectively. V is solution volume (m³) and m is initial cement mass (kg) as weighed.

By this method determined distribution coefficient $R_{d,bc}$ is $6 (\pm 3) \cdot 10^{-3}$ m³/kg for GG water, as well as for DI water at low L/S ratio and pH 12.5. At high L/S ratio $R_{d,bc}$ is significantly higher in both solution types, but results show more scattering (Table 29). The evaluated distribution coefficients $R_{d,bc}(Cs)$ range between 0.065 m³/kg and 0.216 m³/kg in DI and GG water for Ca concentration between $\sim 1 \cdot 10^{-3}$ mol/l and $\sim 2 \cdot 10^{-3}$ mol/l and alkali concentration between $\sim 5 \cdot 10^{-5}$ mol/l and $\sim 3 \cdot 10^{-3}$ mol/l. This variation of $R_{d,bc}$ up to factor 3 indicates influence of experimental conditions on Cs adsorption. We observe for experiments at high L/S ratio and pH ~ 11.6 that higher alkali concentrations go along with decreasing Cs retention.

Table 29 Distribution coefficients $R_{d,bc}$ for Cs adsorption on severely degraded HCP at 2 m³/kg L/S ratio. All solutions were spiked with 10⁻⁷ mol/l CsCl and NiNO₃, as well as variable amounts of Na₂SeO₄. Ca, Na and K concentrations are approximated quantities, derived from experiments without Cs addition.

Sample	Solution	$R_{d,bc}(Cs)$	Cs	Na ₂ SeO ₄	pH	Ca	K	Na
		m ³ /kg	(Added) mol/l	(Added) mol/l	-	mol/l	mol/l	mol/l
B11	DIW	0.216	1·10 ⁻⁷	0.8·10 ⁻⁶	11.66	~2.0·10 ⁻³	~2.9·10 ⁻⁵	~4.6·10 ⁻⁵
B22	DIW	0.113	1·10 ⁻⁷	2.1·10 ⁻⁴	11.62	~2.0·10 ⁻³	~2.9·10 ⁻⁵	~4.6·10 ⁻⁴
B15	GGW	0.173	1·10 ⁻⁷	1.0·10 ⁻⁶	11.55	~1.2·10 ⁻³	~1.3·10 ⁻⁴	~2.0·10 ⁻³
B24	GGW	0.065	1·10 ⁻⁷	2.1·10 ⁻⁴	11.47	~1.2·10 ⁻³	~1.3·10 ⁻⁴	~3.3·10 ⁻³

7.3.2 Retention in Flow-Through Conditions

7.3.2.1 Cs Solid Phases

In flow-through experiments on Cs retention we do not observe any retention of Cs by HCP according to outflow solution analyses (chapter 7.3.2.2). Hence, the adsorbed amount of Cs on HCP is too low to be detectable by SEM. Therefore, we only analysed Cs concentrations in solutions.

7.3.2.2 Cs Solutions

Cs retention in flow-through conditions is studied in a range of added Cs concentrations from 1·10⁻⁶ to 1·10⁻³ mol/l with DI and GG water. Within analytical error of analyses outflow concentrations of Cs scatter randomly around the starting concentrations at any of the conditions tested (Figure 80). In other words, we observe no retention of Cs in flow-through conditions - neither by sane HCP at initially high pH, nor by degraded HCP at finally lower pH.

In contrast to batch experiments, added Cs concentrations are orders of magnitude higher than background concentrations in flow-through experiments. Therefore, we cannot distinguish between mobilised and added Cs for determination of distribution coefficients as we did for batch experiments (chapter 7.3.1.2).

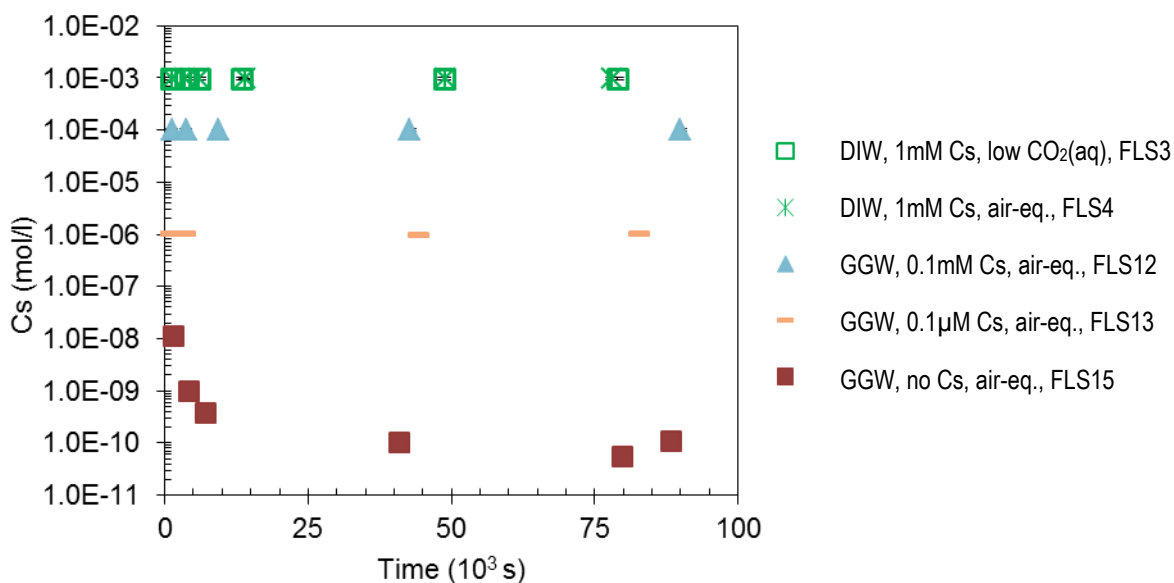


Figure 80 Measured Cs concentrations in outflow solutions from flow-through experiments without added Cs (filled squares) and with varying Cs addition (other symbols).

In flow-through experiments without added Cs the concentrations in outflow solutions are mostly below the calibrated range of concentrations of the analysis method. In the case of experiment FLS15, performed with GG water, we decreased our detection limit for Cs compared to other experiments and observe that Cs is mobilised from HCP (Figure 80). In total a release of ~ 34 % of HCP's Cs inventory is reached over the whole experiment, i.e. a similar fraction of Cs as in batch experiments (chapter 7.3.1.2). Further, the evolution of Cs release is similar to the one of Ca in flow-through experiments, with initially fast decreasing concentrations and then approximately constant release at later stages of degradation.

7.3.3 Discussion and Conclusions

In batch experiments we observe weak sorption of Cs on HCP at low L/S ratio and comparatively stronger sorption at high L/S ratio. In the case of flow-through experiments no retention occurs – Cs behaves like a tracer.

At low L/S ratio, i.e. at pH 12.5, we correct measured Cs concentrations by background concentrations to derive the distribution coefficient $R_{d,bc}$. The obtained value of $6 (\pm 3) \cdot 10^{-3} \text{ m}^3/\text{kg}$ for SRPC equilibrated with both, DI and GG water, is slightly higher than distribution coefficients in literature (chapter 3.3.4). This might be due to the comparatively higher L/S ratio of $0.1 \text{ m}^3/\text{kg}$ used in our study to investigate Cs retention at portlandite equilibrated conditions. This means that Na and K concentrations are already significantly diluted compared to studies using, e.g. $0.01 \text{ m}^3/\text{kg}$. However, in a real nuclear waste repository the portlandite controlled degradation stage at pH 12.5 is expected to last longer than the initial degradation stage during which alkali concentrations are very high (Figure 4).

As expected, retention of Cs by HCP is stronger at high L/S ratio, i.e. at pH ~ 11.6, compared to low L/S ratio. We derive distribution coefficients between $0.06 \text{ m}^3/\text{kg}$ and $0.2 \text{ m}^3/\text{kg}$ for Cs sorption on severely degraded HCP in both types of solutions. There is little data available in literature to compare

with our at low pH regime derived distribution coefficients. From experimental data by Ochs, Pointeau et al. (2006) using Portland Cement, we interpolate a value in the range of 0.1 to 0.2 m³/kg for pH ~ 11.6, which agrees well with our measurements.

We tested the surface complexation based model by Ochs, Pointeau et al. (2006), meant to derive distribution coefficients for Cs on Portland cement by considering Na and Ca as competing ions for sorption sites. As required by the model, we used experimental results on pH, as well as Na, Ca and Cs concentrations as input parameters. C/S ratio of C-S-H and sorption-site density are derived numerically from pH. Measured $R_{d,bc}$ and calculates K_d are compared in Figure 81.

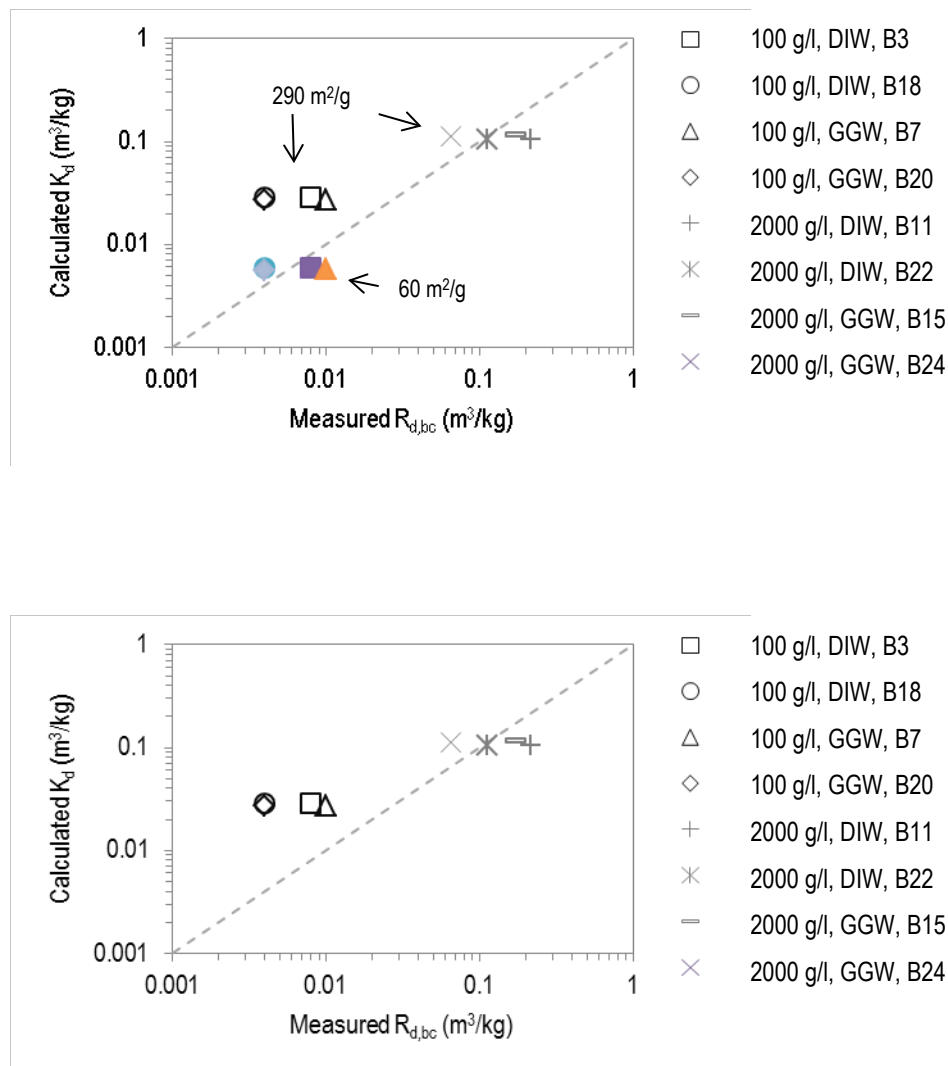


Figure 81 Comparison of measured $R_{d,bc}$ and calculated K_d values according to Ochs, Pointeau et al. (2006) at equilibrium conditions. The dashed line indicates equality between measured and calculated values. Solution type, L/S ratio and the experiment number are given in the legend. Dash signs represent experiments with final pH 11.55-11.65 and geometric symbols represent experiments at pH 12.5.

Plotted values suggest that Cs retention in experiments is more sensitive to variations of alkali concentrations than Cs retention in the model which is sensitive to fundamentally different L/S ratios, only. According to the model Cs distribution coefficient is effectively influenced by alkalis if

concentrations exceed 10^{-3} mol/l significantly. In our experiments at low L/S ratio Na concentration of $2.8 \cdot 10^{-3}$ mol/l in GG water does not show an effect on calculated K_d compared to DI water with about one order of magnitude less Na, but equal Ca concentration. This also applies for calculated K_d at high L/S ratio. In contrast to experiments in equilibrium with portlandite, calculated and experimental results match well for the more severely degraded HCP. Results of the present study indicate that for low Cs concentrations, as used in our study, already lower alkali concentrations than considered in the model by Ochs, Pointeau et al. (2006) reduce the retention of Cs by HCP.

During flow-through experiments no retention by degrading HCP is observed, not even at presumably more favourable conditions with lower pH and decalcified HCP, i.e. also decalcified C-S-H. According to Iwaida, Nagasaki et al. (2002) the main mechanism of Cs adsorption might be structural uptake, involving hydroxylation and breaking of silicate chains (chapter 3.3.4). This reaction would compete with polymerisation of C-S-H to longer Dreierketten during degradation (chapter 3.1), hampering Cs retention in transient conditions. We suppose that other elements or species which only or mainly adsorb to silanol sites are less hampered by polymerisation of C-S-H during degradation.

Alternatively to structural uptake, we expected unspecific, electrostatical adsorption of Cs to C-S-H when pH drops below ~ 11.5 in the reactor. At these conditions surface charge of HCP (C-S-H) becomes negative (chapter 3.3.1) and Cs might be electrostatically retained. However, we do not observe Cs retention in flow-through experiments.

Trapote-Barreira, Cama et al. (2014) showed that polymerisation reaction of C-S-H is fast enough to occur within few hours residence time. They measured Ca and Si concentrations, as well as pH in the outflow solutions similar to our study. However, in our flow-through experiments residence time is less than a minute and it is possible that the structural rearrangement of C-S-H is not fast enough to evolve normally. If this affects development of silanol sites as well as surface charge, it may be speculated that during dissolution of C-S-H surface charge reverses, as discussed for Se(VI) in chapter 7.2.3. This would explain why Cs is not retained by HCP in flow-through conditions. To our knowledge, surface charge of C-S-H or HCP has never been measured in conditions comparable to our flow-through experiments.

Besides sorption, we also observed mobilisation of Cs from HCP in batch and flow-through experiments. Cementitious material contains variable trace amounts of Cs stemming from the raw products used in manufacturing of cement. In contrast to Se(VI), Cs inventory in HCP is larger, allowing for detectable amounts in solutions.

In our batch experiments with Sulfadur HCP at $0.1 \text{ m}^3/\text{kg}$ L/S ratio a smaller fraction of the Cs inventory is released to solution than at $2 \text{ m}^3/\text{kg}$ L/S ratio, indicating that a higher degree of degradation fosters Cs mobilisation. A limited total release of Cs, between 29 % and 45 %, from the HCP inherent inventory in flow-through and batch experiments confirms the observations of previous studies that a considerable fraction of Cs present during cement hydration is practically immobile. This suggests the possibility of structurally incorporated Cs in HCP.

Different parameters may influence mobilisation of Cs from HCP. Results from batch experiments indicate a tendency of GG water to enhance Cs mobilisation. We suggest three related mechanisms that are partially opposed in their effects. First, more severe degradation of the HCP by GG water, as demonstrated in chapter 6.1.1, enhances release of physically trapped or incorporated Cs. Second, the increasing number of available silanol sites on more polymerised C-S-H counteracts Cs mobilisation. Third, elevated content of alkali elements which compete with low aqueous Cs concentrations in GG water for sorption sites fosters Cs mobilisation. This effect becomes increasingly important with lower pH when higher fractions of alkali metals are present as charged, non-hydrolysed cations. However, the observed net effect when using granitic groundwater is stronger mobilisation of cement inherent Cs. This indicates that the increasing number of silanol sites due to fostered degradation of C-S-H is outweighed by competition with alkali elements.

In the case of high added Ni concentrations we observe decreased mobilisation of HCP inherent Cs at pH ~ 11.6. At these conditions presence of Ni in batch experiments alters the solid phase assembly of degraded HCP through formation of a new Ni-phase (chapter 7.1.1). Decreased mobilisation of Cs is either due to increased sorption to stronger degraded C-S-H, or by adsorption to the newly formed Ni-S-H phase which cannot be distinguished here.

We assume that the mechanisms controlling mobilisation of HCP inherent Cs are the same for intentionally cemented Cs in a nuclear waste disposal. Since we find that more than 50 % of Cs inventory are immobile, we may expect that also adsorbed Cs may be stronger retained and structurally incorporated. However, according to adsorption-desorption experiments in literature, recrystallisation was not observed, yet and probably would require extremely long time-scales for laboratory experiments. Alternatively, Cs may be incorporated in metastable C-S-H which only forms during hydration.

8 Conclusions

The aim of this study was to identify the processes affecting retention of Cs(I), Ni(II) and Se(VI) on Sulphate Resisting Portland Cement during its degradation, from sane to advanced degradation states. The focus was put on the underlying mechanisms and possible remobilisation of previously retained radionuclides due to the changing composition of the HCP. Cs, Ni and Se were chosen as radionuclides because they are considered as safety relevant for nuclear waste disposal, represent different chemical characteristics and their stable isotopes can be used in experiments. To address shortcomings of previous studies in this field a combined approach was developed. First, a thin-layer flow-through reactor from Bruno, Casas et al. (1991) was adapted and improved for the purpose of studying radionuclide retention during HCP degradation. Second, degradation, adsorption and uptake were studied in equilibrated batch systems.

Results from mostly far-from-equilibrium experiments in the newly designed flow-through reactor were in line with the established HCP degradation scheme regarding evolution of outflow solution composition as well as solid phase degradation. The evolution of the system was satisfactorily reproduced by a kinetic transport model for which a set of kinetic constants was optimised and can be used for other modelling studies. Moreover, with the thin-layer flow-through reactor it is possible to discern the different degradation stages on-line by analysis of pH, Ca and Si concentrations in outflow solutions.

Further, the thin-layer flow-through reactor was found to allow for reproducible degradation experiments using little amount of Portland cement: In far-from-equilibrium degradation experiments only 30 to 55 mg solid were sufficient. Use of the reactor hence accelerates experiments compared to other flow-through setups. Therefore, this setup could be used for future retention studies with HCP where time or stability of the atmosphere are important factors. Atmosphere control is difficult, even when working in a glove box, but crucial for several systems. Important examples are carbonate in cementitious systems and redox-sensitive elements.

To better represent geochemical conditions at a disposal site all experiments conducted in batch and flow-through setups were done with two types of solutions: deionised (DI) water and an artificial granitic groundwater (GG water). In batch experiments it was found that net capacity of GG water to degrade HCP is greater than the net capacity of DI water. Further, carbonation, leading to calcite precipitation, was identified as the major detrimental process induced by granitic groundwater. Flow-through experiments with GG water showed much faster decrease of pH than observed with DI water, due to neutralisation of liberated hydroxyl by high hydrogen carbonate content in GG water. This carbonate buffering effect was confirmed by mass balance calculations and modelling. Nevertheless, carbonate buffering of pH had no accelerating effect on dissolution rates of HCP. After flow-through experiments no difference was found between DI and GG water regarding C-S-H phase degradation. Considering fast flowing groundwater at a disposal site, this implies that the mere presence of sane cementitious phases does not guarantee alkaline geochemical conditions. Moreover, the maximum groundwater exchange rate

allowing for establishment of equilibrium conditions is not only determined by the dissolution rate of cement phases, but additionally by the hydrogen carbonate content/neutralisation capacity of the groundwater. The higher the groundwater concentration of hydrogen carbonate, the lower the exchange rate at which the solution pH is not controlled by cementitious materials.

Calcium-aluminosulphate phases, especially ettringite, have been considered and studied for their capability to retain anionic species like Se(VI). In this context, ettringite is sometimes considered to be present in cementitious materials even in severely degraded HCP, controlled by decalcified C-S-H (pH 10.5 or even below). In this study ettringite was the stable S(VI) controlling phase at equilibrium with portlandite in DI water as well as in GG water. However, destabilisation of calcium-aluminosulphate phases was already observed when HCP degraded to equilibrium pH of 11.6 in batch conditions. Even with GG water, containing relatively high S(VI) concentration, ettringite dissolved completely at this pH and S(VI) concentrations were not solubility controlled. In both systems S(VI) was found to be only inventory limited. Therefore, conclusions from existing studies suggesting that ettringite or other calcium-aluminosulphate hydrates would be present in degraded Portland cement and might even buffer pH have to be regarded with caution. In this study, Portland cement equilibrated at pH 11.6 did not contain primary anion adsorbing sulphates, neither ettringite nor monosulphoaluminate. This means that besides geochemical conditions, mass balances of the specific system should be taken into account when studying a disposal scenario.

The experimental study was complemented by thermodynamic modelling of HCP degradation in equilibrium conditions (batch) and kinetically controlled conditions (flow-through). Results from these modelling approaches satisfactorily reproduced the experimentally observed evolution regarding solid phases and solution composition in DI and GG water systems. Moreover, modelling proofed as a useful tool in assisting interpretation of results from flow-through experiments, especially regarding the influence of carbonate and initially rising Si concentrations. The mechanisms responsible for the latter observation were the reprecipitation of C-S-H inside the reactor and that from portlandite liberated Ca and OH⁻ ions influenced the kinetics of parallel dissolving C-S-H. The alternative explanation that simple wash-out of fines leads to initially rising Si concentrations was therefore ruled out. Furthermore, modelling allowed to estimate the degraded fraction of difficult-to-quantify C-S-H in flow-through experiments which otherwise was inaccessible. For further studies of HCP degradation it is suggested to investigate different particle size fractions and flow rates to determine the controlling effect of heterogeneous C-S-H degradation.

Some mismatch between model and experiments was found regarding the Al-S(VI) system in cementitious conditions. This is a common observation in other modelling studies. In this work performed modelling neglected Fe due to its immobility and due to experimental concentrations below detection limit. This biased model results for Al and S(VI) since Al(III) and Fe(III) are dependent due to formation of solid-solutions. It is concluded that the fate of Fe under cementitious conditions is one of the issues regarding better thermodynamic description of Al and S(VI) behaviour.

For safety assessment studies it is relevant to include effects of pore closure by precipitation in pores (clogging) as it influences water flow and therewith mobility of radionuclides. To predict occurrence of pore-clogging in scenarios by modelling it has to be described mechanistically, based on model parameters. Often, a simplified approach describes pore-clogging by the volume increase going along with transformation of original minerals/phases to secondary carbonates. In this case, closure of pore space and blocking of further percolation is reduced to a question of mass balance. However, all results from batch and flow-through experiments of this study suggested that calcite formation might happen as a physically decoupled dissolution-precipitation reaction. This implies that advective transport of dissolved phases may occur before calcite precipitation takes place, thereby questioning local mass balance approaches. As long as the mechanisms controlling the location where secondary carbonates precipitate have not been revealed, occurrence of clogging should be validated experimentally for the exactly defined conditions in a specific scenario.

The acquired understanding of degradation processes was taken as a basis to study Cs, Ni and Se retention by SRPC. Each of these potential radionuclides showed specific behaviour at different experimental conditions.

The formation of Ni-phases in equilibrated HCP was investigated at pH 12.5 (sane HCP) and pH 11.6 (degraded HCP). When portlandite is present it was found that due to precipitation aqueous Ni concentration drops below $\sim 10^{-8}$ mol/l (detection limit) in DI water and in GG water. This agrees with findings from literature and affirms the qualification of cementitious materials to lower mobility of Ni. At pH 11.6 aqueous Ni concentration drops below $\sim 10^{-7}$ mol/l (detection limit). At this stage a Ni-Al LDH-like phase was identified in a single spot. However, another Ni phase precipitated massively (see below). Up to now, Ni-Al LDH has only been reported to be stable above pH 12.8 in contact with cementitious materials. From the observed, amplified stability range of this phase it is concluded that LDH phases represent a relatively stable sink for Ni, in fresh as well as in aged cement systems.

Moreover, batch experiments showed at pH 11.6 a so far non-described amorphous Ni containing precipitate. SEM analyses and aqueous Si concentrations indicate a nickel-silicate-hydrate (here called Ni-S-H) phase that partly replaced C-S-H at high Ni load. Formation of this phase exerted a deleterious effect on the HCP by destabilisation of C-S-H. Ni-S-H was formed and stable in slightly as well as in severely carbonated HCP (in DI and GG water, respectively). This is an important aspect for real disposal sites as abundant or limited availability of carbonate does not seem to control formation of this phase. However, structure and thermodynamics of the Ni-S-H phase should be investigated by synthesis or extraction from precipitate formed with HCP in the system. This would allow assessment of its stability and relevance for Ni retention.

Consolidating results from the present work and other published studies a sequence of the Ni controlling solid phases during degradation of Portland cement was established. It bases on experiments at oxic conditions and is given as function of porewater pH. According to the presented experiments

calcite formation has no influence on Ni retention. This selection is valid for medium carbonate concentrations as in atmosphere equilibrated water up to high carbonate content in granitic groundwater:

Phases	Ni(OH) ₂ / Ni-Al LDH (±Ni-S-H)	→	Ni(OH) ₂ / Ni-S-H (±Ni-Al LDH)	→	Ni-phyllsilicate
pH (approx.)	< 13.5	12.5 - 11.7	11.6	11.5 - 10	< 10

Unfortunately, Ni could not be studied with the thin-layer flow-through reactor due to adsorption of Ni to parts of the setup.

Contrarily to Ni, Se(VI) experiments were only performed below solubility limits (about 10⁻⁴ mol/l). The sorption of Se(VI) to HCP at equilibrated conditions was low. In sane HCP at pH 12.5 distribution coefficients K_d of 0.11±0.01 m³/kg and 0.095±0.009 m³/kg were measured in DI and GG water, respectively. XRD and SEM analyses identified ettringite in these systems which is suspected to be the main adsorbing phase among all encountered phases at these conditions.

For degraded HCP, from which portlandite and ettringite have already been dissolved, effectively no sorption of Se(VI) was observed. Due to the analytical limitations this means that K_d was below 0.1 m³/kg (detection limit). Lower partitioning of Se(VI) to HCP at pH 11.6 than at pH 12.5 suggests that initially retained Se(VI) can be remobilised in a real scenario as HCP degradation progresses. Unfortunately, in literature no experimental study was encountered reporting observations for these conditions. It is therefore recommended to extend future sorption studies at the degraded stage with a focus on absence or presence of ettringite.

Flow-through experiments showed that aqueous Se(VI) was initially retarded by the HCP (retardation factor ~30 and K_d ~0.02 m³/kg) in DI water as well as in GG water. Over a long period, a small fraction of Se(VI) was then adsorbed to the HCP in both solutions (apparent distribution coefficient ~9·10⁻⁴ m³/kg). Partitioning to the solid only ceased at the end of experiments. Post-mortem SEM analysis of the degraded HCP showed dissemination of Se with C-S-H phases, indicating that it adsorbed to C-S-H. As other studies measured minor or no retention of Se(VI) on C-S-H it was expected that retention would be very weak in flow-through experiments when HCP is degraded. Still, even from the strongly degraded HCP, from which calcium-aluminosulphates had been dissolved and C-S-H was decalcified, no remobilisation of Se(VI) was observed. This indicates that under flow-through conditions Se(VI) sorption by C-S-H is favoured which could be explained by the distorted surface structure of C-S-H during dissolution, or by electrostatic effects in transient conditions (explained below).

Cs is in practice not solubility limited, hence all the experiments were performed without any solubility restriction. In equilibrium conditions measured distribution coefficients of Cs to sulphate resisting HCP were equal for DI and GG water at pH 12.5 and summed to (6±3)·10⁻³ m³/kg, calculated from background corrected concentrations. This is slightly higher than distribution coefficients encountered in literature, probably owing to lower concentration of competing alkali elements in solution. These elements are readily dissolved from HCP, but the applied liquid/solid ratio of 0.1 m³/kg in the presented experiments is comparatively high for investigations at pH 12.5, leading to more diluted

concentrations. In a waste repository employing cementitious materials the portlandite controlled degradation state of pH 12.5 is expected to be dominant over longer time than the initial period with high alkali concentrations. However, the conditions controlled by (almost) sane HCP with pH > 13 are also relevant once Cs is mobilised as part of the instant release fraction from the waste matrices, i.e. shortly after closure of a site for radioactive waste disposal.

Batch experiments with degraded HCP at pH ~11.6 showed distribution coefficients of Cs depending on Na, K and Ca concentrations, for both, DI and GG water. The background corrected distribution coefficients varied between 0.06 and 0.2 m³/kg for the range 1 < Ca [mmol/l] < 2 and 0.05 < (Na+K) [mmol/l] < 3. There is few literature data available on higher distribution coefficients measured at pH ~ 11.6 with Portland cement. From experimental data by Ochs, Pointeau et al. (2006) a similar value of 0.1-0.2 m³/kg can be derived, agreeing well with here measured values. All in all, batch experiments confirmed the expected increase of distribution coefficients for Cs to Portland cement with increasing degree of degradation.

In flow-through experiments Cs adsorbed neither in DI water nor in granitic groundwater to the crushed HCP. Therewith, it was neither retarded initially nor retained at the end of flow-through experiments when the HCP was substantially degraded. This was surprising (especially considering the degraded states) for two reasons: first, retention was expected to increase at this state and second, Cs adsorption on C-S-H is considered a fast process why a kinetic limitation was not expected.

There is no consensus in literature about which phase(s) retain(s) Cs in Portland cement. Based on observations from both, batch and flow-through experiments, a mechanistic explanation was deduced that relates to the specific sorption of Cs to silanol sites. Under flow-through conditions these silanol sites continuously polymerise as Dreierketten grow. This probably makes them more difficult to reach for the large Cs cation. Contrarily, in batch experiments where incongruent dissolution of C-S-H stops at equilibrium, polymerisation does not disturb Cs sorption throughout experiments and permits partitioning to the solid.

Combining experimental observations on Cs and Se(VI) retention, the behaviour of both elements did not seem to be conclusive as results were unexpected at a first glance. It seems that under the studied flow-through conditions other mechanisms become important than under equilibrium conditions. Taking into account that Cs does not adsorb to C-S-H in flow-through experiments it is difficult to understand why Se(VI) does adsorb in flow-through experiments at degraded states of the HCP. This is surprising because in batch experiments Cs is stronger retained at degraded states while Se(VI)) adsorbs less to C-S-H than Cs at these conditions.

One explanation is that, contrarily to the effect of C-S-H polymerisation on Cs, polymerisation leads to enhanced Se(VI) adsorption. This is possible if Se(VI) and Cs do not adsorb to the same site and/or if selenate becomes part of the C-S-H structure at flow conditions. However, a similar phenomenon has not been described before and cannot be verified with the actual data. An alternative, hypothetical explanation is that during dissolution in flow-through conditions the surface charge of C-S-H

is reversed. According to literature, surface charge is negative at equilibrium conditions which also was expected to be the dominant surface charge of C-S-H during thin-layer flow-through experiments. Increased retention of Se(VI) anions and decreased retention of Cs cations could be explained by electrostatic effects due to reversal of surface charge, e.g. caused by accumulation of massively released Ca at the surface of incongruently dissolving C-S-H.

Irrespective of the mechanism controlling retention of the very soluble and mobile alkali element Cs in flow-through conditions, results indicate the susceptibility of Cs to transient conditions. Batch sorption experiments performed in this study as well as dynamic batch experiments performed in other studies show increased sorption of Cs to degraded HCP, but might be misleading when estimating the retention of Cs for a disposal site. Inhibition of Cs sorption to Portland cement under flow conditions, as observed in this study, is relevant in a real case, if those parts of the cementitious barrier that are in contact with Cs contaminated (ground)water degrade at fast rates due to fast flow. Therefore, K_d values measured in equilibrated systems for Cs sorption on portlandite depleted HCP should only be applied, if water flow is expected to be slow, which is normally the case. Otherwise, there is a risk to overestimate Cs retention in real disposal sites with more dynamic water flow. Further research is needed to determine the bounding conditions concerning the flow rate.

This study showed that the persistency of radionuclide retention by adsorption in degrading cementitious systems is not only a question of distribution coefficients at different degradation states, but also a question of how fast these degradation states are reached. At deep disposal sites groundwater flow is suspected to be very slow. Exceptions are, e.g., flow along cracks in crystalline rock. Moreover, flow rates of at/near surface disposal sites can be considerable. Therefore, similar thin-layer flow-through experiments should be conducted with variation of flow rates, allowing to bound regimes where different retention mechanisms dominate.

9 Bibliography

- Abdelouas, A. and B. Grambow (2012). 4 - Aquatic chemistry of long-lived mobile fission and activation products in the context of deep geological disposal. Radionuclide Behaviour in the Natural Environment. C. Poinssot and H. Geckeis, Woodhead Publishing: 70-102.
- Achternbosch, M., K.-R. Bräutigam, M. Gleis, N. Hartlieb, C. Kupsch, U. Riechers and P. Stemmermann (2003). Heavy metals in Cement and concrete Resulting from the co-incineration of wastes in cement kilns with regard to the legitimacy of waste utilisation. Wissenschaftliche Berichte. FZKA. Karlsruhe, Forschungszentrum Karlsruhe in der Helmholtz-Gemeinschaft. **FZKA 6923**.
- Aggarwal, A., M. J. Angus and J. Ketchen (2000). Sorption of radionuclides onto specific mineral phases present in repository cements. AEA Technology Report.
- Alder, J. C. and D. F. McGinnes (1994). Model Radioactive Waste Inventory for Swiss Waste Disposal Projects. Switzerland, Nagra. **1**.
- Altmaier, M., V. Brendler, D. Bosbach, K. B., C. Marquardt, V. Neck and A. Richter (2004). Sicherheitstechnische Einzelfragen - Geochemische Prozesse bei der Ausbreitung von Schadstoffen aus einem Endlager für radioaktive Abfälle. Einzelaspekte Geochemische Prozesse. Karlsruhe, Germany, Institute for Nuclear Waste Disposal.
- American Society for Testing and Materials (1990). Practice for making and curing concrete test specimens in the laboratory (ASTM Standard C190-90a. In: 1994 Annual book of ASTM standards. Vol. 4.02. Philadelphia (PA).
- ANDRA (2005). Architecture et gestion du stockage géologique. Dossier 2005 Argile, ANDRA: 497.
- Appelo, C. A. J., E. Verweij and H. Schäfer (1998). "A hydrogeochemical transport model for an oxidation experiment with pyrite/calcite/exchangers/organic matter containing sand." Applied Geochemistry **13**(2): 257-268.
- Atkins, M., F. Glasser, L. P. Moroni and J. J. Jack (1993). Thermodynamic Modeling of Blended Cements at Elevated Temperatures (50°C–90°C), D.O.E. **Report No. DOE/HMIP/RR/94.011, 1993**.
- Atkins, M. and F. P. Glasser (1992). "Application of portland cement-based materials to radioactive waste immobilization." Waste Management **12**(2-3): 105-131.
- Atkinson, A., N. M. Everitt and R. M. Guppy (1989). Time dependence of a cementitious repository. Scientific basis for Nuclear waste management XII. W. Lutze and R. C. Ewing, Materials Research Society. **127**.
- Atkinson, A., K. Nelson and T. M. Valentine (1986). "Leach test characterisation of cement-based nuclear waste forms." Nuclear and Chemical Waste Management **6**(3-4): 241-253.
- Babushkin, V. I., G. M. Matveyev and O. P. Mchedlov-Petrosyan (1985). Thermodynamics of silicates. Berlin, Springer-Verlag.
- Baur, I. and C. A. Johnson (2003a). "The solubility of selenate-Aft ($3\text{CaO}\cdot\text{Al}_2\text{O}_3\cdot 3\text{CaSeO}_4\cdot 37.5\text{H}_2\text{O}$) and selenate-AFm ($3\text{CaO}\cdot\text{Al}_2\text{O}_3\cdot\text{CaSeO}_4\cdot x\text{H}_2\text{O}$)." Cement and Concrete Research **33**(11): 1741-1748.
- Baur, I. and C. A. Johnson (2003b). "Sorption of Selenite and Selenate to Cement Minerals." Environmental Science & Technology **37**(15): 3442-3447.
- Baur, I., P. Keller, D. Mavrocordatos, B. Wehrli and C. A. Johnson (2004). "Dissolution-precipitation behaviour of ettringite, monosulfate, and calcium silicate hydrate." Cement and Concrete Research **34**(2): 341-348.
- Berner, U. (1999). Concentration Limits in the Cement Based Swiss Repository for Long-lived, Intermediate-level Radioactive Wastes (LMA). Switzerland, Paul Scherrer Institut.
- Berner, U. R. (1988). "Modeling the Incongruent Dissolution of Hydrated Cement Minerals." Radiochimica Acta **44-5**: 387-393.

- Berner, U. R. (1992). "Evolution of pore water chemistry during degradation of cement in a radioactive waste repository environment." Waste Management **12**(2-3): 201-219.
- Bienvenu, P., P. Cassette, G. Andreoletti, M.-M. Bé, J. Comte and M.-C. Lépy (2007). "A new determination of ⁷⁹Se half-life." Applied Radiation and Isotopes **65**(3): 355-364.
- Black, L., C. Breen, J. Yarwood, K. Garbev, P. Stemmermann and B. Gasharova (2007). "Structural Features of C-S-H(I) and Its Carbonation in Air-A Raman Spectroscopic Study. Part II: Carbonated Phases." Journal of the American Ceramic Society **90**(3): 908-917.
- Blanc, P., X. Bourbon, A. Lassin and E. C. Gaucher (2010). "Chemical model for cement-based materials: Thermodynamic data assessment for phases other than C-S-H." Cement and Concrete Research **40**(9): 1360-1374.
- Bollmann, K. (2000). *Ettringitbildung in nicht wärmebehandelten Betonen*, Bauhaus-Universität Weimar: 205.
- Bonen, D., T. J. Johnson and S. L. Sarkar (1994). "Characterization of principal clinker minerals by FT-Raman microspectroscopy." Cement and Concrete Research **24**(5): 959-965.
- Bonhoure, I., I. Baur, E. Wieland, C. A. Johnson and A. M. Scheidegger (2006). "Uptake of Se(IV/VI) oxyanions by hardened cement paste and cement minerals: An X-ray absorption spectroscopy study." Cement and Concrete Research **36**(1): 91-98.
- Bosbach, D. (2010). "<EMU 2010 ch10 Bosbach solid solution nuclear waste disposal thermodynamics.pdf>."
- Bosbach, D. (2010). Solid-solution formation and the long-term safety of nuclear-waste disposal Ion partitioning in ambient-temperature aqueous systems. M. Prieto and H. Stoll.
- Bradbury, M. H. and F. A. Sarott (1994). Sorption Databases for the Cementitious Near-Field of a UILW Repository for Performance Assessment. Technical Report. Würenlingen and Villingen, Nagra: 131.
- British Standards Institution (1995). Cement - composition, specifications and conformity criteria. Part 1. Common cements. London: BSI. **DD ENV 197-1**.
- Bruno, J., D. Bosbach, D. A. Kulik and A. Navrotsky (2007). Chemical thermodynamics of solid solutions of interest in nuclear waste management: a state-of-the-art report. Paris, OECS.
- Bruno, J., I. Casas and I. Puigdomènech (1991). "The kinetics of dissolution of UO₂ under reducing conditions and the influence of an oxidized surface layer (UO₂+x): Application of a continuous flow-through reactor." Geochimica et Cosmochimica Acta **55**(3): 647-658.
- Bruno, J. and R. C. Ewing (2006). "Spent nuclear fuel." Elements **2**: 343-349.
- Bullard, J. W., E. Enjolras, W. L. George, S. G. Satterfield and J. E. Terrill (2010). "A parallel reaction-transport model applied to cement hydration and microstructure development." Modelling and Simulation in Materials Science and Engineering **18**(2): 025007.
- Bullard, J. W., H. M. Jennings, R. A. Livingston, A. Nonat, G. W. Scherer, J. S. Schweitzer, K. L. Scrivener and J. J. Thomas (2011). "Mechanisms of cement hydration." Cement and Concrete Research **41**(12): 1208-1223.
- Butcher, E. J., C. R. Cheeseman, C. J. Sollars and R. Perry (1993). "Flow-through leach testing of solidified waste using a modified triaxial cell." Environmental Technology **14**(2): 113-124.
- Carbol, P. and I. Engkvist (1997). Compilation of radionuclide sorption coefficients for performance assessment, SKB.
- Châtelet, L., J. Y. Bottero, J. Yvon and A. Bouchelaghem (1996). "Competition between monovalent and divalent anions for calcined and uncalcined hydrotalcite: anion exchange and adsorption sites." Colloids and Surfaces A: Physicochemical and Engineering Aspects **111**(3): 167-175.
- Chen, J. J., J. J. Thomas, H. F. W. Taylor and H. M. Jennings (2004). "Solubility and structure of calcium silicate hydrate." Cement and Concrete Research **34**(9): 1499-1519.

- Colleparidi, M. (2003). "A state-of-the-art review on delayed ettringite attack on concrete." Cement and Concrete Composites **25**(4-5): 401-407.
- Côté, P. (1986). Contaminant Leaching From Cement-based Waste Forms under Acidic Conditions. Doctor of philosophy Dissertation, Université Montréal.
- Cowper, M. M., A. Green, B. J. Myatt, S. W. Swanton and S. J. Williams (2005). A Laboratory Study of the Impact of Picolinate and Anion Exchange Resin Degradation Products on Nickel, Americium and Plutonium Behaviour in a Repository, United Kingdom Nirex Limited.
- Curti, E. (1997). Coprecipitation of radionuclides: basic concepts, literature review and first applications. PSI Bericht. Würenlingen and Villingen, Paul Scherrer Institut: 116.
- Dai, Y., J. E. Post and A. D. E. (1995). "Crystal structure of minehillite: Twinning and structural relationships to reyerite." American Mineralogist **80**: 173-178.
- Damidot, D. and F. P. Glasser (1992). "Thermodynamic investigation of the $\text{CaO-Al}_2\text{O}_3\text{-CaSO}_4\text{-H}_2\text{O}$ system at 50°C and 85°C." Cement and Concrete Research **22**(6): 1179-1191.
- Damidot, D. and F. P. Glasser (1993). "Thermodynamic investigation of the $\text{CaO-Al}_2\text{O}_3\text{-CaSO}_4\text{-H}_2\text{O}$ system at 25°C and the influence of Na_2O ." Cement and Concrete Research **23**(1): 221-238.
- Damidot, D., B. Lothenbach, D. Herfort and F. P. Glasser (2011). "Thermodynamics and cement science." Cement and Concrete Research **41**(7): 679-695.
- DBE (2009). Anforderungen an Salzbeton als Baustoff für Abdichtungsbauwerke im Steinsalz. Planfeststellungsverfahren zur Stilllegung des Endlagers für radioaktive Abfälle Morsleben, DBE im Auftrag des BfS.
- DBE. (2011). "Deutsche Gesellschaft zum Bau und Betrieb von Endlagern für Abfallstoffe mbH; Morsleben > History." Retrieved December 13, 2014, from <https://www.dbe.de/en/our-sites/morsleben/2/index.php>.
- Diederik, J. (2009). Benchmarking of the cement model and detrimental chemical reactions including temperature dependent parameters, Ondraf/Niras.
- Duchesne, J. and E. J. Reardon (1995). "Measurement and prediction of portlandite solubility in alkali solutions." Cement and Concrete Research **25**(5): 1043-1053.
- Elakneswaran, Y., A. Iwasa, T. Nawa, T. Sato and K. Kurumisawa (2010). "Ion-cement hydrate interactions govern multi-ionic transport model for cementitious materials." Cement and Concrete Research **40**(12): 1756-1765.
- Elakneswaran, Y., T. Nawa and K. Kurumisawa (2009). "Zeta potential study of paste blends with slag." Cement and Concrete Composites **31**(1): 72-76.
- Enresa (2010). Almacén Centralizado de Residuos Radiactivos de Baja y Media Actividad El Cabril, enresa.
- Evans, J., E. Lepel, R. Sanders, C. Wilkerson, W. Silker, C. Thomas, K. Abel and D. Robertson (1984). Long-lived activation products in reactor materials, Pacific Northwest Laboratory **Final Report**.
- Evans, N. D. M. (2008). "Binding mechanisms of radionuclides to cement." Cement and Concrete Research **38**(4): 543-553.
- Faucon, P., F. Adenot, J. F. Jacquinet, J. C. Petit, R. Cabrillac and M. Jorda (1998). "Long-term behaviour of cement pastes used for nuclear waste disposal: review of physico-chemical mechanisms of water degradation." Cement and Concrete Research **28**(6): 847-857.
- Fujii, K. and W. Kondo (1974). "Kinetics of the Hydration of Tricalcium Silicate." Journal of the American Ceramic Society **57**(11): 492-497.
- Galan, I., F. P. Glasser, D. Baza and C. Andrade (2015). "Assessment of the protective effect of carbonation on portlandite crystals." Cement and Concrete Research **74**(0): 68-77.

Gamsjäger, H., J. Bugajski, T. Gajda, R. J. Lemire and W. Preis (2005). Chemical thermodynamics of nickel. Chemical Thermodynamics. F. J. Mompean, M. Illemassène and J. Perrone. Amsterdam, North Holland Elsevier Science Publishers B.V.

Garrault, S. and A. Nonat (2001). "Hydrated Layer Formation on Tricalcium and Dicalcium Silicate Surfaces: Experimental Study and Numerical Simulations." Langmuir **17**(26): 8131-8138.

Giffaut, E., M. Grivé, P. Blanc, P. Vieillard, E. Colàs, H. Gailhanou, S. Gaboreau, N. Marty, B. Madé and L. Duro (2014). "Andra thermodynamic database for performance assessment: ThermoChimie." Applied Geochemistry **49**: 225-236.

Glasser, F. (2002). The stability of ettringite. International RILEM Workshop on Internal Sulfate Attack and Delayed Ettringite Formation. Switzerland. **TC 186-ISA**.

Glasser, F. P. (1997). "Fundamental aspects of cement solidification and stabilisation." Journal of Hazardous Materials **52**(2-3): 151-170.

Glasser, F. P. (2001). "Mineralogical aspects of cement in radioactive waste disposal." Mineralogical Magazine **65**(5): 621-633.

Glasser, F. P. (2002). "Characterisation of the Barrier Performance of Cements." MRS Proceedings **713**.

Glasser, F. P., J. Marchand and E. Samson (2008). "Durability of concrete — Degradation phenomena involving detrimental chemical reactions." Cement and Concrete Research **38**(2): 226-246.

Glaus, M. A. and L. R. Van Loon (2008). "Degradation of Cellulose under Alkaline Conditions: New Insights from a 12 Years Degradation Study." Environmental Science & Technology **42**(8): 2906-2911.

Gluth, G. (2001). Die Porenstruktur von Zementstein und seine Eignung zur Gastrennung, Technische Universität Berlin.

González-Siso, M., X. Gaona, L. Duro, M. Altmaier and J. Bruno (2015). Solubility and hydrolysis of Ni(II) under alkaline to hyperalkaline conditions.

Gougar, M. L. D., B. E. Scheetz and D. M. Roy (1996). "Ettringite and C₃S/H Portland cement phases for waste ion immobilization: A review." Waste Management **16**(4): 295-303.

Grandia, F., J. M. Galíndez, D. Arcos and J. Molinero (2010). Quantitative modelling of the degradation processes of cement grout - Project CEMMOD, SKB.

Hanna, J. V., L. P. Aldridge and E. R. Vance (2000). "Cs Speciation in Cements." MRS Online Proceedings Library **663**: null-null.

Harris, A. W., M. C. Manning, W. M. Tearle and C. J. Tweed (2002). "Testing of models of the dissolution of cements—leaching of synthetic CSH gels." Cement and Concrete Research **32**(5): 731-746.

Heberling, F., D. Bosbach, J.-D. Eckhardt, U. Fischer, J. Glowacky, M. Haist, U. Kramar, S. Loos, H. S. Müller, T. Neumann, C. Pust, T. Schäfer, J. Stelling, M. Ukrainczyk, V. Vinograd, M. Vučak and B. Winkler (2014). "Reactivity of the calcite–water-interface, from molecular scale processes to geochemical engineering." Applied Geochemistry **45**(0): 158-190.

Heberling, F., T. P. Trainor, J. Lützenkirchen, P. Eng, M. A. Denecke and D. Bosbach (2011). "Structure and reactivity of the calcite–water interface." Journal of Colloid and Interface Science **354**(2): 843-857.

Hewlett, P. (2004). Lea's Chemistry of Cement and Concrete. Oxford, Elsevier.

Hidalgo, A., S. Petit, C. Domingo, C. Alonso and C. Andrade (2007). "Microstructural characterization of leaching effects in cement pastes due to neutralisation of their alkaline nature." Cement and Concrete Research **37**(1): 63-70.

Hoffmann, U. and S. L. S. Stipp (2001). "The behavior of Ni²⁺ on calcite surfaces." Geochimica et Cosmochimica Acta **65**(22): 4131-4139.

- Holgersson, S., Y. Albinsson, B. Allard, H. Borén, I. Pavasars and I. Engkvist (1998). "Effects of Glucosaccharinate on Cs, Ni, Pm and Th Sorption onto, and Diffusion into Cement." Radiochimica Acta **82**(s1): 393.
- Hong, S.-Y. and F. P. Glasser (1999). "Alkali binding in cement pastes: Part I. The C-S-H phase." Cement and Concrete Research **29**(12): 1893-1903.
- Hong, S.-Y. and F. P. Glasser (2002). "Alkali sorption by C-S-H and C-A-S-H gels: Part II. Role of alumina." Cement and Concrete Research **32**(7): 1101-1111.
- Hummel, W., U. Berner, E. Curti, F. J. Pearson and T. Thoenen (2002). Nagra/PSI Chemical Thermodynamic Data Base 01/01. Technical Report. Wettingen, Switzerland, Nagra. **02-16**.
- Hummel, W. and E. Curti (2003). "Nickel Aqueous Speciation and Solubility at Ambient Conditions: A Thermodynamic Elegy." Monatshefte für Chemie - Chemical Monthly **134**(7): 941-973.
- IAEA (2009). Classification of radioactive waste. IAEA Safety Standards. Vienna, Austria, International Atomic Energy Agency.
- IAEA (2012). The Safety Case and Safety Assessment for the Disposal of Radioactive Waste. IAEA Safety Standards. Vienna, Austria, International Atomic Energy Agency.
- Iwaida, T., S. Nagasaki, S. Tanaka, T. Yaita and S. Tachimori (2002). "Structure alteration of C-S-H (calcium silicate hydrated phases) caused by sorption of caesium." Radiochimica Acta **90**(9-11/2002).
- Jakob, A., F. A. Sarott and P. Spieler (1999). Diffusion and sorption on hardened cement pastes - experiments and modelling results. PSI-Bericht, PSI, NAGRA-NTB: 194.
- Jeschke, A. A., K. Vosbeck and W. Dreybrodt (2001). "Surface controlled dissolution rates of gypsum in aqueous solutions exhibit nonlinear dissolution kinetics." Geochimica et Cosmochimica Acta **65**(1): 27-34.
- Jiménez, A. and M. Prieto (2015). "Thermal Stability of Ettringite Exposed to Atmosphere: Implications for the Uptake of Harmful Ions by Cement." Environmental Science & Technology **49**(13): 7957-7964.
- Johnson, C. A. and F. P. Glasser (2003). "Hydrotalcite-Like Minerals (M₂Al(OH)₆(CO₃)_{0.5}.XH₂O, where M = Mg, Zn, Co, Ni) in the Environment: Synthesis, Characterization and Thermodynamic Stability." Clays and Clay Minerals **51**(1): 1-8.
- Johnson, E. A., M. J. Rudin, S. M. Steinberg and W. H. Johnson (2000). "The sorption of selenite on various cement formulations." Waste Management **20**(7): 509-516.
- Jörg, G., R. Bühnemann, S. Hollas, N. Kivel, K. Kossert, S. Van Winkel and C. L. v. Gostomski (2010). "Preparation of radiochemically pure ⁷⁹Se and highly precise determination of its half-life." Applied Radiation and Isotopes **68**(12): 2339-2351.
- Juilland, P., E. Gallucci, R. Flatt and K. Scrivener (2010). "Dissolution theory applied to the induction period in alite hydration." Cement and Concrete Research **40**(6): 831-844.
- Kersten, M. (1996). "Aqueous Solubility Diagrams for Cementitious Waste Stabilization Systems. 1. The C-S-H Solid-Solution System." Environmental Science & Technology **30**(7): 2286-2293.
- Kienzler, B., M. Altmaier, C. Bube and V. Metz (2012). Radionuclide Source Term for HLW Glass, Spent Nuclear Fuel, and Compacted Hulls and End Pieces (CSD-C Waste). Vorläufige Sicherheitsanalyse Gorleben (VSG). **KIT-INE 003/11, KIT Scientific Reports 7624**.
- Kühn, T. (2008). Synthese und Charakterisierung von zinkhaltigen Layered Double Hydroxides mit organischen Zwischenschichtanionen. Dr. rer.nat Dissertation, Martin-Luther-Universität Halle Wittenberg.
- Kulik, D. A. (2011). "Improving the structural consistency of C-S-H solid solution thermodynamic models." Cement and Concrete Research **41**(5): 477-495.

Kumar, A., S. Komarneni and D. M. Roy (1987). "Diffusion of Cs⁺ and Cl⁻ through sealing materials." Cement and Concrete Research **17**(1): 153-160.

Lakshatanov, L. Z. and S. L. S. Stipp (2007). "Experimental study of nickel(II) interaction with calcite: Adsorption and coprecipitation." Geochimica et Cosmochimica Acta **71**(15): 3686-3697.

Langmuir, D., P. Hall and J. Drever (1997). Aqueous Environmental Geochemistry. New Jersey, Prentice Hall.

Lasaga, A. C. (1998). Kinetic Theory in Earth Science. Princeton, Princeton University Press.

Lichtner, P. C. and J. W. Carey (2006). "Incorporating solid solutions in reactive transport equations using a kinetic discrete-composition approach." Geochimica et Cosmochimica Acta **70**(6): 1356-1378.

Livi, K. J. T., G. S. Senesi, A. C. Scheinost and D. L. Sparks (2009). "Microscopic Examination of Nanosized Mixed Ni–Al Hydroxide Surface Precipitates on Pyrophyllite." Environmental Science & Technology **43**(5): 1299-1304.

Loser, R., B. Lothenbach, A. Leemann and M. Tuchschnid (2010). "Chloride resistance of concrete and its binding capacity – Comparison between experimental results and thermodynamic modeling." Cement and Concrete Composites **32**(1): 34-42.

Lothenbach, B., G. Le Saout, M. Ben Haha, R. Figi and E. Wieland (2012). "Hydration of a low-alkali CEM III/B–SiO₂ cement (LAC)." Cement and Concrete Research **42**(2): 410-423.

Lothenbach, B., G. Le Saout, E. Gallucci and K. Scrivener (2008). "Influence of limestone on the hydration of Portland cements." Cement and Concrete Research **38**(6): 848-860.

Lothenbach, B., T. Matschei, G. Möschner and F. P. Glasser (2008). "Thermodynamic modelling of the effect of temperature on the hydration and porosity of Portland cement." Cement and Concrete Research **38**(1): 1-18.

Lothenbach, B., L. Pelletier-Chaignat and F. Winnefeld (2012). "Stability in the system CaO–Al₂O₃–H₂O." Cement and Concrete Research **42**(12): 1621-1634.

Lothenbach, B. and E. Wieland (2006). "A thermodynamic approach to the hydration of sulphate-resisting Portland cement." Waste Manag **26**(7): 706-719.

Lothenbach, B. and F. Winnefeld (2006). "Thermodynamic modelling of the hydration of Portland cement." Cement and Concrete Research **36**(2): 209-226.

Lothenbach, B., F. Winnefeld, C. Alder, E. Wieland and P. Lunk (2007). "Effect of temperature on the pore solution, microstructure and hydration products of Portland cement pastes." Cement and Concrete Research **37**(4): 483-491.

Matschei, T. and F. Glasser (2011). Buffering in cementitious systems based on OPC. ICCC XIII. Madrid.

Matschei, T., B. Lothenbach and F. P. Glasser (2007a). "The AFm phase in Portland cement." Cement and Concrete Research **37**(2): 118-130.

Matschei, T., B. Lothenbach and F. P. Glasser (2007b). "Thermodynamic properties of Portland cement hydrates in the system CaO–Al₂O₃–SiO₂–CaSO₄–CaCO₃–H₂O." Cement and Concrete Research **37**(10): 1379-1410.

Mattigod, S., D. Rai, A. Felmy and L. Rao (1997). "Solubility and solubility product of crystalline Ni(OH)₂." Journal of Solution Chemistry **26**(4): 391-403.

Moon, D. H., D. G. Grubb and T. L. Reilly (2009). "Stabilization/solidification of selenium-impacted soils using Portland cement and cement kiln dust." J Hazard Mater **168**(2-3): 944-951.

Morandau, A., M. Thiéry and P. Dangla (2014). "Investigation of the carbonation mechanism of CH and C-S-H in terms of kinetics, microstructure changes and moisture properties." Cement and Concrete Research **56**(0): 153-170.

- Möschner, G., B. Lothenbach, R. Figi and R. Kretzschmar (2009). "Influence of citric acid on the hydration of Portland cement." Cement and Concrete Research **39**(4): 275-282.
- Möschner, G., B. Lothenbach, J. Rose, A. Ulrich, R. Figi and R. Kretzschmar (2008). "Solubility of Fe-ettringite (Ca₆[Fe(OH)₆]₂(SO₄)₃·26H₂O)." Geochimica et Cosmochimica Acta **72**(1): 1-18.
- Müller-Hoepe, N., D. Buhrmann, O. Czaikowski, H. Engelhardt, H. Herbert, C. Lerch, M. Linkamp, K. Wieczorek and M. Xie (2012). Integrität geotechnischer Barrieren - Teil 1 Vorbemessung. Vorläufige Sicherheitsanalyse Gorleben (VSG), GRS, DBEtec.
- Myneni, S. C. B., S. J. Traina and T. J. Logan (1998). "Ettringite solubility and geochemistry of the Ca(OH)₂-Al₂(SO₄)₃-H₂O system at 1 atm pressure and 298 K." Chemical Geology **148**(1-2): 1-19.
- Myneni, S. C. B., S. J. Traina, T. J. Logan and G. A. Waychunas (1997). "Oxyanion Behavior in Alkaline Environments: Sorption and Desorption of Arsenate in Ettringite." Environmental Science & Technology **31**(6): 1761-1768.
- Nachbaur, L. (1998). "Electrokinetic Properties which Control the Coagulation of Silicate Cement Suspensions during Early Age Hydration." Journal of Colloid and Interface Science **202**(2): 261-268.
- Niedersächsisches Ministerium für Umwelt, E. u. K. (2002). Planfeststellungsbeschluss für die Errichtung und den Betrieb des Bergwerkes Konrad in Salzgitter, Niedersächsisches Ministerium für Umwelt, Energie und Klimaschutz
- Niemann, L. (2005). Die Reaktionskinetik des Gipsabbindens, Universität Karlsruhe (TH).
- Ochs, M., B. Lothenbach and E. Giffaut (2002). "Uptake of oxo-anions by cements through solid-solution formation: experimental evidence and modelling." Radiochimica Acta **90**(9-11/2002).
- Ochs, M., I. Pointeau and E. Giffaut (2006). "Caesium sorption by hydrated cement as a function of degradation state: experiments and modelling." Waste Manag **26**(7): 725-732.
- Odler, I. (2003). "The BET-specific surface area of hydrated Portland cement and related materials." Cement and Concrete Research **33**(12): 2049-2056.
- OECD-NEA (2012). Cementitious Materials in Safety Cases for Geological Repositories for Radioactive Waste: Role, Evolution and Interactions. A workshop organised by the OECD/NEA Integration Group in the Safety Case and hosted by ONDRAF/NIRAS NEA.
- OECD (1984). Geological disposal of radioactive waste: An overview of the current status of understanding and development. Paris, OECD.
- Olin, A., B. Noläng, E. G. Osadchii, L. Öhman and E. Rosén (2005). Chemical Thermodynamics of selenium. France, Elsevier.
- ONDRAF/NIRAS (2011). Waste Plan for the long-term management of conditioned high-level and/or long-lived radioactive waste and overview of related issues. Brussels, ONDRAF/NIRAS.
- Paikaray, S., M. J. Hendry and J. Essilfie-Dughan (2013). "Controls on arsenate, molybdate, and selenate uptake by hydrotalcite-like layered double hydroxides." Chemical Geology **345**: 130-138.
- Palmer, D. A., P. Bénézech and D. J. Wesolowski (2005). Solubility of Nickel Oxide and Hydroxide in Water. International Conference on the Properties of Water and Steam. Kyoto. **14**: 6.
- Palmer, D. A., P. Bénézech, C. Xiao, D. J. Wesolowski and L. M. Anovitz (2011). "Solubility Measurements of Crystalline NiO in Aqueous Solution as a Function of Temperature and pH." Journal of Solution Chemistry **40**(4): 680-702.
- Palmer, D. A. and H. Gamsjäger (2010). "Solubility measurements of crystalline β-Ni(OH)₂ in aqueous solution as a function of temperature and pH." Journal of Coordination Chemistry **63**(14-16): 2888-2908.

- Papadokostaki, K. G. and A. Savidou (2009). "Study of leaching mechanisms of caesium ions incorporated in Ordinary Portland Cement." J Hazard Mater **171**(1-3): 1024-1031.
- Parkhurst, D. L. and C. A. J. Appelo (2013). Description of Input and Examples for PHREEQC version 3-A Computer Program for Speciation, Batch-Reaction, One-Dimensional Transport, and Inverse Geochemical Calculations. U.S. Geological Survey Techniques and Methods. <http://pubs.usgs.gov/tm/06/a43/>, USGS. **chap. A43**: 497.
- Peltier, E., R. Allada, A. Navrotsky and D. L. Sparks (2006). "Nickel solubility and precipitation in soils: a thermodynamic study." Clays and Clay Minerals **54**(2): 153-164.
- Peltier, E., D. van der Lelie and D. L. Sparks (2010). "Formation and Stability of Ni-Al Hydroxide Phases in Soils." Environmental Science & Technology **44**(1): 302-308.
- Perkins, R. B. and C. D. Palmer (1999). "Solubility of ettringite ($\text{Ca}_6[\text{Al}(\text{OH})_6]_2(\text{SO}_4)_3 \cdot 26\text{H}_2\text{O}$) at 5–75°C." Geochimica et Cosmochimica Acta **63**(13-14): 1969-1980.
- Pfingsten, W. (2001). Indications for self-sealing of a cementitious repository for low and intermediate-level waste. Technical Report. Switzerland, Nagra.
- Pilkington, N. J. and N. S. Stone (1990). The solubility and sorption of nickel and niobium under high pH conditions. Safety studies. Oxfordshire, UK, NIREX Radioactive Waste Disposal.
- Pointeau, I. (2000). Etude mécanistique et modélisation de la rétention de radionucléides par les silicates de calcium hydratés (CSH) des ciments (Mechanistic study and modeling of radionuclide retention for CSH phases of cement).
- Pointeau, I., N. Coreau and P. E. Reiller (2008). "Uptake of anionic radionuclides onto degraded cement pastes and competing effect of organic ligands." Radiochimica Acta **96**(6/2008).
- Pointeau, I., D. Hainos, N. Coreau and P. Reiller (2006a). "Effect of organics on selenite uptake by cementitious materials." Waste Management **26**(7): 733-740.
- Pointeau, I., N. Marmier, F. Fromage, M. Fedoroff and E. Giffaut (2001). "Cesium and Lead Uptake by CSH Phases of Hydrated Cement." MRS Online Proceedings Library **663**: null-null.
- Pointeau, I., P. Reiller, N. Mace, C. Landesman and N. Coreau (2006b). "Measurement and modeling of the surface potential evolution of hydrated cement pastes as a function of degradation." J Colloid Interface Sci **300**(1): 33-44.
- Pokrovsky, O. S. and J. Schott (2004). "Experimental study of brucite dissolution and precipitation in aqueous solutions: surface speciation and chemical affinity control." Geochimica et Cosmochimica Acta **68**(1): 31-45.
- Pöllmann, H. (2010). Mineralisation of Wastes and Industrial Residues. Aachen, Shaker Verlag.
- Pöllmann, H., H. J. Kuzel and R. Wenda (1990). "Solid solution of ettringites part I: incorporation of OH^- and CO_3^{2-} in $3\text{CaO} \cdot \text{Al}_2\text{O}_3 \cdot 32\text{H}_2\text{O}$." Cement and Concrete Research **20**(6): 941-947.
- Poon, C. S., Z. Q. Chen and O. W. H. Wai (2001). "The effect of flow-through leaching on the diffusivity of heavy metals in stabilized/solidified wastes." Journal of Hazardous Materials **81**(1-2): 179-192.
- Putnis, A. (2009). "Mineral Replacement Reactions." Reviews in Mineralogy and Geochemistry **70**(1): 87-124.
- Rajamathi, M., G. N. Subbanna and P. V. Kamath (1997). "On the existence of nickel hydroxide phase which is neither α nor β ." Journal of Materials Chemistry **7**(11): 2293-2296.
- Regnault, O., V. Lagneau and H. Schneider (2009). "Experimental measurement of portlandite carbonation kinetics with supercritical CO_2 ." Chemical Geology **265**(1-2): 113-121.
- Richardson, I. G. (2004). "Tobermorite/jennite- and tobermorite/calcium hydroxide-based models for the structure of C-S-H: applicability to hardened pastes of tricalcium silicate, β -dicalcium silicate, Portland cement, and blends of

- Portland cement with blast-furnace slag, metakaolin, or silica fume." Cement and Concrete Research **34**(9): 1733-1777.
- Richardson, I. G. (2008). "The calcium silicate hydrates." Cement and Concrete Research **38**(2): 137-158.
- Rojo, I., M. Grivé, M. Rovira, O. Riba, D. García, C. Domènech and J. De Pablo (2010). Immobilization and long-term evolution of selenate in Portland cement. Scientific Basis for Nuclear Waste Management XXXIV. K. Smith, S. Kroeker, B. Uberuaga and K. Whittle, Materials Research Society. **1265**.
- Rojo, I., M. Rovira, V. Martí, J. de Pablo, X. Gaona, E. Colàs and M. Grivé (2007). Uptake of selenate on hydrated and degraded cement: batch and dynamic experiments. Mobile Fission and Activation Products in Nuclear Waste Disposal N. E. AGENCY. La Baule, France. **NEA 06310**: 43-53.
- Ruiz-Agudo, E., K. Kudłacz, C. V. Putnis, A. Putnis and C. Rodriguez-Navarro (2013). "Dissolution and Carbonation of Portlandite [Ca(OH)₂] Single Crystals." Environmental Science & Technology **47**(19): 11342-11349.
- Sarott, F. A., M. H. Bradbury, P. Pandolfo and P. Spieler (1992). "Diffusion and adsorption studies on hardened cement paste and the effect of carbonation on diffusion rates." Cement and Concrete Research **22**(2-3): 439-444.
- Savage, D., J. M. Soler, K. Yamaguchi, C. Walker, A. Honda, M. Inagaki, C. Watson, J. Wilson, S. Benbow, I. Gaus and J. Rueedi (2011). "A comparative study of the modelling of cement hydration and cement-rock laboratory experiments." Applied Geochemistry **26**(7): 1138-1152.
- Savage, D. and M. Stenhouse (2002). SFR 1 Vault Database. SKI Report, SKI. **02:53**: 52.
- Scheckel, K. G., A. C. Scheinost, R. G. Ford and D. L. Sparks (2000). "Stability of layered Ni hydroxide surface precipitates—a dissolution kinetics study." Geochimica et Cosmochimica Acta **64**(16): 2727-2735.
- Scheidegger, A. M., E. Wieland, A. C. Scheinost, R. Dähn and P. Spieler (2000). "Spectroscopic Evidence for the Formation of Layered Ni–Al Double Hydroxides in Cement." Environmental Science & Technology **34**(21): 4545-4548.
- Scheidegger, A. M., E. Wieland, A. C. Scheinost, R. Dähn, J. Tits and P. Spieler (2001). "Ni phases formed in cement and cement systems under highly alkaline conditions: an XAFS study." Journal of Synchrotron Radiation **8**(2): 916-918.
- Scheinost, A. C. and D. L. Sparks (2000). "Formation of Layered Single- and Double-Metal Hydroxide Precipitates at the Mineral/Water Interface: A Multiple-Scattering XAFS Analysis." J Colloid Interface Sci **223**(2): 167-178.
- Schmidt, T., B. Lothenbach, M. Romer, K. Scrivener, D. Rentsch and R. Figi (2008). "A thermodynamic and experimental study of the conditions of thaumasite formation." Cement and Concrete Research **38**(3): 337-349.
- Schweizer, C. R. (1999). Calciumsilikathydrat-Mineralien, ETH Zürich.
- Scrivener, K. L. and E. M. Gartner (1987). "Microstructural Gradients in Cement Paste Around Aggregate Particles." MRS Online Proceedings Library **114**.
- Séby, F., M. Potin-Gautier, E. Giffaut and O. F. X. Donard (1998). "Assessing the speciation and the biogeochemical processes affecting the mobility of selenium from a geological repository of radioactive waste to the biosphere." Analisis **26**(5): 193-198.
- Seewald, J. S. and W. E. Seyfried Jr (1991). "Experimental determination of portlandite solubility in H₂O and acetate solutions at 100–350 °C and 500 bars: Constraints on calcium hydroxide and calcium acetate complex stability." Geochimica et Cosmochimica Acta **55**(3): 659-669.
- Shock, E. L., D. C. Sassani, M. Willis and D. A. Sverjensky (1997). "Inorganic species in geologic fluids: Correlations among standard molal thermodynamic properties of aqueous ions and hydroxide complexes." Geochimica et Cosmochimica Acta **61**(5): 907-950.

Skagius, K., M. Pettersson and M. Wiborgh (1999). Compilation of data for the analysis of radionuclide migration from SFL 3-5. SKB Report, Svensk Kärnbränslehantering AB. **R-99-13**: 123.

SKB (2006). Long-term safety for KBS-3 repositories at Forsmark and Laxemar – a first evaluation. Main Report of the SR-Can project. Stockholm, Sweden, Svensk Kärnbränslehantering AB.

Solem-Tishmack, J. K., G. J. McCarthy, B. Dockett, K. E. Eylands, J. S. Thompson and D. J. Hassett (1995). "High-calcium coal combustion by-products: Engineering properties, ettringite formation, and potential application in solidification and stabilization of selenium and boron." Cement and Concrete Research **25**(3): 658-670.

Stark, J. (2011). "Recent advances in the field of cement hydration and microstructure analysis." Cement and Concrete Research **41**(7): 666-678.

Steeffel, C. I. and P. C. Lichtner (1998). "Multicomponent reactive transport in discrete fractures II: Infiltration of hyperalkaline groundwater at Maqarin, Jordan, a natural analogue site." Journal of Hydrology **209**(1-4): 200-224.

Stumm, W. and J. J. Morgan (1996). Aquatic chemistry: chemical equilibria and rates in natural waters. New York, Wiley. **3. ed.**: 1022.

Subhas, A. V., N. E. Rollins, W. M. Berelson, S. Dong, J. Erez and J. F. Adkins (2015). "A novel determination of calcite dissolution kinetics in seawater." Geochimica et Cosmochimica Acta **170**: 51-68.

Sugiyama, D. and T. Fujita (2006). "A thermodynamic model of dissolution and precipitation of calcium silicate hydrates." Cement and Concrete Research **36**(2): 227-237.

Sverjensky, D. A., E. L. Shock and H. C. Helgeson (1997). "Prediction of the thermodynamic properties of aqueous metal complexes to 1000°C and 5 kb." Geochimica et Cosmochimica Acta **61**(7): 1359-1412.

Taylor, H. F. W. (1997). Cement chemistry. London, Thomas Telford.

Taylor, H. F. W. (2002). Sulfates in Portland clinker and cement. International RILEM TC Workshop on Internal Sulfate Attack and Delayed Ettringite Formation. London, Thomas Telford.

Terai, T., A. Mikuni, Y. Nakamura and K. Ikeda (2007). "Synthesis of ettringite from portlandite suspensions at various Ca/Al ratios." Inorganic Materials **43**(7): 786-792.

Thoenen, T. and D. A. Kulik (2003). Nagra/PSI Chemical Thermodynamic Data Base 01/01 for the GEM-Selektor (V.2-PSI) Geochemical Modelling Code: Release 28-02-03. **TM-44-03-04**: 43.

Thomas, J. J., J. J. Chen, A. J. Allen and H. M. Jennings (2004). "Effects of decalcification on the microstructure and surface area of cement and tricalcium silicate pastes." Cement and Concrete Research **34**(12): 2297-2307.

Thomas, J. J. and H. M. Jennings. (2013). "The science of concrete." monograph Retrieved 12.4.2013, from http://iti.northwestern.edu/cement/monograph/Monograph3_6.html.

Tits, J., M. H. Bradbury, E. Wieland and M. Mantovani (1998). The Uptake of Cs, Sr, Ni, Eu and Th by CSH Phases under high pH Cement Pore Water Conditions. Switzerland, Paul Scherrer Institut.

Trapote-Barreira, A., J. Cama and J. M. Soler (2014). "Dissolution kinetics of C–S–H gel: Flow-through experiments." Physics and Chemistry of the Earth, Parts A/B/C **70-71**(0): 17-31.

Van Gerven, T., G. Cornelis, E. Vandoren, C. Vandecasteele, A. C. Garrabrants, F. Sanchez and D. S. Kosson (2006). "Effects of progressive carbonation on heavy metal leaching from cement-bound waste." AIChE Journal **52**(2): 826-837.

Vejmelka, P., G. Rudolph, W. Kluger and R. Köster (1990). Die Konditionierung radioaktiver Abfallösungen durch Zementierung. Karlsruhe, Germany, KfK.

Verein Deutscher Zementwerke, e. V. (2001). "Trace elements in German standard cements 2001." Retrieved 11.3.2010, from <https://www.vdz->

online.de/fileadmin/gruppen/vdz/3LiteraturRecherche/UmweltundRessourcen/spurenelemente/spurenel2001_engl.pdf.

Verein Deutscher Zementwerke, e. V. (2002). Zement-Taschenbuch 2002. Düsseldorf, Germany, Verein Deutscher Zementwerke e.V.

Vespa, M., R. Dähn, E. Gallucci, D. Grolimund, E. Wieland and A. M. Scheidegger (2006a). "Microscale Investigations of Ni Uptake by Cement Using a Combination of Scanning Electron Microscopy and Synchrotron-Based Techniques." Environmental Science & Technology **40**(24): 7702-7709.

Vespa, M., R. Dähn, D. Grolimund, M. Harfouche, E. Wieland and A. M. Scheidegger (2006b). "Speciation of heavy metals in cement-stabilized waste forms: A micro-spectroscopic study." Journal of Geochemical Exploration **88**(1-3): 77-80.

Vespa, M., R. Dähn, D. Grolimund, E. Wieland and A. M. Scheidegger (2006c). "Spectroscopic Investigation of Ni Speciation in Hardened Cement Paste." Environmental Science & Technology **40**(7): 2275-2282.

Vespa, M., E. Wieland, R. Dähn, D. Grolimund and A. M. Scheidegger (2007). "Determination of the elemental distribution and chemical speciation in highly heterogeneous cementitious materials using synchrotron-based micro-spectroscopic techniques." Cement and Concrete Research **37**(11): 1473-1482.

Viallis-Terrisse, H., A. Nonat and J.-C. Petit (2001). "Zeta-Potential Study of Calcium Silicate Hydrates Interacting with Alkaline Cations." Journal of Colloid and Interface Science **244**(1): 58-65.

Viallis-Terrisse, H., A. Nonat, J. C. Petit, C. Landesman and C. Richet (2002). "Specific interaction of cesium with the surface of calcium silicate hydrates." Radiochimica Acta **90**(9-11/2002).

Vuorinen, U. and M. Snellman (1998). Finnish reference waters for solubility, sorption and diffusion studies, POSIVA.

Wieland, E., J. Tits and M. H. Bradbury (2004). "The potential effect of cementitious colloids on radionuclide mobilisation in a repository for radioactive waste." Applied Geochemistry **19**(1): 119-135.

Wieland, E., J. Tits, A. Ulrich and M. H. Bradbury (2006). "Experimental evidence for solubility limitation of the aqueous Ni(II) concentration and isotopic exchange of ⁶³Ni in cementitious systems." Radiochimica Acta **94**(1/2006).

Wieland, E. and L. R. Van Loon (2003). Cementitious Near-Field Sorption Data Base for Performance Assessment of an ILW Repository in Opalinus Clay. PSI-Bericht, Paul Scherrer Institut. **Nr. 03-06**: 74.

Zhang, M. and E. J. Reardon (2003). "Removal of B, Cr, Mo, and Se from Wastewater by Incorporation into Hydrocalumite and Ettringite." Environmental Science & Technology **37**(13): 2947-2952.

10 Annex

10.1 Experimental Parameters

Table 30 Experimental conditions and results from batch experiments with Sulfadur HCP. Red number indicate quantification below the lower linear calibration limit.

Experiment		B01	B02	B03	B04	B17	B18
solution type		DI water	DI water	DI water	DI water	DI water	DI water
cement	g	4.0007	4.0005	3.9993	4.0000	2.0003	2.0001
Volume	l	0.400	0.400	0.400	0.400	0.200	0.200
L/S ratio	m ³ /kg	0.100	0.100	0.100	0.100	0.100	0.100
Cs (added)	mol/l			1.00E-07			1.00E-07
Ni (added)	mol/l		5.00E-04	9.98E-08		5.00E-04	9.98E-08
Se(VI) (added)	mol/l			9.95E-07	9.95E-05		9.95E-05
Eh	mV		202	213	225		222
el. conductivity	μS/cm	8263	8410	8125	8310	8193	7987
pH		12.49	12.50	12.50	12.51	12.47	12.48
Al	mol/l	5.30E-06	3.27E-06	4.63E-06	4.76E-06	3.40E-06	5.38E-06
Ca	mol/l	2.43E-02	2.47E-02		2.35E-02		
Cl	mol/l	< 3.32E-5	< 3.32E-5		2.06E-06		
K	mol/l	7.35E-04	7.51E-04		7.38E-04		
Mg	mol/l	2.74E-06	2.62E-06	2.34E-06		2.65E-06	
Na	mol/l	1.17E-04	9.24E-05		3.21E-04		
Si	mol/l	7.11E-06	7.27E-06	6.88E-06	8.81E-06	7.20E-06	7.47E-06
S(VI)	mol/l	4.91E-05	8.53E-05	8.71E-05	6.24E-05		
Cs	mol/l	1.10E-07	1.10E-07	2.03E-07	1.06E-07	1.14E-07	2.07E-07
Ni	mol/l	5.35E-09	5.38E-09		1.70E-08	1.54E-08	
Se(VI)	mol/l		5.73E-09	4.85E-07	4.44E-05	6.88E-09	4.99E-05

Continued

Experiment		B05	B06	B07	B08	B19	B20
solution type		GG water					
cement	g	3.9996	4.0002	3.9997	4.0001	1.9998	2.0009
Volume	l	0.400	0.400	0.400	0.400	0.200	0.200
L/S ratio	m ³ /kg	0.100	0.100	0.100	0.100	0.100	0.100
Cs (added)	mol/l			1.00E-07			1.00E-07
Ni (added)	mol/l		5.00E-04	9.98E-08		5.00E-04	9.98E-08
Se(VI) (added)	mol/l			9.95E-07	9.95E-05		9.95E-05
Eh	mV				219		223
el. conductivity	μS/cm	8170	8680	8547	8510	8447	8547
pH		12.49	12.52	12.51	12.51	12.49	12.50
Al	mol/l	4.53E-06	2.80E-06	4.02E-06	4.68E-06	2.88E-06	5.26E-06
Ca	mol/l	2.35E-02	2.36E-02		2.14E-02		
Cl	mol/l	1.22E-03	1.30E-03	1.32E-03	1.30E-03		
K	mol/l	8.43E-04	8.83E-04		8.85E-04		
Mg	mol/l	2.52E-06	2.51E-06	2.37E-06		2.74E-06	
Na	mol/l	2.70E-03	2.88E-03		3.11E-03		
Si	mol/l	7.74E-06	6.99E-06	6.83E-06	7.74E-06	7.25E-06	8.04E-06
S(VI)	mol/l	5.40E-05	8.34E-05	8.33E-05	8.37E-05		
Cs	mol/l	1.11E-07	1.12E-07	2.01E-07	1.03E-07	1.13E-07	2.06E-07
Ni	mol/l	4.60E-09	4.44E-09	1.03E-08		7.35E-09	
Se(VI)	mol/l	7.80E-09	8.65E-09	5.37E-07	4.91E-05	6.89E-09	5.06E-05

Continued

Experiment		B09	B10	B11	B12	B21	B22
solution type		DI water	DI water	DI water	DI water	DI water	DI water
cement	g	0.9998	1.0001	1.0007	1.0001	0.3992	0.4004
Volume	l	2.000	2.000	2.000	2.000	0.800	0.800
L/S ratio	m ³ /kg	2.000	2.000	1.999	2.000	2.004	1.998
Cs (added)	mol/l			1.00E-07			1.00E-07
Ni (added)	mol/l		5.00E-04	9.98E-08		5.00E-04	9.98E-08
Se(VI) (added)	mol/l			9.95E-07	2.02E-04		1.95E-04
Eh	mV	254		241	268	255	224
el. conductivity	μS/cm	1302	1300	1286	1341	1249	1303
pH		11.63	11.61	11.66	11.66	11.56	11.62
Al	mol/l	2.34E-05	2.16E-05	2.25E-05	2.44E-05	2.36E-05	2.39E-05
Ca	mol/l	2.02E-03	2.30E-03		1.88E-03		
Cl	mol/l	1.87E-07		2.02E-07	3.78E-07		
K	mol/l	< 9.03E-5	2.82E-05		2.98E-05		
Mg	mol/l						
Na	mol/l	<1.54E-4	4.58E-05		4.59E-04		
Si	mol/l	1.76E-04	1.41E-04	1.73E-04	1.84E-04	1.39E-04	1.92E-04
S(VI)	mol/l	4.00E-05	7.08E-05	5.10E-05	6.44E-05		
Cs	mol/l	6.99E-09	6.00E-09	9.80E-08	7.78E-09	6.06E-09	1.02E-07
Ni	mol/l			2.31E-07			
Se(VI)	mol/l			8.14E-07	2.06E-04		2.06E-04

Continued

Experiment		B13	B14	B15	B16	B23	B24
solution type		GG water					
cement	g	1.0004	1.0004	1.0017	1.0005	0.3999	0.4005
Volume	l	2.000	2.000	2.000	2.000	0.800	0.800
L/S ratio	m ³ /kg	1.999	1.999	1.997	1.999	2.001	1.998
Cs (added)	mol/l			1.00E-07			1.00E-07
Ni (added)	mol/l		5.00E-04	9.98E-08	0	5.00E-04	9.98E-08
Se(VI) (added)	mol/l			9.95E-07	2.03E-04		1.98E-04
Eh	mV	265		279	289		228
el. conductivity	μS/cm	1198	1183	1181	1209	1130	1214
pH		11.55	11.49	11.55	11.55	11.42	11.47
Al	mol/l	1.58E-05	1.33E-05	1.65E-05	1.58E-05	1.41E-05	1.76E-05
Ca	mol/l	1.20E-03	1.22E-03		1.09E-04		
Cl	mol/l	1.34E-03	1.35E-03	1.34E-03	1.34E-03		
K	mol/l	5.43E-05	1.33E-04		1.32E-04		
Mg	mol/l						
Na	mol/l	1.36E-03	2.57E-03		3.29E-03		
Si	mol/l	3.05E-04	2.31E-04	3.04E-04	3.06E-04	2.16E-04	3.05E-04
S(VI)	mol/l	1.44E-04	1.45E-04	1.54E-04	1.54E-04		
Cs	mol/l	7.75E-09	5.44E-09	1.01E-07	9.14E-09	5.84E-09	1.06E-07
Ni	mol/l			4.31E-07			
Se(VI)	mol/l			1.03E-06	2.07E-04		2.09E-04

Table 31 Conditions of flow-through experiments. Experiment FL 1 was carried out open to the atmosphere; all other experiments were performed in N₂ atmosphere. Sample names are composed of the columns “experiment series” and “sample”, e.g., the outflow solution (20 ml) of experiment “FL 1-4” was collected between 2630 and 3550 s after start of experiment. The cement mass is given as weighed in the laboratory before starting degradation of cement.

Experiment Series	Sample	Initial cement (g)	Background electrolyte	Pump rate (ml/min)	Time (s)	Cumulated flow (ml)
FL 1-		0.05-0.1				
	1		-	3.08	390	20
	2		-	1.00	1590	40
	3		-	1.15	2630	60
	4		-	1.30	3550	80
	5		-	0.79	5070	100
FL 2-		0.0187				
	1		-	1.88	640	20
	2		-	1.91	1300	41
	3		-	1.83	1955	61
	4		-	1.86	2600	81
	5		-	1.80	3265	101
	6		-	1.87	3938	122
FL 3-		0.0248				
	1		-	0.94	1271	20
	2		-	0.86	2670	40
	3		-	0.80	4179	60
	4		-	0.75	5787	80
	5		-	0.94	7058	100
FL 4-		0.0505				
	1		-	1.50	802	20
	2		-	1.48	1611	40
	3		-	1.48	2424	60
	4		-	1.48	3234	80
	5		-	1.48	4066	100.5
	6		-	1.45	4894	120.5
	7		-	1.46	5717	140.5
	8		-	1.45	6542	160.5
	9		-	1.46	7363	180.5
FL 5-		0.0472				
	1		-	1.07	1117	20
	2		-	1.03	2277	40
	3		-	1.04	3529	61.6
	4		-	1.03	4689	81.6
	5		-	1.02	5860	101.6
	6		-	1.04	8458	146.6
	7		-	1.02	11099	191.6
	8		-	1.02	13930	239.6
	9		-	1.01	16740	287.1
	10		-	1.01	17930	307.2

Continued

Experiment	Sample	cement (g)	Background electrolyte	Pump rate ml/min	Time (s)	Cumulated flow (ml)
FL 6-		0.0169				
	1		-	0.60	2002	20
	2		-	0.62	3936	40
	3		-	0.62	5887	60
	4		-	0.61	7853	80
	5		-	0.61	11767	120
	6		-	0.61*	*	147
FL 7-		0.0396				
	1		-	0.74	2437	30
	2		-	0.74	5290	65
	3		-	0.74	8520	105
	4		-	0.73	12213	150
	5		-	0.73	15933	195
	6		-	0.73	19647	240
	7		-	0.72	23165	282.5
	8		-	0.71	75030	897.5
	9		-	0.71	76766	918
FL 8-		0.0288				
	1		0.1M NaClO ₄	1.12	1665	31
	2		0.1M NaClO ₄	1.09	3322	61
	3		0.1M NaClO ₄	1.09	5060	92.5
	4		0.1M NaClO ₄	1.07	6744	122.5
	5		0.1M NaClO ₄	1.07	8423	152.5
	6		0.1M NaClO ₄	1.07	10939	197.5
	7		0.1M NaClO ₄	1.08	13442	242.5
	8		0.1M NaClO ₄	1.07	16234	292.5
FL 9-		0.035				
	1		0.1M NaClO ₄	0.69	950	11
	2		0.1M NaClO ₄	0.67	2731	31
	3		0.1M NaClO ₄	0.69	5337	61
	4		0.1M NaClO ₄	0.68	59840	681
	5		0.1M NaClO ₄	0.66	61650	701
	6		0.1M NaClO ₄	0.67	65680	746
	7		0.1M NaClO ₄	0.66	69984	793
	8		0.1M NaClO ₄	0.66	74640	844.5

* In experiment FL 6-6 the reservoir was depleted and the exact time is not known

Table 32 Experimental conditions of flow-through experiments with Sulfadur HCP

Series Name	Input solution	Cement mass g	Filter	Sample	Time s	Sampling period s	Cumulated Volume ml	Collected solution mass g	Flow rate ml/min
FLS 1	DI water	0.0559	0.2 μ m Nylon	FLS 1-1	1137	1137	20.4	20.4	1.08
				FLS 1-2	2343	1206	41.8	21.4	1.07
				FLS 1-3	3539	1196	63.1	21.3	1.07
				FLS 1-4	4721	1182	84.0	20.9	1.06
				FLS 1-5	5899	1178	104.8	20.8	1.06
				FLS 1-6	7104	1205	126.1	21.3	1.06
				FLS 1-7	13071	5967	231.2	105.1	1.06
				FLS 1-8	19280	6209	339.2	108.0	1.04
				FLS 1-9	22608	3328	396.1	53.9	1.03
				FLS 1-10	80802	58194	1396.1		1.03
				FLS 1-11	88200	7398	1521.9	125.8	1.02
FLS 2	DI water	0.0565	0.2 μ m Nylon	FLS 2-1	1200	1200	21.6	21.6	1.08
				FLS 2-2	3000	1800	53.8	32.2	1.07
				FLS 2-3	4800	1800	85.9	32.1	1.07
				FLS 2-4	6600	1800	117.8	31.9	1.06
				FLS 2-5	9395	2795	167.2	49.4	1.06
				FLS 2-6	12103	2708	214.9	47.6	1.06
				FLS 2-7	17678	5575	312.3	97.4	1.05
				FLS 2-8	20745	3067	365.8	53.6	1.05
				FLS 2-9	76318	55573	1296.2	930.4	1.00
				FLS 2-10	79230	2912	1344.2	48.0	0.99
				FLS 2-11	81960	2730	1389.6	45.4	1.00
				FLS 2-12	84081	2121	1424.7	35.0	0.99
FLS 3	DI water	0.0553	0.2 μ m Nylon	FLS 3-1	2400	2400	43.2	43.2	1.08
				FLS 3-2	4800	2400	85.5	42.3	1.06
				FLS 3-3	7200	2400	127.6	42.2	1.05
				FLS 3-4	19800	12600	344.9	217.3	1.03
				FLS 3-5	77745	57945	1330.6	985.7	1.02
				FLS 3-6	80220	2475	1371.3	40.7	0.99
FLS 4	DI water	0.0549	0.2 μ m Nylon	FLS 4-1	2403	2403	39.8	39.8	0.99
				FLS 4-2	4802	2399	79.3	39.5	0.99
				FLS 4-3	7200	2398	118.8	39.5	0.99
				FLS 4-4	21000	13800	344.9	226.1	0.98
				FLS 4-5	76800	55800	1251.2	906.3	0.97
				FLS 4-6	79200	2400	1289.9	38.7	0.97
FLS 5	GG water	0.0551	0.2 μ m Nylon	FLS 5-1	2400	2400	41.1	41.1	1.03
				FLS 5-2	4800	2400	82.0	40.9	1.02
				FLS 5-3	7200	2400	122.9	40.9	1.02
				FLS 5-4	19200	12000	326.5	203.6	1.02
				FLS 5-5	74400	55200	1256.2	929.7	1.01
				FLS 5-6	77400	3000	1306.3	50.0	1.00
				FLS 5-7	101160	23760	1699.8	393.5	0.99
				FLS 5-8	104235	3075	1750.6	50.8	0.99

Continued

Series Name	Input solution	Cement mass	Filter	Sample	Time	Sampling period	Cumulated Volume	Collected solution mass	Flow rate
		g			s	s	ml	g	ml/min
FLS 9	DI water	0.0551	0.2 μ m Nylon	FLS 9-1	2402	2402	39.2	39.2	0.98
				FLS 9-2	4815	2413	78.6	39.4	0.98
				FLS 9-3	7200	2385	117.5	38.9	0.98
				FLS 9-4	16140	8940	263.4	145.9	0.98
				FLS 9-5	80040	63900	1298.8	1035.4	0.97
				FLS 9-6	86400	6360	1400.2	101.4	0.96
FLS 10	DI water	0.0558	0.2 μ m Nylon	FLS 10-1	2400	2400	46.4	46.4	1.16
				FLS 10-2	4830	2430	91.6	45.3	1.12
				FLS 10-3	7210	2380	134.7	43.1	1.09
				FLS 10-4	9720	2510	179.7	45.0	1.08
				FLS 10-5	74010	64290	1249.5	1069.8	1.00
				FLS 10-6	83982	9972	1410.3	160.8	0.97
				FLS 10-7	86492	2510	1450.7	40.4	0.97
FLS 11	GG water	0.0559	0.45 μ m Nylon	FLS 11-1	2400	2400	37.5	37.5	0.94
				FLS 11-2	4815	2415	76.6	39.1	0.97
				FLS 11-3	7205	2390	115.6	39.0	0.98
				FLS 11-4	12213	5008	197.0	81.4	0.98
				FLS 11-5	76651	64438	1224.6	1027.6	0.96
				FLS 11-6	88665	12014	1413.8	189.2	0.94
				FLS 11-7	91551	2886	1459.1	45.4	0.94
FLS 12	GG water	0.0556	0.45 μ m Nylon	FLS 12-1	2480	2480	40.8	40.8	0.99
				FLS 12-2	4942	2462	82.3	41.5	1.01
				FLS 12-3	7740	2798	129.2	46.9	1.01
				FLS 12-4	10795	3055	177.3	48.1	0.94
				FLS 12-5	74810	64015	1227.7	1050.4	0.98
				FLS 12-6	88570	13760	1450.5	222.8	0.97
				FLS 12-7	91450	2880	1497.0	46.5535	0.97
FLS 13	GG water	0.0552	0.45 μ m Nylon	FLS 13-1	2400	2400	40.5	40.5	1.01
				FLS 13-2	4812	2412	80.6	40.2	1.00
				FLS 13-3	7200	2388	120.3	39.7	1.00
				FLS 13-4	11730	4530	195.2	74.9	0.99
				FLS 13-5	76620	64890	1244.0	1048.8	0.97
				FLS 13-6	88973	12353	1440.9	196.9	0.96
FLS 14	DI water	0	0.45 μ m Nylon	FLS 14-1	1835	1835	31.5	31.5	1.03
				FLS 14-2	3700	1865	63.5	32.0	1.03
FLS 15	GG water	0.056	0.45 μ m Nylon	FLS 15-1	2860	2860	48.5	48.5	1.02
				FLS 15-2	5674	2814	95.5	47.0	1.00
				FLS 15-3	8527	2853	143.1	47.6	1.00
				FLS 15-4	73080	64553	1194.9	1051.8	0.98
				FLS 15-5	86672	13592	1414.2	219.3	0.97
				FLS 15-6	90005	3333	1467.7	53.6	0.96

10.2 Input Files in Phreeqc Format

Input file for modelling degradation of Sulfadur HCP in DI water according to batch experiments:

```
PHASES
fix_pe
    e- = e-
    log_k = 0
K-hydroxide
    KOH + H+ = H2O + K+
    log_K = 26      #constant chosen to dissolve it immediately
Na-hydroxide
    NaOH + H+ = H2O + Na+
    log_K = 26      #constant chosen to dissolve it immediately
CaO
    CaO + 2H+ = Ca+2 + H2O
    log_K = 26      #constant chosen to dissolve it immediately
TobH
    (CaO)2(SiO2)3(H2O)5 = 3 SiO(OH)3- + 2 Ca+2 + 1 OH-
    log_k -18.394
T5C
    (CaO)2.5(SiO2)2.5(H2O)5 = 2.5 SiO(OH)3- + 2.5 Ca+2 + 2.5 OH-
    log_k -23.27
T2CMOD
    (CaO)3(SiO2)2(H2O)5 = 2 SiO(OH)3- + 3 Ca+2 + 4 OH-
    log_k -25.8
SOLUTION 1
temp 25
pH 12.480
pe 4
redox O(-2)/O(0)
units mol/kgw
density 1
Al 1.221e-005
C 6.52e-006
Ca 1.956e-002
O(0) 1 O2(g) -0.7
S 1.832e-005
Si 3.898e-005
-water 1 # kg
EQUILIBRIUM_PHASES 1
calcite 0 0.011
portlandite 0 0.3236
fix_pe -4 O2(g)
K-hydroxide 0 0.0072
Na-hydroxide 0 0.0012
gypsum 0 0.0064
Al(OH)3am 0 0.008
CaO 0 0.0246
Anhydrite 0 0
Brucite 0 0
C2AH8 0 0
C4AH13 0 0
CAH10 0 0
CH4(g) 0 0
CO2(g) 0 0
Ettringite 0 0.00293
H2(g) 0 0
H2S(g) 0 0
```

```

N2(g) 0 0
O2(g) 0 0
SiO2am 0 0
Thaumasite 0 0
hemicarboaluminate 0 0
hydrotalciteC 0 0
hydrotalciteOH 0 0.00248
monocarboaluminate 0 0
monosulfoaluminate 0 0
stratlingite 0 0
syngenite 0 0
tricarboaluminate 0 0
SOLID_SOLUTIONS 1
  CSH3T
    -comp T2CMOD 0.1686
    -comp T5C 0
    -comp TobH 0
INCREMENTAL_REACTIONS true
REACTION 1
H2O 1
C 4.297e-7
  15265.25 moles in 200 steps
end

```

Input file for modelling degradation of Sulfadur HCP in GG water according to batch experiments:

```

PHASES
fix_pe
  e- = e-
  log_k = 0
K-hydroxide
  KOH + H+ = H2O + K+
  log_K = 26 #constant chosen to dissolve it immediately
Na-hydroxide
  NaOH + H+ = H2O + Na+
  log_K = 26 #constant chosen to dissolve it immediately
CaO
  CaO + 2H+ = Ca+2 + H2O
  log_K = 26 #constant chosen to dissolve it immediately
TobH
  (CaO)2(SiO2)3(H2O)5 = 3 SiO(OH)3- + 2 Ca+2 + 1 OH-
  log_k -18.394
T5C
  (CaO)2.5(SiO2)2.5(H2O)5 = 2.5 SiO(OH)3- + 2.5 Ca+2 + 2.5 OH-
  log_k -23.27
T2CMOD
  (CaO)3(SiO2)2(H2O)5 = 2 SiO(OH)3- + 3 Ca+2 + 4 OH-
  log_k -25.8
SOLUTION 1
temp 25
pH 12.480
pe 4
redox O(-2)/O(0)
units mol/kgw
density 1
Al 1.221e-005
C 6.52e-006
Ca 1.956e-002
O(0) 1 O2(g) -0.7
S 1.832e-005
Si 3.898e-005
-water 1 # kg
EQUILIBRIUM_PHASES 1

```

```

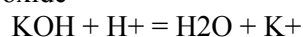
calcite 0 0.011
portlandite 0 0.3236
fix_pe -4 O2(g)
K-hydroxide 0 0.0072
Na-hydroxide 0 0.0012
gypsum 0 0.0064
Al(OH)3am 0 0.008
CaO 0 0.0246
Anhydrite 0 0
Brucite 0 0
C2AH8 0 0
C4AH13 0 0
CAH10 0 0
CH4(g) 0 0
CO2(g) 0 0
Ettringite 0 0.00293
H2(g) 0 0
H2S(g) 0 0
N2(g) 0 0
O2(g) 0 0
SiO2am 0 0
Thaumasite 0 0
hemicarboaluminate 0 0
hydrotalciteC 0 0
hydrotalciteOH 0 0.00248
monocarboaluminate 0 0
monosulfoaluminate 0 0
stratlingite 0 0
syngenite 0 0
tricarboaluminate 0 0
SOLID_SOLUTIONS 1
CSH3T
-comp T2CMOD 0.1686
-comp T5C 0
-comp TobH 0
INCREMENTAL_REACTIONS true
REACTION 1
H2O 1
CaCl2:2H2O 4.500e-6
MgSO4:7H2O 1.800e-6
NaCl 1.260e-5
KCl 1.800e-6
NaHCO3 3.240e-5
MgCl2:6H2O 1.800e-7
Na2SiO3:9H2O 9.001e-7
HCl 1.783e-6
15276.25 moles in 200 steps
end

```

Input file for modelling degradation of Sulfadur HCP according to degradation experiments in the thin-layer flow-through reactor. Example with DI water, equilibrated in air:

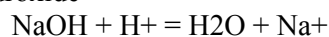
PHASES

K-hydroxide



$$\log_K = 26$$

Na-hydroxide



$$\log_K = 26$$

TobH



log_k -18.394

T5C



log_k -23.27

T2CMOD



log_k -25.8

SOLUTION 0

temp 25
pH 5.52
pe 4
redox O(-2)/O(0)
units mol/kgw
density 1
C 2.344e-005
O(0) 1 O2(g) -0.7
-water 0.1 # kg

SOLUTION 1-11

temp 25
pH 12.48
pe 4
redox O(-2)/O(0)
units mol/kgw
density 1
Ca 0.0196
O(0) 1 O2(g) -0.7
-water 0.1 # kg

end

RATES

brucite

-start
1 A0 = parm(1)
10 rate = 1E-10 * (1 - SR("brucite"))
20 moles = rate * time
30 save moles
-end

Calcite

-start
1 A0 = parm(1)
10 rate = A0 * 7.5E-7 * (m / m0) * (1 - SR("Calcite"))
20 moles = rate * time
30 save moles
-end

Ettringite

-start
1 A0 = parm(1)
10 rate = A0 * 2e-9 * (m / m0) * (1 - SR("Ettringite"))
20 moles = rate * time
30 save moles
-end

Gypsum

start
1 A0 = parm(1)
10 rate = A0 * 0.5e-5 * (m / m0) * (1 - SR("Gypsum"))
20 moles = rate * time
30 save moles

```

-end
  hydrotalciteOH
-start
1 A0 = parm(1)
10 rate = A0 * 2E-10 * (m / m0) * (1 - SR("hydrotalciteOH"))
20 moles = rate * time
30 save moles
-end
  K-hydroxide
-start
1 A0 = parm(1)
10 rate = 1E-3 * (m / m0) * (1 - SR("K-hydroxide"))
20 moles = rate * time
30 save moles
-end
  Na-hydroxide
-start
1 A0 = parm(1)
10 rate = 1E-3 * (m / m0) * (1 - SR("Na-hydroxide"))
20 moles = rate * time
30 save moles
-end
  Portlandite
-start
1 A0 = parm(1)
10 rate = A0 * 1.3E-06 * (m / m0) * (1 - SR("Portlandite"))
20 moles = rate * time
30 save moles
-end
  T2CMOD
-start
1 A0 = parm(1)
10 rate = A0 * (m / m0) * 7E-9 * (1 - SR("T2CMOD"))
20 moles = rate * time
30 save moles
-end
  T5C
-start
1 A0 = parm(1)
10 rate = 3.1E-11 * (1 - SR("T5C"))
20 moles = rate * time
30 save moles
-end
  TobH
-start
1 A0 = parm(1)
10 rate = A0 * (m / m0) * 3.1e-11 * (1 - SR("TobH"))
20 moles = rate * time
30 save moles
-end
INCREMENTAL_REACTIONS true
TRANSPORT
  -cells          11
  -shifts         25000
  -time_step      4.2
  -diffusion_coefficient 0

```

```

-thermal_diffusion 1 0
-multi_d false
KINETICS 1-10
brucite
-formula Mg(OH)2 1
-m 0
-parms 0
-tol 1e-008
Calcite
-formula CaCO3 1
-m 7.85E-04
-parms 3.93E-02
-tol 1e-008
Ettringite
-formula Ca6Al2(SO4)3(OH)12:26H2O 1
-m 2.09E-04
-parms 2.63
-tol 1e-008
Gypsum
-formula CaSO4:2H2O 1
-m 4.56E-04
-parms 3.93E-02
-tol 1e-008
hydrotalciteOH
-formula Mg4Al2(OH)14:3H2O 1
-m 1.77E-04
-parms 1.964
-tol 1e-010
K-hydroxide
-formula KOH 1
-m 5.14E-04
-parms 4.90E-02
-tol 1e-008
Na-hydroxide
-formula NaOH 1
-m 8.64E-05
-parms 5.88E-03
-tol 1e-008
Portlandite
-formula Ca(OH)2 1
-m 2.31E-02
-parms 12
-tol 1e-008
T2CMOD
-formula (CaO)3(SiO2)2(H2O)5 1
-m 5.52e-3
-parms 2.72e+1
-tol 1e-008
T5C
-formula (CaO)2.5(SiO2)2.5(H2O)5 1
-m 0
-parms 0
-tol 1e-008
TobH
-formula (CaO)2(SiO2)3(H2O)5 1
-m 8.05E-04

```

```
-parms 4.37E+01
-tol 1e-008
-steps 1
-step_divide 1
-runge_kutta 3
-bad_step_max 500
-cvode true
-cvode_steps 100
-cvode_order 5
END
```

10.3 Chemical Analyses from flow-through experiments using Holcim-1 HCP

Table 33 A and B: Flow-through experiment performed in ambient air and N₂ atmosphere, respectively. All concentrations given in mol/l. Red colour indicates values below, blue indicates values above linear calibration range and yellow background flags results lying less than 10 % out of linear calibration range. Where concentrations show “<<”, there was no quantifiable signal detected. Each experimental series is represented in one block, divided in two parts: The upper part giving all information making strict exclusions basing on analytical detection limits; the lower part of each block (marked as *italics*) giving only the quantifications of samples that were identified out of calibration range in the upper part.

Table A:

Sample	Sample volume (ml)	pH	Al	Si	Sr	Ba	Ca	Na	K	S(VI)	N(V)	Cl(I)
FL 1-1	20	12.15	3.16E-05	<7.22E-5	1.73E-06	1.11E-06	5.88E-03	< 8.7E-5	3.46E-04	1.53E-04	<<1.61E-05	3.01E-04
FL 1-2	20	11.89	2.50E-05	1.38E-04	1.34E-06	6.04E-07	2.42E-03	< 8.7E-5	7.59E-04	1.47E-04	3.56E-04	>5.64E-4
FL 1-3	20	11.69	1.89E-05	1.85E-04	1.45E-06	3.39E-07	1.15E-03	<< 8.7E-5	3.40E-04	1.59E-04	<<1.61E-06	3.28E-04
FL 1-4	20	11.54	1.70E-05	2.33E-04	1.44E-06	<3.67E-07	9.76E-04	<< 8.7E-5	1.67E-04	1.64E-04	<<1.61E-06	1.64E-04
FL 1-5	20	11.40	1.64E-05	2.40E-04	1.17E-06	<3.67E-07	8.51E-04	<< 8.7E-5	3.31E-04	1.13E-04	<<1.61E-06	2.86E-04
<i>FL 1-1</i>				5.98E-05				1.90E-05				
<i>FL 1-2</i>								1.21E-06				6.94E-04
<i>FL 1-3</i>												
<i>FL 1-4</i>						2.18E-07						
<i>FL 1-5</i>						1.46E-07						

Table B:

Sample	Sample volume (ml)	pH	Al	Si	Sr	Ba	Ca	Na	K	S(VI)	N(V)	Cl(I)
FL 2-1	20	11.63	-	-	-	-	1.06E-03	<<8.70E-5	<<5.12E-5	9.15E-05	1.12E-04	1.07E-05
FL 2-2	21	11.26	-	-	-	-	1.21E-04	<<8.70E-5	<<5.12E-5	4.66E-05	7.08E-06	2.71E-06
FL 2-3	20	11.05	-	-	-	-	5.11E-05	<<8.70E-5	<<5.12E-5	3.56E-05	6.03E-06	<2.82E-6
FL 2-4	20	10.95	-	-	-	-	<4.99E-5	<<8.70E-5	<<5.12E-5	2.97E-05	5.23E-06	<2.82E-6
FL 2-5	20	10.84	-	-	-	-	<4.99E-5	<<8.70E-5	<<5.12E-5	2.39E-05	4.86E-06	<2.82E-6
FL 2-6	21	10.76	-	-	-	-	<4.99E-5	<<8.70E-5	<<5.12E-5	2.06E-05	4.62E-06	<2.82E-6
FL 2-1												
FL 2-2												
FL 2-3												2.41E-06
FL 2-4							4.05E-05					2.03E-06
FL 2-5							3.00E-05					1.79E-06
FL 2-6							2.01E-05					2.00E-06
FL 3-1	20	11.56										
FL 3-2	20	11.26										
FL 3-3	20	11.06	An error in the setup of the reactor was discovered after the experiment. Therefore, no analyses of ions were performed even though evolution of pH was inconspicuous									
FL 3-4	20	10.91										
FL 3-5	20	10.75										
FL 4-1	20	11.84	1.65E-05	1.01E-04	1.34E-06	8.02E-07	3.58E-03	<8.70E-05	<5.12E-5	1.30E-04	1.38E-05	4.23E-04
FL 4-2	20	11.49	1.07E-05	1.37E-04	8.88E-07	2.28E-07	2.40E-04	<4.35E-05	<2.56E-5	9.13E-05	1.62E-06	2.68E-06
FL 4-3	20	11.30	9.73E-06	1.46E-04	7.50E-07	1.36E-07	>4.99E-4	<<4.35E-06	7.40E-06	7.61E-05	1.47E-06	<2.82E-6
FL 4-4	20	11.18	9.04E-06	1.42E-04	6.49E-07	9.58E-08	6.20E-04	<8.70E-06	5.69E-06	6.57E-05	<1.61E-06	<2.82E-6
FL 4-5	20.5	11.08	8.57E-06	1.34E-04	5.63E-07	7.46E-08	7.81E-04	<8.70E-06	<5.12E-6	5.50E-05	<<1.61E-06	<2.82E-6
FL 4-6	20	11.02	8.38E-06	1.27E-04	4.88E-07	6.18E-08	6.70E-04	<8.70E-06	<5.12E-6	4.66E-05	<1.61E-06	<2.82E-6
FL 4-7	20	10.97	8.42E-06	1.26E-04	4.32E-07	5.43E-08	5.59E-04	<4.35E-06	3.91E-06	3.79E-05	<<1.61E-06	<2.82E-6
FL 4-8	20	10.90	8.19E-06	1.21E-04	3.79E-07	4.71E-08	5.29E-04	<4.35E-06	2.70E-06	3.28E-05	<1.61E-06	<2.82E-6
FL 4-9	20	10.87	7.76E-06	1.16E-04	3.33E-07	6.04E-08	4.79E-04	<4.35E-06	2.58E-06	2.79E-05	<1.61E-06	<2.82E-6

Continued

Sample	Sample volume (ml)	pH	Al	Si	Sr	Ba	Ca	Na	K	S(VI)	N(V)	Cl(I)
FL 4-1								2.56E-05	3.33E-05			
FL 4-2								7.07E-06	1.05E-05			
FL 4-3							1.26E-03					2.31E-06
FL 4-4								3.06E-06			1.25E-06	2.17E-06
FL 4-5								2.48E-06	4.57E-06			1.70E-06
FL 4-6								2.93E-06	4.34E-06		1.02E-06	1.85E-06
FL 4-7								2.35E-06				1.70E-06
FL 4-8								1.65E-06			1.04E-06	1.61E-06
FL 4-9								1.82E-06			1.15E-06	1.74E-06
FL 5-1	20	11.91	1.81E-05	1.06E-04	1.54E-06	8.45E-07	4.60E-03	<8.70E-5	5.03E-05	1.60E-04	1.58E-05	2.62E-05
FL 5-2	20	11.50	1.29E-05	1.75E-04	1.19E-06	2.32E-07	1.58E-03	<4.35E-5	<2.56E-5	-	-	-
FL 5-3	21.6	11.31	1.12E-05	1.90E-04	1.00E-06	1.39E-07	-	-	-	9.85E-05	<<1.61E-6	<<2.82E-6
FL 5-4	20	11.20	1.13E-05	2.01E-04	8.00E-07	1.01E-07	6.93E-04	<8.70E-6	5.68E-06	-	-	-
FL 5-5	20	11.12	1.06E-05	1.88E-04	6.69E-07	8.43E-08	9.12E-04	<8.70E-6	<5.12E-6	6.74E-05	<<1.61E-6	2.96E-06
FL 5-6	45	11.02	1.00E-05	1.74E-04	4.74E-07	7.06E-08	7.02E-04	<8.70E-6	<5.12E-6	-	-	-
FL 5-7	45	10.89	9.80E-06	1.56E-04	3.12E-07	4.76E-08	5.07E-04	<4.35E-6	<2.56E-6	2.20E-05	<<1.61E-6	<2.82E-6
FL 5-8	48	10.77	9.43E-06	1.39E-04	2.16E-07	3.68E-08	4.18E-04	<4.35E-6	<2.56E-6	1.12E-05	<<1.61E-6	<2.82E-6
FL 5-9	47.5	10.67	9.41E-06	1.18E-04	1.55E-07	3.66E-08	3.28E-04	<4.35E-6	<2.56E-6	-	-	-
FL 5-10	20.1	10.60	9.36E-06	1.11E-04	1.27E-07	2.55E-08	2.64E-04	<4.35E-6	<2.56E-6	-	-	-
FL 5-1								2.48E-05				
FL 5-2								6.80E-06	1.37E-05			
FL 5-3												
FL 5-4								2.22E-06				
FL 5-5								1.81E-06	3.98E-06			
FL 5-6								1.29E-06	2.42E-06			
FL 5-7								7.13E-07	1.21E-06			1.96E-06
FL 5-8								5.34E-07	1.34E-06			2.22E-06
FL 5-9								5.88E-07	8.08E-07			
FL 5-10								9.56E-07	1.00E-06			

Continued

Sample	Sample volume (ml)	pH	Al	Si	Sr	Ba	Ca	Na	K	S(VI)	N(V)	Cl(I)
FL 6-1	20	11.53	-	-	-	-	7.16E-04	<<4.35E-6	<<5.12E.5	8.33E-05	1.64E-05	2.86E-05
FL 6-2	20	11.15	-	-	-	-	-	-	-	-	-	-
FL 6-3	20	10.92	-	-	-	-	5.03E-04	<<4.35E-6	<5.12E.6	3.43E-05	<<1.61E.6	4.53E-06
FL 6-4	20	10.78	-	-	-	-	3.47E-04	<<4.35E-6	<5.12E.6	-	-	-
FL 6-5	40	10.66	-	-	-	-	2.96E-04	<<4.35E-6	<2.56E-6	-	-	-
FL 6-6	27	10.55	-	-	-	-	2.24E-04	<<4.35E-6	<2.56E-6	1.17E-05	<<1.61E.6	3.32E-06
FL 6-1												
FL 6-2												
FL 6-3									3.64E-06			
FL 6-4									4.25E-06			
FL 6-5									2.15E-06			
FL 6-6									2.08E-06			
FL 7-1	30	11.77	1.36E-05	1.30E-04	1.37E-06	5.84E-07	>2.00E-3	8.37E-05	2.81E-05	1.39E-04	1.14E-05	1.74E-05
FL 7-2	35	11.33	1.10E-05	1.69E-04	8.43E-07	1.46E-07	-	-	-	8.33E-05	<1.61E-6	3.30E-06
FL 7-3	40	11.13	9.98E-06	1.51E-04	5.52E-07	7.69E-08	7.97E-04	<8.70E-6	<5.12E.6	5.08E-05	<<1.61E-6	<2.82E-6
FL 7-4	45	10.98	9.33E-06	1.35E-04	3.76E-07	5.34E-08	-	-	-	3.03E-05	<<1.61E-6	<2.82E-6
FL 7-5	45	10.84	8.90E-06	1.15E-04	2.71E-07	3.70E-08	3.78E-04	6.31E-06	<2.56E-6	1.80E-05	<<1.61E-6	4.77E-06
FL 7-6	45	10.72	8.50E-06	1.04E-04	2.07E-07	3.79E-08	-	-	-	-	-	-
FL 7-7	42.5	10.64	8.33E-06	9.28E-05	1.63E-07	2.50E-08	2.70E-04	1.15E-06	<2.56E-6	-	-	-
FL 7-8	615	10.25	8.44E-06	5.65E-05	6.90E-08	1.55E-08	5.11E-05	<4.35E-6	<2.56E-6	4.87E-06	3.12E-06	<2.82E-6
FL 7-9	20.5	10.03	6.98E-06	3.12E-05	3.07E-08	<1.44E-08	4.29E-05	<4.35E-6	<2.56E-6	1.34E-06	<<1.61E-6	<2.82E-6
FL 7-1							3.37E-03					
FL 7-2											1.36E-06	
FL 7-3								1.61E-06	3.51E-06			2.41E-06
FL 7-4												2.12E-06
FL 7-5									2.75E-07			
FL 7-6												
FL 7-7									4.21E-07			
FL 7-8								3.57E-06	3.49E-07			2.44E-06
FL 7-9						9.24E-09		3.24E-07	4.23E-07			2.07E-06

Continued

Sample	Sample volume (ml)	pH	Al	Si	Sr	Ba	Ca	Na	K	S(VI)	N(V)	Cl(I)
FL 8-1	31	11.67	1.77E-05	1.76E-04	1.54E-06	6.51E-07	3.64E-03	>6.96E-3	2.84E-05	6.62E-05	<<5.16E-5	<9.03E-5
FL 8-2	30	11.18	1.20E-05	2.25E-04	9.98E-07	1.83E-07	8.33E-04	>6.96E-3	<2.05E-5	<3.33E-5	<<5.16E-5	<<9.03E-5
FL 8-3	31.5	10.99	1.14E-05	2.04E-04	6.53E-07	1.23E-07	3.44E-04	>6.96E-3	<2.05E-5	-	-	-
FL 8-4	30	10.85	1.08E-05	1.86E-04	4.49E-07	9.74E-08	2.05E-04	>6.96E-3	<2.05E-5	<<3.33E-5	<<5.16E-5	<<9.03E-5
FL 8-5	30	10.75	-	-	-	-	1.96E-04	>6.96E-3	<2.05E-5	-	-	-
FL 8-6	45	10.64	1.07E-05	1.51E-04	2.42E-07	7.57E-08	2.80E-04	>6.96E-3	<2.05E-5	-	-	-
FL 8-7	45	10.51	-	-	-	-	1.18E-04	>6.96E-3	<2.05E-5	-	-	-
FL 8-8	50	10.38	9.62E-06	9.62E-05	1.25E-07	<7.18E-08	1.05E-04	>6.96E-3	<2.05E-5	-	-	-
FL 8-1								9.75E-02				
FL 8-2								9.45E-02	5.45E-06	2.11E-05		1.75E-05
FL 8-3								9.40E-02	3.03E-06			
FL 8-4								9.25E-02	2.28E-06			
FL 8-5								1.03E-01	1.30E-06			
FL 8-6								6.99E-02	3.52E-06			
FL 8-7								9.71E-02	1.06E-06			
FL 8-8						5.93E-08		1.02E-01	1.17E-06			
FL 9-1	11	11.88	-	-	-	-	>3.99E-3	>6.96E-3	6.93E-05	9.61E-05	8.55E-05	9.62E-05
FL 9-2	20	11.49	1.64E-05	2.32E-04	1.45E-06	4.01E-07	2.04E-03	>6.96E-3	<2.05E-5	3.13E-05	<<4.96E-5	<8.68E-5
FL 9-3	30	11.22	1.42E-05	2.33E-04	9.85E-07	2.02E-07	8.05E-04	>6.96E-3	<2.05E-5	-	-	-
FL 9-4	620	10.43	1.01E-05	9.44E-05	1.58E-07	6.03E-08	1.61E-04	>6.96E-3	<2.05E-5	-	-	-
FL 9-5	20	9.86	8.62E-06	4.98E-05	<5.76E-08	5.38E-08	6.03E-05	>6.96E-3	<2.05E-5	-	-	-
FL 9-6	45	9.83	9.00E-06	4.18E-05	<5.76E-08	4.25E-08	4.02E-05	>5.8E-3	<1.71E-5	-	-	-
FL 9-7	47	9.80	8.36E-06	3.81E-05	<5.76E-08	4.00E-08	-	-	-	-	-	-
FL 9-8	51.5	9.73	7.72E-06	3.87E-05	<1.15E-07	<7.18E-08	3.68E-05	>5.8E-3	<1.71E-5	-	-	-
FL 9-1							4.95E-03	9.07E-02				
FL 9-2								9.01E-02	1.28E-05			9.86E-06
FL 9-3								9.04E-02	4.79E-06			
FL 9-4								9.05E-02	7.43E-06			
FL 9-5					3.66E-08			9.04E-02	2.69E-06			
FL 9-6					3.31E-08			9.13E-02	6.23E-07			
FL 9-7					2.94E-08							
FL 9-8					2.56E-08	3.89E-08		9.22E-02	8.48E-07			

*1 sample FL 7-8 probably contaminated

Comments to the results of Flow-through experiments:

In experiment FL 1 K and Cl⁻ concentrations were biased by pH-measurement (storage solution of electrode is 3 M KCl solution) that was done in the solutions before analysis of the dissolved ions. The analysis of Ca, Na and K in sample FL 4-3 deviates from expectation based on the trend of concentrations. It was analysed in another run by IC some days later than other samples.

Contamination

In SEM analysis of degraded HCP after experiment FL 9, a grain of composition 12.0 Tc , 1.5 Mo, 4.4 Cl, 32.2 O and 50.6 C (atomic%, elements below 1% omitted). Therefore, in ICP-MS analysis the masses of ⁹⁹Tc was also observed, even though not quantified. There was no Tc detected in any of the analysed solutions (TN2, FL 4, FL 5 and FL 7 to FL 9).

10.4 SEM-Analyses

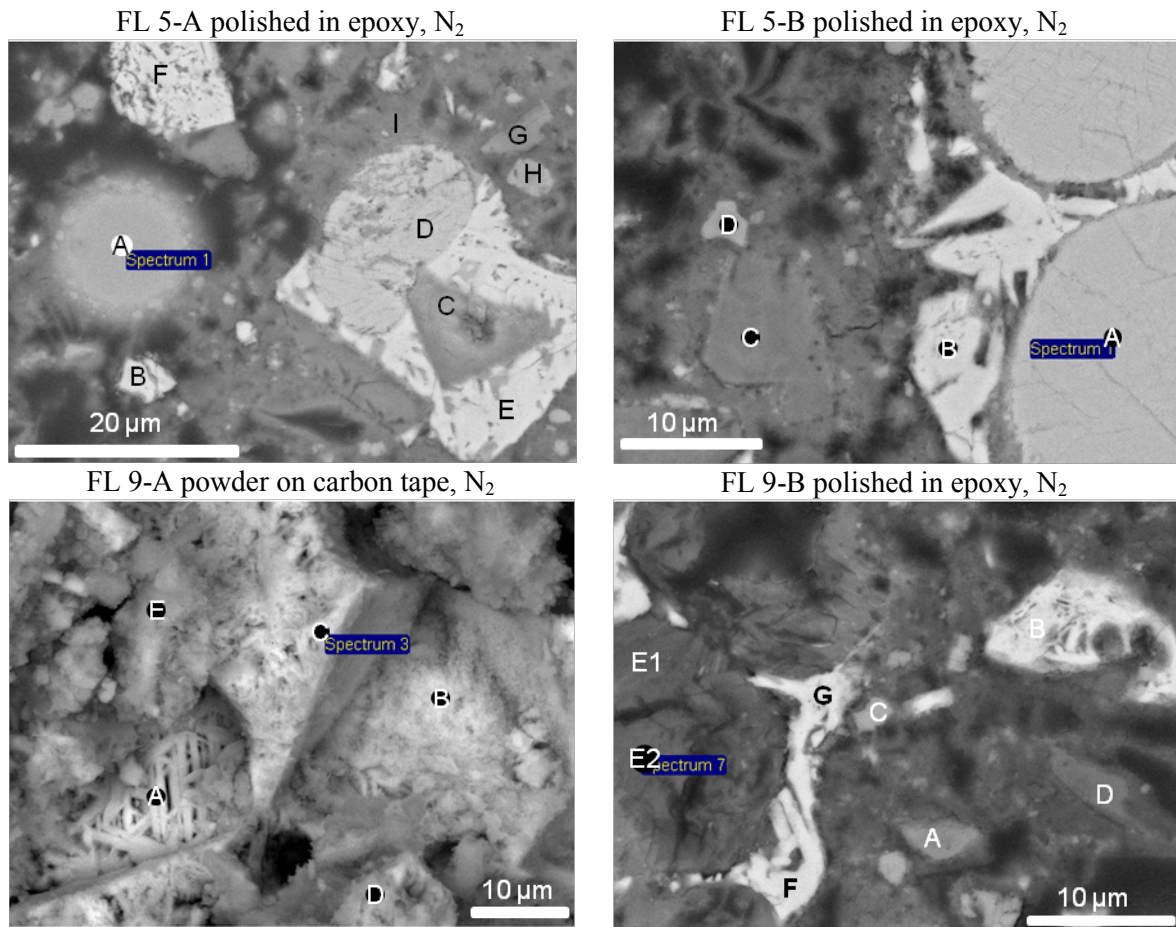


Figure 82 Cement samples, analysed by FESEM after flow-through experiments with Holcim-1 HCP. Points and areas marked in figures were analysed for elements and results are shown in Table 34

Table 34 Results from point analyses and line scan areas indicated in Figure 82. First column indicates elements including which electron transfer was used for quantification. Results are given in atomic percent. In the lower part ion correlations are shown.

Sample Spot	FL 5-A								
	A	B	C	D	E	F	G	H	I
Suggested phase	Fly ash contamination?	C4AF	dicalcium silicate	dicalcium silicate	C4AF	C4AF	Dolomite	Calcite	C-S-H 1.4
C K	14.98	12.86	14.64	10.1	11.2	11.66	21.07	20.11	28.7
O K	58.4	55.52	49.13	56.85	54.46	55.17	59.11	60.65	44.53
Na K	0.13	0.07	0	0.07	-0.04	0.08	-0.02	-0.07	-0.03
Mg K	1.32	1.12	0.98	0.18	1.15	0.95	7.14	0.25	0.16
Al K	5.64	6.05	1.22	1.05	5.97	5.79	0.61	0.19	0.83
Si K	15.17	1.57	10.15	10.04	1.81	1.84	2.99	1.55	10.47
S K	0.08	0.34	1.9	0.57	0.34	0.72	0.12	-0.01	0.17
Cl K	0.01	0.04	0.08	0.01	0.05	0.04	0.1	0.02	0.14
Ca K	1.52	15.47	21.23	20.64	17.39	16.8	8.82	17.09	14.81
Fe K	1.68	6.96	0.68	0.57	7.52	6.88	0.1	0.13	0.21

Sample Spot	FL 5-B				FL 9-A				
	A	B	C	D	A	B	C	D	E
Suggested phase	C2S	C4AF	C-S-H1.3	Calcite	C4AF		C4AF	C-S-H 1.1	C-S-H 1.1
C	11.3	9.61	18.12	20.4	3	5.56	4.62	7.91	10.98
O	54.6	56.63	51.69	53.32	36.27	25.34	61.96	62.6	52.08
Na	0.08	0.06	0.07	0.03	0.82	0.63	0.98	2.65	1.41
Mg	0.16	1.15	0.22	0.13	1.08	0.16	0.98	1.33	0.6
Al	0.79	5.92	1.11	0.26	8.47	0.75	6.54	3.45	3.05
Si	10.4	1.57	12.29	3.28	4.03	2.55	3.09	8.12	13.26
S	0.68	0.64	0.12	0.22	-0.05	0.11	0.11	0.08	0.35
Cl	0.04	0.04	0.06	0.02	0.41	0.67	0.3	1.01	0.77
K	0.02	0.11	-0.05	-0.1	-0.14	0.02	-0.02	0.07	-0.01
Ca	21.5	16.97	15.69	22.37	29.99	36.03	13.33	6.55	14.61
Fe	0.56	7.1	0.55	0.19	15.46	28.13	7.8	6.04	2.79

Sample Spot	FL 9-B								
	A	B	C	D	E1	E2	F	G	
Suggested phase	Dolomite	C4AF	Calcite	C-S-H 0.7	C-S-H 0.5	C-S-H 0.4	C4AF	C4AF	
C	20.44	12.09	27.58	41.45	44.4	40.9	13.37	13.76	
O	60.47	57.13	52.56	43.14	39.7	43.1	54.56	54.57	
Na	-0.03	0.12	0.25	0.49	0.31	0.48	0.16	0.09	
Mg	9.82	1.05	0.21	0.17	1.1	0.24	1.05	1.09	
Al	0.26	6.53	0.68	1.41	2.33	2.7	6.75	6.82	
Si	0.31	1.66	2.54	7.4	6.56	7.83	1.27	1.37	
S	0.13	0.26	0.11	0.26	0.41	0.21	0.27	0.15	
Cl	0.1	0.08	0.26	0.3	0.29	0.3	0.08	0.04	
K	-0.01	-0.01	0.01	0.01	-0.03	0.01	-0.03	0	
Ca	8.45	14.79	15.67	5.04	3.56	3.2	15.76	15.41	
Fe	0.1	6.08	0.14	0.38	1.35	0.97	6.56	6.43	

Table 35 Single-spot analyses from sample B6, reported in At.-%. Instrument and correction parameters: kV : 15.01 Tilt: 0.00 Take-off:35.03 AmpT: 102.4., Detector Type: SUTW, Sapphire Resolution:129.39 Lsec:30, EDAX ZAF Quantification (Standardless), Oxygen by difference, calculated without carbon to 100 % element sum. Sample spots are indicated in Figure 63

Element (At. %)	B6 SP_1_01	B6 SP_1_02	B6 SP_1_03	B6 SP_1_04	B6 SP_1_05	B6 SP_1_06	B6 SP_1_07	B6 SP_1_08	B6 SP_1_09	B6 SP_1_10	B6 SP_1_11	B6 SP_1_13
	Core	Core	Core	Core	Ni-rim	Ni-rim	Ni-rim	Ni-rim	Ni-rim	Core*	Core*	C2S
Al	1.2	1.3	1.7	1.2	3.8	2.5	3.7	4.4	4.8	1.0	1.2	4.2
Ca	10.8	11.0	17.7	13.2	8.3	9.6	8.9	7.3	9.2	9.2	15.1	20.1
Fe	1.9	1.3	4.1	1.0	1.6	1.1	1.5	1.8	1.8	1.3	1.3	9.1
Mg	3.4	2.8	1.1	1.6	3.9	2.1	3.6	3.6	4.6	1.6	2.7	1.0
Ni		0.2	0.7	0.5	14.5	10.7	15.3	18.6	14.2		0.1	
Oxygen	61.1	61.4	58.7	61.1	57.0	58.7	56.7	55.9	56.4	62.5	60.2	56.0
S	0.0	0.2	0.5	0.3	1.1	0.8	1.3	1.2	1.3	0.2	0.2	0.4
Si	21.6	21.8	15.7	21.1	9.9	14.5	9.1	7.2	7.8	24.1	19.3	9.1

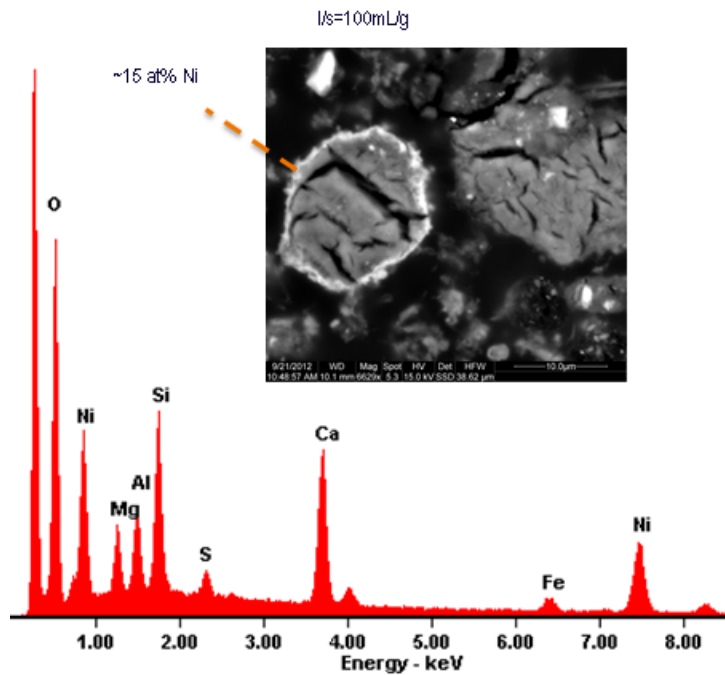


Figure 83 SEM-EDX spectrum of Ni-rim from experiment B6.

Table 36 Ni-S-H single-spot analyses from sample B14, reported in At.-%. Instrument and correction parameters: kV : 15.01 Tilt: 0.00 Take-off:35.03 AmpT: 102.4., Detector Type: SUTW, Sapphire

Resolution:129.39 Lsec:30, EDAX ZAF Quantification (Standardless), Element Normalised, calculated without carbon to 100 % element sum.

Element (At. %)	B14 Image1 Spot05	B14 Image1 Spot06	B14 Image1 Spot07	B14 Image2 Spot01	B14 Image2 Spot02	B14 Image2 Spot03	B14 Image2 Spot05-g	B14 Image3 Spot01-01	B14 Image4 Spot01	B14 Image4 Spot02	B14 Image4 Spot05
O	56.0	51.2	53.9	54.3	48.6	53.8	53.4	53.7	50.1	53.2	52.6
Mg	29.4	34.9	32.4	31.3	34.6	32.1	31.8	31.7	33.1	32.1	32.1
Al	1.6	1.4	1.5	1.4	1.5	1.5	1.6	2.1	1.9	1.7	1.4
Si	0.8	0.7	0.8	0.8	0.8	0.7	0.7	1.0	1.1	0.7	1.0
S	5.2	5.3	4.9	5.3	4.7	5.2	5.1	5.0	5.4	5.6	5.5
Cl				0.2							
Ca	0.3										
Fe	0.8	1.0	0.8	1.0	3.9	1.8	1.2	1.2	1.3	1.0	1.7
Ni	0.8	0.9	0.7	0.9	0.9	1.0	0.8				
Total	100.0	100.0	100.0	100.0	100.0	100.0	100.0	100.0	100.0	100.0	100.0

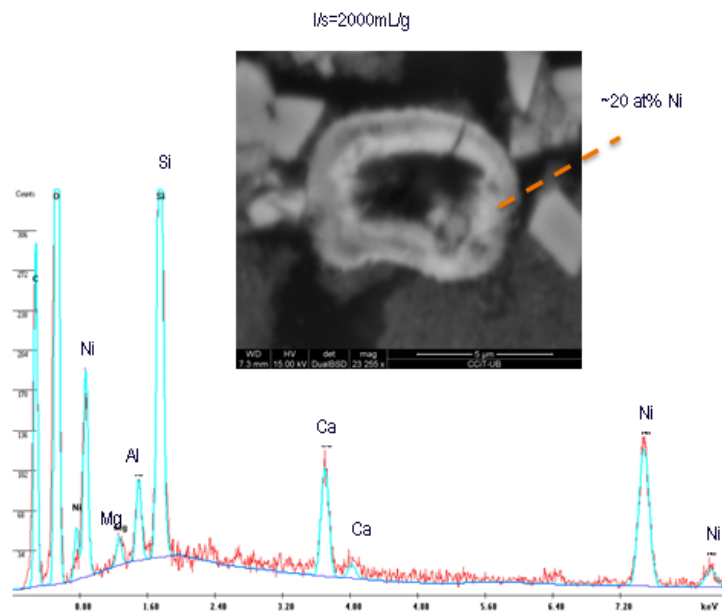


Figure 84 SEM-EDX spectrum of Ni-ring from experiment B14.

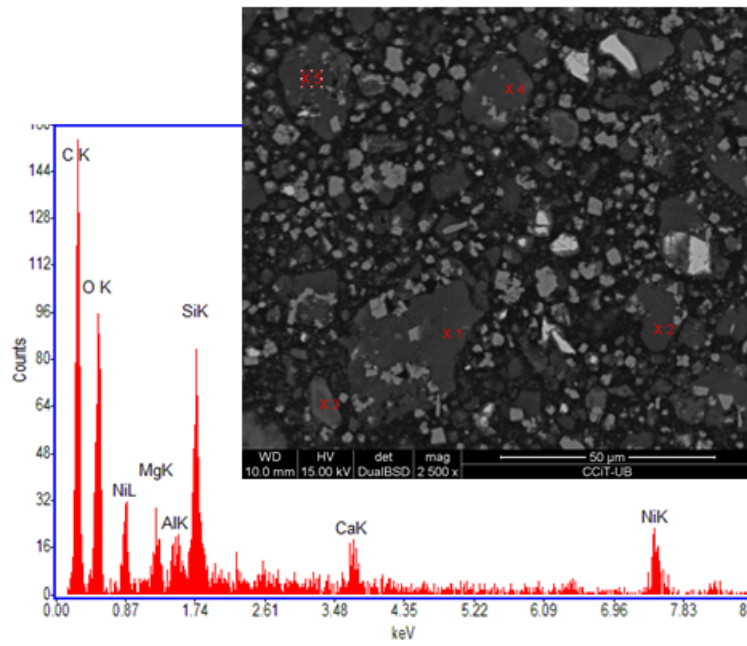


Figure 85 SEM-EDX spectrum of Ni-S-H (spot 1) from experiment B14

10.5 XRD-Analyses

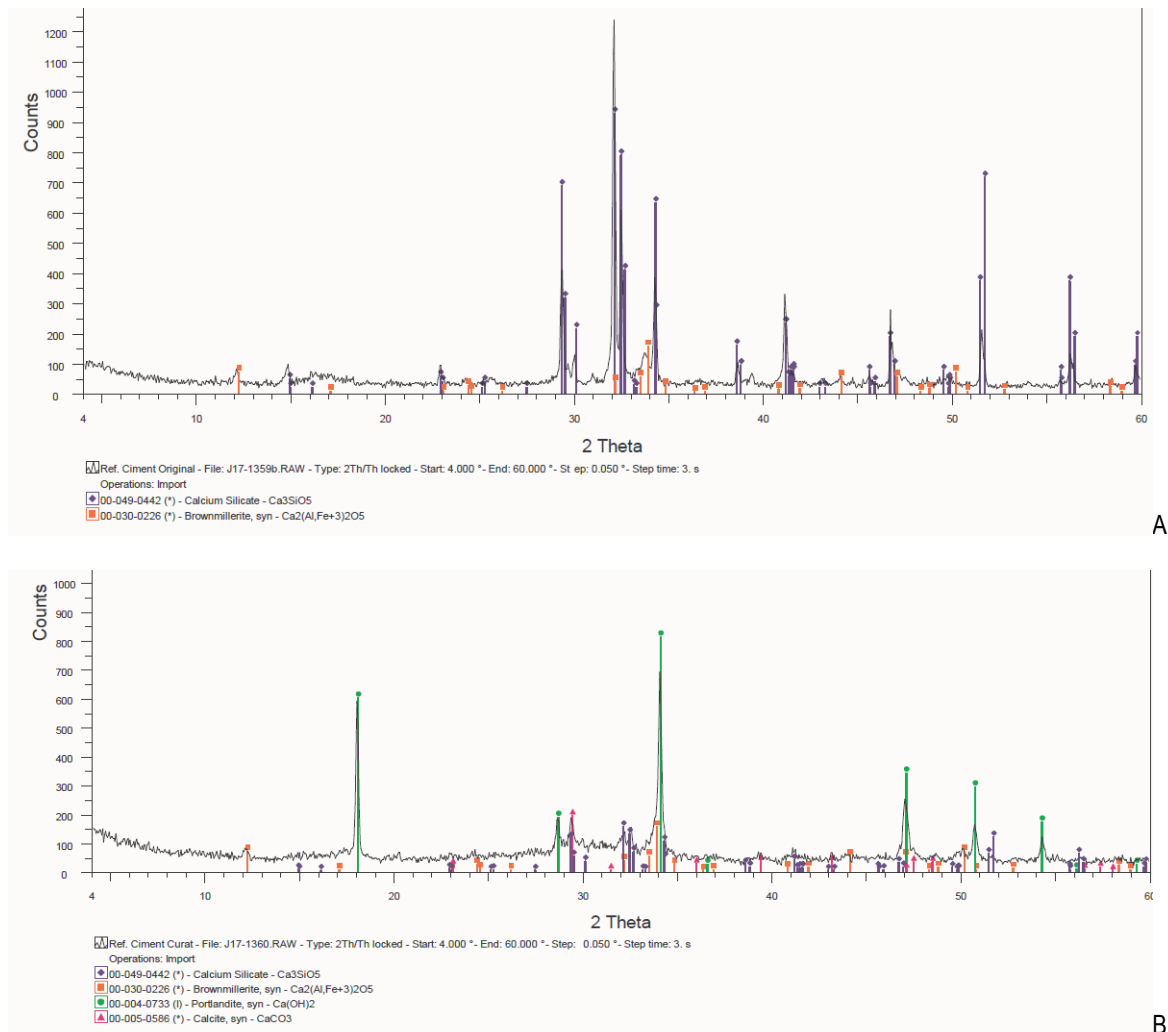


Figure 86 XRD diffractograms of A) Holcim-1 clinker - only C3S and brownmillerite were identified and B) 28 days long hydrated Holcim-1 HCP, shortly after hardening. C3S, brownmillerite, portlandite and CaCO₃ were identified (all work for these 2 figures was performed previously by CTM).

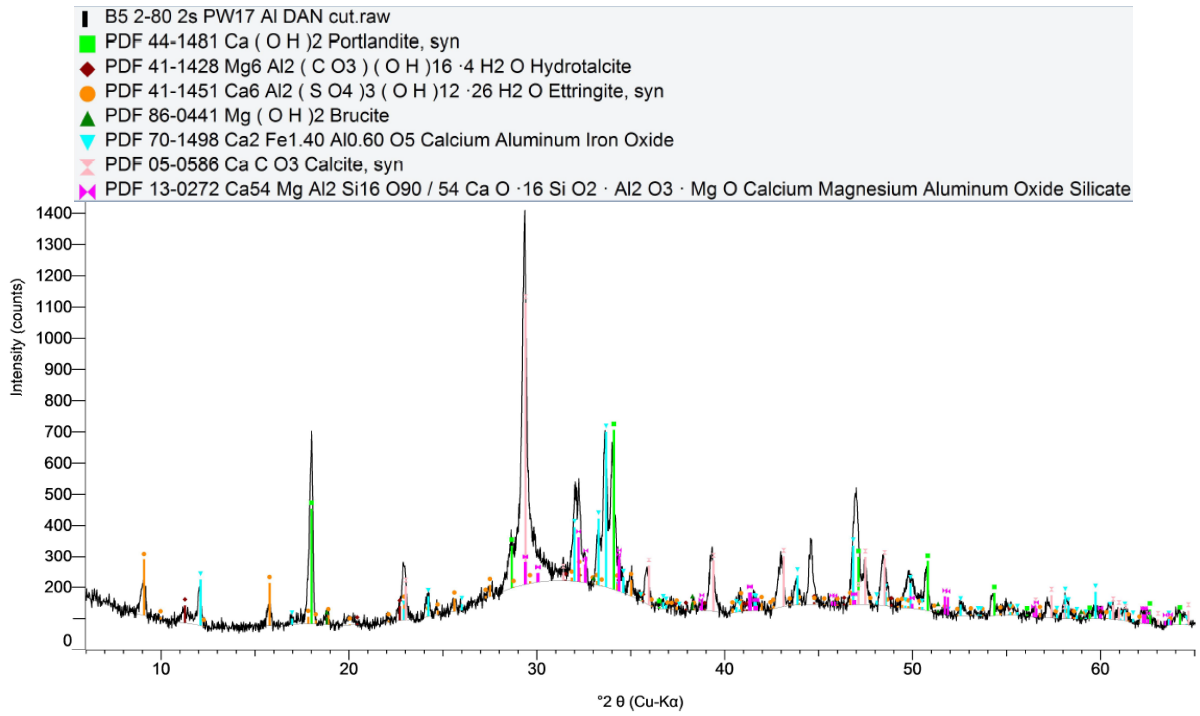


Figure 87 X-ray diffractogram of sample B5 and identified phases.